The mechanical properties of fault zones and earthquake cycle dynamics along the northern margins of the Iranian Plateau

Nicholas Wallace Dodds

Thesis submitted to the University of Oxford

for the degree of Doctor of Philosophy in Earth Sciences



Department of Earth Sciences,

University of Oxford

Hilary Term, 2021

Supervised by Professor Richard Walker and Professor Barry Parsons

Declaration

The contents of this thesis are all my own work (Nicholas Dodds), except where otherwise stated; see the author list at the start of each chapter for co-author affiliations. The views and opinions expressed herein are mine and not necessarily those of any other person or body unless so attributed.

Chapter 2: Nicholas Dodds wrote the manuscript, with contributions from Richard Walker, Christoph Gruetzner and Paul Wordsworth. The research involved several field excursions to Turkmenistan (2015–2019) by Nicholas Dodds, Richard Walker and Christoph Gruetzner, which included the paleoseismological investigations. Nicholas Dodds completed the remote geomorphological analysis of satellite optical imagery. Luminescence dating was conducted by Ed Rhodes and radiocarbon dating by Beta Analytics. Archaeological/historical context and translations were provided by Paul Wordsworth.

Chapter 3: Nicholas Dodds wrote the manuscript, with support and direction from Simon Daout and Barry Parsons. InSAR time-series analysis, inversion and modelling were done by Nicholas Dodds, with supervision from Simon Daout. Discussions with Richard Walker helped provide geological context to the results.

Chapter 4: Nicholas Dodds wrote the manuscript, with support and direction from Barry Parsons. InSAR time-series analysis, inversion and interpretation were done by Nicholas Dodds, with supervision from Simon Daout and Barry Parsons. Discussions with Richard Walker helped provide geological context to the results.

Abstract

The mechanical properties of fault zones and earthquake cycle dynamics along the northern margins of the Iranian Plateau

Nicholas Wallace Dodds
St Anne's College, Oxford

Hilary Term, 2021

This thesis presents, in integrated format, research investigating the mechanics of the earthquake cycle and the kinematics of continental deformation along the northern margins of the Iranian Plateau. The research focuses on improving the characterisation of seismic hazard surrounding the South Caspian Basin (SCB), an aseismic block moving independently of its surroundings within the Arabia-Eurasia collision. Fault zones surrounding the basin are in proximity to numerous urban agglomerations, which have a combined population exceeding 15 million. Motivated by improving the characterisation of seismic hazard in the region, this research aims to improve our understanding of the motion of the SCB with respect to its surroundings. I measure the rate and distribution of strain accumulation on the major faults facilitating the motion of the basin with Sentinel-1 InSAR time-series. I also characterise how the resulting strain is released from earthquake ruptures preserved in the geological record, from geomorphological analysis of satellite optical imagery and paleoseismological investigation of faults. The first study presents geomorphological analysis and field observations of an estimated M_W 7.8 paleo-rupture along the Main Köpetdag fault (MKDF), Turkmenistan. The MKDF is seismically-quiescent within historical records, despite its kinematic significance facilitating the motion of the SCB. However, paleoseismological investigation brackets the timing of this rupture to 600–800 years B.P.. This indicates a major earthquake is missing from historical records in neighbouring Iran, which suggests that the paucity of historical earthquakes in Turkmenistan may be misleading. The second study presents ascending and descending Sentinel-1 InSAR time-series of surface deformation from interseismic motion along the MKDF. I model the fault-parallel motion across the MKDF, and combine this with a recent geological slip-rate to constrain 8.7 $\pm$ 1.1 mm/yr right-lateral motion across the MKDF. I also measure >1 mm/yr of uplift directly to the north of the MKDF, aligning with

mapped frontal thrusts to the main strike-slip fault, and model this deformation with a strain-partitioning geometry. Using these measurements, I revise velocity triangles to constrain Iran-Eurasia-SCB kinematics. The final study presents a regional-scale velocity field derived from Sentinel-1 InSAR time-series. This presents a spatially-continuous image of the lateral extrusion of the SCB facilitated by conjugate strike-slip motion along the MKDF, and Shahroud Fault Zone (SFZ) in NE Iran. The westward component is observed to start abruptly at the Bäherden-Quchan Fault Zone (BQFZ). As well as these observations, I measure the rate of motion and present observations of the distribution of deformation along numerous major active faults through the eastern Alborz and Köpetdag, including the MKDF-SFZ conjugate system, BQFZ, and thrust faults in the eastern Köpetdag. The research I present in this thesis will provide invaluable contributions to improve the characterisation of the seismic hazard posed by faults surrounding the basin. Effective communication of these hazards will allow this knowledge to be integrated into societal awareness and infrastructure developments in the rapidly growing economies in this part of the modern Silk Roads. In future, this improved understanding should enable the mitigation of the devastating hazards posed by earthquakes along the northern margins of the Iranian Plateau.

Extended Abstract

The mechanical properties of fault zones and earthquake cycle dynamics along the northern margins of the Iranian Plateau

Nicholas Wallace Dodds

St Anne's College, Oxford

Hilary Term, 2021

This thesis presents, in integrated format, research investigating the mechanics of the earthquake cycle and kinematics of continental deformation along the northern margins of the Iranian Plateau, through the Köpetdag and Eastern Alborz mountain ranges of Turkmenistan and northeastern Iran. The research focuses on improving the characterisation of seismic hazard surrounding the South Caspian Basin (SCB), an aseismic block moving independently of its surroundings within the Arabia-Eurasia collision. Fault zones surrounding the basin are in proximity to numerous urban agglomerations, including the capital cities Tehran (Iran), Aşgabat (Turkmenistan), and Baku (Azerbaijan), which have a combined population exceeding 15 million.

Motivated by improving the characterisation of seismic hazard in the region, this research aims to improve our understanding of the motion of the SCB with respect to its surroundings. However, accurately estimating the rate and distribution of

strain accumulation and the resulting strain release along faults surrounding the SCB is difficult to constrain with conventional techniques. The rate, direction and pole of rotation of the basin is difficult to determine with GPS velocities due to the depth of water (>1000 m) and sediments (>25 km) that overlie the basement. Similarly, it is uncertain as to whether records of earthquakes, even in a region with exceptional historical records of earthquakes, are able to characterise strain release in the relatively slow-moving continental interiors. To resolve this uncertainty, I measure the rate and distribution of strain accumulation on the major faults facilitating the extrusion of the SCB with Sentinel-1 InSAR time-series. I also characterise how the resulting strain is released from earthquake ruptures preserved in the geological record, from geomorphological analysis of high-resolution satellite optical imagery and paleoseismological investigations of faults.

In Chapter 2, I present geomorphological analysis of high-resolution optical satellite imagery, field observations, and paleoseismological investigations along an inferred paleo-rupture along the Main Köpetdag fault (MKDF), Turkmenistan. The MKDF is one of the longest (≈500 km) and most rapidly moving (9.1 ± 1.3 mm/yr) faults of the Arabia-Eurasia collision zone. The fault defines the northern range front of the Köpetdag mountains and the northernmost expression of deformation within the Iranian Plateau at longitudes east of the Caspian Sea. Despite its kinematic significance, the fault has little in the way of seismicity within instrumental and historical records. The field observations indicate a fresh paleo-earthquake rupture along a ≈200-km-long section of the fault with abundant streams offset across it. I use high-resolution (40 cm) WorldView-2 satellite optical imagery to measure stream offsets and compile them into a cumulative offset probability density function (COPD). The high quality COPD yields peaks at 7.5 ±1.5 m and 12.5 ±1.5 m, which I interpret to arise from the most recent and penultimate surface rupturing earthquakes; although we note that it is not possible to separate events

with lower quality measurments which instead yield a single peak at 10 ±4 m. The paleo-earthquake rupture displaces archaeological remains, including extensive field boundaries of likely Medieval age, and a paleoseismic trench across the fault brackets the age of the most recent displacement at 600–800 years B.P.. From our measurements of displacement we estimate that the most recent palaeo-earthquake had a moment magnitude of ≈7.8 ±0.3. Despite its high magnitude, this event is missing from earthquake records from nearby Iran, suggesting that the paucity of historical earthquake records in Turkmenistan may be misleading. The Baharly, Döwgala, and Gökdepe segments of the MKDF, which extend eastwards to the city of Aşgabat, do not show fresh surface expression of faulting. Two IRSL ages of 3.4 ± 0.5 ka and 2.5 ± 0.2 ka from a river cutting exposure along the Baharly segment predate the most-recent surface rupture. I conclude that individual segments of the MKDF fault are capable of rupturing in large magnitude earthquakes, with the ends of individual ruptures controlled by segment boundaries. The occurrence of large earthquakes, combined with the rapid slip-rate, suggest that the MKDF constitutes a significant hazard to a populated region of Turkmenistan and in neighbouring northeast Iran.

In Chapter 3, I present ascending and descending Sentinel-1 InSAR time-series of surface deformation from interseismic motion along the MKDF. Previous measurements of the slip-rate across the fault have been highly variable, with a recent geological slip-rate supporting evidence for rapid strain accumulation across the fault from direct geodetic measurements. The time-series generation implements a processing strategy for the correction and performance analysis of tropospheric models from GACOS, which suggests a 25–40% under-estimation in the amplitude of the tropospheric path delay in this region. I model the fault-parallel motion across the MKDF, and combine this with a recent geological slip-rate to constrain 8.7 ± 1.1 mm/yr right-lateral motion across the MKDF. I also measure >1 mm/yr of uplift

directly to the north of the MKDF, aligning with mapped frontal thrusts to the main strike-slip fault. I model this deformation with a strain-partitioning geometry, to estimate that the shortening across the frontal thrusts accommodates 4.3 ± 1.5 mm/yr of fault-perpendicular convergence. This implies that the convergence measured by GPS velocities within the Köpetdag and East Caspian Lowlands is transferred to the north of the MKDF. I revise velocity triangles of the region to suggest that deformation along the conjugate MKDF and SFZ is representative of the motion of the SCB; moving at 9.7 mm/yr in a direction of 329° relative to Eurasia. However reconciling the modelled shortening across the frontal thrusts suggests that the rate of convergence across the MKDF is possibly slightly over-estimated, likely due to difficulty associated with high-magnitude agricultural/hydrological subsidence along the Karakum Canal irrigated zone which overprints the tectonic signal along the thrust faults.

The final study in Chapter 4 presents a regional-scale velocity field derived from Sentinel-1 InSAR time-series of the onshore extent of the SCB. The extrusion of the SCB is facilitated by conjugate strike-slip motion along the MKDF and the Shahroud Fault Zone (SFZ) in the Eastern Alborz, NE Iran. However whether strain is accommodated only by motion along the two major strike-slip faults in the conjugate system, or is partitioned on to other structures inside (i.e. through the East Caspian Lowlands, Köpetdag, or Eastern Alborz) and outside the conjugate system (both to the north of the MKDF, and to the south of the SFZ) remains an important question in establishing the motion of the SCB. To resolve this, I derive regional velocity fields in both the ascending and descending LOS, covering 600 km × 600 km of the region; and decompose these into the east-west (V_E) and sub-vertical (V_{UN}) components. I present a spatially-continuous image of the lateral extrusion of the SCB, with the westward component observed to start abruptly at the Bäherden-Quchan Fault Zone (BQFZ). The extrusion is facilitated by strike-slip

motion along the MKDF and SFZ, which have distinct velocity steps resolved in the V_E component of 4–4.5 mm/yr and 5.5–6 mm/yr mm/yr respectively. Projecting this velocity-step to fault parallel motion provides lower-bound fault parallel slip-rates along these faults of 4.8–5.4 mm/yr along the MKDF and 6.0–6.6 mm/yr along the SFZ. However the velocity fields suggest the interior of the SCB is moving faster than this, with ≈-8 mm/yr resolved in the V_E component relative to the Turan platform. I explore the differences in the distribution of deformation across the MKDF and SFZ, and suggest this relates to the rheology of the crust surrounding these fault zones. Furthermore we observe interseismic deformation across numerous structures through the Köpetdag and Eastern Alborz, including distributed deformation across the BQFZ, parallel fault segments in the SFZ, frontal thrusts to the MKDF, and reverse faults in the eastern Köpetdag.

The research I present in this thesis will provide invaluable contributions to improve the characterisation of the seismic hazard posed by faults surrounding the SCB. Effective communication of these hazards will allow this knowledge to be integrated into societal awareness and infrastructure developments in the rapidly growing economies in this part of the modern Silk Roads. In future, this improved understanding should enable the mitigation of the devastating hazards posed by earthquakes along the northern margins of the Iranian Plateau.

Acknowledgements

To begin with, I want to thank my supervisors Richard Walker and Barry Parsons for their support, guidance and encouragement over the past four and a half years. Richard, thank you for sharing your encyclopedic knowledge of continental faults and earthquake records, and also your interest in their relation to historical context and antiquity. Most of all thank you for giving me the opportunity to explore the Köpetdag and Turkmenistan; I have enough stories from with you, Christoph and Neill to last a life time from the three field excursions, fueled by the finest Turkmen spirits, cuisine and hospitality, and I hope that there will be more to come in the future. Barry, thank you for the ever present support, allowing me the freedom to explore my own research interests, whilst also challenging me to maximise my potential. Two of my favourite quotes that you passed on during the course of my thesis will always stay with me; the first, "there are seven days in a week"; and the second, "one should go through papers and delete all uses of the word important". Thank you both for cultivating the fantastic and diverse research group in Oxford, which has provided a continually interesting environment to work in and a network of both contacts and friendships around the world.

I would like to thank everyone who has been part of the COMET group during my time here, including all the students and postdocs who have passed through. Simon, thank you for incredibly patiently teaching me almost everything I know about time-series processing and rescuing me at various points during the last few

years. The chapters of this thesis would be in a very different state without your support, and hopefully I will continue to develop the foundation of skills that you have provided me with in the future. JD, you have been an angel in disguise, sat at the next door desk to me through this thesis. Through all the ups and down, trials and tribulations, emotional and desk-thumping outbursts, you were an ever-present voice of support and reason. I have such amazing memories of our working adventures to Colorado, Corsica, and Washington DC, to name just a few, and will be coming to do the same in the Philippines as soon as travel allows for it again. Initially with Austin and Baptiste, and followed by Neill and Ian, thank you for providing such a reliable outlet and pub-based discussion group over my time here. Qi, thank you for the patiently smiling support and alternative perspectives as we worked through many of our shared processing and modelling challenges, and just as a side note you were the only continuous group member over the course of my thesis. Thank you to Eleanor, David, Yu, and Marion, who showed me the ropes during the early stages of my thesis. Thank you also to the others who joined the group during the second half of my thesis; Roberta, Wendy and Ben, the continuous flow of students in the COMET group really demonstrated to me that trying to teach something to someone else is the best way to learn yourself.

Next I want to thank the various groups of friends I have made during my time in Oxford. From the very beginning at St Anne's and continuing through to now living in Bristol with one of you, thank you to Rob and Chris; an earth scientist, a historian and an artist walk into a bar, who thought they would be great friends. Thank you to all the Bartlemas Boys through the years who made our house so fun; the originals, Sam, James and Vicky, and the mid-thesis transfers, Maj, Ed, and Issy. Thank you to everyone past and present at the Oxford University Rugby League Football Club and the three blues varsity-winning seasons I played a part in; to name just a few of you, Tavs, Phil, Brady and Jamesy, it was the best rugby environment

I have and ever will play in, SCS 1976. Thank you to the landlocked OWP surf and skate crew, Felix and James, for keeping things interesting and suggesting the occasional afternoon escape to the waves. Thank you to Louis and Hamish for the ever-grounding anti-social morning coffee club in the department and the numerous eventful evenings throughout our time in Oxford. To all of you and all the others not mentioned, I hope to stay in touch with as many of you as possible in the years ahead!

Finally, I want to especially thank all of my family. To my parents, Vicky and Nigel, and my sisters, Immy and Issy, thank you for the ever-present support and encouragement. Last but by no means least, for everything you have done and still do for me, and for all the times over the past year you have made me dance around the kitchen and sing,

> Say it's all right, say it's all right,
> It's all right, have a good time,
> 'Cause it's all right, whoa, it's all right.
>
> Now listen to the beat, kinda pat your feet,
> You've got soul, and everybody knows,
> That it's all right, whoa, it's all right.
>
> When you wake up early in the morning,
> Feeling sad like so many of us do,
> Just hum a little soul, make life your goal,
> And surely something's got to come to you.

Thank you to Lucy and Margot.

Contents

Declaration iii

Abstract v

Extended Abstract vii

Acknowledgements xiii

Contents xx

List of Figures xxvi

List of Tables xxvii

1 Introduction **1**

1.1 The character of deformation and seismic hazard in continental interiors 1

1.2 Accurately estimating tectonic strain accumulation 5

1.3 Estimating strain release from records of earthquakes 7

1.4 Characterising seismic hazard along the northern margins of the Iranian Plateau 10

1.5 Thesis structure and overview 16

1.5.1 Publications arising from this thesis 17

2 A large-magnitude Medieval earthquake on the Main Köpetdag (Kopeh Dagh) fault, Turkmenistan **19**

2.1 Introduction 22

2.2 Active tectonics and earthquakes in NE Iran and Turkmenistan . . . 25

2.2.1 Active tectonics 25
2.2.2 Earthquakes of the Köpetdag 28
2.3 Methods 31
2.4 Tectonic geomorphology and palaeoseismology of the MKDF 32
2.4.1 Tectonic geomorphology 32
2.4.2 Palaeo-earthquake ruptures on the central section of the MKDF 33
2.4.3 Analysis of geomorphological offsets 42
2.4.4 Timing of earthquake rupture 45
2.5 Discussion 56
2.6 Conclusion 61

3 Interseismic deformation and strain partitioning along the Main Köpetdag Fault, Turkmenistan, with Sentinel-1 InSAR time-series 63
3.1 Introduction 66
3.2 Sentinel-1 InSAR time-series processing 73
3.2.1 Tropospheric phase-delay correction 75
3.2.2 LOS time-series inversion and analysis 80
3.2.3 Investigating systematic biases in time-series inversions 88
3.3 Modelling interseismic motion along the MKDF 89
3.3.1 Preparation of LOS velocity fields 89
3.3.2 Modelling deformation with a vertical-strike-slip fault 90
3.3.3 Introducing structural complexity with a strain-partitioning geometry 94
3.4 Discussion 95
3.4.1 Tropospheric phase-delay corrections 95
3.4.2 Surface deformation from hydrological processes 96
3.4.3 The rate of interseismic motion and evidence for strain partitioning along the MKDF 99

3.4.4 Kinematics of the South Caspian Basin 103
3.5 Conclusion 106
3.6 Acknowledgments 107

4 Towards strain-rate mapping with Sentinel-1 InSAR time-series through the Köpetdag and Eastern Alborz 127

4.1 Introduction 129
4.2 InSAR processing and time-series generation 133
4.2.1 Time-series inversion, interferometric network refinement and tropospheric phase-delay corrections 135
4.2.2 Whether to remove tropospheric phase-delay model corrections from time-series analysis? 137
4.3 Generating a regional-scale velocity field 142
4.3.1 Combining frames along-track using overlaps 142
4.3.2 Reduction of frame extent along the Caspian Sea 145
4.3.3 Comparison of across-track overlaps 147
4.3.4 Referencing LOS velocity fields to a stable Eurasia reference frame 150
4.3.5 Decomposing the ascending and descending LOS into V_E and V_{UN} 157
4.4 Imaging the extrusion of the South Caspian Basin 166
4.4.1 The Main Köpetdag fault - a plate-boundary type fault? . . . 170
4.4.2 Distributed deformation through the Shahroud Fault Zone . . 174
4.4.3 The Bäherden-Quchan Fault Zone and its role in tectonic models of NE Iran 176
4.4.4 Accommodation of convergence through the eastern Köpetdag 181
4.4.5 The kinematics of conjugate fault systems and mechanics of lateral extrusion 182

4.5 Conclusion 187

5 Concluding remarks **209**

5.1 Directions for future research 212

Bibliography **217**

A InSAR LOS definitions, decompositions and derivations **235**

A.1 Definition of the InSAR line-of-sight in a Cartesian reference 235

A.2 Decomposing InSAR LOS velocity fields to V_E and V_{UN} 238

A.3 A method to merge InSAR LOS velocity fields across adjacent tracks 239

B Supplementary Data **241**

B.1 Chapter 2 Supplementary Material 241

List of Figures

1.1 Global distribution of earthquake with >10,000 deaths (circles scaled by deaths, coloured by magnitude) . . . 3

1.2 Histogram of earthquake deaths versus magnitude, separated into plate boundary and intraplate settings . . . 4

1.3 Tectonic setting of the Iranian Plateau (elevation, active faults, GPS velocity field, earthquakes) . . . 11

1.4 South Caspian Basin crustal structure from *Jackson et al.* (2002) . . 15

2.1 Active faults and earthquakes within the Arabia-Eurasia collision . . 23

2.2 Active faults of the eastern Caspian . . . 26

2.3 Eastern part of MKDF palaeo-rupture . . . 35

2.4 A fault-offset alluvial fan on the MKDF . . . 36

2.5 WorldView-2 imagery and field photos along the central section of the MKDF palaeo-rupture . . . 37

2.6 Purnuwar fault-offset field boundaries . . . 39

2.7 Western extent of MKDF palaeo-rupture . . . 40

2.8 Palaeo-rupture and thrust scarps near to Uşak . . . 41

2.9 MKDF Cumulative Offset Probability Density (COPD) analysis . . . 44

2.10 MKDF COPD segments . . . 46

2.12 Trench log and photo mosaic of Delimgor site . . . 50

2.13 Small trench site in eastern part of the palaeo-rupture . . . 52

2.14 Photo mosaic and eastern trench log MKDF 53
2.15 River-cutting exposure along Baharly segment of MKDF 54

3.1 Overview of active tectonics surrounding the South Caspian Basin . . 67
3.2 The coverage of the Sentinel-1 InSAR data processed from tracks D064 and A159 69
3.3 Processing strategy for applying tropospheric path-delay corrections . 77
3.4 Performance analysis of the tropospheric path-delay model corrections for tracks D064/A159 80
3.5 LOS velocity maps for D064 and A159 83
3.6 Fault perpendicular profiles MKD1–4 86
3.7 Fault perpendicular profiles MKD5–8 87
3.8 Modelling approach with profile MKD6 92
3.9 Modelling profile MKD7 93
3.10 Time-series displacements of individual pixels 98
3.11 South Caspian Basin-Iran-Eurasia velocity triangle 105
3.12 Track D064 interferometric network, perpendicular baselines versus temporal baselines 110
3.13 Track A159 interferometric network, perpendicular baselines versus temporal baselines 111
3.14 Testing empirical correction of IFGs by estimating phase-elevation relationships 112
3.15 InSAR time-series for track D064 without atmospheric corrections . . 113
3.16 Tropospheric path-delay correction with GACOS for IFG 20171229-20180311 114
3.17 Tropospheric path-delay correction with GACOS for IFG 20161104-2016122 115

3.18 Tropospheric path-delay correction with GACOS for IFG 20181212-20190105 . . . 116
3.19 LOS velocity rate-maps and corresponding 1σ uncertainty maps for tracks D064 and A159 . . . 117
3.20 Illustration showing expected LOS observations from dextral motion on the MKDF . . . 118
3.21 Investigating the effects of biases with the removal of short baseline interferograms from network . . . 119
3.22 Empirical covariance estimation for track D064 . . . 120
3.23 Inverted rate of strike-slip versus profile length along the MKDF . . . 121
3.24 Modelling the LOS velocity in profile MKD5 . . . 122
3.25 Profile MKD6 inverting for the location of the strike-slip fault . . . 123
3.26 Profile MKD6 inverting LOS velocity with the addition of conservation of motion on the frontal thrust . . . 124
3.27 Fault cross-section exposure from a gravel quarry showing vertical orientation along the MKDF . . . 125

4.1 Overview of the active tectonics surrounding the South Caspian Basin 130
4.2 Ascending Sentinel-1 InSAR track coverage across the Köpetdag and eastern Alborz . . . 131
4.3 Descending Sentinel-1 InSAR track coverage across the Köpetdag and eastern Alborz . . . 132
4.4 Comparison of uncorrected and GACOS corrected LOS velocity maps for D064 . . . 139
4.5 Comparison of uncorrected and GACOS corrected LOS velocity maps for D166 . . . 140
4.6 Across-track overlap LOS velocity profiles for D064-D166 before and after GACOS correction . . . 141

4.7 Across-track overlap LOS velocity profiles for GACOS corrected A159-A086 . . . 142
4.8 A159 along-track frame merging strategy and results . . . 144
4.9 D064 along-track frame merging strategy and results . . . 145
4.10 D137 along-track frame merging strategy and results; introduction of tilt in range . . . 148
4.11 Across-track overlap LOS comparison and histogram for D064-D166 . 150
4.12 Across-track overlap LOS comparison and histogram for D137-D064 . 151
4.13 Across-track overlap LOS comparison and histogram for A159-A086 . 152
4.14 Descending LOS velocity maps prior to GPS referencing, common reference frame . . . 153
4.15 Ascending LOS velocity maps prior to GPS referencing, common reference frame . . . 154
4.16 GPS referencing strategy for track D064 . . . 156
4.17 Track overlap A159-A086 histogram comparison for ramp-tying versus GPS-tying LOS velocity fields . . . 158
4.18 Track overlap D064-D166 histogram comparison for ramp-tying versus GPS-tying LOS velocity fields . . . 159
4.19 Track overlap histogram comparison of ramp-tying vs. GPS-tying LOS velocity fields for D137-D064 . . . 160
4.20 GPS-referenced ascending LOS tracks to a quasi-Stable Eurasia reference frame . . . 161
4.21 GPS-referenced descending LOS tracks to a quasi-Stable Eurasia reference frame . . . 162
4.22 Visualisation of input data into the V_E and V_{UN} decomposition . . . 163
4.23 Hillshade-rendered V_E map with fault labels . . . 164
4.24 Hillshade-rendered V_{UN} map with fault labels . . . 165

4.25 North-south oriented profiles of V_E across the SFZ-SCB-MKDF . . . 168
4.26 East-West oriented profile across the apex of the wedge of extruding South Caspian Basin material . . . 169
4.27 Annotated map of tectonic and non-tectonic signals in the V_E component 171
4.28 Annotated map of tectonic and non-tectonic signals in the V_{UN} component . . . 172
4.29 Fault-perpendicular profiles of V_E across the MKDF . . . 173
4.30 Fault-perpendicular profiles of V_{UN} across the MKDF . . . 175
4.31 Fault-zone perpendicular V_E profiles across the SFZ . . . 177
4.32 V_E and LOS profiles through parallel faults in the SFZ . . . 178
4.33 East-west profile of LOS velocity and decomposition components through the BQFZs . . . 180
4.34 Competing kinematic tectonic models for the Köpetdag and Eastern Alborz from *Shabanian et al.* (2009) . . . 181
4.35 V_{UN} profile with evidence for deformation along reverse faults in the eastern Köpetdag . . . 183
4.36 Velocity triangle of the MKDF-SFZ conjugate system . . . 184
4.37 Strain rate maps of Anatolia from *Weiss et al.* (2020) . . . 186
4.38 Kinematics of the Tajik depression from *Metzger et al.* (2020) . . . 187
4.39 Perpendicular baseline versus temporal baseline plots for track D137N 190
4.40 Perpendicular baseline versus temporal baseline plots for track D064N 190
4.41 Perpendicular baseline versus temporal baseline plots for track D064S 191
4.42 Perpendicular baseline versus temporal baseline plots for track D166 . 191
4.43 Perpendicular baseline versus temporal baseline plots for track A159N 191
4.44 Perpendicular baseline versus temporal baseline plots for track A159S 192
4.45 Perpendicular baseline versus temporal baseline plots for track A086 . 192
4.46 LOS velocity for descending frame T166 . . . 193

4.47 LOS velocity for descending frame T064N 194
4.48 LOS velocity for descending frame T064S 195
4.49 LOS velocity for descending frame T137N 196
4.50 LOS velocity for descending frame T137S 197
4.51 LOS velocity for ascending frame T086 198
4.52 LOS velocity for ascending frame T159N 199
4.53 LOS velocity for ascending frame T159S 200
4.54 GACOS performance metrics for ascending frames 201
4.55 GACOS performance metrics for descending frames 202
4.56 Comparing the difference between GACOS and ERA5 corrections on D064 203
4.57 GPS referencing strategy for track D166 204
4.58 GPS referencing strategy for track D137 205
4.59 GPS referencing strategy for track A159 206
4.60 GPS referencing strategy for track A086 207

A.1 Illustration of the definition of the LOS vector 237

List of Tables

2.1 Details from Beta Labs 49
2.2 Details from IRSL dating 55
3.1 Previous estimates of slip-rates along the MKDF 109

Chapter 1

Introduction

1.1 The character of deformation and seismic hazard in continental interiors

The distribution and characteristics of earthquakes within the continental interiors is intrinsically different to those along tectonic plate boundaries involving oceanic crust (e.g. *McKenzie*, 1972; *Molnar and Tapponnier*, 1975; *Molnar*, 1988). Tectonic plate boundaries involving oceanic crust conform to the theory of plate tectonics. Earthquakes are confined to narrow bands, accommodating strain from relative motion along the margins of rigid plates, and can be approximated by deformation along a single fault (e.g. *McKenzie and Parker*, 1967). In contrast, the distribution of earthquakes within continental interiors tells a very different story. Here, earthquakes are located in broad zones of deformation, hundreds to thousands of kilometres wide (e.g. *Thatcher*, 2009), with strain distributed across networks of interacting fault systems and structures.

Additional complexity of deformation within the continents arises from structural, thermal and compositional heterogeneity, introduced over its much longer existence when compared to oceanic crust. Strain is typically concentrated along pre-existing

structures (e.g. *Sykes*, 1978) and rheological contrasts (e.g. *Molnar and Dayem*, 2010). Pre-existing structures from previous orogenic generations can be re-activated in different orientations under the present stress regime (e.g. *Sibson*, 1985), although it is not necessarily possible to determine the character of faulting in continental crust from the motion of its surroundings (e.g. *Jackson and McKenzie*, 1988). Rheological heterogeneity, due to differences in composition and thermal structure within the crust, introduces complexity in fault zone behaviour and deformation at depth (e.g. *Fagereng and Beall*, 2021; *Copley et al.*, 2021). The resulting deformation within continental interiors reflects this complexity, with a wide range of faulting styles, earthquake characteristics, and kinematic configurations (e.g. *McKenzie*, 1972; *Jackson and McKenzie*, 1984).

The challenge presented by characterising deformation within the continents is motivated by improving our understanding of seismic hazard. *England and Jackson* (2011) present that the majority of fatalities from earthquakes have occurred in continental interior settings (Figures 1.1 and 1.2). This is despite plate boundaries hosting the highest magnitude and more frequent large events. *England and Jackson* (2011) attributes the comparably reduced fatalities from plate boundary events (Figure 1.2) to the better characterisation of seismic hazard and preparedness of local populations in plate boundary settings. The long recurrence intervals of earthquakes in continental interior settings results in local populations being unaware of the hazard posed by earthquakes and governments lacking societal infrastructure for recovery. Consequently *England and Jackson* (2011) argue that current and future research efforts should prioritise understanding seismic hazard within continental interiors.

Individual faults in continental interiors can accommodate currently unresolvable rates of deformation, yet still have the capability to generate devastating high-magnitude ($> M_W$ 8) earthquakes (e.g. *Jackson*, 2001). The broad distribution

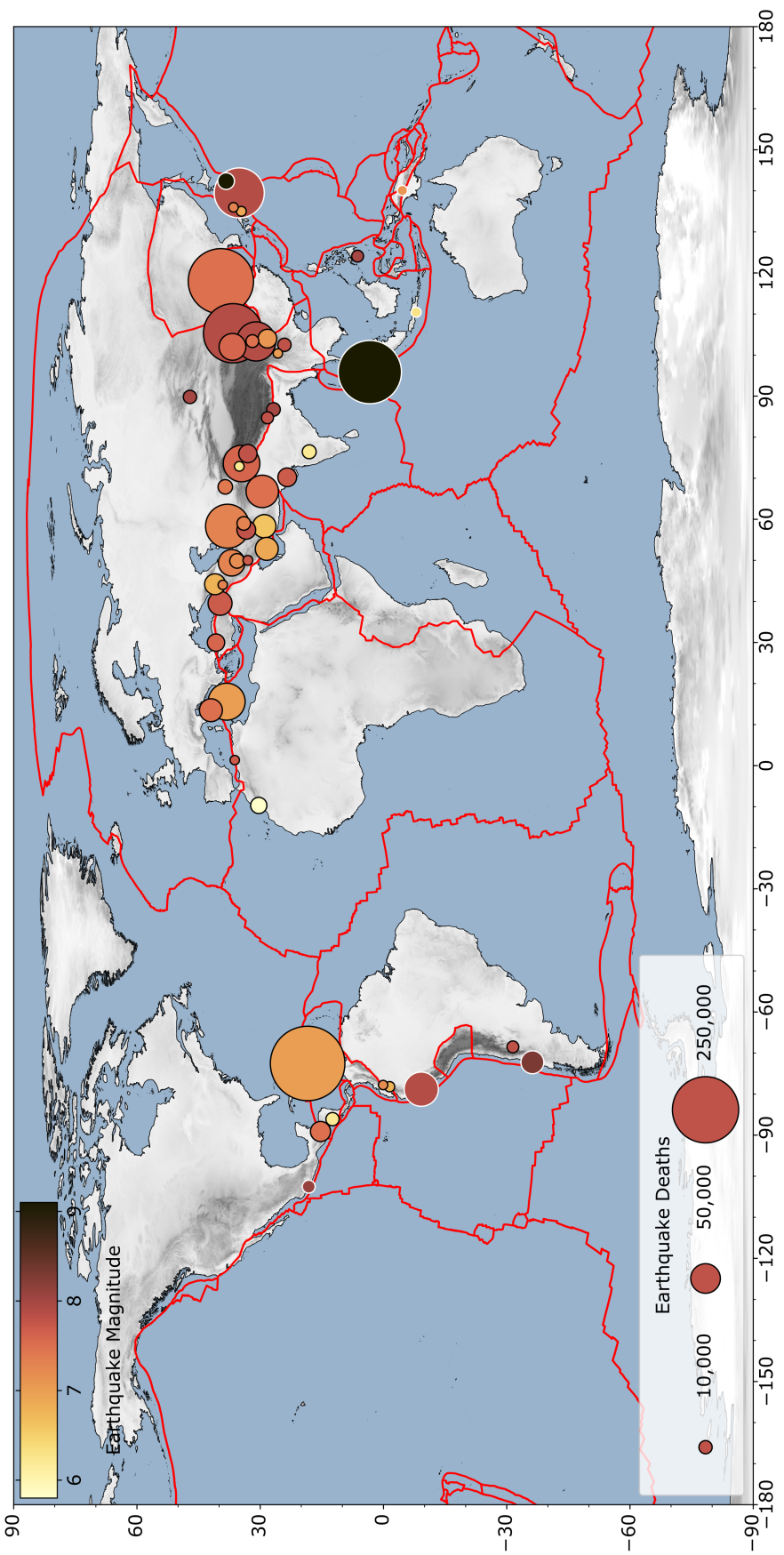


Figure 1.1: A global map of earthquakes from 1900–2021 with greater than 10,000 fatalities. The diameter of each circle is scaled linearly by the number of earthquake deaths, and the colour corresponds to the magnitude of each event (data from National Centers for Environmental Information, National Oceanic and Atmospheric Administration). Earthquakes that occurred on a plate boundary are outlined in white, those that did not in black. Also shown in red are plate margins from *Bird* (2003). Figure is an updated version from (*England and Jackson*, 2011).

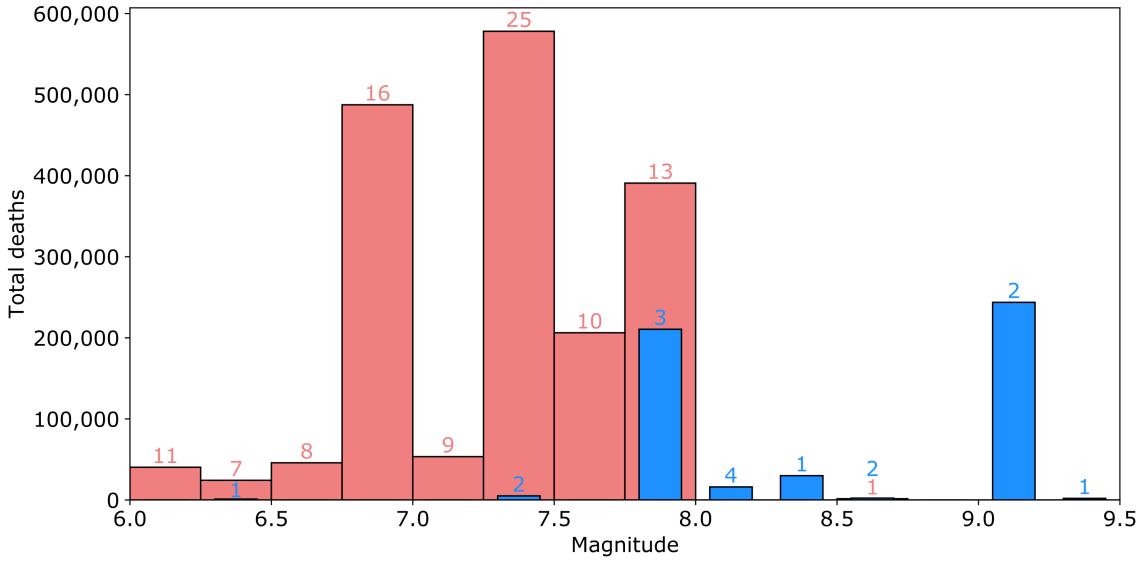


Figure 1.2: Updated figure from *England and Jackson* (2011), highlighting that earthquakes in continental interiors (pink) have killed significantly more people than earthquakes in plate boundary (blue) settings: earthquake deaths (events with >1000 fatalities) versus magnitude (events with magnitude (M_W) >6), in bins of 0.25 magnitude units width, from 1900–2021 (the number of events in each bin is labelled above the bar). Events are divided according to their tectonic setting; plate boundary (blue), and intraplate (red). Earthquake data is from the National Centers for Environmental Information, National Oceanic and Atmospheric Administration.

of deformation across intricate networks of faults makes the source and character of the hazard difficult to precisely determine prior to events. However *Jackson and Conway* (2006) details how it is not simply a case of identifying earthquake generating faults, as populations are brought into close proximity to them by the advantages of habitation in regions with features generated by deformation, including water resources, strategic control and trade-routes. Furthermore *Bilham* (2009) presents a bleak future outlook, detailing how the projected doubling in Earth's population in the next half century will result in earthquakes occurring in locations that might previously have had low population density, thus exposing urban agglomerations with ever-increasing populations to seismic hazard.

The characterisation of seismic hazard in a region can be simply expressed by quantifying terms on either side of a strain balance. On one side of the

balance is strain accumulation, which includes both the rate and distribution of tectonic strain. On the opposing side is strain release, which can be estimated using the strain released in earthquakes. The following sections introduce the theory and development of methods used to accurately estimate these terms, before demonstrating their importance and challenges in the regional context of this thesis, along the northern margins of the Iranian Plateau.

1.2 Accurately estimating tectonic strain accumulation

The concept of the earthquake cycle was first developed by *Reid* (1910) to explain displacements measured with repeated triangulation measurements in California during the 1880s, and immediately after the devastating 1906 San Francisco earthquake, across the San Andreas fault. This provided the first geodetic observation of interseismic motion, which *Reid* (1910) developed into elastic rebound theory. In this theory, strain accumulates from far-field tectonic stresses gradually on a locked fault between two plates (the interseismic phase), until their internal rigidity is exceeded. At this point a sudden motion ruptures the fault, with the energy from the accumulated strain released as an earthquake (the coseismic phase). An additional phase of deformation following the coseismic phase is now also accepted, following observations of an extended (months to years) period of enhanced deformation after earthquakes around the world. This postseismic deformation is attributed to a combination (e.g. *Segall*, 2004) of afterslip (post-seismic creep) (e.g. *Marone et al.*, 1991), viscoelastic relaxation at depth (e.g. *Pollitz*, 1997), and localised poroelastic deformation (e.g. *Scholz and Kranz*, 1974).

The development and advancement of geodetic methods has subsequently been used to accurately measure rates and spatial patterns of tectonic deformation (e.g.

Kreemer et al., 2014). GNSS measurements have primarily provided constraints on the relative velocities and rotations of block interiors around the world. In addition, the ever-increasing density of GNSS measurements, although predominantly limited in extent to affluent nations in plate boundary settings (e.g. New Zealand, Japan, California), has illuminated concentrations of strain at wavelengths of tens to hundreds of kilometres, corresponding to deformation across individual fault zones (e.g. *Shen et al.*, 2011). This has been supported by the development of InSAR time-series methods, which have provided spatially-continuous velocity maps of surface deformation at even higher spatial resolution (e.g. *Grandin et al.*, 2012; *Hussain et al.*, 2016). The integration of both these geodetic methods has been used to image strain-rate across continental-scale faults and interacting structures (e.g. *Weiss et al.*, 2020), and will eventually be used to generate velocity fields across entire orogenic belts (e.g. *Lazecký et al.*, 2020; *Durand et al.*, 2019).

Comparing geodetically-measured rates of deformation to geological measurements can be used to investigate the relationship between present-day deformation and longer-term earthquake behaviour along faults (e.g. *Dolan et al.*, 2016; *Johnson*, 2013; *Segall*, 2002). Geological slip-rates constrain the timing of the cumulative deformation across faults to provide long-term average deformation rates over thousands of years (e.g. *Mousavi et al.*, 2021). The differences between geodetic and geologic deformation rates have been attributed to the large epistemic uncertainties of both measurements (e.g. *Gold et al.*, 2009), although it has also been suggested that differences reflect temporal variations of deformation in the continents. In particular, the differences between deformation rates have variously been attributed to changes in earthquake recurrence intervals (e.g. *Becker and Schmeling*, 1998), earthquake clustering (e.g. *Rockwell et al.*, 2000), structural interaction (e.g. *Peltzer et al.*, 2001; *Dolan et al.*, 2004), off-fault permanent strain and viscous relaxation of the lower crust and upper mantle (e.g. *Johnson*, 2013).

Modelling the spatial patterns of interseismic deformation observed with geodetic methods also presents an opportunity to probe the mechanical properties of fault zones, which can then be integrated with information from other geological and geophysical datasets. *Savage and Burford* (1973) presented the first model of measurements of interseismic deformation across the San Andreas fault, using a buried infinitely-long vertical screw dislocation in an elastic half-space (*Okada*, 1992). This models interseismic deformation as stable sliding in the lower crust beneath a locked fault, so that the surface deformation reflects the elastic response of the upper crust to localised shear at depth. The mathematical simplicity and general success of this model have resulted in its continued use to the present day (e.g. *Vergne et al.*, 2001). Alternative models have also been proposed, such as instead modelling interseismic deformation as viscous laterally-distributed shear across a finite width in the lower lithosphere (e.g. *Prescott and Nur*, 1981). However even with high quality geodetic measurements, it is not always possible to distinguish between these two end-member models because an elastic upper crust acts as a deformation filter (e.g. *Wright et al.*, 2001). Subsequent interseismic models have introduced further complexity to explain asymmetry in observations of interseismic deformation, with structural complexity at depth (e.g. *Daout et al.*, 2019) and variations in rheology across a fault zone (e.g. *Jolivet et al.*, 2008).

1.3 Estimating strain release from records of earthquakes

On the opposing side of the balance, accurately estimating strain release is typically quantified using the seismic moment release in earthquakes. Instrumental seismological catalogues accurately determine earthquake locations, focal mechanisms and moment tensors. These records provide impressions of

regional-scale kinematics (e.g. *McKenzie*, 1972), and can be used to compute the strain release rate for a given volume (e.g. *Kostrov and Riznichenko*, 1974), or to extend empirical earthquake frequency-magnitude relationships (e.g. *Gutenberg and Richter*, 1950) to estimate maximum moment magnitudes (e.g. *Molnar*, 1979). However recurrence intervals between earthquakes on individual faults within slow-moving continental interiors may be hundreds to thousands of years, exceeding the temporal extent of instrumental catalogues. Therefore in this setting, these observations are insufficient to fully characterise the deformation (e.g. *Grant and Sieh*, 1994; *Weldon et al.*, 2004; *Goldfinger et al.*, 2013; *Gold et al.*, 2017).

In some regions of the world, historical sources provide access to records of earthquakes over much greater periods of time (e.g. *Ambraseys and Melville*, 2005; *Wang*, 2004). Historical records of earthquakes have the potential to augment the length of seismological records, however the level of completeness will vary in space and time. It is not clear whether seismic gaps along identified faults within the deforming zones are due to incompleteness of the historical record (*Ambraseys and Melville*, 2005). As a result seismological catalogues are informative when considering regional deformation, but become less useful when considering progressively smaller regions or in continental interior settings with slow rates of strain release.

Geomorphological and paleoseismological investigations can provide valuable access to the signature of earthquakes further back in time along faults in the slow-moving continental interiors (e.g. *Klinger et al.*, 2011; *Ainscoe et al.*, 2019). Paleoseismology is used to constrain the timing and recurrence intervals of earthquake ruptures, whilst both geomorphology and paleoseismology are used to measure displacements from repeated surface rupturing events. These methods have presented evidence for numerous temporal and displacement characteristics along faults, including irregular recurrence times of earthquakes (e.g. *Gold et al.*, 2017; *Zinke et al.*, 2017), temporal clustering of events (e.g. *Rockwell et al.*, 2000), and

characteristic slip behaviour from surface ruptures along faults (e.g. *Zielke et al.*, 2010; *Klinger et al.*, 2011). As well as the temporal behaviour of earthquakes, these methods have provided the link between displacements observed in individual earthquakes, to the generation of topography from cumulative deformation in repeated cycles of earthquakes through time (e.g. *Jackson et al.*, 1982). Exactly how measurements of present deformation rates and displacements in earthquakes connect to the expression of deformation in the landscape and the generation of topography in mountain belts over millions of years remains poorly understood (e.g. *Thatcher*, 2009).

Accurately estimating strain release is complicated further by ever-increasing geodetic observations of stable-sliding aseismic deformation and episodic aseismic deformation events (e.g. *Chen and Bürgmann*, 2017; *Harris*, 2017). These observations demonstrate that there are numerous physical mechanisms by which tectonic strain is released, which must all be considered when quantifying the release of strain. This also introduces significant complexity when considering the interaction between locked seismogenic portions and adjacent aseismic portions of faults (e.g. *Avouac*, 2015). Similarly, geodetic observations of fold growth have suggested the generation of topography can also result from aseismic processes and unrecoverable off-fault deformation during all phases of the earthquake cycle (e.g. *Copley and Jolivet*, 2016). This can be driven either by transient stresses from nearby earthquakes and postseismic mechanisms, or during the interseismic period (e.g. *Copley and Jolivet*, 2016).

1.4 Characterising seismic hazard along the northern margins of the Iranian Plateau

The Iranian Plateau is a broad zone of continental deformation within the Alpine-Himalayan belt, created by the tectonic motion of the Arabia-Eurasia collision. The plateau accommodates approximately 25 mm/yr of north-south convergence, constrained by GPS velocities (e.g. *Vernant et al.*, 2004; *Khorrami et al.*, 2019). In Figure 1.3, both topography and seismicity define the zone of deformation, which extends for over 2000 km from north to south and east to west. Deformation is distributed across networks of faults (Figure 1.3b), with the kinematics and seismic potential of the region relatively well described by GPS velocities (Figure 1.3c) (e.g. *Mousavi et al.*, 2013), the surface expression of faulting (e.g. *Walker and Jackson*, 2004), instrumental seismology (e.g. *Jackson et al.*, 2002), and an extensive historical record of earthquakes (Figure 1.3d) (e.g. *Ambraseys and Melville*, 2005). From Figure 1.3, it is evident that deformation is concentrated in several mountain ranges that comprise the margins of the plateau; the Köpetdag, Alborz, Talesh and Zagros. In contrast, the interior of the Iranian Plateau has been shown to be deforming very slowly (<2 mm/yr) (e.g. *Walpersdorf et al.*, 2014; *Walker and Jackson*, 2004). In addition, there are concentrations of seismicity around low-elevation deserts and basins, which are suggested to behave as rigid blocks embedded within their deforming surroundings (e.g. Dasht-e-Lut, Dasht-e-Kavir, South Caspian Basin; Figure 1.3; *Jackson and McKenzie* (1984)).

As an example of a relatively young collision zone, the Iranian Plateau presents an opportunity to study the onset of continental collision. The timing of the initial Arabia-Eurasia collision is widely debated (5–65 Ma), although there is considerable evidence for initiation during the Late Eocene (35 Ma) following the closure of the Tethys Ocean (e.g. *Allen and Armstrong*, 2008). However, most presently

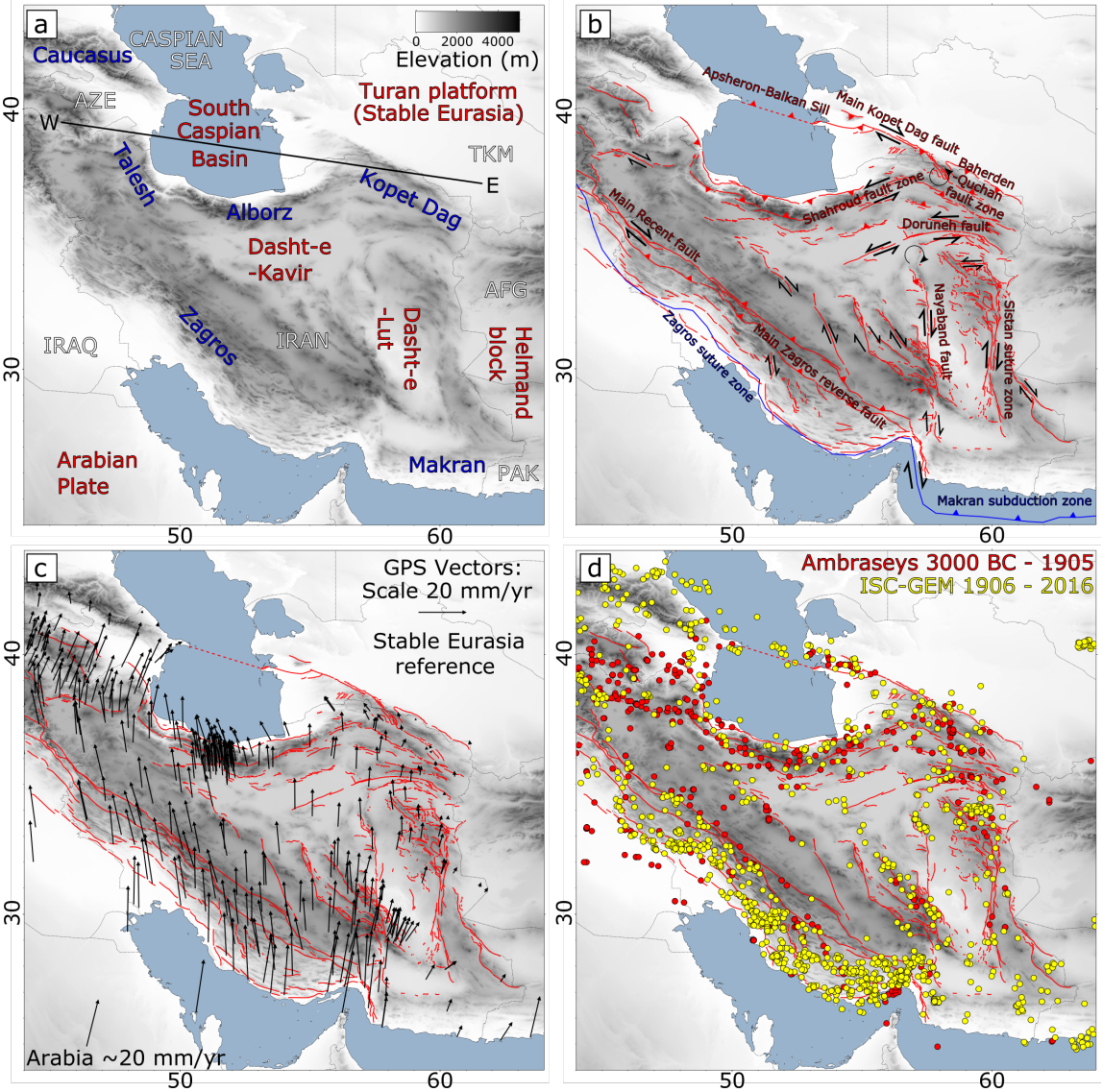


Figure 1.3: An overview of the tectonic setting of the Iranian Plateau. a) Elevation in grey-scale from the SRTM-30 m DEM, with the orogenic belts that comprise the Iranian plateau labelled in blue, and proposed rigid blocks labelled in red (e.g. *Jackson et al.*, 2002). b) Active fault map of the Iranian Plateau in red (*Walker et al.*, 2021), with kinematic indicators also shown; the Arabian plate boundary is delineated in blue running through the Makran subduction zone and Zagros suture zone. c) GPS velocity field relative to a stable Eurasia reference frame (*Khorrami et al.*, 2019) showing how convergence from the Arabia-Eurasia collision is accommodated through the Iranian plateau. d) Historical earthquakes from the catalogue of *Ambraseys and Melville* (2005) (3000 BC–1905) plotted as red dots, with instrumentally-recorded earthquakes from the ISC-GEM catalogue (1906–2016) plotted as yellow dots (International Seismological Centre (2021), ISC-GEM Earthquake Catalogue).

active structures have been shown to have displacements that accumulate at present deformation rates in ≈3–10 Ma, which has been used to suggest that deformation intensified at this time across the collision zone (e.g. *Allen et al.*, 2004; *Hollingsworth et al.*, 2008; *Walker et al.*, 2021). Eventually these deformation processes generate the topography within major orogens, such as throughout the 7000 km-long zone of general convergence in the Alpine-Himalayan belt. Deformation is accommodated across a wide variety of fault structures, configurations, and levels of maturity, providing insight into the mechanics and kinematic interaction within developing collision zones. Therefore investigating deformation here provides a foundation to understand the evolution of continental mountain belts around the world.

In addition, the Iranian Plateau presents an excellent natural laboratory for investigating active deformation, primarily because of the fast rates of motion within the Arabia-Eurasia collision. From a geodetic perspective, rapid deformation is more resolvable, especially through the sources of noise that hamper signals with these techniques. From a geomorphological and geological point of view, the cumulative expression of fast-moving deformation is more distinguishable in the landscape as the impact of time-dependent erosional processes on tectonic signals is reduced (e.g. *Zielke et al.*, 2015). With seismological and paleoseismological methods, faster deformation results in a higher frequency of earthquakes, which simply provides more data and observations. The fast rates of deformation are also accompanied by optimal environmental conditions for characterising deformation with several of these techniques. High aridity results in excellent coherence with InSAR time-series methods (e.g. *Mousavi et al.*, 2015; *Walters et al.*, 2013) and enhanced preservation of fault-offset geomorphic markers (e.g. *Hollingsworth et al.*, 2010). Similarly, limited anthropogenic disruption mitigates epistemic uncertainties, especially of measurements in the deserts and high-elevation plateaus.

Most of the convergence accommodated by the Iranian Plateau is concentrated

along the ranges at the far northern and southern extents (e.g. *Walpersdorf et al.*, 2014). The southern margin is defined by the thin-skinned deformation concentrated within the NW-SE trending Zagros fold and thrust belt. Here oblique compression is partitioned between major strike-slip faults and reverse faults (e.g. *Walpersdorf et al.*, 2006), which have hosted a series of historically devastating earthquakes in this region (e.g. *Nissen et al.*, 2019). The southeastern and eastern margin is initially well-defined by subduction through the Makran region, although further north the convergence is accommodated through a diffuse zone of north-south (parallel to the convergence), long (>100 km) strike-slip faults which follow the Iran-Afghanistan border (e.g. *Walpersdorf et al.*, 2014). The western portion of the Iranian Plateau is characterised by thick-skinned faulting in the Caucasus. This is bordered to the west by the continental-scale North and East Anatolian strike-slip fault systems, which facilitate the westward extrusion of neighbouring Anatolia also within the Arabia-Eurasia collision (e.g. *Weiss et al.*, 2020; *Jackson and McKenzie*, 1984).

Along the northern margins of the Iranian Plateau, the kinematics are, however, considerably more complex. The northward GPS velocity of NE Iran relative to Eurasia decreases eastward across this region, from 11 mm/yr at Tehran (52°E) to 1.5 mm/yr at Mashhad (60°E) (*Khorrami et al.*, 2019), due to the oblique convergence of the Arabia-Eurasia collision. Remaining north-south convergence is predominantly concentrated through the Köpetdag and Alborz mountain ranges, of Turkmenistan and Iran. These zones are adjacent to the aseismic, low relief expanse of the Turan Platform, which extends northwards and is assumed to comprise part of the Eurasian plate (e.g. *Jackson et al.*, 2002). However, the surface expression of deformation is instead dominated by the influence of the South Caspian Basin (SCB), an aseismic block moving independently to its surroundings (e.g. *Jackson et al.*, 2002). Faults surrounding the SCB are in proximity to the capital cities Tehran (Iran, >8.5 million), Baku (Azerbaijan, >2 million) and Aşgabat (Turkmenistan, >1 million),

and major population centres such as Mashhad (Iran, > 3 million). In addition, the basin hosts hydrocarbon reserves of intense commercial interest, which also motivates understanding tectonic controls on the basin stratigraphy.

The motion of the basin is facilitated by conjugate strike-slip motion across two major fault zones; the Main Köpetdag fault (MKDF), Turkmenistan, and the Shahroud fault zone (SFZ), Iran. The motion of the SCB towards the northwest (e.g. *Copley and Jackson*, 2006) results in the subduction of the basin along the Absheron-Balkan Sill to the north and under-thrusting beneath the Talesh to the west. Despite its kinematic significance, the direction, rate of motion and pole of rotation of the SCB are poorly constrained relative to its surroundings, primarily due to the depth of water (>1000 m) and sediments (>25 km) that overlie the basement (e.g. *Green et al.*, 2009). Receiver function (*Mangino and Priestley*, 1998) and surface wave analysis (*Priestley et al.*, 2001), shown in Figure 1.4, suggests that the basin is an unusually thickened remnant of oceanic crust (*Jackson et al.*, 2002). However the extent of GPS networks are limited to the shorelines of the Caspian Sea in northeast Iran (e.g. *Djamour et al.*, 2010), and are unable to directly resolve the true motion of the basin with GPS-derived block models (*Mousavi et al.*, 2013).

Considering the opposing side of the strain accumulation-release balance, there is an extensive historical record of earthquakes in the region surrounding the SCB stretching back several thousand years (*Ambraseys and Melville*, 2005), as well as a relatively dense instrumental record of earthquakes (e.g. *Jackson et al.*, 2002). There are prominent historical records of devastating earthquakes throughout this region, including on major structures such as the SFZ (e.g. *Hollingsworth et al.*, 2008); although some of these are debated (*Berberian*, 2014). There are however notable apparent seismic gaps along major structures, such as along the MKDF (e.g. *Walker et al.*, 2021). As a result, it is unclear if the representation of strain release provided by seismological records are able to fully characterise the strain release in the region.

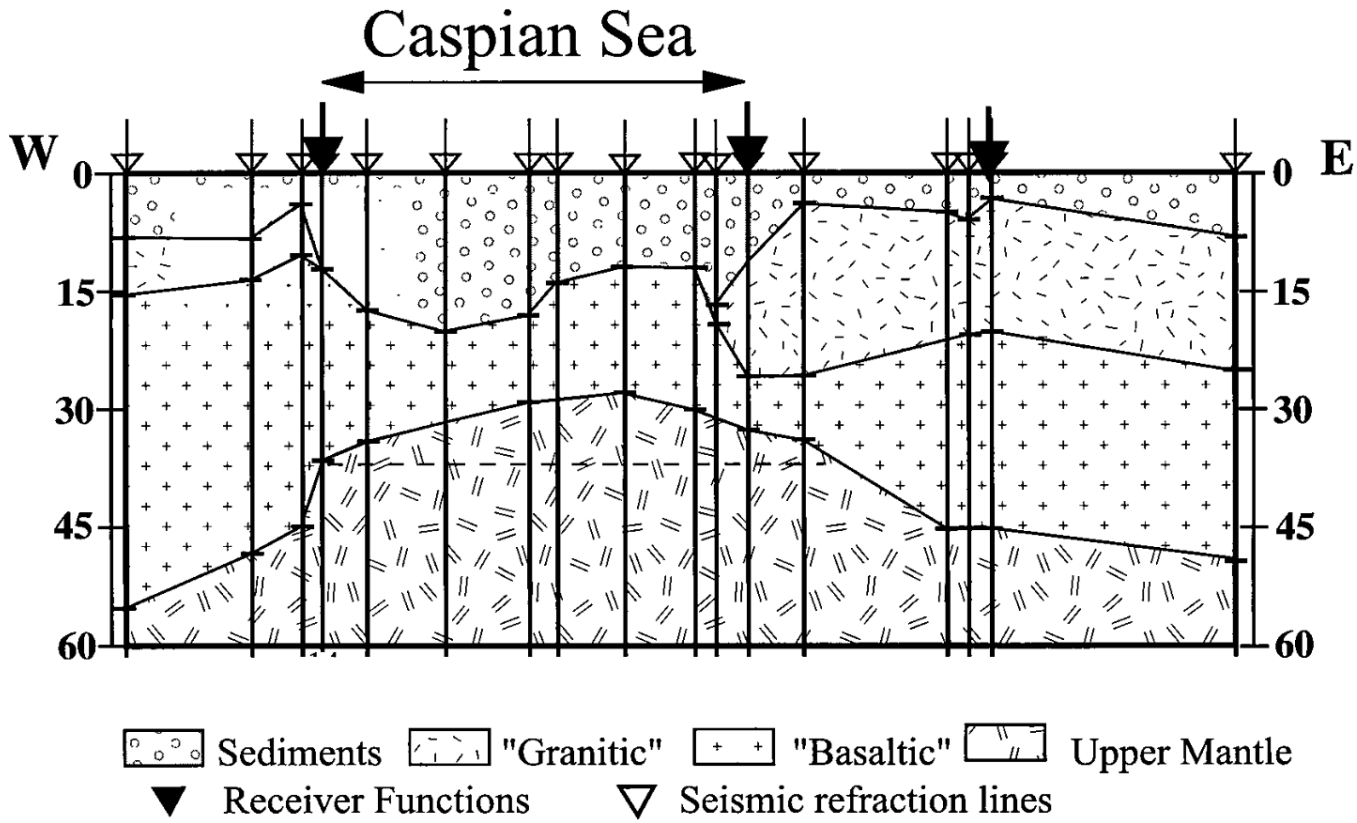


Figure 1.4: From *Jackson et al.* (2002) (after *Mangino and Priestley* (1998)), a crustal and uppermost mantle cross-section between the Kura Basin to the west of the South Caspian Basin (-39.5°N, 46.0°E) and the East Caspian lowlands and the Köpetdag mountains to the east (-37.5°N, 61.5°E); see Figure 1.3a for location of profile. The approximate extent of the South Caspian Basin is denoted by the double-headed horizontal arrow above the cross-section. The structure is summarized in terms of four generalized rock types: low-velocity sediments; the upper 'granitic' crust consisting of rocks with V_P 5.8–6.5 km/s; the lower 'basaltic' crust consisting of rocks with V_P 6.5–7.8 km/s; and the upper mantle. The vertical arrows at the top of the cross-section denote points where receiver function analysis (large solid arrows) or Russian refraction analysis (small open arrows) provide a constraint on the crustal structure (*Mangino and Priestley*, 1998). The surface wave study of *Priestley et al.* (2001) is for the path denoted by the double-headed arrow above the cross-section. The dashed line at 35 km depth beneath the basin denotes the approximate position of the Moho from the surface wave analysis.

Reflecting on the discussion presented above, if we consider both sides of the strain accumulation and strain release balance, there is currently a limited understanding of the seismic hazard posed by faults surrounding or kinematically-related to the SCB. However as detailed in the previous section, we have other methods at our disposal to accurately estimate the terms in this strain balance. InSAR time-series methods can be used to directly measure the relative motion across the boundary faults of the SCB and provide an accurate estimation of strain accumulation (e.g. *Walters et al.*, 2013; *Mousavi et al.*, 2015). Similarly by combining paleoseismological and geomorphological observations, we have the capability to better characterise strain release by analysing ruptures along major faults pre-dating or missing from earthquake records. Therefore this thesis employs a multi-disciplinary approach using these techniques, to improve the characterisation of seismic hazard in a region that conventional techniques are potentially unable to characterise.

1.5 Thesis structure and overview

This thesis presents, in integrated format, research investigating the mechanics of the earthquake cycle and the kinematics of continental deformation along the northern margins of the Iranian Plateau. Accurately estimating the tectonic strain accumulation and strain release is imperative when characterising the seismic hazard posed by active faults in the region. However the seismic potential of faults surrounding the SCB, through the Köpetdag and Eastern Alborz, is difficult to constrain with conventional techniques. Therefore this thesis aims to determine the rate and distribution of strain accumulation along major bounding faults of the SCB using InSAR time-series methods. Furthermore, this thesis aims to improve estimates of strain release from earthquakes in the region using paleoseismological and geomorphological investigations of earthquake ruptures preserved in the geological record. The research presented in subsequent chapters is as follows:

Chapter 2 describes field observations and high-resolution optical satellite imagery analysis of the extent and character of a paleo-rupture along the MKDF, Turkmenistan. This is combined with geomorphological and paleoseismological analysis to constrain the magnitude, rupture mechanics and timing of this earthquake rupture. The omission of this rupture from earthquake records in Iran is then interpreted within a historical context.

Chapter 3 presents a Sentinel-1 InSAR time-series investigation of the MKDF, Turkmenistan. I measure and model interseismic motion across the fault, and present evidence of motion along frontal thrusts of the fault system. The measurements are combined with a recent Quaternary geological slip-rate to evaluate the role of the fault in the kinematics of the SCB.

Chapter 4 presents the results from a regional-scale study using Sentinel-InSAR time-series. Amongst numerous observations of interseismic motion along faults and insight into the kinematics of deformation through the Köpetdag and Eastern Alborz, the study presents a spatially continuous image of the extrusion of the onshore extension of the SCB.

Chapter 5 is a reflection on the previous chapters. This provides broader discussion of results presented in this thesis, and remarks on direction for future research.

1.5.1 Publications arising from this thesis

Much of the research in this thesis is part of an ongoing Turkmenistan-UK scientific collaboration. Chapters 2 and 3 have been submitted for publication (currently in review), and Chapter 4 is in preparation for submission (to the Journal of Geophysical Research: Solid Earth).

a) **Dodds, N.**, Begenjev, G., Bezmenov, Y., Gruetzner, C., Mirzin, R., Rhodes, E., Walker, R.T., Wordsworth, P. (2021). *A Large-Magnitude Medieval Earthquake*

on the Main Köpetdag (Kopeh Dagh) Fault, Turkmenistan. Submitted to Bulletin of the Seismological Society of America.

b) **Dodds, N.**, Daout, S., Walker, R.T., Begenjev, G., Bezmenov, Y., Mirzin, R., Doin, M.-P., Parsons, B. (2021). *Interseismic Deformation and Strain Partitioning along the Main Köpetdag Fault, Turkmenistan, with Sentinel-1 InSAR Time-series.* Submitted to Geophysical Journal International.

Additional publications to which I have contributed as co-author over the duration of this thesis:

a) Walker, R.T., Bezmenov, Y., Begenjev, G., Carolin, S., **Dodds, N.**, Gruetzner, C., Jackson, J., Mirzin, R., Rhodes, E. (2021). *Slip-rate on the Main Köpetdag (Kopeh Dagh) Strike-slip fault, Turkmenistan, and the active tectonics of the South Caspian.* Tectonics, 40.

b) Mousavi, Z., Fattahi, M., Khatib, M., Talebian, M., Pathier, E., Walpersdorf, A., Sloan, R.A., Thomas, A.L., Rhodes, E., Clive, F., **Dodds, N.**, Walker, R.T. (2021). *Constant slip-rate on the Doruneh strike-slip fault, Iran, averaged over Late Pleistocene, Holocene, and decadal timescales.* Tectonics, 40.

Chapter 2

A large-magnitude Medieval earthquake on the Main Köpetdag (Kopeh Dagh) fault, Turkmenistan

Nicholas Dodds[1], G. Begenjev[2], Y. Bezmenov[2], C. Gruetzner[3], R. Mirzin[2], E. Rhodes[4,5], R.T Walker[1], P. Wordsworth[6]

[1]COMET, Department of Earth Sciences, Oxford University, Oxford, OX1 3AN, UK.
[2]Institute of Seismology and Physics of the Atmosphere, National Academy of Sciences of Turkmenistan, Aşgabat, Turkmenistan.
[3]Friedrich Schiller University Jena, Institute of Geological Sciences, Jena, Germany.
[4]Department of Geography, University of Sheffield, Sheffield, S10 2TN, UK.
[5]Department of Earth, Planetary, and Space Sciences, University of California Los Angeles, Los Angeles, CA 90095-1567, USA.
[6]Institute of Archaeology, 36 Beaumont Street, Oxford, OX1 2PG

Abstract

The Main Köpetdag[†] Fault (MKDF) of Turkmenistan is one of the longest (≈500 km) and most rapidly moving (9.1 ± 1.3 mm/yr) faults of the Arabia-Eurasia collision zone and yet, in contrast to adjacent parts of Turkmenistan and Iran, it has little in the way of observed seismicity. Our field observations along the MKDF indicate a fresh palaeo-earthquake rupture along a ≈200-km-long section of the fault with abundant streams offset across it. We use 40 cm optical satellite imagery from the WorldView-2 satellite to measure stream offsets and compile them into a cumulative offset probability density function (COPD). The high quality COPD yields peaks at 7.5 ±1.5 m and 12.5 ±1.5 m, which we interpret to arise from the most recent and penultimate surface rupturing earthquakes; although we note that it is not possible to separate events with lower quality measurments which instead yield a single peak at 10 ±4 m. The palaeo-earthquake rupture displaces archaeological remains, including extensive field boundaries of likely Medieval age, and a palaeoseismic trench across the fault brackets the age of the most recent displacement at 600–800 years B.P.. From our measurements of displacement we estimate that the most recent palaeo-earthquake may have had a moment magnitude of 7.8 ±0.3, and yet is missing from earthquake records from nearby Iran, indicating that the paucity of historical earthquake records in Turkmenistan may be misleading. The Baharly, Döwgala, and Gökdepe segments of the MKDF, which extend eastwards to the city of Aşgabat, do not show fresh surface expression of faulting. Two IRSL ages of 3.4 ± 0.5 ka and 2.5 ± 0.2 ka from a river cutting exposure along the Baharly segment

[†]We use Turkmen spellings for geographical and town names as these are the accepted spellings in Turkmenistan, rather than the Persian or Russian equivalents as often used in papers describing the regional tectonics. Thus Köpetdag rather than Kopeh Dagh, Aşgabat rather than Ashkhabad.

predate the most-recent surface rupture. We conclude that individual segments of the MKDF fault are capable of rupturing in large magnitude earthquakes, with the ends of individual ruptures controlled by segment boundaries. The occurrence of large earthquakes, combined with the rapid slip-rate, suggest that the MKDF constitutes a significant hazard.

2.1 Introduction

The on-going continental collision between Arabia and Eurasia results in widespread active faulting and earthquakes across a zone spanning 2000 km from east to west and 1500 km from north to south (Figure 2.1). The relatively compact geographical extent, recent onset of presently-active deformation, and the excellent preservation of the active fault geomorphology in the arid environment has led to its use as a natural laboratory in the study of faulting and continental tectonics (e.g. *Jackson and McKenzie*, 1984; *Walker et al.*, 2021; *Rizza et al.*, 2013; *Ritz et al.*, 2006). The widespread active faulting also constitutes a source of earthquake hazard within Iran and its surroundings. Numerous destructive earthquakes have occurred within recent decades, with forensic investigations leading to advances in understanding of earthquake rupture processes (e.g. *Nissen et al.*, 2019; *Mackenzie et al.*, 2016; *Zhou et al.*, 2015; *Talebian et al.*, 2004).

Active tectonic studies in Iran are aided by the exceptionally long historical records that exist throughout much of the region (e.g. *Ambraseys and Melville*, 1982; *Berberian and Yeats*, 1999). The recurrence interval between earthquakes on individual active faults with the Arabia-Eurasia collision zone may be hundreds, or even thousands of years, such that the existing catalogues of instrumentally-recorded earthquakes do not highlight all zones of hazard (e.g. *Hollingsworth et al.*, 2010; *Mousavi et al.*, 2021; *Klinger et al.*, 2000). The historical sources provide a database spanning much longer periods of time that, when combined with instrumental records, provide valuable insight for earthquake hazard studies. However, the level of completeness of the historical catalogues will vary through space and time and it is not clear whether seismic gaps within the deforming zones are due to incompleteness of the historical record.

One observation from the combined instrumental and historical earthquake record is that earthquakes across the Arabia-Eurasia collision zone do not typically have

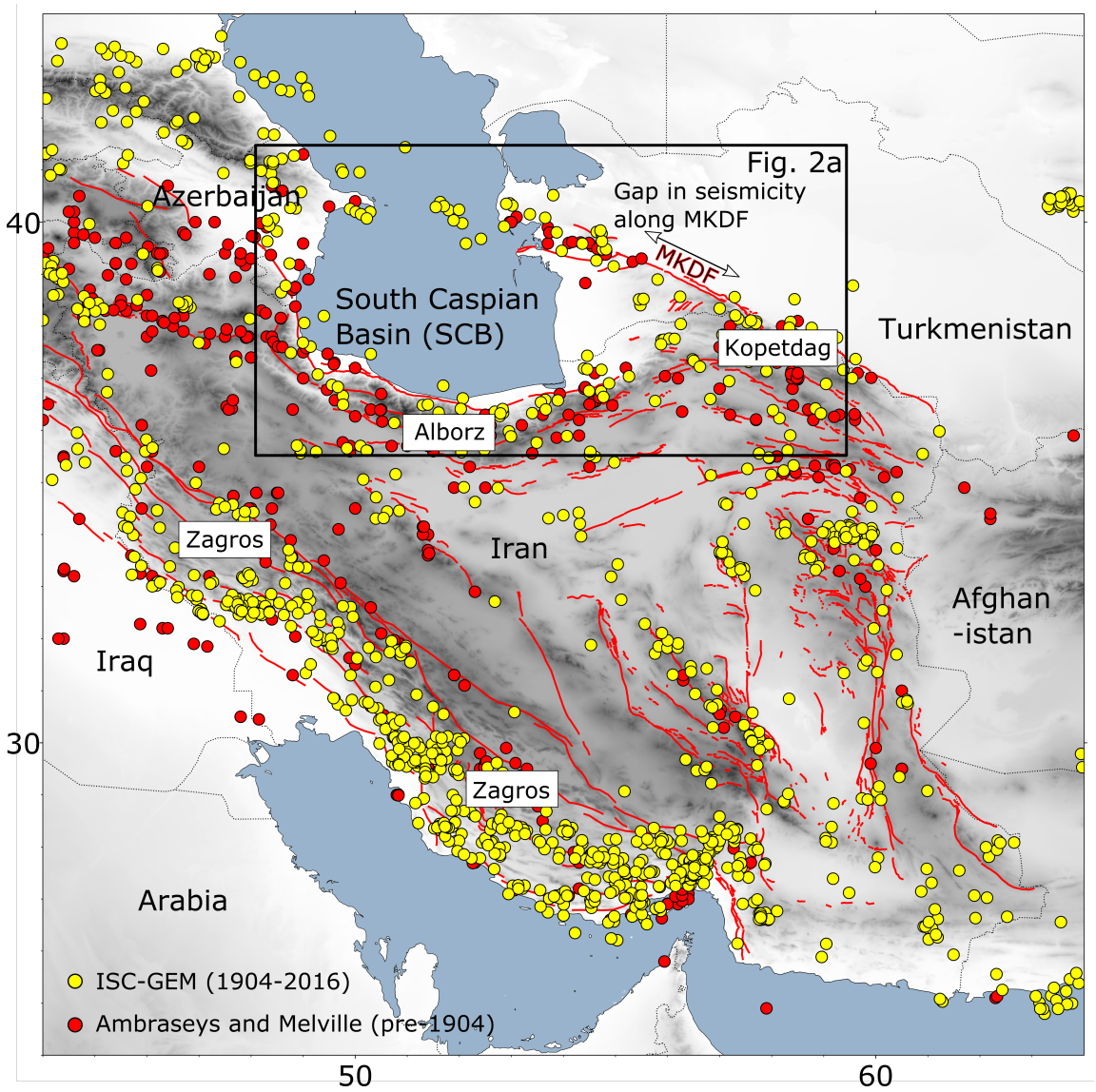


Figure 2.1: Active faults and earthquakes within the Arabia-Eurasia collision zone. Pre-20th Century earthquakes ($M_W > 5.0$), from *Ambraseys and Melville* (1982), are shown as red circles. Locations for earthquakes ($M_W > 5.0$) from 1904 to 2016 are from the ISC-GEM Global Instrumental Earthquake Catalogue (see Data and Resources Section) and are displayed as yellow circles. Active faults are plotted as red lines. The black box shows the region covered by Figure 2.2.

magnitudes that exceed M_W 7.5. The 16 September 1978 Tabas earthquake is the largest instrumentally recorded event, with M_W 7.3 (e.g. *Walker et al.*, 2003). The 856 C.E. Qumis/Damghan earthquake, which may have ruptured the Astaneh fault segment in the eastern Alborz (*Hollingsworth et al.*, 2010), is potentially the largest documented event, with an estimated M_W of 7.8. However, the size of this earthquake

is still debated (e.g. *Berberian*, 2014). The absence of earthquakes with $M_W >$ 7.5 is surprising, given that the Arabia-Eurasia collision zone contains a number of strike-slip faults that are relatively unsegmented, and are of sufficient lengths (>100 km) to potentially rupture in larger earthquakes (e.g. *Hollingsworth et al.*, 2010; *Mousavi et al.*, 2021). Along several of these long strike-slip faults there is no documented or instrumentally recorded history of earthquakes.

One apparent seismic gap is along the Main Köpetdag Fault (MKDF); a predominantly right-lateral, strike-slip fault that defines the northern edge of the Köpetdag of Turkmenistan and Iran (Figure 2.1). The MKDF is an important element in the regional tectonics, as it likely accommodates the right-lateral component of motion between the South Caspian Basin and stable Eurasia (e.g. *Jackson et al.*, 2002; *Hollingsworth et al.*, 2010; *Walker et al.*, 2021). It has a prominent expression in the geomorphology and is moving rapidly, with an estimated lateral slip-rate of ≈9 mm/yr from both late Quaternary and geodetic estimates (*Walker et al.*, 2021; *Walters et al.*, 2013). A large proportion of Turkmenistan's population is located along a narrow zone running parallel to the MKDF, such that it constitutes a significant earthquake hazard.

We investigate the potential for large earthquakes on the MKDF, combining evidence from field mapping, palaeoseismic trenching, and from the analysis and measurements made from high-resolution optical satellite imagery. In the following sections we first describe the regional tectonic setting and the earthquakes that are known to have occurred in Turkmenistan and adjacent parts of Iran. We then introduce our methods, before presenting the results of our field-based and remote sensing analysis. Finally, we discuss our results in the general context of the controls on rupture of major strike-slip faults as well as more locally, in terms of the level of completeness of the earthquake record in Turkmenistan, and in terms of the implications for seismic hazard in Turkmenistan and Iran.

2.2 Active tectonics and earthquakes in NE Iran and Turkmenistan

2.2.1 Active tectonics

The Arabia-Eurasia continental collision results in ≈25 mm/yr of northward-directed shortening between Arabia and Eurasia at a longitude of 55° E (e.g. *Vernant et al.*, 2004; *Walpersdorf et al.*, 2014; *Khorrami et al.*, 2019). Northward-directed GPS velocities relative to Eurasia decrease to zero at the eastern border of Iran, introducing a broad N-S right-lateral shearing across eastern parts of Iran (e.g. *Walker and Jackson*, 2004; *Walpersdorf et al.*, 2014). Some of the shortening is accommodated within the Zagros mountains of southern Iran, with much of the remainder occurring within the Alborz and Köpetdag (e.g. *Hollingsworth et al.*, 2010) (Figure 2.1). GPS velocities indicate up to ≈10 mm/yr of N-S shortening across the various ranges of NE Iran and Turkmenistan, including the Köpetdag in the longitude range 56-58° E (Figure 2.2a).

The ≈300°-trending Köpetdag range extends for ≈900 km, from Afghanistan in the east, to the shores of the Caspian Sea in the west (Figures 2.1 and 2.2a). Active faulting occurs along the entire length of the northern margin of the Köpetdag, but with a style that changes at the approximate longitude of Aşgabat, the capital city of Turkmenistan. East of Aşgabat the faulting appears to be predominantly reverse faulting, associated with northward Arabia-Eurasia convergence, whereas right-lateral strike-slip faulting appears to dominate west of the city.

GPS stations sited in the lowlands east of the Caspian Sea, between the Eastern Alborz and Western Köpetdag, show NW-directed velocities relative to Eurasia, related to the motion of the South Caspian Basin (SCB). The SCB is an aseismic block that moves independently to its surroundings (e.g. *Jackson et al.*, 2002; *Copley and Jackson*, 2006; *Djamour et al.*, 2010). *Walker et al.* (2021) estimate that the

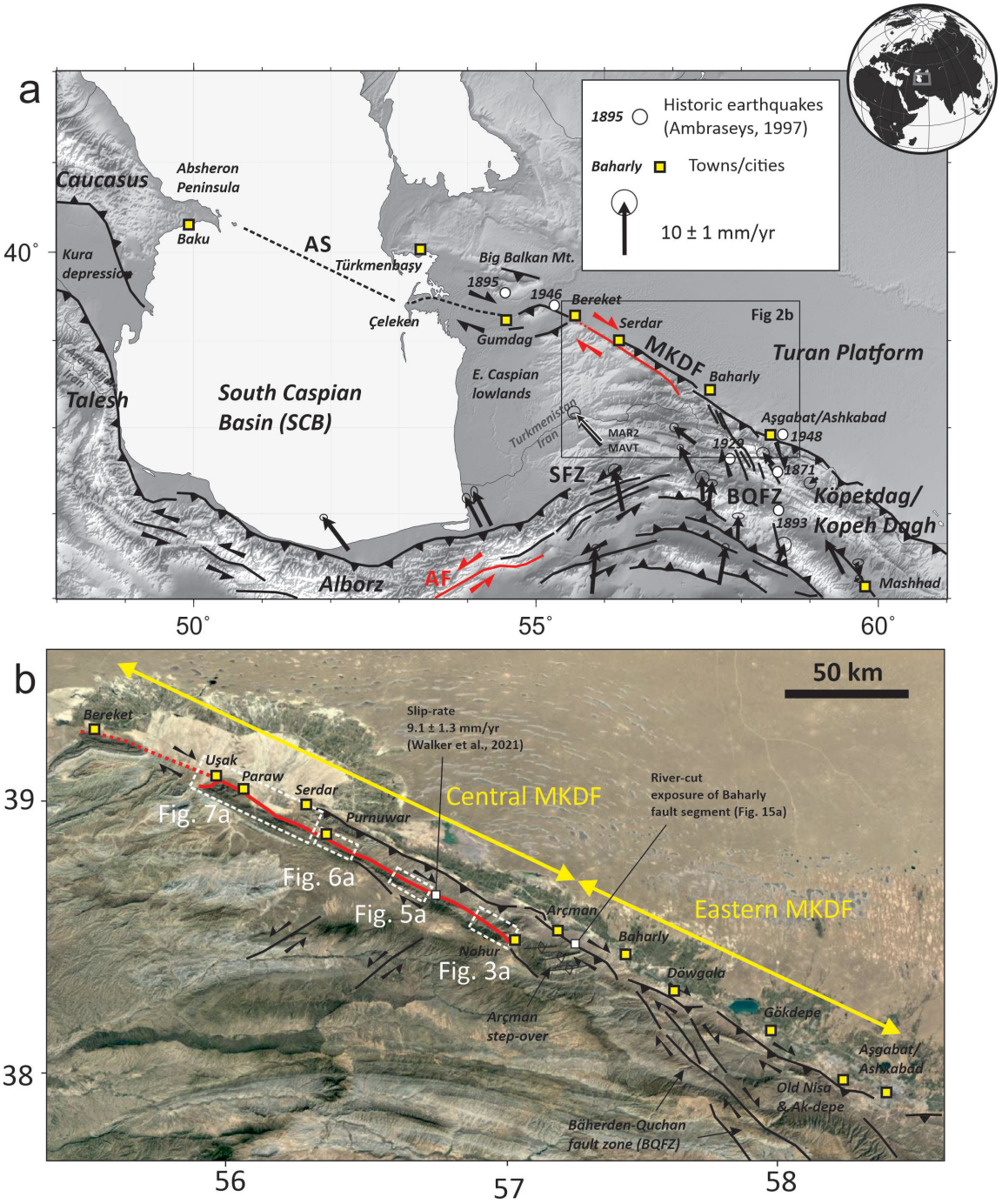


Figure 2.2: (a) Active faults of the eastern Caspian. The major fault zones are labelled. Main Köpetdag Fault (MKDF), Shahroud fault zone (SFZ) with the Astaneh Fault segment (AF) also labelled, Absheron Sill (AS), Bäherden-Quchan fault zone (BQFZ). GPS vectors within NE Iran from *Mousavi et al.* (2013) are plotted as black arrows. The location of historical earthquakes with $M_W > 5.0$ are plotted with white circles (*Ambraseys and Melville*, 2005). (b) ESRI basemap satellite imagery showing the central and eastern sections of the MKDF (*Hollingsworth et al.*, 2008). Mapped faults are displayed in black, with the red highlighting inferred palaeo-rupture. The boxes outline the location of subsequent figures in the text, not including the preceding chapter number (for example on the map 'Figure 3' refers to Figure 2.3 in Chapter 2).

South Caspian is moving 10.4 ± 1.1 mm/yr in direction 333°, ± 5°, relative to Eurasia and at 4.8 ± 0.8 mm/yr in direction 236°, ± 14°, relative to Iran, with the right-lateral MKDF along the Köpetdag, and the left-lateral Shahroud Fault Zone (SFZ) within the eastern Alborz, together accommodating the range-parallel components of motion of the SCB (e.g. *Hollingsworth et al.*, 2006, 2010). The MKDF has a late Quaternary slip rate of 9.1 ± 1.3 mm/yr (*Walker et al.*, 2021), which is consistent with an InSAR-derived strain accumulation of 8.5 ± 3.5 mm/yr across the fault (*Walters et al.*, 2013). The Shahroud fault zone consists of several overlapping segments. InSAR measurements of strain accumulation are consistent with available GPS measurements, yielding a left-lateral rate of 4.8 ± 0.8 mm/yr across the zone (*Djamour et al.*, 2010; *Mousavi et al.*, 2013, 2015), which are themselves consistent with late Quaternary rates of left-lateral faulting summed across the Abr and Khuj segments of the Shahroud fault (*Javidfakhr et al.*, 2011).

The MKDF and SFZ terminate eastwards at the NNW-SSE right-lateral faults of the Bäherden-Quchan fault zone (BQFZ, Figure 2.1). The intersection of the BQFZ with the MKDF marks the start of a progressive change in the style of deformation from the lateral extrusion of the South Caspian Basin, facilitated by conjugate strike-slip motion along the MKDF and SFZ, to crustal thickening in the eastern Köpetdag (*Hollingsworth et al.*, 2008). The distributed right-lateral faulting of the BQFZ is thought to accommodate along-strike extension within the Köpetdag range, as confirmed by recent GPS velocities (*Mousavi et al.*, 2013), and separates the easternmost parts of the Köpetdag range that accommodate N-S Iran-Eurasia shortening, from more westerly parts that are influenced by WNW expulsion of the SCB.

2.2.2 Earthquakes of the Köpetdag

Despite being relatively quiet over the instrumental period, there is a long record of large magnitude and destructive earthquakes across NE Iran (e.g. *Tchalenko and Skempton*, 1975; *Ambraseys and Melville*, 1982; *Ambraseys*, 1997; *Berberian and Yeats*, 1999; *Jackson et al.*, 2002; *Hollingsworth et al.*, 2010). These include significant earthquakes associated with the widespread reverse faults as well as along the major strike-slip faults of the eastern Alborz and Köpetdag ranges (e.g. *Hollingsworth et al.*, 2010). In contract to adjacent parts of Iran, there are no historical records of earthquakes in Turkmenistan prior to the late 19th Century, which could either reflect a real absence of earthquakes, or might be indicative of significant gaps within the historical record of this region. An additional challenge in the recognition of earthquakes in Turkmenistan is shown by *Ambraseys* (1997) who notes that the seismic intensities of the 8 July 1895 Krasnovodsk earthquake (Figure 2.2a) were asymmetric, with a much wider felt area to the north and northeast, where there is only sparse population, than to the heavily populated south. The apparent north-south difference in the reported seismic intensity is probably a combination factors, possibly because the population to the north at the time of this earthquake were more sensitive to the hazard posed by earthquakes, or that the Turan shield to the north is an ancient craton with low seismic attenuation (e.g. *Ambraseys*, 1997).

The 1895 Krasnovodsk (now Türkmenbaşy) earthquake (M_s ≈7.5) is one of the earliest recorded significant events in Turkmenistan. *Ambraseys* (1997) use the distribution of severe damage to the railroad, which extended from Big Balkan mountain in the west to Serdar in the east, to constrain its approximate epicentral region. No surface ruptures have been identified, no focal mechanism exists, and its depth is not well resolved. The 4 November 1946 Balkan earthquake (M_s 7.0) affected a similar area to the 1895 event, though was smaller in magnitude. The 14 March 1983 (M_b 5.2) Gumdag had a centroid depth of 27 km and the 22 February 1984

(M_W 5.7) Burun earthquake had a centroid depth of 31 km. Both were associated with surface ruptures in the East Caspian Lowlands (*Jackson et al.*, 2002; *Trifonov et al.*, 2009). The 2000 Balkanabat earthquake (M_W 7.0) had a thrust mechanism and a 31 km centroid depth, but no reported surface ruptures. The instrumentally determined depths for earthquakes west of longitude 55° E are significantly deeper than those for earthquakes further east within the Köpetdag and NE Iran (*Jackson et al.*, 2002), and may represent the burial of the basement structures of the Köpetdag under significant thicknesses of sediment. This sediment is predominantly derived from the palaeo-Amu Darya (Oxus), which currently flows into what remains of the Aral Sea but prior to as recently as the 16th Century continued to the Caspian Sea.

The most destructive earthquake known within Turkmenistan is the 1948 M_W 7.3 Aşgabat (previously Ashkhabad) earthquake (e.g. *Tchalenko and Skempton*, 1975; *Berberian and Yeats*, 2001), which devastated the capital of Turkmenistan (Aşgabat) and killed an estimated 10–110,000 people (the high uncertainty attached to the fatalities results from poor media reporting during the Turkmen SSR). A first-motion focal mechanism for the earthquake has a near-vertical NW-SE striking nodal plane, however the other is not well-determined due to the station distribution, and so it is uncertain whether this event represents a low-angle thrust or strike-slip earthquake (*McKenzie*, 1972). There were reports of surface deformation, though the relationship to geological structures is not clear (*Tchalenko and Skempton*, 1975; *Trifonov*, 1978; *Ambraseys and Melville*, 1982). There is archaeological evidence for destructive earthquakes in proximity to Aşgabat, with inferred earthquake damage at the Parthian city of Old Nisa dated from the first century B.C.E to the first century C.E. (*Pilipko*, 2007), and from the Bronze Age settlement of Ak-Depe at 3000-2000 B.C.E (location in the southwest of Aşgabat) (*Liapin*, 2006). In both instances, the interpretation of the damage (whether caused by seismic forces or not) and the dating are ambiguous. For example, an additional date of the fifth

century C.E. was proposed by some of the earlier excavators at Nisa, but does not appear in later publications (*Davidovich*, 1951). At Nisa, and at other sites, therefore, there are significant doubts as to the chronology of these events, which will only be resolved through significant additional archaeological investigation in parallel with seismological studies. There have also been several large earthquakes on the right-lateral faults of the BQFZ, within the interior of the Köpetdag (Figure 2.2a; *Hollingsworth et al.* (2006)). These include the 1851, 1871, 1872, 1893 and 1895 Quchan earthquake sequence with $M \approx 6.8$–7.2, the 1 May 1929 ($M_s \approx 7$) Baghan earthquake, which produced up to 50 km of surface rupture (*Tchalenko and Skempton*, 1975), and the 4 February 1997 Bojnurd earthquake with M_W 6.4 (*Hollingsworth et al.*, 2006).

The Astaneh segment of the left-lateral Shahroud fault zone shows palaeoseismic evidence for rupture in the early Medieval period (prior to 1300 C.E. and significantly later than 600 B.C.E.; *Hollingsworth et al.* (2010)). This rupture may have occurred during the M_s 7.5–7.9 856 A.D. Qumis/Damghan earthquake (*Ambraseys and Melville*, 2005, 1982). This earthquake is thought to have resulted in >200,000 fatalities in the population centres along the southern Alborz margin, including Damghan and the now abandoned city of Shahr-e-Qumis, though the size and effects of the earthquake, and its magnitude, are debated (*Berberian*, 2014). A paleoseismic trench across the Astaneh segment also showed evidence of rupture 600–4600 B.C.E. and 4600–9600 B.C.E. (*Hollingsworth et al.*, 2010).

In contrast to the examples from Aşgabat, the BQFZ, and the eastern Caspian lowlands there is a striking absence of earthquakes along much of the length of the MKDF itself. The fault along this 300 km 'seismic gap' is composed of a small number of overlapping segments. The westernmost of these is ≈200 km in length, such that even this single segment may be capable of rupturing in large-magnitude earthquakes. The fault is slipping rapidly (9.1 ± 1.3 mm/yr, *Walker et al.* (2021)),

and the absence of recorded historical earthquakes, if real, could indicate that significant amounts of strain have accumulated across it. In the following sections we assess likely timings, magnitudes, and role of segmentation in the palaeoseismic record of earthquake rupture along the MKDF.

2.3 Methods

To analyse the geomorphological signature of palaeo-earthquake ruptures, we use high-resolution (≈0.4 m pixel) pan-sharpened optical imagery from the WorldView-2 satellite, obtained through the Digital Globe Foundation. We use a near-infrared false colour band combination (band 7 (near-IR 1), band 5 (red), and band 3 (green)) to highlight near surface soil moisture differences. The WorldView-2 imagery enables us to map out the palaeo-rupture scarps and measure offsets along the fault. Offsets of up to 20 m were identified and measured using the methods described by *Kurtz et al.* (2018), with minimum, maximum and preferred measurements of offset obtained for each feature. A quality is assigned for each measurement based upon obliquity of the offset marker to the fault strike, sinuosity of the marker, and the sharpness of the marker. We verify the remote-sensing analysis with field observations at multiple points along the fault. Age control in the trenches and river cuttings comes from either radiocarbon dating or single-grain Infra-red-stimulated luminescence (IRSL) dating of feldspar grains, using methods as described in *Walker et al.* (2021).

2.4 Tectonic geomorphology and palaeoseismology of the MKDF

2.4.1 Tectonic geomorphology

Hollingsworth et al. (2008) divide the MKDF into three sections based upon the surface expression of faulting and seismicity. In our study we focus primarily on the central section, between longitudes 55–57° E (Figure 2.2b), where the fault is relatively simple in structure, predominantly right-lateral strike-slip, and well preserved in the geomorphology.

The central section begins, in the west, at the town of Bereket (Figure 2.2b). The fault continues eastward as a single oblique right-lateral and reverse scarp for 80 km to Serdar. East of Serdar the right-lateral and reverse components of slip appears to be partitioned onto parallel strike-slip and reverse faults, separated by a distance of ≈10 km across strike. Folded and exhumed basin sediments of Tertiary age are exposed in the area between the parallel fault segments (e.g. *Ghassemi and Garzanti*, 2019). The relatively soft basin sediments have been eroded into badlands by rivers and streams flowing northward from the Köpetdag. Remnants of several extensive alluvial terraces are preserved within the badlands, and are also displaced right-laterally across the strike-slip fault by amounts up to ≈950 m. The oldest preserved alluvial terrace is ≈100 ka in age (*Walker et al.*, 2021). The strike-slip fault trace is particularly well preserved along this section as it cuts through the foothills of the Köpetdag at a relatively high elevation and far from any population centre and infrastructure. Only localised vertical motion is present at small bends along the otherwise linear trace. Numerous streams and other small-scale landforms record metre-scale right-lateral offsets that can be observed in the field and in remote sensing imagery. At longitude ≈57° E the active fault trace bends to the south and ends in the mountains southwest of Arçman, at what we term the 'Arçman restraining

bend' (Figure 2.2b).

The eastern section of the MKDF overlaps with the central section across the Arçman restraining bend. There are at least three distinct segments within the eastern section of the MKDF (Figure 2.2b). The Baharly segment is ≈50 km long, forming the northern margin of the Arçman restraining bend in the west, and ending in the east at the intersection with the right-lateral faults of the BQFZ (Figure 2.2). The Döwgala segment extends for a further ≈30 km to end at a left-step of ≈5 km in the fault trace. The eastern end of the Döwgala segment is at roughly the eastern limit of the BQFZ. East of the Döwgala segment, the MKDF continues along the margin of the Köpetdag past Gökdepe to Aşgabat, though with generally subdued geomorphological expression.

In the following sections we first examine the evidence for earthquake rupture along the ≈200 km-long Central Section (Section 2.4.2), and then quantify the offsets using a Cumulative Offset Probability Density (COPD) approach (Section 2.4.3). We then present results from a palaeoseismic site along the central section where we are able to provide age control on the most recent surface-rupturing earthquake, along with a second trench where we likely see the cumulative effects of several earthquakes, and yet could not distinguish individual events (in Section 2.4.4). We then present one palaeoseismic site that enables us to provide a limiting age for the most recent earthquake on the adjacent Baharly segment (also in Section 2.4.4).

2.4.2 Palaeo-earthquake ruptures on the central section of the MKDF

The central strike-slip section of the MKDF, between the Arçman restraining bend in the east and the town of Serdar in the west, is extremely well preserved. The fault trace in this region is manifest as steep continuous scarps, even within the floodplains of active fluvial systems, and displays numerous 6–9 m offsets of streams,

and occasionally archaeological remains. We infer from the continuity and level of preservation that we are observing a surface rupture from a previously unrecognized earthquake. Examples of the morphology of the inferred palaeo-earthquake rupture in satellite imagery and in the field are shown, from east to west, in Figures 2.3 to 2.8.

Figure 2.3 shows the eastern part of the inferred palaeo-earthquake rupture, which shows the right-laterally offset fluvial channels and shutter ridges that are characteristic of the central segment as a whole. In Figure 2.3b we show WorldView-2 imagery with the MKDF trace displacing and offsetting alluvial terraces and stream channels by amounts of several tens of metres. In Figure 2.3c we show a close-up image of two small and closely-spaced streams in the centre of Figure 2.2b. The margins of these two small channels are displaced by similar amounts (≈7–8 m) as also verified from field measurements, which show a sharp offset of the channel margin at the fault trace (Figure 2.3d). Around one kilometre northwest of the streams shown in Figure 2.3b–d, a small boulder fan is deposited across the fault (Figure 2.4). A series of closely spaced streams within this ≈400 m-wide boulder fan are consistently offset by values ranging from 6.7 to 8.1 m. The rupture continues to the eastern end of the region represented in Figure 2.3a but with decreasing amounts of right-lateral slip (e.g. Figure 2.3e). Beyond the eastern end of Figure 2.3a the rupture becomes increasingly difficult to trace, with the most southeasterly occurrence in the low hills west of the village of Nohur (Figure 2.2b). Given the very clear geomorphic expression of the rupture in the representative examples in Figures 2.3 and 2.4, and the lack of clear fault scarp east of Nohur, we assume that rupture terminates eastwards at Nohur.

Figure 2.5a shows the MKDF fault close to the Delimgor farm. Several ≈300 m right-lateral displacements are visible along with the inferred palaeo-earthquake rupture. In the region shown in the satellite image (Figure 2.5a) the fault has

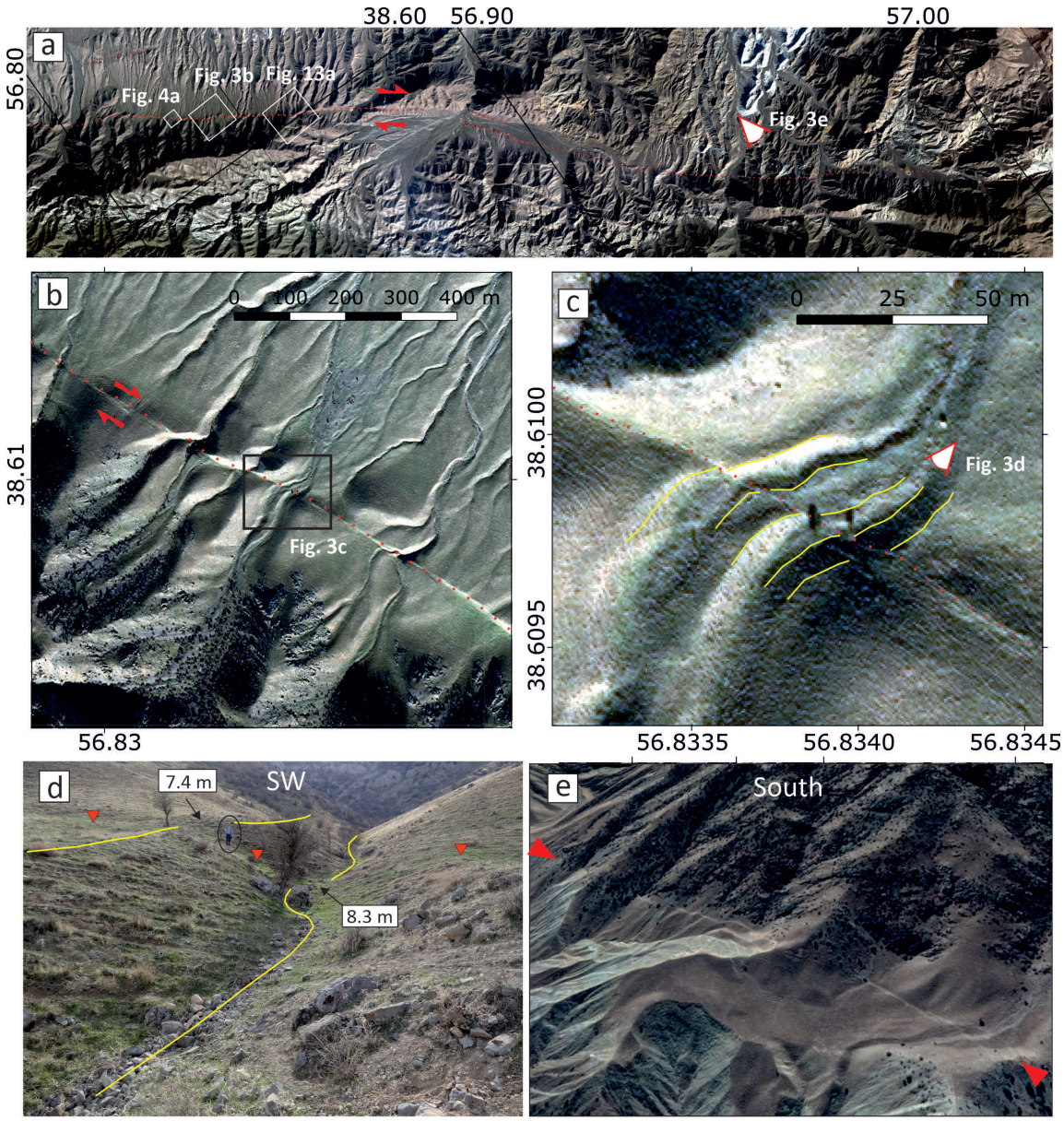


Figure 2.3: (a) WorldView-2 image showing the eastern part of the palaeo-rupture (See Figure 2.3a for location). The fault follows the red dotted line. (b) Typical geomorphology of the MKDF, with sharply-defined fault trace and right-lateral stream deflections at various scales. (c) A close-up view of drainage channels offset right-laterally by 7.4–8.3 m, which we infer to result from a single earthquake. (d) Field photo of the channel labelled in 'c', with the top and bottom of the sloping channel bank displaced by similar amounts. Person, circled, for scale. (e) Oblique view looking south along the inferred palaeo-rupture.

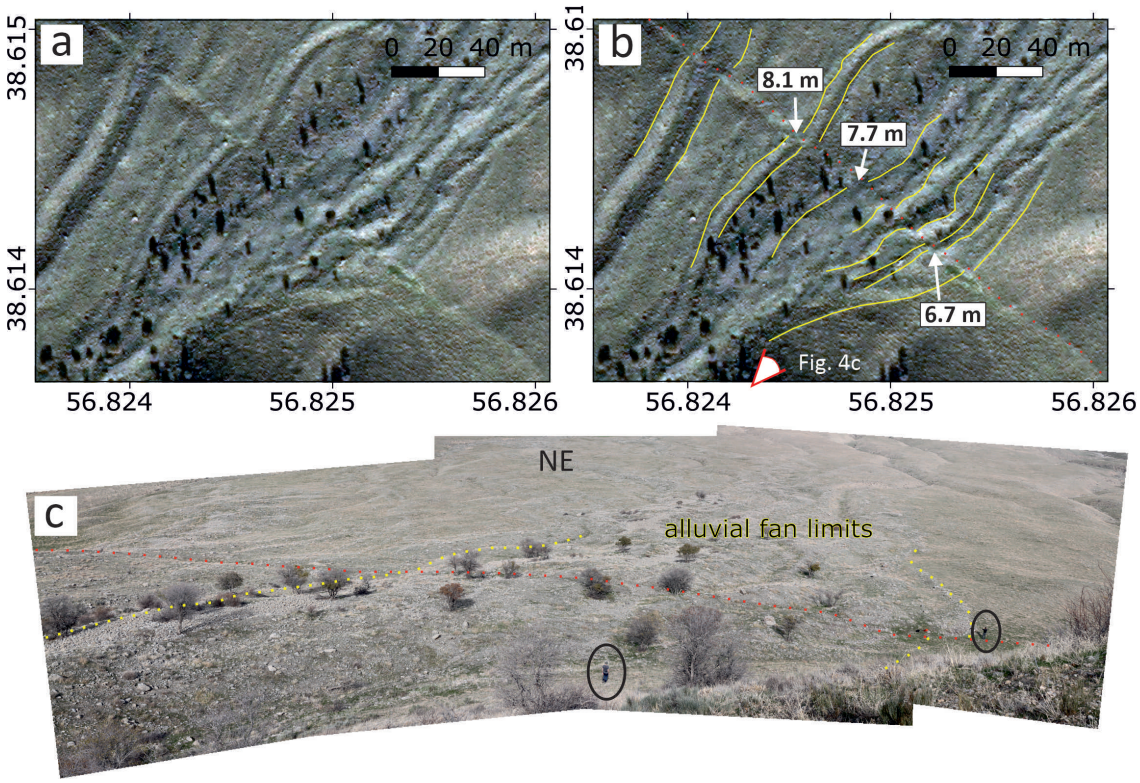


Figure 2.4: (a) A small boulder fan recording a high density of single-event offsets (see Figure 2.3a for location). (b) The same image as in 'a', with channels in yellow. All channels are displaced right-laterally, with our preferred offset measurements varying from 6.7 to 8.1 m. (c) Photo-mosaic looking northeast at the fan surface and through-going fault (red dotted line). The edges of the fan (yellow dotted lines) are displaced by a similar amount to the channels within it. People, circled, for scale.

diverged from its overall 300° trend, leading to a slight extensional component of slip. This extensional component is manifest, overall, as a south-facing scarp. Northward-flowing drainage from the Köpetdag mountains has ponded against the south-facing scarp at various points along this section, and we excavated a trench at one of these ponded sites adjacent to the farm (Section 2.4.4). Figure 2.5b is an oblique view looking south towards the fault near the left-hand part of Figure 2.5a, showing the typical palaeo-earthquake morphology with streams offset by 7–8 m and with the fault trace still visible within the floodplain of an active fluvial system. The field photograph in Figure 2.5c looks southwards towards a north-facing scarp, which is introduced at a localized pull-apart along the fault trace (Figure 2.5a).

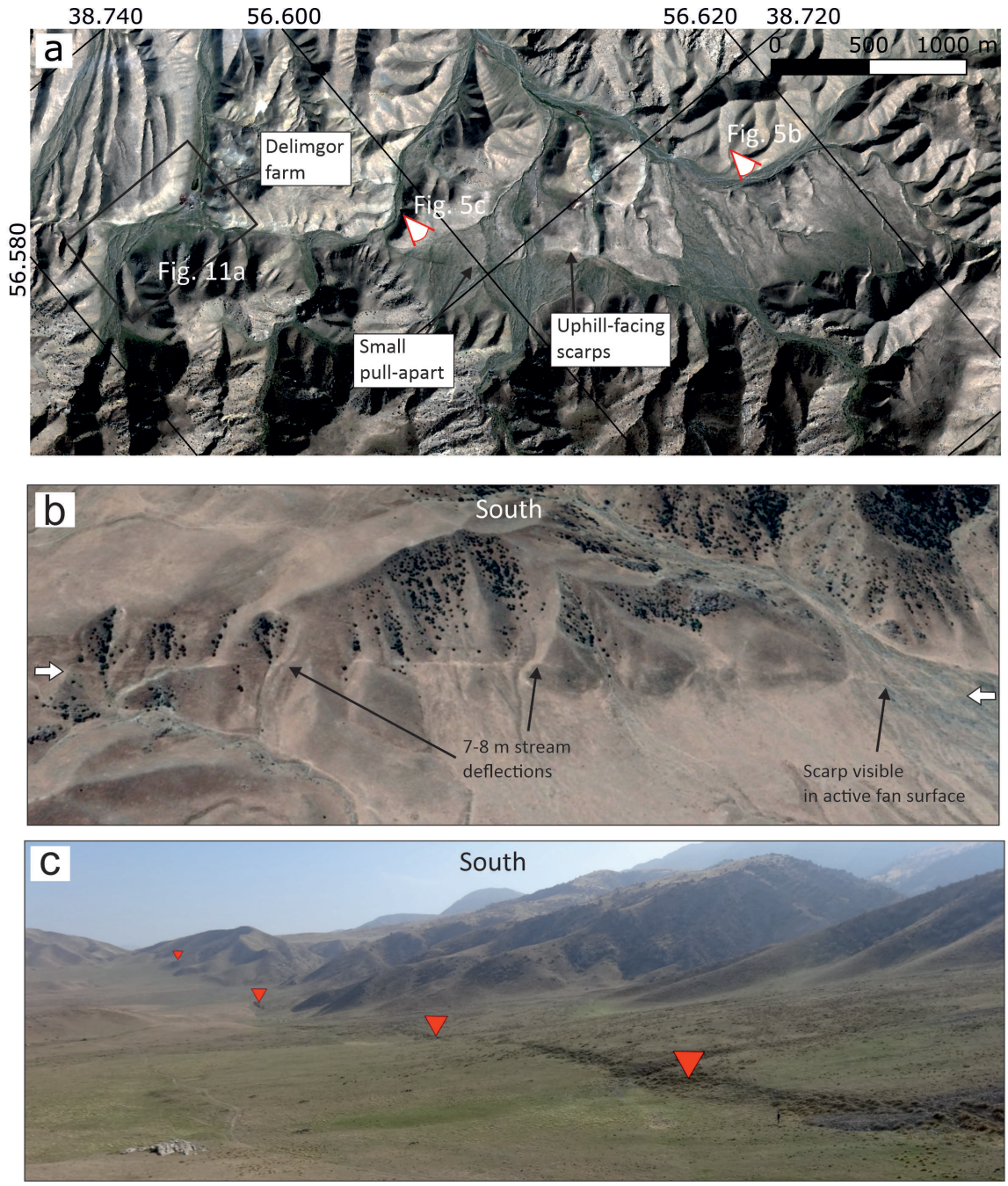


Figure 2.5: a) WorldView-2 image of the MKDF in the vicinity of the Delimgor farm and trench site (See Figure 2.2b for location). The fault bends in this section, introducing an extensional component that is manifest as uphill-facing scarps and a small pull-apart basin. (b) Oblique view looking south at the palaeo-rupture showing typical features associated with it, including a sharp fault trace, a number of 7–8 m stream deflections, and continuity of fault trace even within active fluvial systems. (c) Field photograph looking south along the rupture, note the person for scale in the foreground (location: 38.723° N, 56.597° E).

The region around Purnuwar town, south of Serdar, is shown in Figure 2.6. The town is sited at the western end of a linear valley bound by the MKDF to the south, and anticlinal folds to the north. The inferred palaeo-rupture is still very clear in the morphology in this section, and there are abundant stream displacements across it. The fault-bounded valley contains abundant cultural remains, including settlement mounds at Purnuwar itself, along with extensive qanat networks, and a widespread agricultural landscape of ancient field boundaries. Figure 2.6b is a WorldView-2 image showing the fault trace cutting through a network of field boundaries ≈10 km southeast of Purnuwar. Field boundaries that cross the fault show consistent right-lateral offsets of 6.8–13.6 m. We visited this site and verified the sharp offset of these boundaries (Figure 2.6b, inset).

The MKDF exits the mountains southwest of Serdar, and continues northwest along a single oblique fault trace along the base of the Köpetdag (Figure 2.7a). Figure 2.7b shows WorldView-2 imagery of the fault trace close to where it exits the mountains. West of Figure 2.7b there are few geomorphic markers providing piercing points for measurement of lateral offsets, due to the low relief and the greater modification of the landscape by human activities. Several cultural sites do, however, appear to show right-lateral displacement including qanat lines (Figure 2.7c), and the wall of a small site of uncertain age (Figure 2.7d–e). It appears that the fault trace passes just outside the 12th century or earlier walls of Farava (adjacent to modern Paraw, Figure 2.7a).

It is difficult to follow the palaeo-rupture further west of the village of Uşak (Figure 2.7a). The clearest expression of young faulting follows a set of prominent reverse fault scarps southwards from Uşak for ≈5 km (Figure 2.8) before being lost within outcrops of folded Tertiary rocks. It is possible that the most recent earthquake rupture followed this more southerly line. The main range-front fault continues northwest through the villages of Uşak and Isgender, where it cuts across a

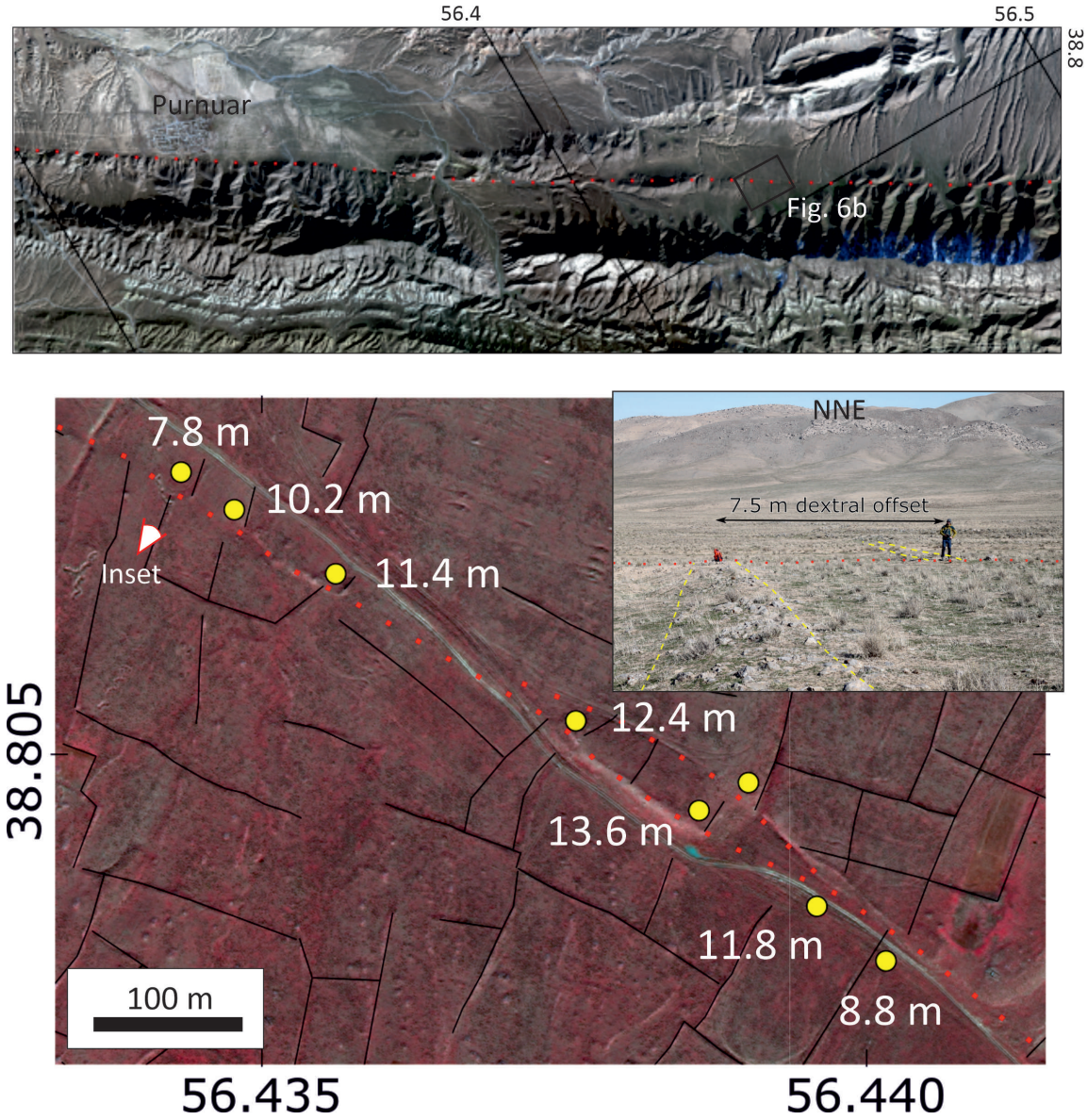


Figure 2.6: (a) WorldView-2 image of the MKDF near Purnuwar (see Figure 2.2b for location). The location of the fault offset ancient field boundaries, relative to present day Purnuwar and the fort at the archaeological site. (b) WorldView-2 false colour composite showing the MKDF (red dotted line), with the field boundaries marked by black lines and measured offsets marked by yellow dots (measurements in image vary from 7.2–13.6 m). The inset is a field photograph of one of the offset field boundaries.

wide light-coloured alluvial fan sourced from easily erodible Tertiary basin sediments exposed in the mountains to the south. The fault trace is poorly preserved in this section, which could be a function of the soft and erodible fan material, but also might suggest that it has not ruptured recently. An apparent 10–14 m right-lateral

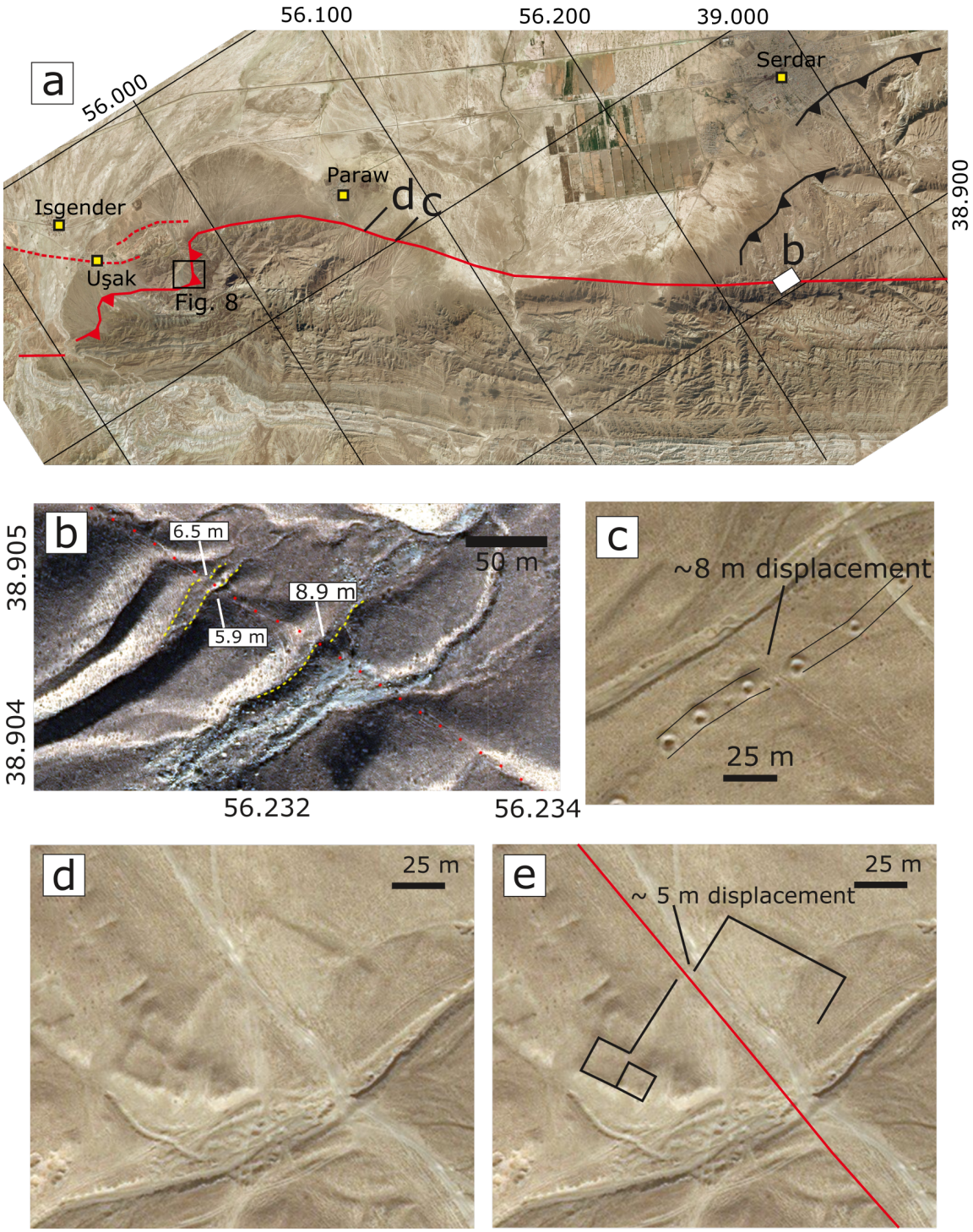


Figure 2.7: (a) Worldview-2 image of the western part of the mapped palaeo-earthquake rupture (see Figure 2.2b for location). (b) Inferred single-event offsets of multiple channels (measured displacements are the yellow markers) with preferred values of 5.9 to 8.9 m. These are the westernmost measurements included in the COPD analysis. (c) An apparent offset of 8 m recorded in qanat systems, east of Paraw. (d) Small archaeological site of unknown age east of Paraw. The site straddles the fault trace. (e) Interpretation of the site. The wall appears to be displaced by 5 m at the fault trace. Black rectangle shows the location of Figure 2.8.

displacement of a qanat line at Isgender has been used as evidence for recent activity (*Trifonov*, 1978; *Hollingsworth et al.*, 2008; *Siame et al.*, 2009). The range-front fault then continues to Uzynsuw and Bereket. The long-term late Quaternary expression of faulting is very clear along this section, with a linear oblique fault scarp, and yet the scarps do not appear to displace the youngest generation of alluvial fans. This suggests that this section of fault has not ruptured at the surface in the recent past.

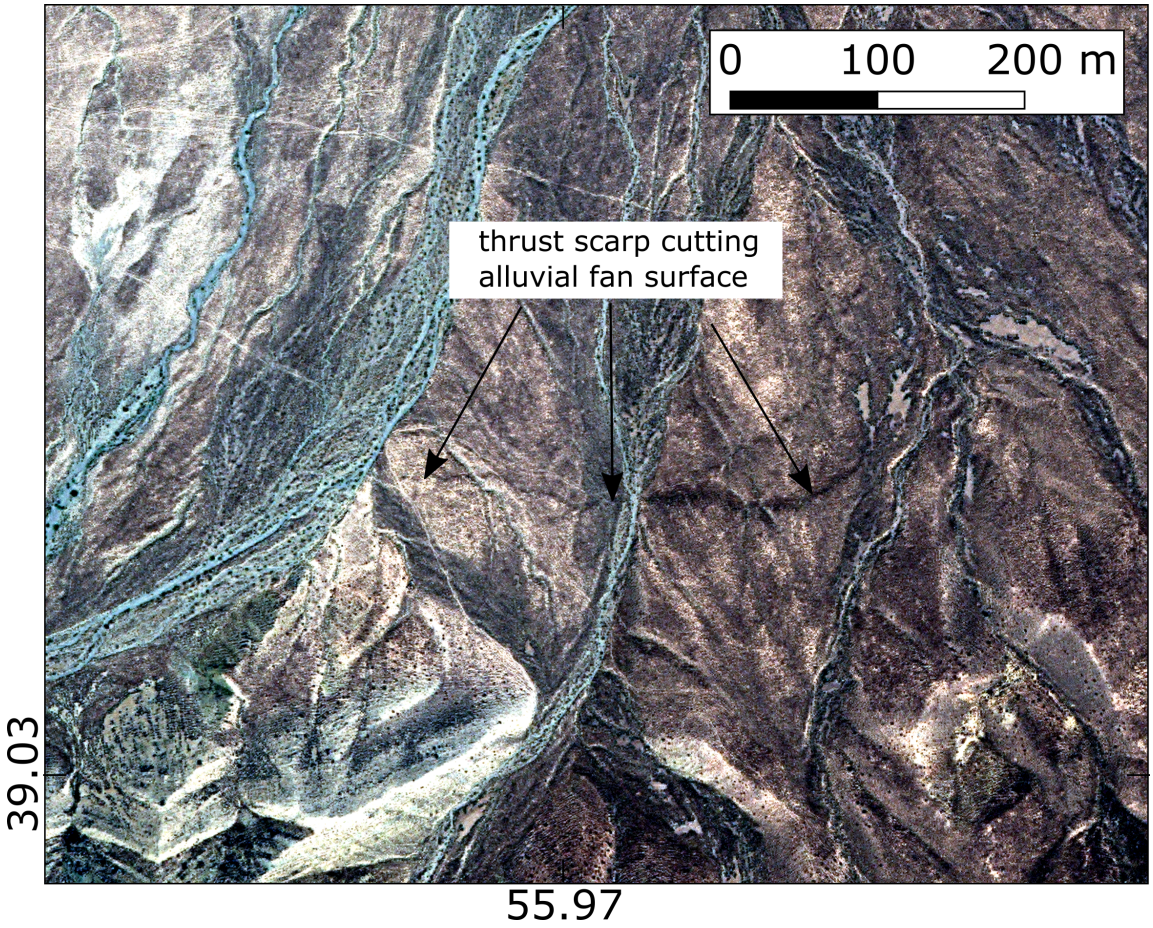


Figure 2.8: A view of the scarps near to the town of Uşak (location shown in Figure 2.7a). The palaeo-rupture deviates to the south of the range front, with thrust scarps displacing young alluvial fan terraces (in comparison to the eroded appearance of the fault heading westward from Uşak). This is possible evidence for the termination of the palaeo-rupture in the vicinity of this location.

The strike-slip MKDF fault runs parallel to a south-dipping thrust scarp between the Arçman restraining bend and Serdar. *Walker et al.* (2021) visted the thrust scarp at Borme (Figure 2.2b). At this site there is an ≈12 m-high scarp preserved

in alluvial older alluvial fan deposits (dated at 35,600 ± 1,800 years by *Walker et al.* (2021)) though a younger alluvial fan is not observably displaced by faulting. This example is typical of the thrust fault scarp along its length, with clear late Pleistocene scarps, but no obvious deformation in the youngest alluvial terrace. This suggests that the palaeo-rupture did not rupture, at least at the surface, along the parallel frontal thrust. The parallel strike-slip and thrust faults are a characteristic strain-partitioning geometry, observed elsewhere particularly along partitioned subduction zones (e.g. Sumatra, Philippines, Alaska). The location of the south-dipping thrust faults to the northeast of the strike-slip fault means that when the faults meet at depth the thrust interface can pass beneath the strike-slip fault without offsetting it, because the slip vector on the strike-slip fault is parallel to the line marking the meeting of the two fault planes. This is the only stable strain-partitioning geometry, allowing long-term finite motions without changing the configuration of faulting, and also requires that below the intersection that motion along the interface is oblique.

2.4.3 Analysis of geomorphological offsets

In Section 2.4.2 we described a number of offset streams and cultural features that are inferred to result from a single earthquake, extending over a zone ≈120 km in length from Nohur in the east to Uşak in the west. We interpret the eastern end of this inferred earthquake rupture to be at Nohur, due to the gradual reduction in displacement and increasingly subtle geomorphic expression of the fault. We suspect that the rupture extended further west of its mapped end at Uşak from the continuation of the fault trace, though the palaeo-rupture is not identifiable due to it entering a zone of soft and easily erodible Tertiary bedrock exposure. The prominent stream offsets of 6–9 m, examples of which are shown in Figures 2.3 to 2.7, were observed from ≈20 km west of Nohur (see example in Figure 2.2b) to southwest

of Serdar (Figure 2.7a–b), where the fault exits the mountains and becomes less well preserved. The frequent and well-preserved stream offsets thus occur over a distance of ≈70 km.

The systematic analysis of fault-offset landforms from surface rupturing earthquakes has frequently been used to reveal the magnitude, segmentation character and timing of earthquake ruptures preserved along faults (e.g. *Zielke et al.*, 2010; *Klinger et al.*, 2011; *Kurtz et al.*, 2018). When combined with palaeoseismological methods, this often provides the only access to the rupture history of multiple earthquake cycles on a fault, especially in the slow moving continental interiors. Using WorldView-2 imagery we were able to make 246 measurements of fault offset along the 70 km of best preserved rupture, as shown in Figure 2.9a, and included as a table (supplementary data). For each offset measurement we followed the methods of *Kurtz et al.* (2018) in assigning minimum, maximum and best-fitting estimates and also a quality rating. Offsets of up to 50 m were included in our analysis.

We then compiled our measurements to assess whether the 6–9 m offsets are likely to have formed in a single earthquake and to calculate the average displacement from the most recent offset along the 70 km length of fault, following the approach detailed in *Kurtz et al.* (2018). The values for each offset are input as a triangular Probability Density Function (PDF), and then stacked to form a Cumulative Offset Probability Density (COPD) function, as shown in Figure 2.9. An assumption is made that the average offset follows a Gaussian distribution, such that the average offset and uncertainty are calculated from the mean and standard deviation of a best-fitting Gaussian distribution. We use Gaussian probability density functions for individual measurements, where the minimum and maximum values correspond to the 2σ-uncertainty.

In the COPD including only the highest confidence measurements, there are two

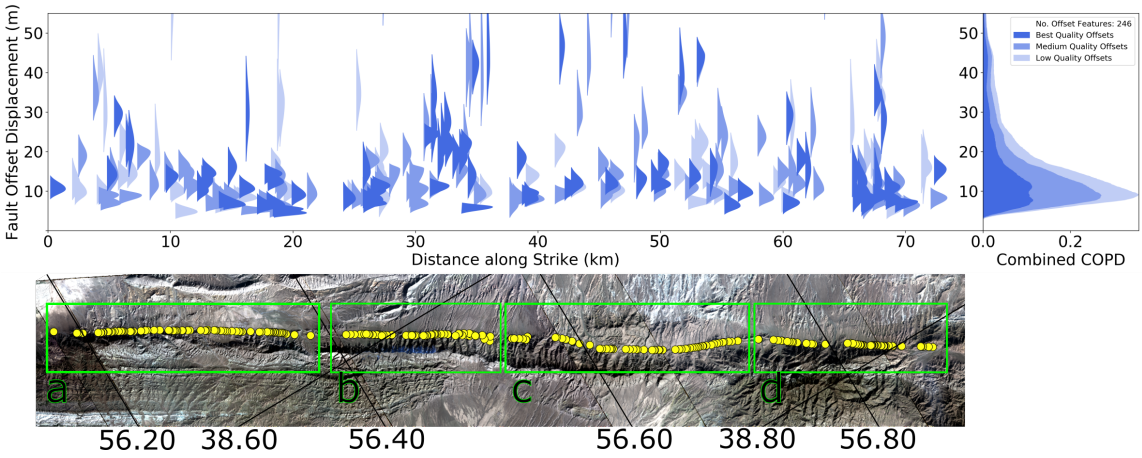


Figure 2.9: Cumulative Offset Probability Density (COPD) analysis. Minimum, preferred and maximum measurements of offset were made at 246 sites along 70 km of the palaeo-rupture. Each measurement site is shown as a yellow dot on the WorldView-2 satellite image. The Probability Density Function (PDF) for each site is then shown as a function of distance from the westernmost measured site, with darker shades of blue representing the best quality measurements, following the criteria set out by *Kurtz et al.* (2018). The PDFs are stacked to form a single COPD, which shows peaks at 7.5 m ± 1.5 m and 12 m ± 1.5 m using the best quality measurements.

distinct peaks at 7.5 m and 12.5 m of displacement. However in the medium and lowest quality measurements, there is no discernible peak separation and instead there is a singular peak at ≈10 m. At displacements greater than 12.5 m the signals in the distribution decay rapidly. This decay is likely to represent the dominance of erosional processes at these larger offset values (*Zielke et al.*, 2015; *Lin et al.*, 2020). The peak at 7.5 m supports the evidence from geomorphological analysis that the lowest offsets, representative of the most recent event along the MKDF, appear to have consistent displacements of 6–9 m (e.g. Figures 2.3 to 2.7).

It is possible that significant variations in amount of slip have occurred over the 70 km of fault length, which could cause miscorrelation of single-event and multiple-event offsets along strike. In Figure 2.10 we compile COPDs from four sub-sets of the offset measurement dataset (regions labelled a–d in Figure 2.9a), in order to look for changes in the positions of peaks in the COPD along the length of the fault. Subsets a, b and d all show the same characteristic peak at 5–9 m

preserved in the geomorphological record, irrespective of whether only high quality offsets or all offsets are used. In subset c the COPD distribution shows a single broad peak at ≈12 m if high quality offsets are used, though the inclusion of lower quality offsets produces a single broad peak at ≈8 m. Whilst it is not impossible that this section of the MKDF ruptured in multiple smaller events, the relatively consistent slip along strike coupled with no evidence of barriers to rupture propagation leads us to suggest that this segment ruptured in a single large event.

2.4.4 Timing of earthquake rupture

The preservation of a discrete earthquake rupture along the central section of the MKDF suggests that it has ruptured in a significant earthquake in the relatively recent historical past. The ruptures cut through and displace field networks of probable medieval age near Purnuwar (Figure 2.6), indicating that the most recent rupture occurred during or after the Medieval period. Further west the ruptures also displace a number of other cultural features of unknown age (Figure 2.7). We now describe our interpretation of a palaeoseismic trench across the fault at Delimgor (Figure 2.5) where sediments have ponded against the fault scarp due to a localized extensional component of slip. We then describe results from a second small trench from the eastern part of the palaeo-rupture (Figure 2.3). Finally, we provide initial constraint on the timing of the most recent earthquake on the Baharly fault segment, which continues eastwards from the preserved earthquake ruptures (Figure 2.2b).

The Delimgor trench site is shown in Figure 2.11. A northeast-flowing river has incised into alluvial deposits and is displaced right-laterally across the fault by ≈300 m. The active river thalweg is set within a low fluvial surface that has been displaced across the fault to form a south-facing scarp ≈2 m high, which we interpret to result from the most recent surface-rupturing earthquake. Sediments derived from a minor north-flowing ephemeral catchment are ponded against the

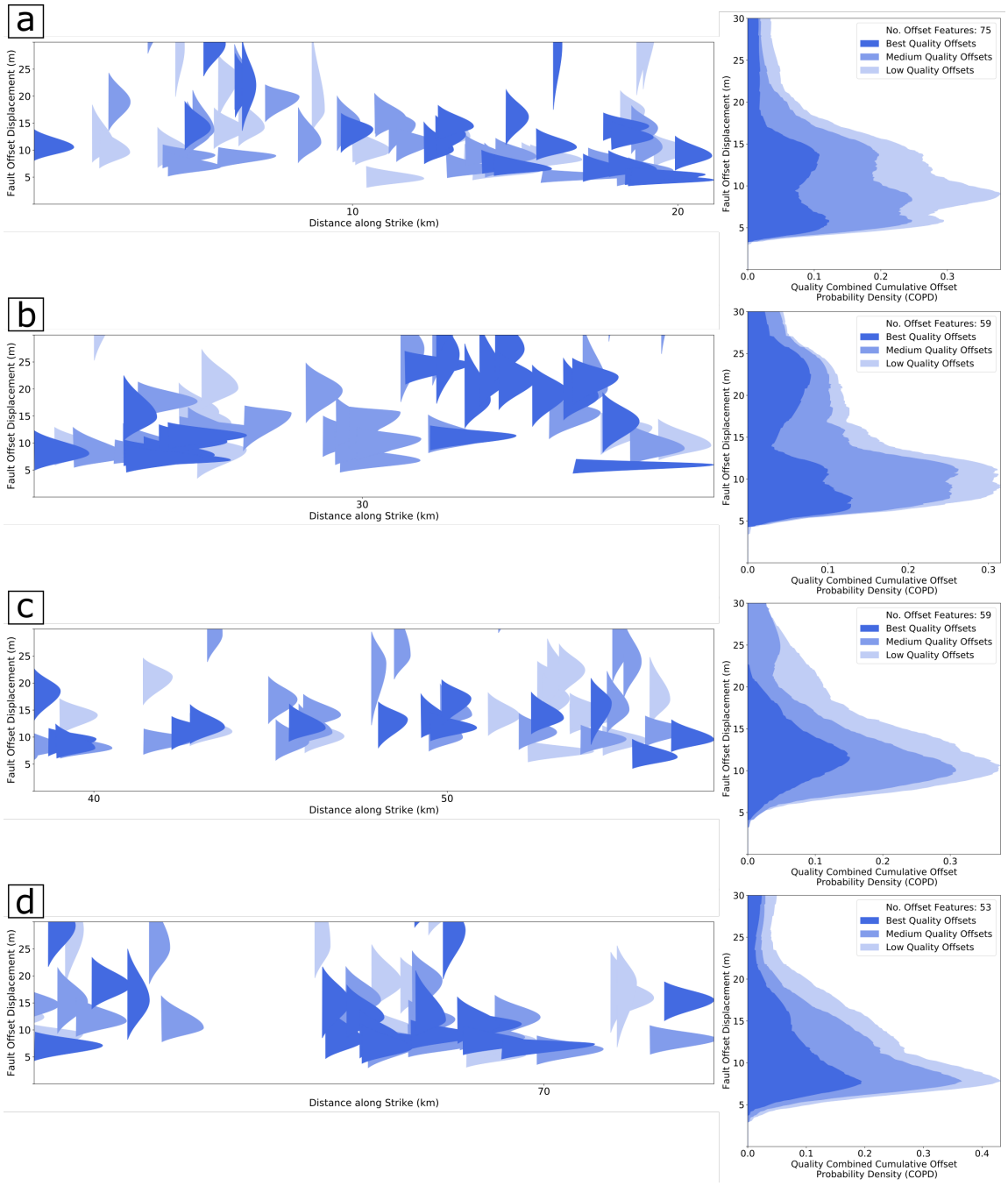


Figure 2.10: Stacked COPDs for four subsets of measurement data, as shown in regions labelled A to D in Figure 2.9. The lowest displacement peak from high quality offset measurements (dark blue) for each segment A-D are as follows: 6.1 m, 7.6 m, 12.0 m and 8.1 m.

south-facing scarp adjacent to the Delimgor farm. A man-made irrigation channel appears to be displaced right-laterally by ≈8 m. We excavated a trench across the ponded area, immediately southwest of the scarp.

In Figure 2.12 we show the southeastern wall of the trench. The northeast, uplifted, side of the fault is on the left-hand side. The remainder of the trench exposes sediments ponded on the downthrown side. Alluvial fan deposits are identified on both sides of the fault. On the upthrown side they extend to the surface. On the downthrown side they are exposed only at the base of our excavation. Here, they are very dark in colour, which we interpret as remnants of palaeosols including fragments of charcoal. A series of finer sediment units have accumulated above the coarse gravels in the downthrown side. The lowest of these units is a wedge of yellowish loess that has a maximum thickness of 20 cm. Above the loess we identified a maximum 10 cm-thick, dark layer with charcoals fragments. We interpret this layer as a palaeosol horizon that developed on top of the loess under stable conditions. These units are interpreted as pre-dating the last earthquake, because they are horizontal, undeformed, and indicate stable conditions.

In the NE part of the trench, there is a wedge of alluvial fan material that has collapsed from the upthrown block. The wedge is relatively steep (≈35°) and thick, which indicates that it was not exposed at the surface for very long, i.e., no diffusion process modified the wedge geometry over a significant amount of time. We interpret this wedge as a colluvial wedge that formed right after the NE side was uplifted in the last surface-rupturing earthquake. A thick layer (30–40 cm) of yellowish, charcoal-bearing loess overlies the wedge and the dark palaeosols. This loess unit is more cemented than the other loess layers in the trench. The loess quickly filled up the sediment trap created by the surface rupture and therefore post-dates the wedge. Above the loess we mapped a thick (40–60 cm) silty-sandy layer of soil with coarse sands and coarse gravels. This layer is overlain by a thin sheet of loess at the

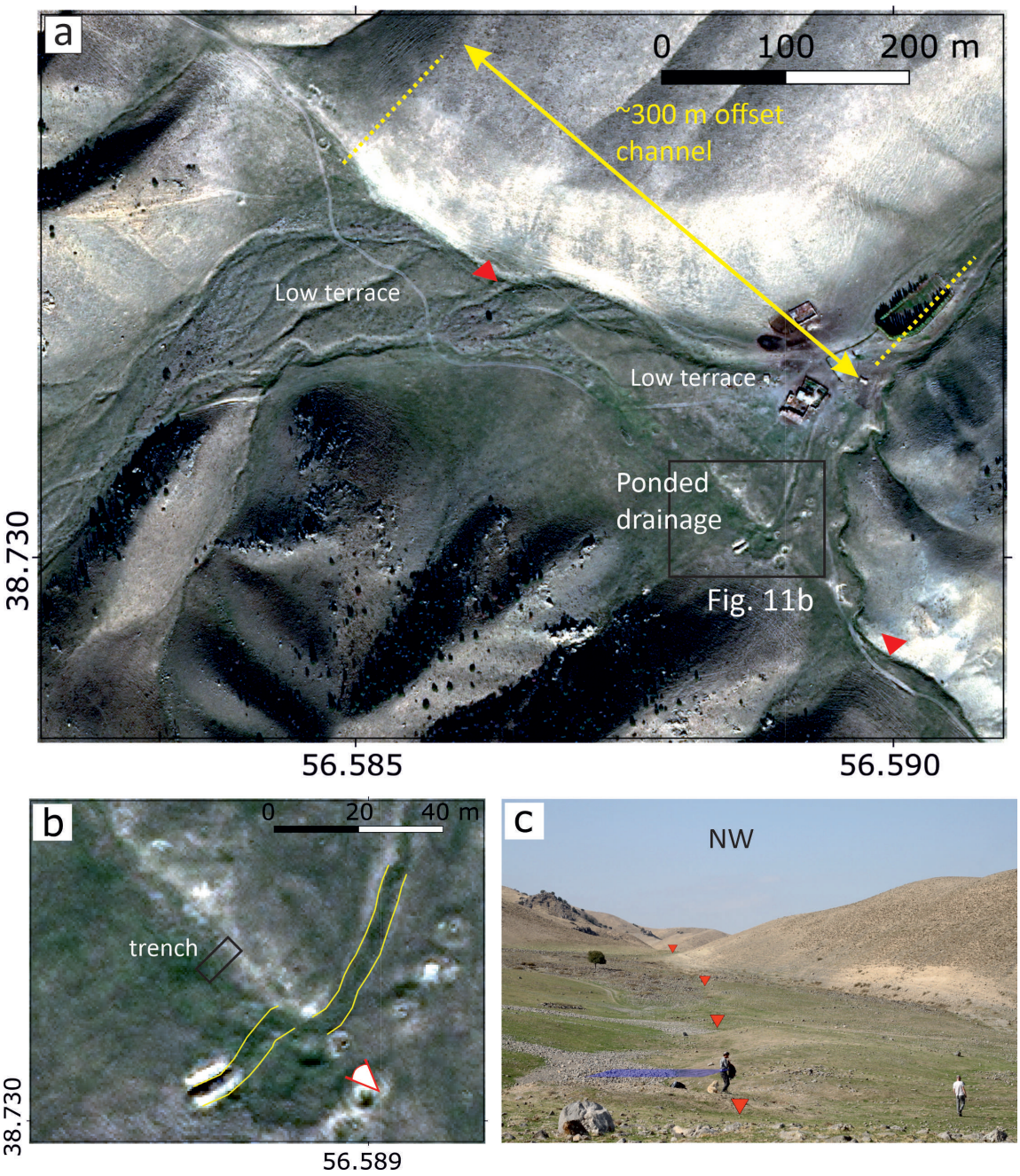


Figure 2.11: WorldView-2 data of the Delimgor trench site, see Figure 2.5a for location. The fault trace extends from bottom-right to top-left of the image. There is an approximately 300 m right-lateral river deflection at the site. The palaeo-earthquake rupture cuts through and displaces a young terrace within the fluvial system. Small fans emanating from nearby hillsides are ponded against the palaeo-earthquake scarp. (b) Close-up of the trench site (shown as a black rectangle). A man-made channel to the southeast of the trench shows possible right-lateral deflection. (c) Field photograph looking northwest along the fault (red arrows) to the trench site, where sediment has ponded against the uphill facing scarp.

Table 2.1: Details from Beta Labs (radiocarbon dating).

Beta ID	**Sample ID**	**Services**	**Conventional Age**	**Calendar Calibration**
485735	DM6	AMS-Standard delivery	610 +/- 30 BP	(95.4%) 1295 - 1404 cal AD (655 - 546 cal BP)
485734	DM5	AMS-Standard delivery	780 +/- 30 BP	(95.4%) 1210 - 1281 cal AD (740 - 669 cal BP)
485733	DM3	AMS-Standard delivery	760 +/- 30 BP	(95.4%) 1219 - 1284 cal AD (731 - 666 cal BP)
485732	DM2	AMS-Standard delivery	460 +/- 30 BP	(95.4%) 1412 - 1468 cal AD (538 - 482 cal BP)
485731	DM1	AMS-Standard delivery	630 +/- 30 BP	(95.4%) 1286 - 1398 cal AD (664 - 552 cal BP)

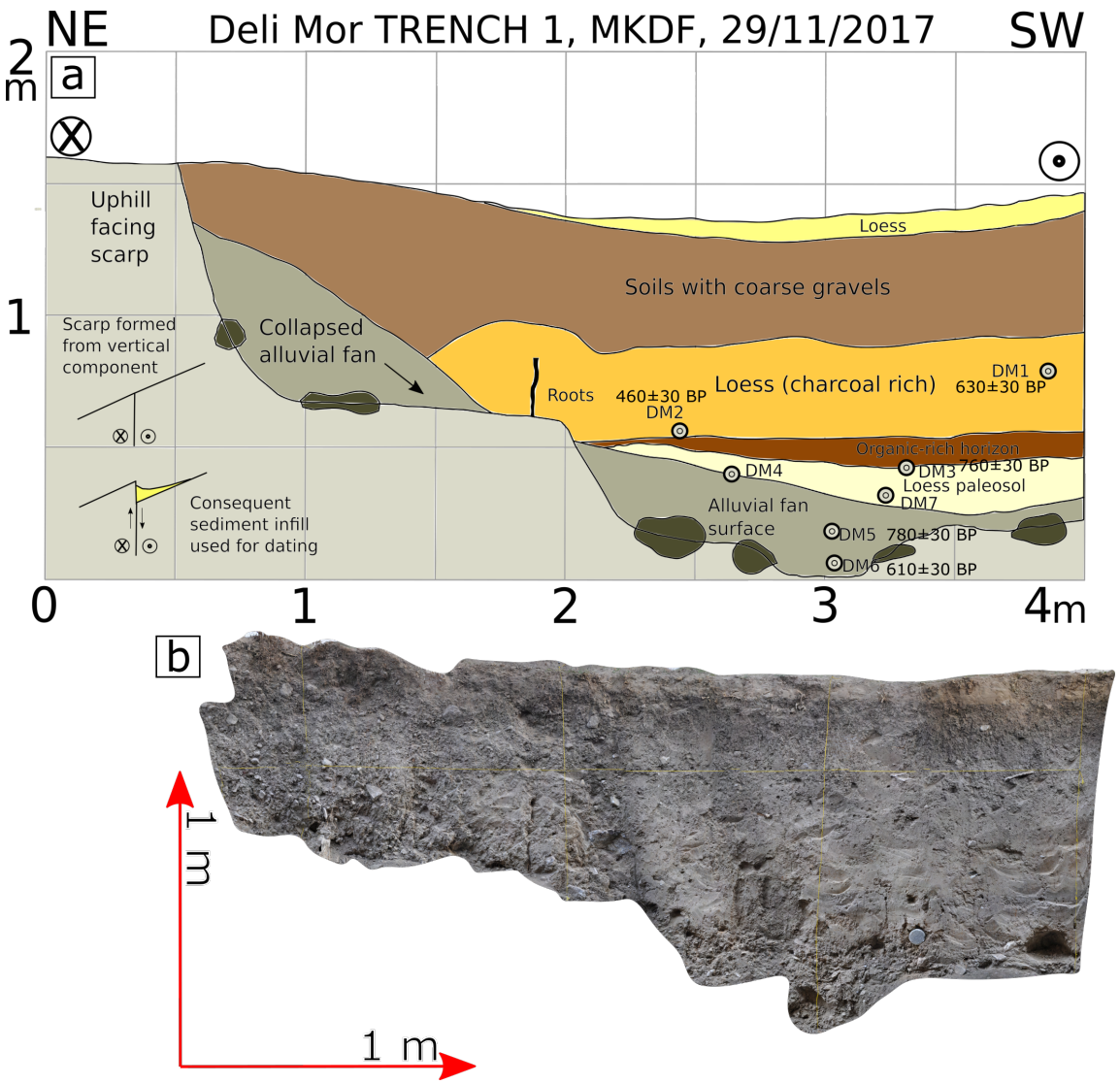


Figure 2.12: (a) Trench log and (b) photo mosaic of the southeast wall of the Delimgor trench. Sample locations are labelled in the trench log, aiming to bracket the offset of the alluvial fan surface; reference sample names to Table 2.1 for dating details.

surface.

Several detrital charcoal and organic-rich fragments were extracted from the trench wall for radiocarbon dating (see Table 2.1). Two samples (DM5 and DM6) were extracted from the uppermost part of the pre-earthquake alluvial deposit. These two samples returned calibrated ages of 1210–1281 C.E. and 1295–1404 C.E. A further three samples (DM3, DM4, DM7) were extracted from what we interpret as the pre-earthquake palaeosol. Only one of these samples (DM3) was successful and

returned a calibrated age of 1219–1282 C.E. Two samples were taken from the loess deposit that we interpret as post-dating the earthquake rupture. DM2 was taken from the base of this post-earthquake unit and returned a calibrated age of 1412–1468 C.E. DM1 was taken for a higher horizon within the same unit and returned a calibrated age of 1286–1398 C.E. The three samples from the pre-earthquake horizons contain material dating from the 1200s, though DM6 is compatible with a younger age of the early 1400s. The two samples from the post-earthquake units are out of stratigraphic order, indicating that the younger of the two is most likely to represent a limiting post-earthquake age, which is dated to the early-mid 1400s. Assuming that the three samples from the pre-earthquake units do not have significant detrital age components, the rupture is dated between the 1200s and the early-mid 1400s.

We excavated a second small trench at 38.601° N, 56.851° E (Figure 2.13), where the MKDF traverses a steep slope and has formed a small uphill-facing scarp that has partially infilled with ponded fine-grained sediments (Figure 2.13b). Coarse cobbles were exposed on the northern, upthrown, side and fine-grained deposits with occasional cobbles were exposed within the central and southern parts of the trench (Figure 2.14). We interpret these fine-grained units as representing the ponding of sediments against the scarp, and hence post-date scarp formation. We did not reach the base of these ponded units in the excavation. Two IRSL samples were extracted from the ponded material near the base of the exposure (Figure 2.14b, Table 2.2). T16-09 was the deeper of the two samples and yielded an age of 4.61 ± 0.26 ka. T16-08 was taken from ≈10 cm higher and yielded an age of 6.29 ± 0.32 ka. Examination of the WorldView-2 imagery shows that the scarp is associated with stream displacements of 17–23 m, such that the ages that we have obtained are likely to predate several of the most recent earthquake cycles. As we cannot distinguish sediment packages associated with individual earthquakes, this trench is not useful in constraining the ages of individual earthquakes.

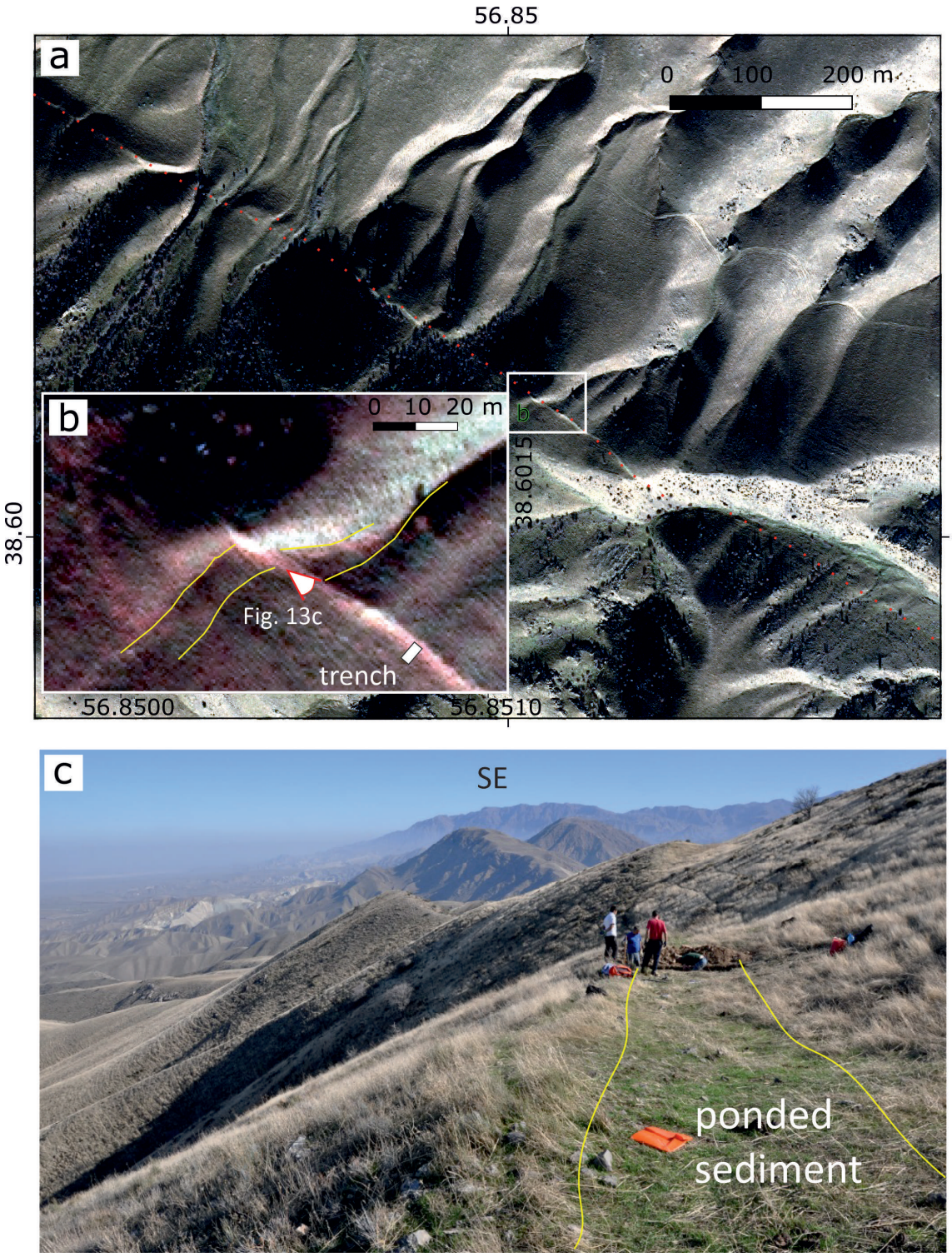


Figure 2.13: (a) WorldView-2 image showing the site of a small trench in the eastern part of the rupture (see Figure 2.3a for location). The fault scarp tracks across a steep northeast-facing hill slope. It has a component of uplift to the northeast and sediment has ponded against it. (b) A close-up image of the trench site location in 'a'. The beheaded stream outlined in yellow is offset by 17-23 m suggesting that the scarp here may be derived from several earthquakes. (c) Field photograph looking southeast across the ponded area (outlined in yellow) and trench.

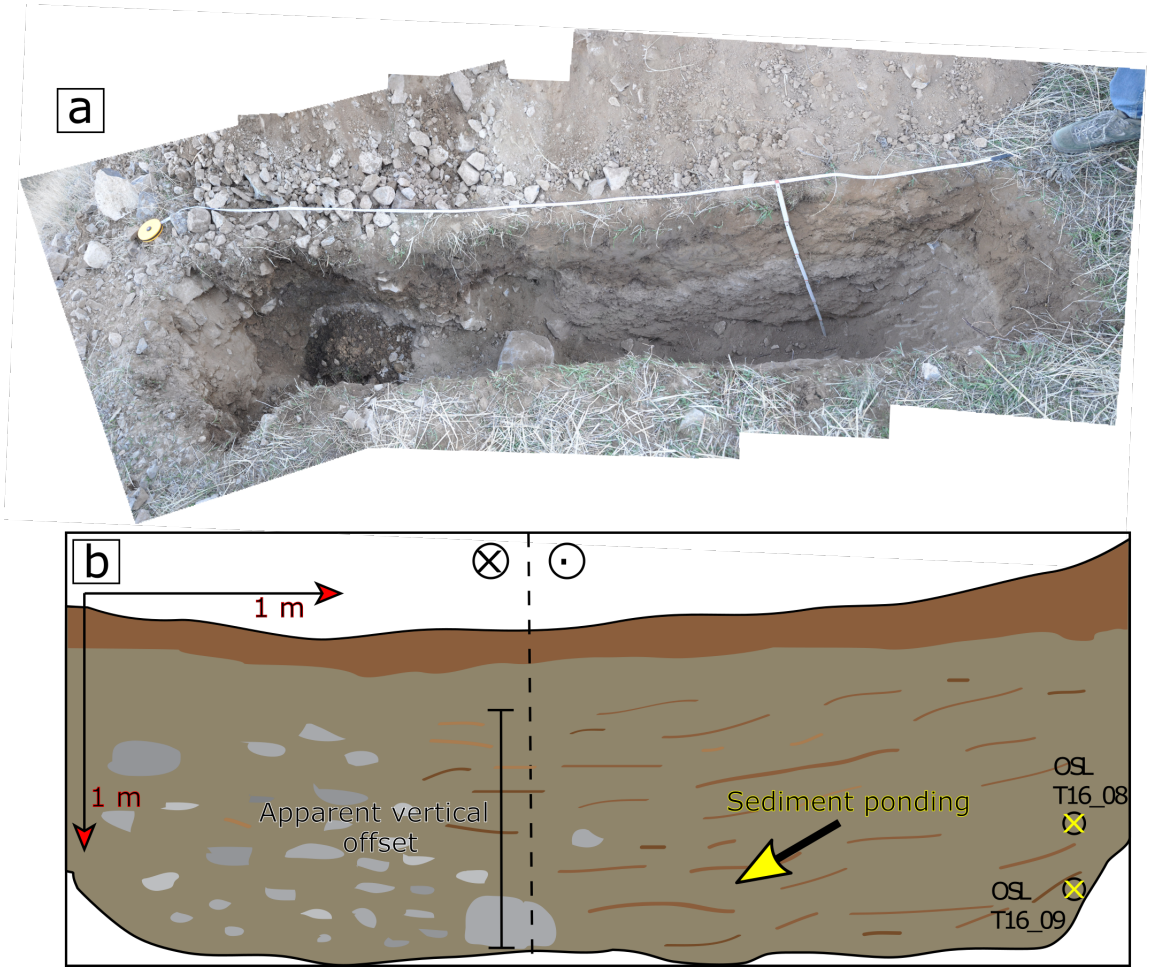


Figure 2.14: (a) Photo-mosaic looking down into the southeast wall of the trench shown in Figure 2.13b-c. (b) Sketch trench log. Fine-grained sediments have accumulated against the uphill facing scarp. The sharp ≈45° SW-dipping contact between fine-grained and coarse colluvium is interpreted as the fault. Two IRSL sample locations are labelled, with dating details provided in Table 2.2.

Segments of the MKDF east of the Arçman restraining bend have a geomorphic expression that is less fresh than along the central section, suggesting that it has been much longer since the most recent surface-rupturing earthquake on these segments than on the central section. We visited an exposure of the Baharly fault segment adjacent to the village of Sünçe (Figure 2.15). The fault is not clear in the alluvial cover (Figure 2.15a–b), but is visible in a river cutting, where gravel and silt layers have been offset vertically by ≈20 cm across a gently south-dipping fault plane (Figure 2.15c–d). IRSL dating of the fine silt layer (Table 2.2), the highest in the

stratigraphy to be displaced by the palaeo-rupture, returns ages of 2.5 ± 0.2 ka and 3.4 ± 0.5 ka that provide an upper bound on the age of the most recent rupture along this segment. The post-earthquake sediments were too coarse to allow dating. Although the Baharly segment has a subdued geomorphic expression, and appears not to have been involved in the Medieval rupture that we have mapped on the segment further to the west, it has experienced surface rupture within the last few thousand years.

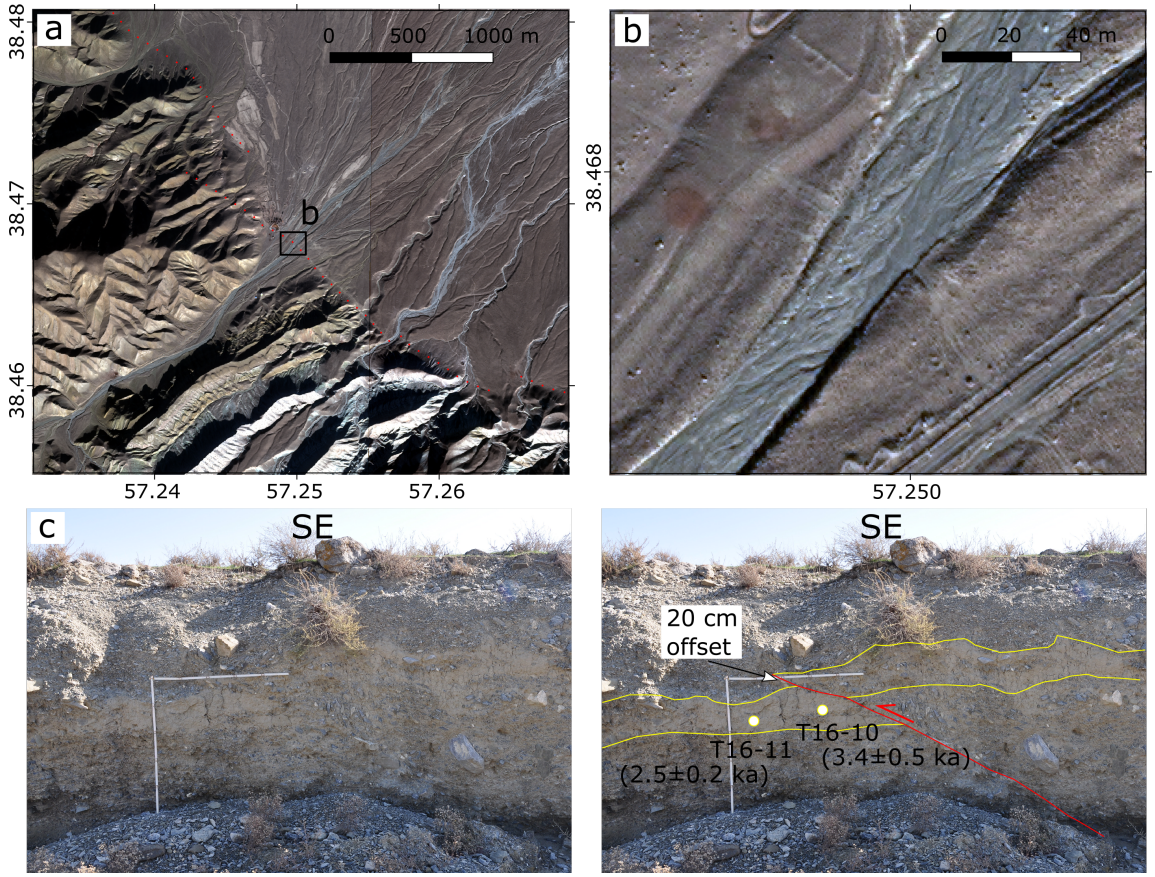


Figure 2.15: (a) WorldView-2 image of a river-cutting through the Baharly segment of the MKDF (See Figure 2.2b for location). (b) Close-up view. The fault is not well expressed in the geomorphology. (c) Photograph looking southeast at a fault exposed in the river-cut (see panel 'b' for location). (d) Interpretation of the stratigraphy. A distinctive silt unit is displaced by ≈20 cm by a fault dipping ≈30° SW. Two IRSL samples were taken from the fine silt layer and pre-date the most recent earthquake on this segment.

Table 2.2: Field code, sample locations, laboratory code and depth for single grain K-feldspar post-IR IRSL at 225°C sediment dating samples. Also shown are sediment concentrations of K (ICP-OES determination), U and Th (ICP-MS determinations), the total dose rate including internal beta dose rate contribution and cosmic dose rate, adjusted for water and grain size attenuation. The numbers of grains measured and the numbers that provided a finite age estimate are shown. Several samples displayed significant clustering of equivalent dose values, and these were analysed using a finite mixture model (FMM); results for these are shown in bold type and represent the values most likley to represent depositional age. The final column shows the proportion of results for that sample apportioned by the FMM to each age estimate. See *Walker et al.* (2021) for further details.

Field ID	**Lab ID**	**Notes**	**Depth (m)**	**Grain nos/signal**	**Doserate (mGy/yr±1σ)**	**Equivalent Dose (Gy±1σ)**	**Age (kyr±1σ)**	**Proportion**
T16-08	Shfd-17058	Near site C; trench	1.00	200/104	3.41±0.16	21.4±0.4	6.29±0.32	
T16-09	Shfd-17059	Near site C; trench	0.75	200/130	3.35±0.16	15.4±0.4	4.61±0.26	
T16-10	Shfd-17060	River south of Sünçe	0.30	200/51	3.30±0.22	1.2±6.6	0.4±2.0	<0.01
						11.3±1.4	**3.4±0.5**	**0.13**
						27.8±3.4	8.4±1.2	0.09
						72.4±5.7	21.9±23	0.22
						150±23	45.4±7.5	0.12
						470±32	142.1±13.7	0.35
						1247±139	377.5±49.2	0.11
T16-11	Shfd-17061	River south of Sünçe	0.30	200/84	2.35±0.19	**5.8±0.3**	**2.5±0.2**	**0.49**
						19.1±1.7	8.1±1.0	0.10
						60.9±4.4	25.9±2.8	0.16
						223±22	95±12	0.16
						604±73	257±37	0.09

2.5 Discussion

The abundant and consistent distribution of offsets along strike, paired with the characteristic appearance of the fault scarp along its length, indicate rupture of the central section of the MKDF in a single major palaeo-earthquake rupture in the Medieval period. The clear geomorphic expression of the rupture extends for ≈120 km, from Nohur in the east to Uşak in the west. We infer that the rupture is likely to have extended further west from Uşak, such that the 120 km measured length is a minimum for the true rupture length. The central 70 km of fault shows a peak in offset measurement at 7.5 ± 1.5 m with a second peak at 12.5 ± 1.5 m that we infer to represent similar amounts of slip in the most recent and penultimate surface ruptures upon this part of the fault.

Seismic moment (M_0) is calculated using $M_0 = \mu AD$ (*Hanks and Kanamori*, 1979), where μ is the shear modulus (rigidity), A is the area of fault plane that slipped (the product of the fault width, W, and length, L), and D is the average slip across the fault plane. For the value of the shear modulus, we use 7.05 ±0.4 $\times 10^{10}$ Pa calculated from the distribution of Young's modulus, E, and Poisson's ratio, ν, variations in the Iranian Plateau in *Eshagh et al.* (2020), and using the relationship, $\mu = \frac{E}{2(\nu+1)}$. We assume a vertical strike-slip fault, and for W use 11 ±6 km from the interseismic model of *Walters et al.* (2013). The value of L we use is 120 km, which is a minimum segment length estimated from mapping of the palaeo-rupture. For the value of D, we primarily use the COPD analysis and field observations to constrain a value of 7.5 ±1.5 m. This yields an estimate of moment magnitude of M_W 7.8, which when accounting for the uncertainties ranges from M_W 7.5–8.0. It is also possible to use the broader peak from the lower quality COPD analysis to constrain 10 ±4 m, which similarly yields M_W 7.5–8.1. Due to the rupture length estimate being a minimum, the estimated moment magnitude also corresponds to a minimum value.

We can also assess the magnitude of the palaeo-rupture from empirical scaling relationships between rupture length, average slip and maximum slip (e.g. *Wells and Coppersmith*, 1994). Applying the fault length to moment magnitude scaling relationship for a strike-slip fault of the form $M_W = a + b\log(SRL)$, where SRL is the surface rupture length (120 km) and the scaling parameters a and b have values of 5.16 and 1.12 respectively, estimates a M_W 7.5 (with standard deviation 0.3), which corresponds well to our seismic moment calculation above. Similarly we can apply an average slip to moment magnitude scaling relationship for a strike-slip fault using $M_W = a+b\log(AD)$, where AD is the average displacement (7.5 m), and a (7.04) and b (0.89) are the scaling parameters. This estimates a moment magnitude of 7.8 with standard deviation 0.3, again comparable within error to our calculation of seismic moment. Comparing our results to these scaling relationships reaffirms the possible suggestion that the distribution of slip measurements we measure does not quite sample the full rupture length and rupture terminations, although this is possibly expected with the preservation of offset geomorphic markers when approaching the along strike extent of a palaeo-rupture.

The most recent earthquake occurred 600–800 years ago. We have no firm constraint on timing of the penultimate surface rupture, which appears to have had roughly equivalent amount of slip to the most recent event. In the absence of firm time constraint on all but the most recent surface-rupturing earthquake, we simply state that the 7.5 ± 1.5 m of slip in the most recent earthquake will accumulate in 600 to 1200 years at the geological slip-rate of 9.1 ± 1.3 mm/yr (*Walker et al.*, 2021).

The earthquake rupture that we have uncovered along the MKDF is important in several respects. First of all, it is amongst the largest of known or inferred earthquake ruptures associated with the Arabia-Eurasia collision zone. The only potential earthquake comparable in size is the M_s 7.5–7.9 856 C.E. Damghan/Qumis earthquake, which ruptured the Shahroud fault zone, conjugate to the MKDF, in the

Eastern Alborz (*Ambraseys and Melville*, 1982; *Hollingsworth et al.*, 2010), though the size and existence of this earthquake are still debated (e.g. *Hollingsworth et al.*, 2010; *Berberian*, 2014).

This palaeo-rupture along the MKDF can also be compared to other long continental strike-slip faults with instrumentally-recorded and detailed forensic investigations of contemporary earthquake ruptures. This analysis suggests that the MKDF might behave similarly to other large intercontinental and intracontinental strike-slip faults, which produce large magnitude earthquakes from partial fault ruptures with end points at structural complexities. The suggested structural control on rupture segmentation of the palaeo-rupture along the MKDF corresponds to observations from modern earthquakes, such as the 2001 M_W 7.8 Kokoxili (*Klinger et al.*, 2005; *Lasserre et al.*, 2005), the 2002 M_W 7.9 Denali (*Wright et al.*, 2003; *Lu et al.*, 2003), and along the North Anatolian fault (e.g. *Stein et al.*, 1997), and also historical ruptures (e.g. *Wesnousky*, 2006; *Elliott et al.*, 2015). Whether these end points are persistent through multiple earthquake cycles remains to be determined (e.g. *Klinger et al.*, 2011). That both the MKDF and Shahroud fault zone have previously ruptured in major earthquakes with long recurrence intervals (*Hollingsworth et al.*, 2010) suggests that these fault zones exhibit plate-boundary-like behaviour within their roles in the extrusion of the South Caspian Basin.

It is surprising that such a large earthquake has remained unknown and is apparently not mentioned in historical records, despite the compilation of records across Iran and surrounding regions (*Berberian*, 1976; *Kondorskaia and Shebalin*, 1977; *Ambraseys and Melville*, 1982). There are two likely reasons why this earthquake was not documented, to our knowledge, by contemporary sources. The first is that the historical record of earthquakes is discontinuous, with a level of completeness that varies spatially and through time (e.g. *Ambraseys and Melville*,

1982). In spatial terms *Ambraseys and Melville* (1982) have proposed the hypothesis that owing to the impact of earthquakes on major routeways and road towns, arterial regions are more commonly covered, as opposed to areas where there is little through-flow of traffic. While historians and geographers resided in major cities across the medieval Islamic world, their focus is not always directed towards coverage of events in adjacent regions. This patchiness is exaggerated in texts whose historiographical approach is to consider the major deeds of specific individuals (as per the tradition for several rulers in the post-Mongol period). Records in the form of quotidian documents might shed greater light on local events and responses, but they are rarely preserved for earlier periods, and even then, those which survive are unevenly distributed in terms of their regions of focus.

The Köpetdag and adjacent parts of Turkmenistan do not have the same level of completeness as some other parts of Iran, for example. For the major cities such as Nisa (Nasa) and Merv, we lack any surviving local histories comparable to those for Bukhara (*Narshakhī*, 1954) and (*Bayhaqī and Bahmanyār*, 1938). We are largely reliant on geographical texts, which prioritise the major routes, and royal narratives, which do not always record earthquake events. Relevant tax and administrative documents which might mention post-disaster recovery in passing are also absent. So in summary, in spite of the general wealth of historical sources for the period of the 12th-14th centuries CE (as summarized comprehensively in *Ambraseys and Melville* (1982)) there is a high likelihood that an event in this area may have been historically overlooked, or that we do not have the evidence.

The second possible reason for a lack of sources detailing such an earthquake, is that the MKDF separates the heavily deformed Iranian Plateau from the stable continental interior of the Turan Platform, which leads to an asymmetry in the distribution of seismic intensities (*Ambraseys and Melville*, 1982). It is interesting in this respect that the nineteenth century traveller Mura'vëv mentions a Khivan

tradition of an earthquake circa. 1290 C.E. that caused the Amu Darya to change its course from the Caspian Sea to the Aral Sea (*Murav'ëv*, 1871, p. 150). Such a seismic shift is in reality unlikely, and it reveals more about the nineteenth century preoccupation to explain Pliny's classical description of Amu Darya flowing into the Caspian. There may, however, be a seed of truth for an early earthquake felt in Khiva, although it is surprising that such a major event would not be mentioned in the comprehensive chronicles by the celebrated local historians Munis and Agahi, also active in the early nineteenth century in this city (*Munis and Agahi*, 1999). With no further textual evidence to support Mura'vëv's claim at the present time it is impossible to say more.

Turning to archaeological evidence, there is much potential given the good preservation of archaeological sites to the north of the Köpetdag on the fringes of the Karakum from all periods. Few, however, have received system excavation over a large enough area to concretely document seismic impact, and the focus of study in the twentieth and twenty-first centuries has been weighted somewhat heavily towards sites from prehistoric and antique periods. Nisa is a case in point, where early excavations of the medieval settlement at New Nisa in the 1950s were later abandoned for the Parthian palatial structures at Old Nisa, where there was seemingly substantially less occupation after the coming of Islam.

Of the archaeological remains mentioned above that actually straddle the major rift of the MKDF none has been systematically investigated, although a fine-grained date for this event could potentially be elucidated through a detailed study of the disrupted field systems, qanats, and structures/enclosures in future. The only major ruins of a settlement are the aforementioned walls of Paraw, identified as the medieval city of Farava (*Litvinskiĭ*, 1951). Historical sources mention a small-sized settlement or outpost at this site infrequently from the 10th century CE onwards, although never in connection with an earthquake. The limited previous archaeological

investigation at the site mapped the walls and extant features, and estimated the occupation dates of the settlement based on surface ceramics. The results of the latter demonstrate thriving occupation of the settlement from the 9th-10th century onwards, an interesting tail-off in ceramics in the 14th century CE with almost a complete absence of 15th century materials (*Litvinskiĭ*, 1951). Given that the mapped fault runs right beside the city, it is likely that the modelled event would have had a catastrophic impact on the urban centre and could very likely explain the abandonment of the settlement at this time in favour of the later settlement of Kizil Arvat (Serdar). On archaeological data this would support a 14th century, as opposed to 13th century date for the event, although this issue could only be conclusively resolved through further excavation at the settlement.

2.6 Conclusion

The existence of a large magnitude earthquake rupture of Medieval age along the MKDF of Turkmenistan is important at local, regional, and global scales. Locally, our result has implications for the hazard posed by the MKDF, a major active fault for which there is no historic record of significant earthquakes over much of its length. An average 7.5 m of slip occurred in a single earthquake rupture between 600–800 years ago. This 7.5 m of displacement would accumulate in 600–1200 years given a slip rate of 9.1 ± 1.3 mm/yr (*Walker et al.*, 2021), providing an urgency in building longer-term palaeoseismic records to establish recurrence intervals and to assess variability between successive earthquake cycles. The uncovering of a large-magnitude earthquake, not mentioned in historical texts, also provides insight into the completeness of historical earthquake records at a more regional scale. It is likely that additional large earthquakes remain to be discovered through continued forensic remote-sensing, palaeoseismology, and through the interpretation of archaeological and historical sources.

Data and Resources

The Supplementary Material contains Supplementary Table B.1 of measured fault offset locations along the MKDF, with the location ID corresponding to the supplementary KML file (`supplement_MKDFoffsetsLocsID.kml`) provided as a digital attachment.

WorldView-2 satellite imagery was courtesy of the DigitalGlobe Foundation; FAIR data access statement: Commercial WorldView-2 data used within this analysis were obtained through application to the DigitalGlobe foundation and are available for purchase from Maxar (`https://www.maxar.com/`). Instrumentally-recorded earthquake locations are from the ISC-GEM Global Instrumental Earthquake Catalogue (International Seismological Centre (2021), ISC-GEM Earthquake Catalogue). Maps were prepared using Generic Mapping Tools software (*Wessel and Smith*, 1995), QGIS and Cartopy.

Acknowledgements

This work was supported by the NERC-ESRC Increasing Resilience to Natural Hazards program 'Earthquakes without Frontiers' (NE/J02001X/1), the Leverhulme Trust Research Project Grant 'EROICA' (RPG-2018-371), by the NERC-funded COMET (GA/13/M/031), and through allocation 0009090 from the Research England GCRF Support Fund. We thank Prof. James Jackson for help in the field, Prof. Siddharth Saxena of the Cambridge Central Asia Forum, Vepa Malikgulyyev, Murad Kakajykov of the UK embassy in Turkmenistan, and the Ambassador of Turkmenistan to the UK for their kind help and logistical support. We thank the President of Turkmenistan for his support of the joint Turkmenistan-UK scientific collaboration.

Chapter 3

Interseismic deformation and strain partitioning along the Main Köpetdag Fault, Turkmenistan, with Sentinel-1 InSAR time-series

Nicholas Dodds[1], Simon Daout[2,1], Barry Parsons[1], Richard Walker[1], Marie-Pierre Doin[2], G. Begenjev[3], Y. Bezmenov[3], R. Mirzin[3]

[1]COMET, Department of Earth Sciences, Oxford University, Oxford, OX1 3AN, UK.
[2]Institut des Sciences de la Terre (ISTerre), Université Grenoble Alpes, Grenoble, France.
[3]Institute of Seismology and Physics of the Atmosphere, National Academy of Sciences of Turkmenistan, Aşgabat, Turkmenistan.

Abstract

The Main Köpetdag Fault (MKDF) is a predominantly right-lateral strike-slip fault, that dissects the northern edge of the Köpetdag mountains of Turkmenistan and Iran. The fault represents the northernmost expression of deformation from the Arabia-Eurasia collision to the east of the Caspian Sea, and plays an important role facilitating the motion of the South Caspian Basin (SCB). Despite the kinematic significance of the MKDF, previous geodetic measurements of the slip-rate across the fault have been highly variable, with a recent geological slip-rate supporting evidence for rapid strain accumulation across the fault. To resolve this ambiguity, we derive Sentinel-1 InSAR time-series from both ascending and descending LOS to measure the interseismic motion across the MKDF. This implements a processing strategy for the correction and performance analysis of tropospheric models from GACOS, which suggests a 25–40% under-estimation in the amplitude of the tropospheric path delay in this region. Modelling the rate of fault-parallel motion across the MKDF and combining this with a geological slip-rate constrains 8.7 ± 1.1 mm/yr right-lateral motion, along with a shallow locking depth of ≈6 km. The LOS time-series resolves greater than 1 mm/yr uplift to the north of the MKDF. Modelling this uplift as deformation on frontal thrusts to the north of the MKDF estimates 4.3 ± 1.5 mm/yr of shortening across the fault system. This implies that the convergence within the Köpetdag and East Caspian Lowlands, to the south of the MKDF, is transferred to the frontal thrust systems to the north of the MKDF. Revising an Iran-Eurasia-SCB velocity triangle of the region suggests that the deformation along the conjugate MKDF and Shahroud fault zones is representative of the motion of the SCB, which is moving at 9.7 ± 1.8 mm/yr in a direction of 329° ± 9° relative to Eurasia. However

reconciling the modelled shortening across the frontal thrusts suggests that the rate of convergence across the MKDF is possibly slightly over-estimated, likely due to difficulty associated with high-magnitude agricultural/hydrological subsidence along the Karakum Canal irrigated zone which overprints the tectonic signal along the thrust faults.

3.1 Introduction

The Main Köpetdag Fault (MKDF) is a predominantly right-lateral strike-slip fault that dissects the northern edge of the Köpetdag mountains of Turkmenistan and Iran (see Figure 3.1). The Köpetdag represent the northernmost expression of deformation within the Arabia-Eurasia collision east of the Caspian Sea, separating the Iranian Plateau, the broad zone of deformation which extends southwards for two thousand kilometres from the Köpetdag and Alborz, from the Turan Platform, part of stable Eurasia, to the north. The MKDF itself is an important element in regional tectonics, as together with the conjugate left-lateral Shahroud Fault Zone (SFZ) it facilitates the northwest motion of the South Caspian Basin (SCB).

The SCB is an aseismic block that moves independently to its surroundings (e.g. *Jackson et al.*, 2002). The basin is surrounded by active belts of earthquake on all sides; onshore through the Köpetdag, Alborz, Talesh, and Caucasus; and offshore along the Absheron-Balkan Sill (ABS), where a marked contrast in the depth of seismicity is suggested to represent subduction (e.g. *Jackson et al.*, 2002). Conjugate strike-slip motion along the right-lateral MKDF and left-lateral SFZ facilitates the motion of the SCB, with both faults terminating at the Bäherden-Quchan Fault Zone (BQFZ). The BQFZ is a distributed network of NNW-SSE right-lateral faults that cuts through the eastern Köpetdag, and likely accommodates the remaining range-parallel extension through vertical axis rotation (e.g. *Jackson et al.*, 2002; *Hollingsworth et al.*, 2006).

Driven by the oblique Arabia-Eurasia collision, the northward GPS velocity of NE Iran relative to Eurasia decreases eastward from 11 mm/yr at Tehran (52° E) to 1.5 mm/yr at Mashhad (60° E) (e.g. *Khorrami et al.*, 2019). The velocity of GPS stations along the southern shoreline of the Caspian Sea and in the East Caspian Lowlands indicates that the motion of the SCB is to the northwest, either by lateral extrusion (*Hollingsworth et al.*, 2008), or rigid body rotation around an Euler pole

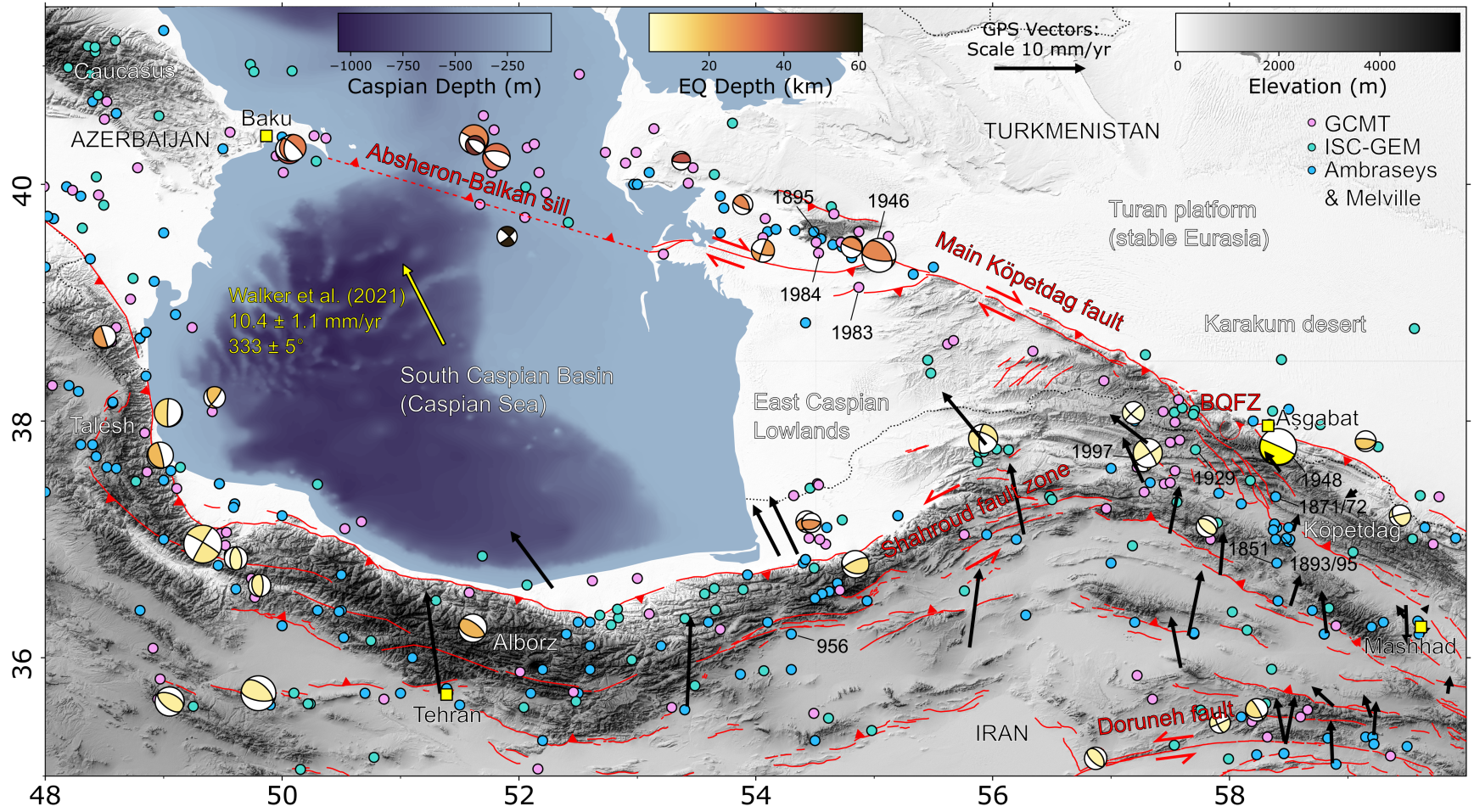


Figure 3.1: An overview of the active tectonics surrounding the South Caspian Basin (SCB). Active faults are delineated by red lines (updated from *Walker et al.* (2021)), with major boundary fault zones around the SCB labelled. The yellow arrow shows the estimated motion of the SCB from *Walker et al.* (2021). Earthquake focal mechanisms and depths are from the Global Waveform Catalogue (*Wimpenny*, 2020); with the addition of the 1948 M 7.3 Aşgabat earthquake (*McKenzie*, 1972). Also shown are earthquake locations from the historical catalogue (3000 BC–1905; in light blue) of *Ambraseys and Melville* (2005), and the instrumental catalogues from ISC-GEM (1906–1975; in light green) and GCMT (1976–2020; in pink). Earthquakes discussed in the text are labelled by year. GPS velocities from *Mousavi et al.* (2013) are shown by black arrows. South Caspian bathymetry is from the General Bathymetric Chart of the Oceans (GEBCO; *Weatherall et al.* (2015)). The grey-scaled rendered elevation-hillshade background is from the Shuttle Radar Topography Mission (SRTM).

located in the Turan Platform (*Mousavi et al.*, 2013; *Djamour et al.*, 2010). However, constraining the precise rates, direction and poles of rotation of the SCB is difficult. There are no direct measurements from the basin interior, due to water depths exceeding 1000 m, and ambiguity between basement motion and deformation within the thick sediment pile (>20 km; *Jackson et al.* (2002)). Resolving the motion of the SCB instead relies on either modelling GPS velocities with block models; or alternatively directly measuring the relative velocity along the boundary faults and projecting this motion onto the SCB.

However GPS-derived block models (e.g. *Mousavi et al.*, 2013; *Djamour et al.*, 2010; *Hollingsworth et al.*, 2008; *Masson et al.*, 2007) are unable to reproduce observed velocities in the East Caspian Lowlands (*Mousavi et al.*, 2013), which represents the onshore extension of the block, with these models typically yielding low right-lateral slip-rates along the MKDF (3 ± 2 mm/yr; previous slip-rate estimates along the MKDF are summarised in Supplementary Table 3.1). *Mousavi et al.* (2013) acknowledges that block models are unable to fit the velocity from the only GPS station located within the interior of the SCB (MAVT in Figure 3.2), and by instead projecting the velocity of this station estimate a higher fault parallel slip-rate along of 6.7 ± 0.5 mm/yr on the MKDF, with 3.4 ± 1.0 mm/yr of range-perpendicular shortening. This supports direct slip-rate measurements from geologic (9.1 ± 1.3 mm/yr from IRSL-dating the abandonment of a large alluvial fan system displaced by the MKDF; *Walker et al.* (2021)) and geodetic (8.5 ± 3.5 mm/yr derived from a descending track Envisat-InSAR time-series; *Walters et al.* (2013)) investigations of the MKDF, which estimate much faster right-lateral motion along the fault.

Using the geological slip-rate along the MKDF and revising an Iran-Eurasia-SCB velocity triangle from *Copley and Jackson* (2006), *Walker et al.* (2021) estimate that the SCB is moving 10.4 ± 1.1 mm/yr relative to Eurasia, in a direction 333° ± 5°. This motion is calculated by assuming that the conjugate strike-slip motion

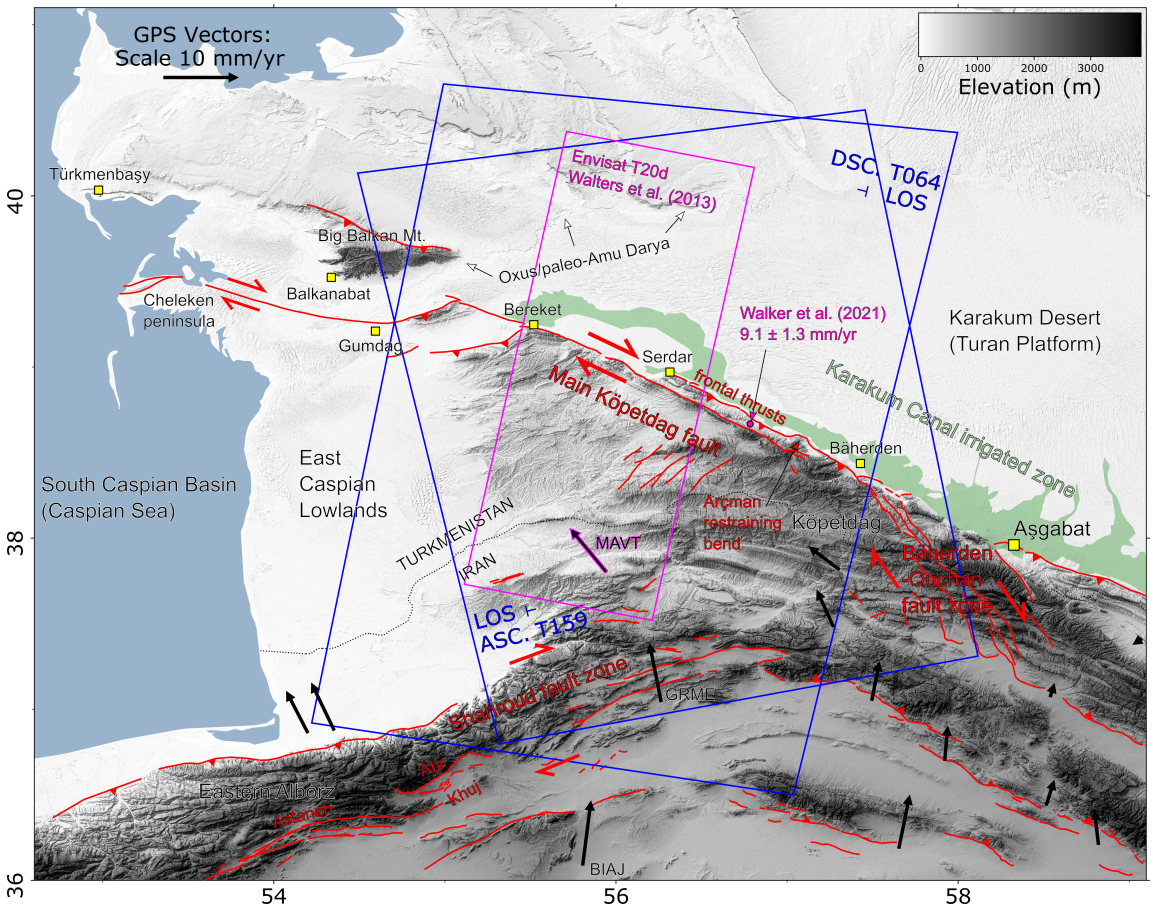


Figure 3.2: The coverage of the Sentinel-1 InSAR data processed from tracks D064 and A159 (outlined in blue); note the optimal LOS orientation of the descending track relative to the MKDF (delineated in red, along with other active faults in the region; mapped faults are from *Walker et al.* (2021)). The Karakum Canal irrigated zone is the green shaded region. GPS vectors within NE Iran from *Mousavi et al.* (2013) are displayed as scaled black arrows, with station names provided for those mentioned in the text. Previous slip-rate estimates along the MKDF are highlighted in pink: the pink circle shows the sample location from the geological slip-rate in *Walker et al.* (2021); GPS station MAVT is highlighted in pink, which *Mousavi et al.* (2013) project to constrain the motion of the SCB relative to the Turan Platform; the pink box outlines the descending Envisat track used by *Walters et al.* (2013).

along the MKDF and SFZ accommodate the range-parallel component of motion of the SCB. The range-parallel motion along the SFZ is 4.8 ± 0.8 mm/yr derived from ascending and descending Envisat-InSAR time-series *Mousavi et al.* (2015); this rate is consistent with GPS velocities from *Mousavi et al.* (2013) and the summed left-lateral late Quarternary rates across the Abr and Khuj segments of the SFZ (*Javidfakhr et al.*, 2011). *Walker et al.* (2021) also measure 0.3 mm/yr of

shortening across the frontal thrust systems to the north of the MKDF, with the remaining shortening from Iran-Eurasia convergence accommodated by deformation either localised along the SFZ, or distributed at the margins of the eastern Alborz and within the East Caspian Lowlands. *Walker et al.* (2021) correlates this deformation with the location of low magnitude earthquakes (e.g. *Nemati et al.*, 2013) and imaging of folds and thrusts within the thick sedimentary sequence (e.g. *Radfar et al.*, 2019) in the East Caspian Lowlands.

The surface expression of the MKDF is defined by a prominent linear fault trace striking ≈303 ° along the range front of the Köpetdag, which emerges at the surface near to Bereket (e.g. *Hollingsworth et al.*, 2008; *Walker et al.*, 2021) (see Figure 3.2). The main right-lateral strike-slip segment runs for over 200 km eastwards from Bereket an abrupt left-stepping transpressional feature, the Arçman restraining bend (*Walker et al.*, 2021). West of Bereket, the MKDF propagates towards the Caspian Sea although is difficult to trace, and is assumed to kinematically connect at depth through the Cheleken Peninsula to the ABS offshore (e.g. *Hollingsworth et al.*, 2008; *Van Dijk et al.*, 2019). At the opposing end of the fault to the east of the Arçman restraining bend, the MKDF continues towards Aşgabat; however, the surface expression of faulting is predominantly from reverse faulting (e.g. *Hollingsworth et al.*, 2008). Additionally along the central segment (≈55–57 °E), there are strain partitioning frontal thrust systems with mapped rupture scarps to the north of the MKDF (e.g. *Walker et al.*, 2021), which are assumed to connect with the strike-slip fault at depth.

There are no recorded earthquakes along the right-lateral strike-slip segment of the MKDF within instrumental or historical records (*Ambraseys and Melville*, 2005), which contrasts with other active faults in the region. To the west, the 1895 Krasnovodsk, modern Türkmenbaşy, M_S 7.5 had an epicentral region constrained to the Oxus Delta and Balkan anticline/range (*Ambraseys and Melville*, 2005), although

no focal mechanism or depth constraint exists, and no surface rupture has been identified. The epicentre of the lower magnitude 1946 M_S 7.0 Balkan also occurred in a similar region. The 1983 M_b 5.2 Gumdag and 1984 M_W 5.4 Burun (an oilfield next to Balkanabat) earthquakes were in a similar location in the East Caspian Lowlands, with surface ruptures identified despite the events have centroid depths >30 km (*Trifonov et al.*, 2009). The deep depths of these earthquakes may represent the burial of structures related to the eastern segment of the MKDF beneath a thick sedimentary pile and kinematic linkage to the significantly deeper ABS (e.g. *Jackson et al.*, 2002).

To the east, the devastating 1948 M_W 7.3 Aşgabat earthquake destroyed the capital city and killed an estimated 10–110,000 people (e.g. *Tchalenko and Skempton*, 1975; *Trifonov*, 1978). The location and focal mechanism for this earthquake (*McKenzie*, 1972) aligns a reverse faulting event with the major anticline to the southeast of Aşgabat, although *Jackson et al.* (2002) notes that the station distribution cannot rule out a strike-slip component. Also in proximity to Aşgabat, there is inferred earthquake damage from the archaeological sites of the Parthian city of Old Nisa (first century B.C.E to the first century C.E.; *Pilipko* (2007)) and the bronze age settlement of Ak-Depe (3000-2000 B.C.E; *Liapin* (2006)), although the timing and interpretation of these are unclear (e.g. *Davidovich*, 1951; *Dodds et al.*, 2021).

Adjacent to the MKDF to the southeast, the BQFZ has hosted the highest magnitude earthquakes recorded in the Köpetdag; including the five event 1851–95 Quchan sequence, the 1929 $M_S \approx 7.0$ Baghan, and 1997 M_W 6.4 Bojnurd earthquakes (e.g. *Hollingsworth et al.*, 2006). Elsewhere in the eastern Alborz, the Astaneh segment of the SFZ likely to have hosted the highest magnitude earthquake in the Arabia-Eurasia collision; the M_S 7.9 865 A.D. Qumis/Damghan earthquake (*Hollingsworth et al.*, 2010; *Ambraseys and Melville*, 2005). Such a high magnitude

event on the conjugate structure to the MKDF potentially hints at the seismic potential of the fault.

Despite the seismic quiescence of the MKDF in instrumental and historical records, geomorphological and paleoseismological analysis of a preserved paleo-rupture is estimated to have generated an earthquake with M_W 7.8 during the Medieval period (600–800 BP) (*Dodds et al.*, 2021). This capability to generate major earthquakes coupled with a rapid slip-rate (e.g. *Walker et al.*, 2021; *Walters et al.*, 2013), indicates that the MKDF constitutes a significant seismic hazard. The hazard is exacerbated by the fault running parallel to the densely-populated irrigated zone along the Karakum Canal, along which most of Turkmenistan's population is concentrated.

InSAR time-series approaches have been used extensively to measure the long wavelength and low magnitude interseismic deformation on faults around the world (e.g. *Wright et al.*, 2013; *Elliott et al.*, 2016). This paper derives descending and ascending Sentinel-1 InSAR time-series of surface deformation from interseismic motion along the MKDF. The measurement aims to improve on the Envisat-InSAR time-series slip-rate from *Walters et al.* (2013), which used a total of 13 IFGs from a single descending track. In contrast with previous generations of InSAR satellites, acquisitions with Sentinel-1 have a higher temporal frequency (6–12 days), greater swath width (>250 km in range), and a higher spatial resolution (pixel size is 5 × 20 m prior to multi-looking).

The previous InSAR study of the MKDF by *Walters et al.* (2013) noted difficulty with high magnitude tropospheric delays in the region from water vapour content probably associated with the Caspian Sea, observed with the Medium-Resolution Imaging Spectrometer (MERIS) instrument. Phase propagation delays through the troposphere are the main limiting factor when deriving estimates of interseismic strain accumulation using InSAR (*Doin et al.*, 2009), as these introduce high

magnitude and long wavelength path delays to the differential radar phase. However the implementation of empirical (e.g. *Béjar-Pizarro et al.* (2013); *Bekaert et al.* (2015); *Tymofyeyeva and Fialko* (2015)) and global weather model corrections (e.g. *Jolivet et al.* (2011); *Doin et al.* (2009); *Daout et al.* (2018)) can mitigate the errors introduced by these signals, and when combined with the high temporal density of Sentinel-1 acquisitions and time-series inversion methods significantly improves the signal-to-noise ratio in LOS velocity fields.

3.2 Sentinel-1 InSAR time-series processing

We process Synthetic Aperture Radar (SAR) data from the ESA Sentinel-1 data archive using the New Small Baseline Subset (NSBAS; *Doin et al.* (2011, 2015); *Grandin* (2015); *Grandin et al.* (2016)) processing chain (based on the ROI_PAC software; *Rosen et al.* (2004)). One descending (D064) and one ascending (A159) track covering the MKDF (see Figure 3.2, >300 km in the azimuth/along-track direction) are processed in interferometric wide-swath (IW) mode (swath width is ≈250 km in range/across-track). The data processed is from October, 2014, to November, 2019. Within the interferogram (IFG) networks, 392 IFGs and 290 IFGs are constructed, from 126 and 96 acquisitions for the ascending and descending track respectively. IFGs are generated with 40 looks in range and 8 looks in the azimuth direction, giving a 160 m × 120 m effective horizontal resolution.

IFGs within the time-series networks have a wide range of temporal baselines, ranging from six days to over one year. This aims to mitigate the influence of systematic biases in InSAR time-series using short temporal baselines that has recently been raised by *Ansari et al.* (2020). The ascending track has an approximately one year acquisition gap from 10/03/2017 – 17/03/2018; however multiple coherent IFGs are constructed over this data gap, allowing the network to be continuous over the entire five year period (IFG networks are shown in Supplementary

Figures 3.12 and 3.13). The range of perpendicular baselines is very low with Sentinel-1 data, with a maximum of ≈200 m. Orbital corrections are applied within the NSBAS processing chain calculated using precise orbit files generated by ESA. This stringent orbit control and corrections results in a high number of coregisterable image pairs and negates the influence of orbital distortions on IFGs in the time-series. Topographic simulation is used for coregistration prior to IFG generation within the NSBAS processing chain. Simulated topography is derived from over-sampling of 30 m SRTM DEM to the resolution of the master SLC, and is coregistered to the master SLC by cross-correlation of the simulated topography with the amplitude of the SLC.

Unwrapping follows a specific routine within the NSBAS processing chain defined in *Grandin et al.* (2012), and is relatively simple due to excellent coherence in the interferograms. The high coherence results from a combination of factors including the aridity in the region, relatively muted topography (generally <1500 m) and, apart from within the Karakum Canal irrigated zone, limited anthropogenic sources of surface deformation. The unwrapping steps are as follows: 1) we replace the amplitude of the IFGs by the phase co-linearity as defined by *Pinel-Puysségur et al.* (2012), as colinearity better discriminates regions of noise than coherence; 2) we then use a coherence-dependent filter that is a weighted average of the complex phase, in triangular sliding windows, by the colinearity (*Doin et al.*, 2011); 3) following this, we impose an unwrapping path that goes from high to low colinearity areas (*Grandin et al.*, 2012). 4) Afterwards we compute the phase difference between the unwrapped phase and a set of less-filtered IFGs obtained with the Goldstein-Werner filter (*Goldstein and Werner*, 1998). The residual is assumed to be between $-\pi$ and π, and added back to the unwrapped phase (*López-Quiroz et al.*, 2009; *Chen et al.*, 2015).

3.2.1 Tropospheric phase-delay correction

The main limiting factor of InSAR measurements on the subtle signals from interseismic strain accumulation arise from phase propagation delays through the troposphere (*Doin et al.*, 2009). This phase delay is often divided into a stratified component, which correlates with the topography and typically dominates the tropospheric signal, and a turbulent component (*Hanssen*, 2001; *Doin et al.*, 2009; *Jolivet et al.*, 2011). To mitigate the effect of tropospheric signals, we use tropospheric phase-delay corrections derived from HRES-ECMWF atmospheric models supplied by GACOS (*Yu et al.*, 2017, 2018b,a). GACOS utilises an iterative tropospheric decomposition model to separate the stratified and turbulent components of the atmospheric model signal, integrating continuous GPS tropospheric delay estimates (*Yu et al.*, 2018a). The corrections are applied to unwrapped IFGs prior to time-series inversion, using a novel approach that simultaneously calculates a statistical analysis of their performance.

Prior to implementing an atmospheric model-derived tropospheric model, we explored the use of empirical corrections in the time-series inversion (phase-elevation and seasonal decomposition). Phase-elevation corrections were not successful due to the variability of the relationship in space (see Supplementary Figure 3.14), which are not easy to capture with a relatively simple relationship. Increasing the complexity of this relationship could increase the trade-off with the deformation, which is co-located with the expected gradient of surface displacement from interseismic motion as the fault is bound by higher topography to the south. This phase-elevation variability is possibly due to the relatively muted topography in comparison to other studies which have utilised such relationships in very mountainous regions (e.g. *Bekaert et al.*, 2015; *Tymofyeyeva and Fialko*, 2015; *Béjar-Pizarro et al.*, 2013)).

Time-series velocity maps can be biased due to aliasing of oddly sampled time-varying atmospheric signals (e.g. *Doin et al.*, 2009; *Daout et al.*, 2018). The

stratified tropospheric phase delay, which correlates with topography, has smooth changes in time and is dominated by a seasonal term (*Doin et al.*, 2009), with an amplitude depending on the variation of temperature, pressure and humidity in space and time. Due to the good temporal sampling of Sentinel-1, we explore the effect of decomposing the time-series into a seasonal function to capture this tropospheric signal. However we observe poor results due to large outliers from this seasonal behaviour (Supplementary Figure 3.15). These abrupt changes are possibly due to water vapour from weather systems moving around the Caspian Sea observed by *Walters et al.* (2013), which result in turbulent tropospheric path delays and bias the linear trend in the velocity estimation.

The tropospheric correction processing strategy is presented in Figure 3.3, and follows a sequence of steps: 1) For each unwrapped IFG, we calculate a tropospheric phase-delay map in radar slant geometry from the GACOS models (supplied per date as a zenith path delay). 2) We solve for a linear ramp and offset in range and azimuth between the unwrapped IFG and tropospheric phase-delay, of the form $IFG = GACOS + RAMP(ax + by + c)$. This residual ramp may reflect residual long-wavelength signals, such as ionospheric, turbulent tropospheric, orbital or plate motion drifts that have not been accounted for, and allows us to tie the model correction to the LOS displacements. 3) To ensure phase closure is maintained over the IFG network, we invert the ramp parameters individually for each epoch in the time-series assuming no covariance between the parameters. 4) For each IFG, we reconstruct the tropospheric phase-delay using the inverted ramp parameters. 5) We then apply the correction by subtracting tropospheric phase-delay from the individual IFGs, with both the data and model referenced to a 50×50 pixels area, using the mean of the phase weighted by the co-linearity, assumed to be a stable non-deforming zone, away from active structures, high topographic gradients, anthropogenic deformation sources, and basin interiors (*Maubant et al.*, 2020).

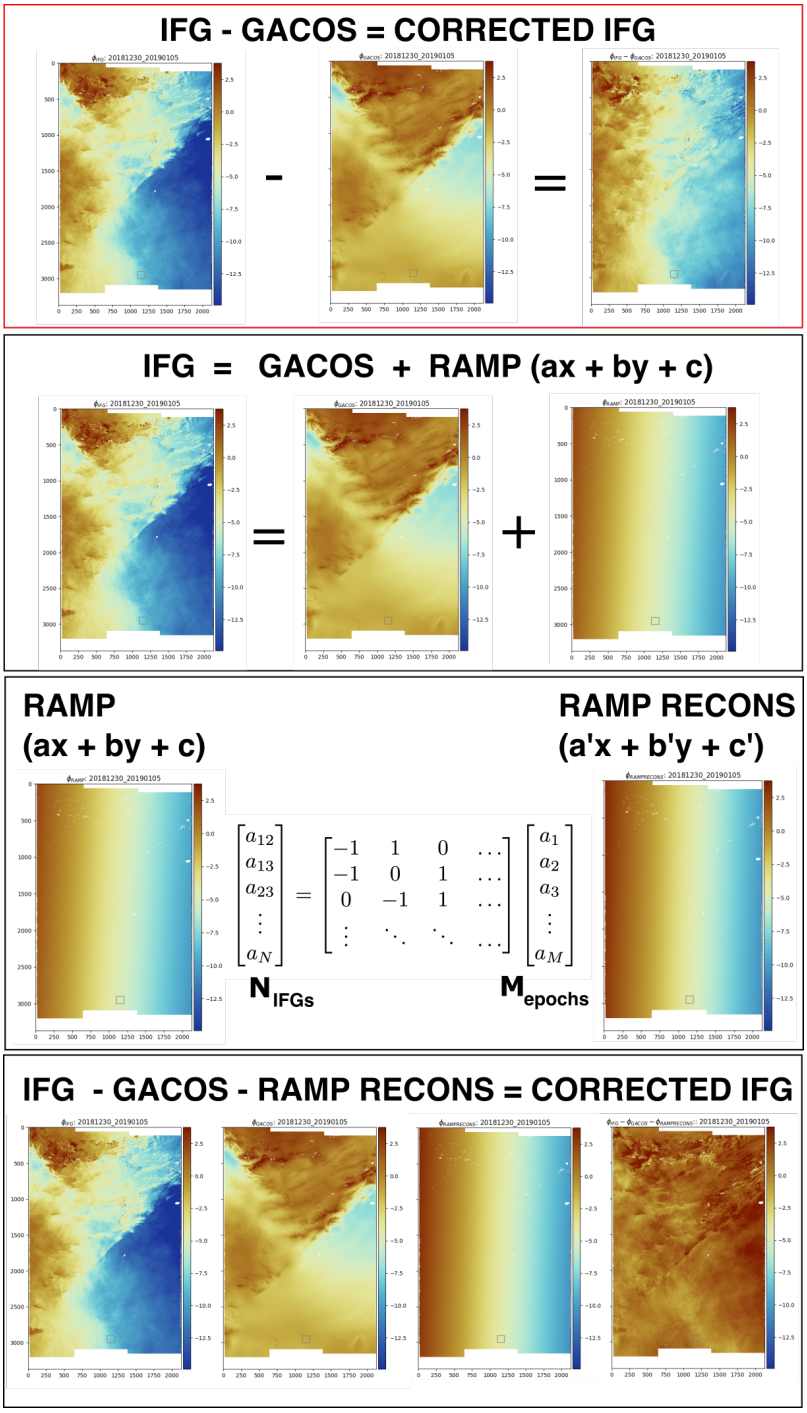


Figure 3.3: Processing strategy for applying tropospheric path-delay corrections, applied to individual interferograms (example from ascending track A159). From top to bottom: applying the GACOS correction directly results in a high amplitude residual signal in the corrected phase (red outlined box); instead solve for a linear ramp between the IFG and the GACOS correction; then we invert the interferometric ramp parameters for ramp parameters at each epoch, re-estimating the interferometric ramp parameters from these in order to ensure phase closure in the time-series; finally apply the correction using $IFG - GACOS - RAMPRECONS$. and reference each corrected IFG to a stable undeforming region. Comparing the final phase maps on the top and bottom panels are representative of the corrections over the entire network, applied prior to time-series inversion.

This approach allows for simultaneous statistical analysis of the performance of the model tropospheric phase-delays during the correction strategy. Determining the performance of tropospheric phase-delay corrections is difficult due to the variable spatial and temporal scales of interest, and variability in reliability depending on the region to which they are applied (*Murray et al.*, 2019). Assessing the spatial performance typically revolves around determining the reduction in the variance or noise characteristics, and residual empirical relationships in the data. Temporal performance metrics involve quantifying the variance of individual pixels through time relative to the inverted functional form of the time-series (here a linear rate). We compute three metrics to assess the performance of the GACOS corrections over the entire time-series network. This makes use of the assumption that for a network of short baseline IFGs, most of the signal in each IFG is from atmospheric path delays. Therefore if an atmospheric correction model is performing well, it should capture the majority of phase variation in the IFG. The metrics are determined for individual IFGs, before being compiled into a histogram to analyse the cumulative performance of the corrections over the entire network of IFGs.

The first of the metrics estimates the gradient of the interferometric phase delay, subtracting the reconstructed linear ramp phase, versus the phase due to atmospheric path delay. This provides a measure of the performance of the amplitude of the atmospheric correction. If the correction is performing perfectly, there should be a linear trend in the phase-phase plot with a gradient ≈ 1. The second calculates the Pearson correlation coefficient ($-1 \leq r \geq 1$) between the IFG phase and the atmospheric correction phase. This measures the spatial performance of the correction, which if the correction is performing well will return a positive linear correlation with $r \approx 1$. The third metric computes the change in variance between the initial interferogram and the corrected interferogram. Good performance of the correction should result in a significant reduction in the variance, as both

topographically-correlated and turbulent tropospheric signals are accounted for by the correction. By calculating the reduction in standard deviation, we account for pairs where the observed phase and model correction phase variation is small. In these cases the gradient and correlation metrics can suggest poor performance as other sources of noise account for most of the signal. Several examples showing the implementation of the correction strategy are presented in Supplementary Figures 3.16 to 3.18.

The results of the performance analysis for the descending and ascending time-series are shown in Figure 3.4. For both the descending and ascending tracks, the performance metrics are consistent. The histogram of the gradients for the time-series are normally distributed with modal values of 0.70 ± 0.19 (D064) and 0.61 $\pm$ 0.19 (A159), with uncertainty equal to the standard deviation of the calculation for all IFGs in the network. Very few model-data pairs have a gradient ≥ 1 (i.e. over correction of the phase by the atmospheric model), or gradient that is either negative (i.e. reverse sign of the atmospheric model) or close to zero. The correlation metrics have a negative skew with modal values of 0.81 $\pm$ 0.14 (D064) and 0.75 $\pm$ 0.14 (A159). Combining the gradient and correlation metrics suggests that the atmospheric correction models are performing excellently spatially, although the amplitude scaling is possibly underestimated in this region. The modal reduction in standard deviation of the interferograms after correction is $\approx$25% for both networks. The rightmost panel in Figure 3.4 presents the relationship between the performance metrics. The model-data pairs with a low gradient generally have a low correlation and poor standard deviation reduction, with several of these cases increasing the standard deviation after correction. The relationship between the gradients and correlations suggests that investigating the source of this swath-scale underestimation of the amplitude of the model correction is important.

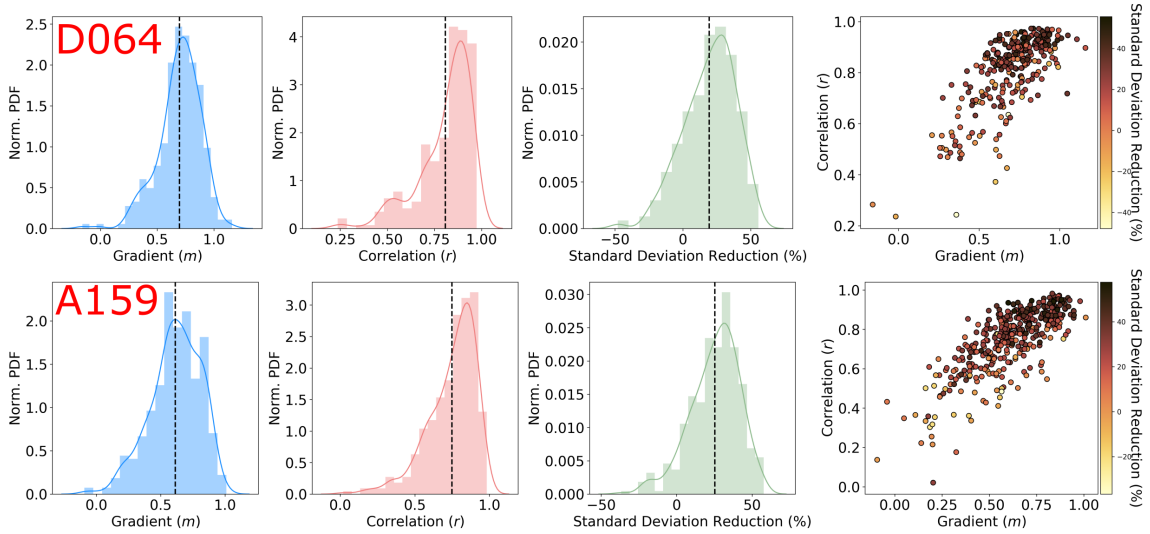


Figure 3.4: Performance analysis of the tropospheric path-delay model corrections on the interferometric phase. Descending track D064 results comprise the top row, ascending track a159 results comprise the bottom row. From left to right: the gradient of the interferometric phase versus the tropospheric path-delay; the correlation coefficient between the observation and the model; the reduction in the standard deviation from correcting the interferogram with this method (normalised percentage); scatter plot showing the relationship between the metrics (gradient vs. correlation, coloured by the standard deviation reduction). Dashed grey lines show the mean value for each metric.

3.2.2 LOS time-series inversion and analysis

Once all IFGs are unwrapped, time-series of the LOS displacements are reconstructed following the approach detailed in *Doin et al.* (2015). The phase delays of unwrapped IFGs, Φ_l, are inverted pixel by pixel, treating them independently from their neighbours, to solve for the incremental phase delay, $\delta\varphi_n$, of each date relative to the preceding date. The total phase delay, φ_k, is then obtained by adding incremental phase delays, assuming that $\varphi_1 = 0$.

The system (Equation (3.1)) is solved using least squares with regularization provided by additional constraints (*López-Quiroz et al.*, 2009). This is required because some pixels have at least a single critical missing link in the IFG network, which results in a rank deficiency and can therefore not be solved only using least squares. The additional constrains are provided in Equations (3.2) to (3.4). We prescribe that the evolution of deformation, φ_k^s, is smooth in time. The phase delay

temporal evolution is obtained by solving the following equations for each pixel:

$$\forall l \in [1, M] \quad \sum_{n=i}^{n=j-1} \delta\varphi_n = \Phi_l \tag{3.1}$$

$$-\alpha W_1 \varphi_1^s = 0 \tag{3.2}$$

$$\forall k \in [2, N] \quad \alpha W_k \left(\sum_{n=1}^{n=k-1} \delta\varphi_n - \varphi_k^s \right) = 0 \tag{3.3}$$

$$\forall k \in [1, N] \quad \gamma\omega_k \frac{\partial^2 \varphi_k^s}{\partial t^2} = 0\,. \tag{3.4}$$

Here M is the number of IFGs in the time-series, constructed from N SAR images/epochs. γ is the smoothing coefficient (set to $\gamma = 0.003$), and ω_k are weights equal to the average time interval within the five points differential scheme used to construct $\frac{\partial^2 \varphi_k}{\partial t^2}$ (used in the smoothing when minimising the laplacian of φ_k). The weighting, α, is set low enough that the reconstructed total phase delay, φ_k, is unaffected by the regularisation, except for pixels where the set of equations is under-determined. For pixels in which the inversion is under-determined, the regularisation allows for an adjustment of disjoint portions of the time-series. The contribution to the misfit in Equation (3.1) is from misclosure in the interferometric network, predominantly from unwrapping errors but also phase decorrelation noise and filtering effects.

During the initial time-series inversion, we map inconsistencies in the interferometric network using the root-mean-square (RMS) misclosure of individual pixels in the time-series (*López-Quiroz et al.*, 2009), calculated as the RMS for all interferograms, N, of the observed interferogram phase, ϕij, and the reconstructed

phase from inverted successive phase delays,

$$\phi_{RMS^{l}_{pixel}} = \frac{1}{N_l}\left[\sum_{N_l}\left(\phi ij^{l} - \sum_{k=i}^{j-1} m_k^l\right)^2\right]^{\frac{1}{2}}. \tag{3.5}$$

This is used to semi-automatically for unwrapping errors which result in high RMS-misclosure, with problematic dates either re-unwrapped, or discarded if the network remains connected. Iterations of the time-series inversion are repeated until no large network inconsistencies remain.

In a final step, we improve the reference frame selection and the time-series decomposition using an iterative procedure and extract an average velocity, V, from a linear fit to the time-series using $\varphi_k = V \times t_k$, with t_k the cumulative time from the first epoch (*Daout et al.*, 2017, 2018). At each iteration, the reference is re-estimated in non-deforming areas, and the misfit between the reconstructed phase delays and the linear evolution is used as weighting in the next iteration. The first iteration is weighted by the RMS of each epoch (output from time-series inversion procedure), to mitigate the contribute of IFGs that have a poor fit to the reconstructed IFGs on the estimation of the final velocity. Similarly the second iteration uses the misfit of each pixel per epoch in the first iteration so that again, epochs with greater deviation from the linear velocity are weighted less.

The resulting products are rate-maps of the average surface LOS velocities in mm/yr (shown in Figure 3.5). Uncertainty maps are also computed, equal to the RMS of the misfit of the cumulative displacements in the time-series to the linear fit (see Supplementary Figure 3.19). Prior to plotting, the time-series velocity maps are masked using the final evaluation of the RMS misclosure for each pixel (*López-Quiroz et al.*, 2009), with a masking threshold of 2.5 mm.

The primary feature of surface deformation in both LOS velocity fields is a long wavelength signal from right-lateral motion across the MKDF (Figure 3.5).

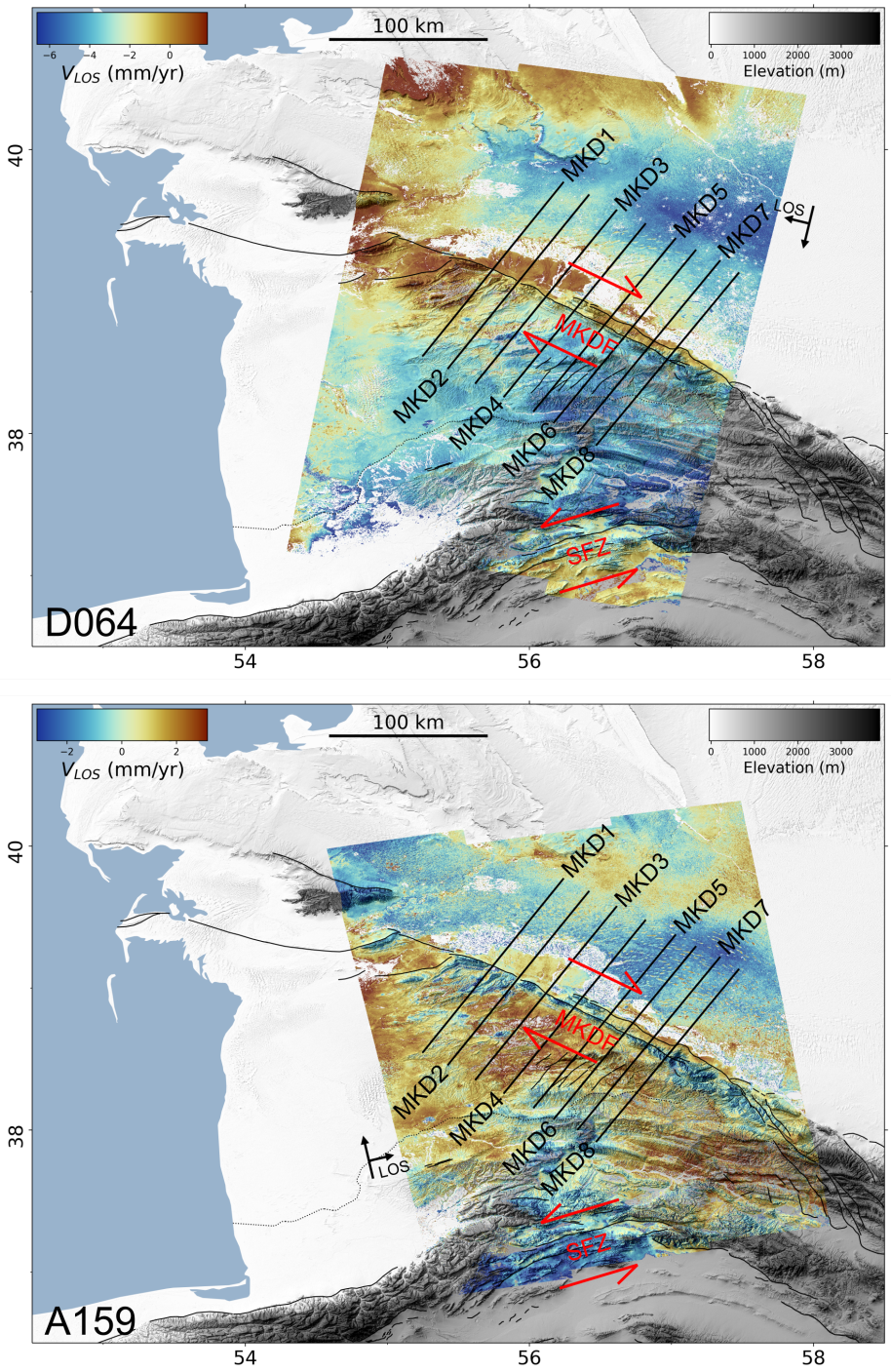


Figure 3.5: LOS velocity maps from the time-series inversions for descending track D064 (top) and ascending track A159 (bottom). Active faults are delineated by black lines (updated from *Walker et al.* (2021)), with the MKDF and SFZ labelled in red. Profiles MKD1–8 (from west to east) are shown by bold the black lines, perpendicular to the strike of the MKDF. Swaths are 20 km wide and 160 km long, centred on the mapped fault trace, containing the data projected onto each profile. Hillshade-rendered topography (from SRTM) is displayed in the background. Red is surface motion towards the satellite LOS, blue is surface motion away from the satellite LOS, with both LOS velocity fields spatially referenced to the far north of the image.

In the optimally-oriented descending LOS, this is demonstrated by the ≈3–4 mm/yr velocity gradient from blue to the south of the fault, to red/orange to the north of the fault. Similarly in the ascending LOS, the gradient has the opposite sign which reflects the right-lateral motion observed from a different LOS and the magnitude of this signal is lower. In both the ascending and descending LOS, a 10–30 km wide zone immediately to the north of the MKDF has a positive signal which suggests a broad zone of uplift. The northern extent of this broad zone of uplift is masked by high-magnitude short-wavelength deformation, high temporal misclosure and decorrelation along the Karakum Canal irrigated zone. Assuming the broad wavelength uplift signal is tectonic in origin, the velocity gradient is consistent with uplift along the mapped frontal thrusts to the north of the MKDF (*Hollingsworth et al.*, 2008; *Walker et al.*, 2021) (see Supplementary Figure 3.20 for an illustration of this motion in the LOS). Shortening across these thrust faults would result in components of both uplift and fault perpendicular motion observed in the ascending LOS, whilst only uplift would be resolved in the descending LOS.

There are several additional signals and sources of deformation observed in the LOS velocity fields. There are low magnitude topographically-correlated residual signals, such as those delineating valleys in the high Köpetdag to the southeast of the ascending track. There are numerous short-wavelength high-magnitude signals associated with hydrological sources, which overprint the longer wavelength tectonic signals. This is particularly evident along the irrigated zone along the Karakum Canal, which has fast-moving negative signals possibly attributed to subsidence from water pumping. There is also uplift in marginal irrigated areas extending away from the canal, especially in the arcuate deviation of the canal zone between Bereket and Serdar. Another observation is the uplift of takyrs, natural clay basins, in the Karakum Desert; the pockmarked effect to the north of the Köpetdag in Figure 3.5). With both the hydrological signals and takyrs, the very short wavelengths of these

signals are indicative of shallow or surface processes.

To begin to investigate the long wavelength tectonic signals along the MKDF, Figures 3.6 and 3.7 present fault-perpendicular profiles of the LOS velocity at regularly spaced along-strike intervals along the length of the MKDF from ≈55–57 °E (profile locations are labelled MKD1–8, from east to west, in Figure 3.5). The profiles project the LOS rate-map and topography from a swath of length 160 km and width of 20 km, with a linear ramp and offset removed from the LOS data. The profiles are centred on the mapped surface trace of the MKDF, and are perpendicular to the strike of the MKDF (123°). The sliding standard deviation of the LOS velocity in each profiles is generally 1–2 mm/yr, apart from in the intersection with the Karakum Canal irrigated zone where the signal is degraded and there is a high proportion of masked pixels. The remaining pixels in this zone reflect the high uncertainty of the signals here, with a significantly increased width of shading to the north of the MKDF in all the profiles in Figures 3.6 and 3.7.

The profiles in Figures 3.6 and 3.7 show the expected long-wavelength signal from right-lateral motion along the MKDF, with opposing sign step changes of 3–4 mm/yr and 1–2 mm/yr resolved in the descending and ascending LOS respectively. The deformation in the profiles does not correlate with variations in topography to the south of the MKDF, although in the ascending LOS there is a short wavelength reversal that correlates with the location of the Köpetdag range front. The wavelength of the tectonic signals is relatively short compared with what might be expected for a typical continental strike-slip fault locking-depth of 15–20 km (e.g. *Vergne et al.*, 2001), with deformation generally concentrated within ≤40 km either side of the fault. To the west, the signal across the MKDF has a longer wavelength, and at both the eastern and western limits of the fault system there are concentrations of deformation that suggest vertical deformation, although this could also correlate with the elevated topography here. In addition, as discussed above,

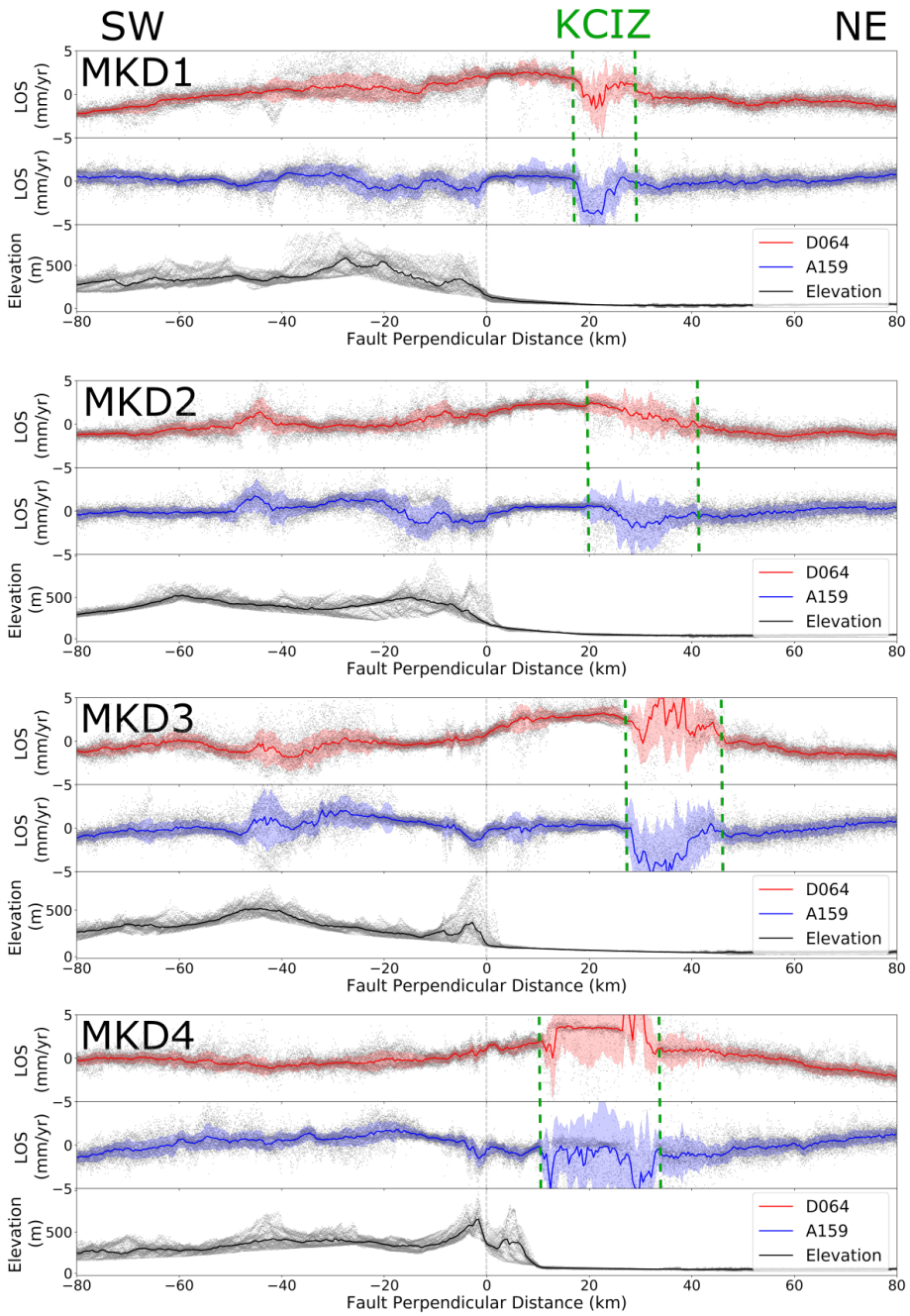


Figure 3.6: Fault perpendicular profiles MKD1–4 from Figure 3.5, labelled from west to east. The profiles are centred with the origin on the mapped surface trace of the MKDF (vertical grey dashed line). Descending D064 (red) and ascending A159 (blue) profiles have a linear trend removed. The coloured line displays a sliding median of the LOS signal, with the shaded region the standard deviation within the window. Topography is shown in the lower panel of each figure in black. The profiles present the defined signal of interseismic motion across the MKDF. The problematic signals from the Karakum Canal irrigated zone are evident to the north of the MKDF (≈10–40 km positive fault perpendicular distance, limits shown by green dashed lines), with high standard deviation and overprinting of the tectonic signal.

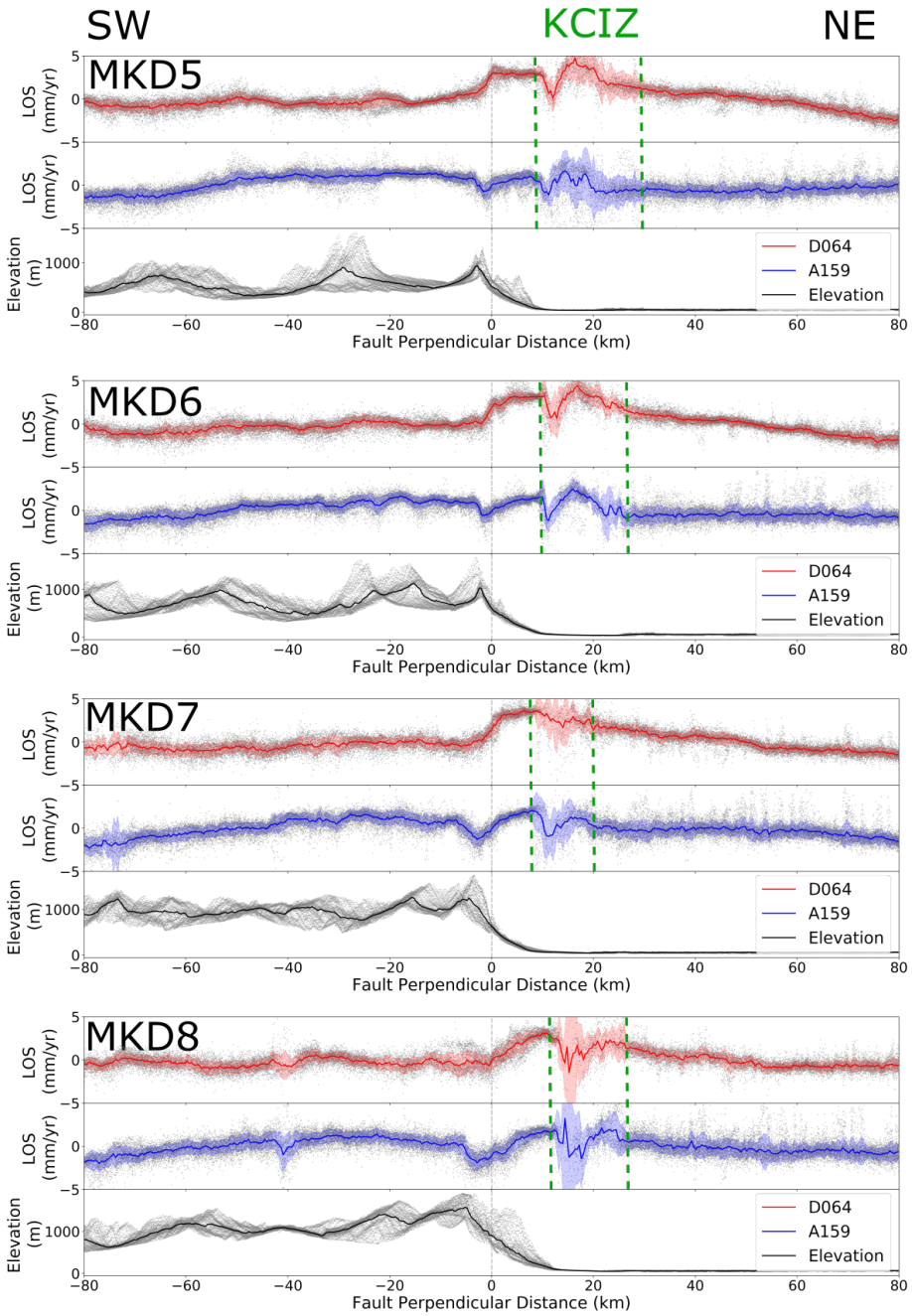


Figure 3.7: Fault perpendicular profiles MKD5–8 from Figure 3.5, labelled from west to east. The profiles are centred with the origin on the mapped surface trace of the MKDF (vertical grey dashed line). Descending D064 (red) and ascending A159 (blue) profiles have a linear trend removed. The coloured line displays a sliding median of the LOS signal, with the shaded region the standard deviation within the window. Topography is shown in the lower panel of each figure in black. The profiles present the defined signal of interseismic motion across the MKDF. The problematic signals from the Karakum Canal irrigated zone are evident to the north of the MKDF (≈10–40 km positive fault perpendicular distance, limits shown by green dashed lines), with high standard deviation and overprinting of the tectonic signal.

in both the descending and ascending LOS there is a 20 ± 10 km zone of positive deformation that we interpret as uplift with a rate of several mm/yr, immediately to the north of the MKDF. If using only resolved with the descending LOS, this signal could be misleading and interpreted to represent an augmented rate of right-lateral motion along the MKDF

3.2.3 Investigating systematic biases in time-series inversions

The influence of systematic biases in InSAR time-series using short temporal baselines has recently been raised by *Ansari et al.* (2020). This bias is believed to arise from abrupt systematic decorrelation of the radar phase in certain portions of asymmetrical surface deformation cycles (e.g. fast wetting and slow drying from precipitation events), which subsequently result in velocity biases in time-series inversions when deformation during the decorrelated periods is not resolved (*Daout et al.*, 2020). The IFG networks for both the ascending and descending tracks have a wide range of temporal baselines, ranging from six days to one year, to mitigate this effect. Following the advice of (*Ansari et al.*, 2020) and *Daout et al.* (2020), we investigate the effect of removing short temporal baseline interferograms on the deformation retrieval with descending track D064 in Supplementary Figure 3.21.

Removing short temporal baseline IFGs with a temporal baselines of ≤12 days has no effect on long wavelength signals in the time-series. The only resolvable difference is within a limited number of pixels associated with rapid subsidence, generally along the Karakum Canal. The majority of these pixels are subsequently masked during our analysis as they typically also have high RMS-misclosure. We also investigate changes to phase-elevation relationships when removing short baseline IFGs, although we observe no changes in these relationships with no discernible difference observed in the residuals in Supplementary Figure 3.21. This was to

investigate possible increases in the effect of biases associated with soil moisture effects in regions of higher topography (e.g. *Daout et al.*, 2020). Having established no evidence for systematic biases in the descending time-series analysis related to short temporal baseline IFGs, we retain a limited number of IFGs with temporal baselines of $\leq$12 days in the final ascending time-series network as they are useful for checking for phase misclosure in the time-series inversion.

3.3 Modelling interseismic motion along the MKDF

To probe the kinematics and mechanics of deformation along the MKDF, we model the surface deformation resolved in the LOS velocity fields. The modelling approach uses Flower2D (*Daout et al.*, 2016a,b), a geodetic tool package for the two-dimensional exploration of fault geometry and slip-rates within a Bayesian framework. For each model, we run 100,000 synthetic surface displacement models with the PyMC Monte Carlo-Markov Chain (MCMC) algorithm. The results show the posterior distribution of parameters, burning the first 50% of models to minimize the effect of the initial model on the posterior distribution.

3.3.1 Preparation of LOS velocity fields

The LOS velocity rate-maps are projected into UTM coordinates (WGS 84/UTM zone 40N) and down-sampled to a resolution of 250 m using a bi-cubic interpolation. This down-sampling is chosen to correspond to the length-scale on which the covariance of the LOS velocities decays with distance using the empirical approach of *Sudhaus and Jónsson* (2009) (see Supplementary Figure 3.22), calculated from the descending LOS velocity field (with the ascending LOS velocity field having a visually similar noise level in both map and profile view). The variable incidence

angle of the LOS with the Sentinel-1 IW mode (29.1°–46.0°) is also accounted for in the models. The uncertainty for each down-sampled pixel also uses a bi-cubic interpolation of the uncertainty rate-maps (in Supplementary Figure 3.19), with the variance of each pixel used to weight the inversion. To provide a comparison to the geological slip-rate from *Walker et al.* (2021), we model profiles that are located in the same approximate region to their sampling (profiles MKD5–7). This also avoids the vertical signals at both the western and eastern limits of the MKDF (profiles MKD1 and 8) and the widest sections of the irrigated zone along the Karakum Canal (which intersect profiles MKD2–4).

3.3.2 Modelling deformation with a vertical-strike-slip fault

Initially, we model surface deformation along the MKDF as interseismic motion along a vertical strike-slip fault resulting from a buried infinite screw dislocation in a two-dimensional elastic half-space (*Savage and Burford*, 1973). This follows the approach from previous modelling of the MKDF by *Walters et al.* (2013), recognising that the MKDF is predominantly a major strike-slip fault in regional tectonic models (e.g. *Jackson et al.*, 2002). *Savage and Burford* (1973) describes the fault-parallel surface velocity, v, at a perpendicular distance from a fault, x, as, $v_3(x_2 = 0) = \frac{\dot{s}}{\pi} \tan^{-1}\left(\frac{x_1}{d_2}\right)$; where $\dot{s}$ is the rate of interseismic motion on the fault below a locking depth, d.

To explore the range of model solutions allowed by the LOS velocity fields, we use a uniform prior distribution the spans all previous slip-rate estimates along the MKDF of 8 ±5 mm/yr. We also solve for the locking depth (uniform prior; 30 ±30 km), although we neglect the results due to the observation of near-fault deformation presented in Figures 3.6 and 3.7. The position of the fault is fixed to the surface trace of the MKDF. In the first iteration of models with this structural configuration, we only use the descending LOS velocity field. The descending LOS is optimally

orientated to resolve fault-parallel motion, whereas the the ascending LOS is also sensitive to fault perpendicular motion (N.B. both LOS are sensitive to vertical motion). The second iteration introduces the ascending velocity field and jointly inverts for the interseismic motion using both LOS.

The posterior distributions of models with this structural configuration are presented in Figures 3.8 and 3.9 (profiles MKD6 and MKD7; profile MKD5 is presented in the Supplementary Material). The velocity step across the MKDF using only the descending LOS is ≈6.5 ±0.5 mm/yr (Figures 3.8 and 3.9 (a)). The inclusion of the ascending LOS supports this rate of motion (Figures 3.8 and 3.9 (b)), with similar rates of motion ≈6.1 ±0.3 mm/yr. The most significant observation in Figures 3.8 and 3.9 is that, as expected, this simple kinematic model is unable to fit the near-fault observations from suspected uplift 10–40 km to the north of the main strike-slip MKDF segment. We propose this signal results from structural complexity at depth, possibly along the mapped thrust faults described in *Walker et al.* (2021).

In addition, we repeat the models using different profile lengths and observe that the slip-rate changes with the length of the profile (see Supplementary Figure 3.23). When profiles are ≤120 km the rate of motion systematically increases. This is probably due to the over-fitting of the uplift signal to the north of the MKDF which adds constructively to the right-lateral signal in the descending LOS. Similarly in profiles exceeding 160 km in length, the slip-rate also increases. We suspect this is due to profiles intersecting non-tectonic signals in the farfield that we have not accounted for. As a result of this, in subsequent models we restrict the profile lengths to 120–160 km.

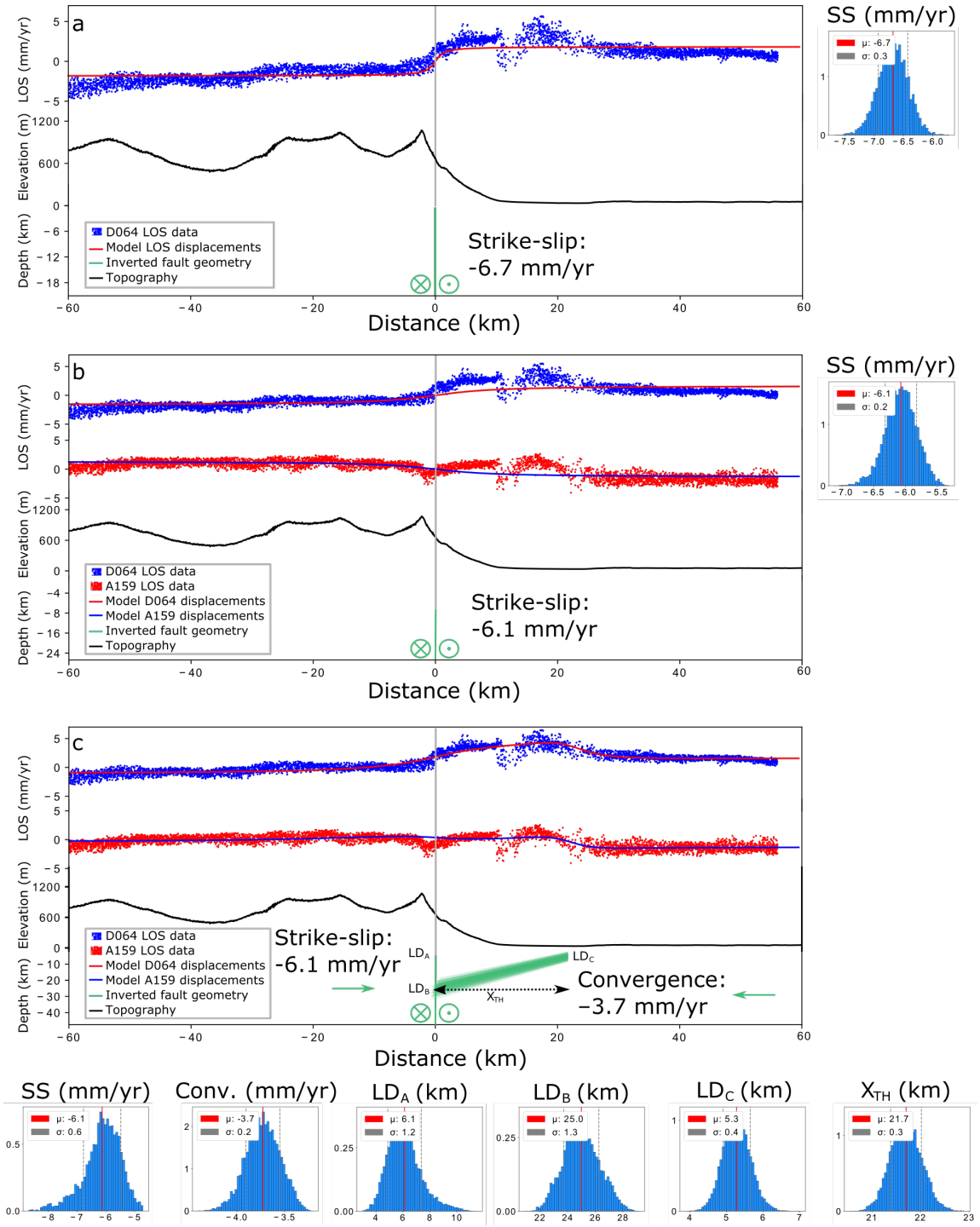


Figure 3.8: Modelling approach with profile MKD6 (120 km length, 20 km width). The results of the Bayesian exploration of the free parameters in each inversion are shown by the histograms on the right. a) Modelling only the optimally-oriented descending LOS with a simple model of a vertical strike-slip fault returns a rate of right-lateral strain accumulation of 6.7 ±0.3 mm/yr. b) Modelling both the descending and ascending LOS with the same simple strike-slip geometry returns a slightly lower rate of 6.1 ±0.2 mm/yr; note the uplift signal to the North (right) of the MKDF, particularly evident in the ascending data. c) A more structurally complex model, with the introduction of a thrust fault to the north of the MKDF; the location of the strike-slip fault is fixed to the MKDF surface trace.

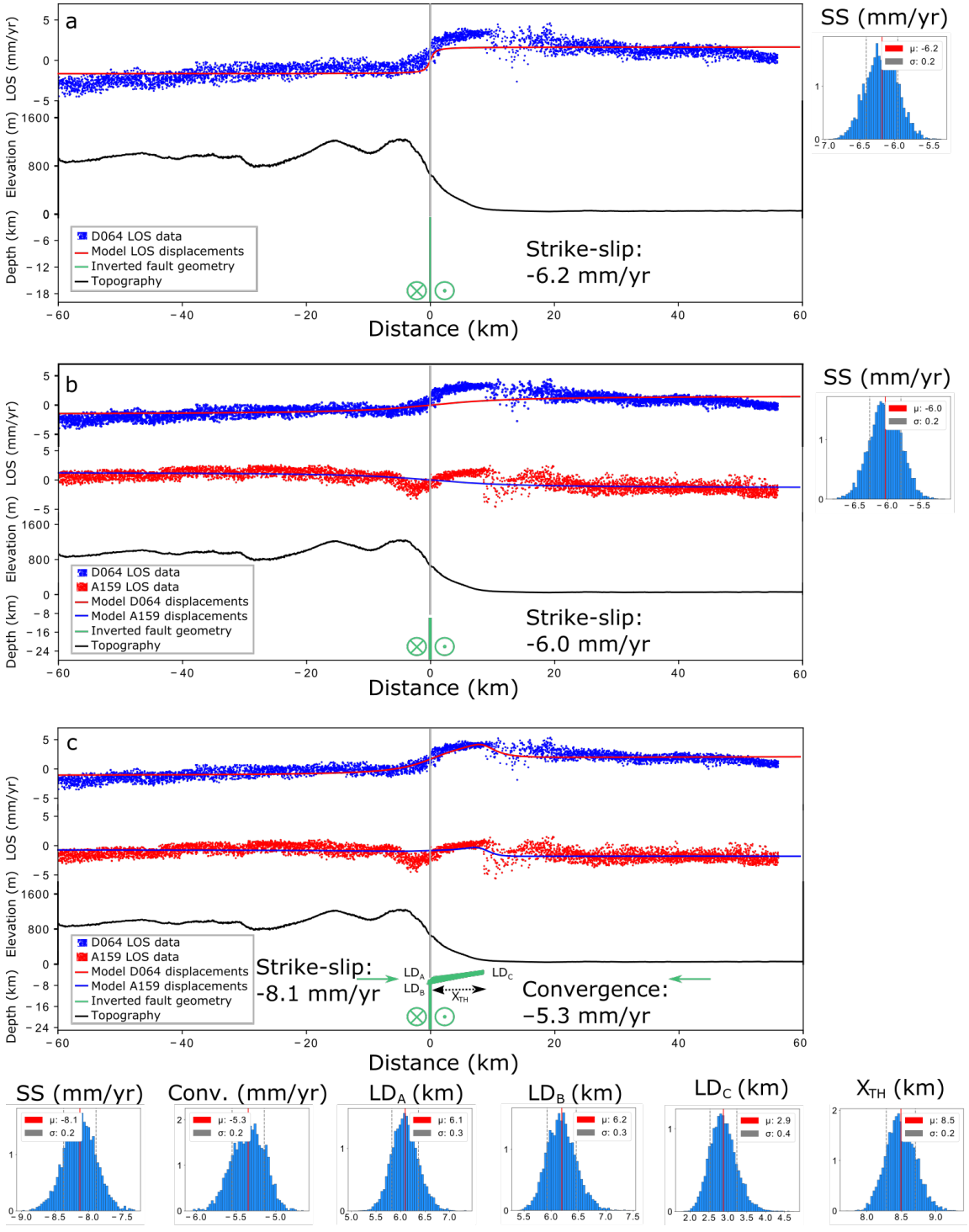


Figure 3.9: Modelling profile MKD7 (120 km length, 20 km width) with the same modelling approach as Figure 3.8 (a–c). In panel c) it is difficult to constrain the precise horizontal extent of the thrust fault to the North due to the overprinting width of ≈10 km of the Karakum Canal irrigated zone. Nevertheless the surface deformation from thrusting to the North of the MKDF is clear in both LOS directions.

3.3.3 Introducing structural complexity with a strain-partitioning geometry

To probe the mechanics of the proposed strain-partitioning geometry, with shortening across frontal thrusts to the north of the MKDF at depth, we model the deformation resolved in the LOS with a model that represents this structural configuration. This model is composed of three segments to construct the proposed strain-partitioning geometry. The model segments consist of 2-D dislocations infinite in the along-strike directions embedded in a homogeneous elastic half-space. These include both semi-infinite and finite dislocations to account for the deformation at shallow depth. To model deep-seated convergence, we use a horizontal semi-infinite dislocation as this does not result in infinite vertical motion during the interseismic period (as opposed to a back-slip approach). The solution used to compute the surface displacements for the ramp segments are for a finite dipping edge dislocations over a confined depth interval (*Segall*, 2005).

The location of a shallow vertical strike-slip segment is fixed to align with the surface trace of the MKDF. This has a locking depth L_A (uniform prior; 30 $\pm$30 km), and is imposed to have the same rate of fault-parallel motion along it as the deep-seated fault. The depth at which these connect, L_B, is defined by the branch depth of the thrust structure, which extends to the north (positive horizontal distance) up to a locking depth L_C (both with uniform priors; 30 $\pm$30 km). We do not allow vertical motion on the strike-slip segment, which imposes partitioning of the strike-slip ("SS") component on to the strike-slip fault and the dip-slip ("Conv.") component on the thrust fault. Any convergence across the fault system is partitioned as shortening across the thrust fault and results in vertical motion at the surface. For the prior distribution of the rate of shortening, we use a Gaussian distribution centred on the convergence rate observed at GPS station MAVT from *Mousavi et al.* (2013) with increased uncertainty (3.5 $\pm$2 (1σ) mm/yr).

The posterior distributions of these models are presented in Figures 3.8 and 3.9 (c). The pattern of uplift observed in both LOS is well fitted by the structural configuration, and the rate of fault-parallel motion is consistent with the previous models (≈6.1 ±0.6 mm/yr). These models also suggest a relatively shallow locking depth of the strike-slip fault 6.1 ± 1.2 km; however this might be influenced by residual topographic signals in the ascending LOS. The posterior distribution of the rate of shortening is 3.0–5.5 mm/yr. The spatial extent of the uplift signal is difficult to constrain due to the overprinting of the tectonic deformation by the signals along the irrigated zone along the Karakum Canal. This partially obscures the locking depth and propagation extent of the thrust fault in our model, and could possibly also contaminate the posterior distribution for rate of shortening. The posterior distributions suggests that the distance the thrust fault extends to the north is variable along strike (≈10–25 km), with a relatively shallow locking depth of 2–6 km. The branch depth (LD_B) is poorly constrained with a broad posterior distribution.

3.4 Discussion

3.4.1 Tropospheric phase-delay corrections

The removal of tropospheric phase-delay signals in the time-series is demonstrated by the reduction in topographic correlation (see profiles in Figures 3.6 and 3.7) and high-amplitude turbulent signals in the LOS time-series velocity fields (Figure 3.5). However the tropospheric correction performance analysis suggests that in this region, tropospheric models systematically under-estimate the amplitude of the correction, using the gradient metric, by 25–40%. This contrasts with the spatial performance of the models using the correlation metric, which reproduce the patterns excellently. One aspect of this is relatively simple to explain; the spatial performance

is inherently better due to the auto-correlation of the interferometric phase and the model tropospheric path delay with topography.

However the systematic behaviour of the scaling amplitude needs further investigation, which suggests that the models are underestimating the amplitude of the tropospheric signals at a swath-width scale. We are hesitant to support methods that scale global weather model-derived tropospheric corrections at variable length scales within a swath (e.g. *Shen et al.*, 2019) before identifying the source of this underestimation, and due to the trade off between deformation and the atmospheric models. The source of the amplitude under-estimation could possibly be accounted for by other sources of long wavelength signals that can introduce variability in path delay at these length scales, such as ionospheric signals. Alternatively global weather models could be missing regional scale water fluxes or incorrectly advecting water vapour, with very few data observations in such a remote region. To investigate this we suggest applying the tropospheric correction performance analysis to other locations globally with possible differences in weather model resolution, to see if better resolved regions have improved scaling relationships between the data and models.

3.4.2 Surface deformation from hydrological processes

As discussed above, within the LOS velocity fields we also observe deformation from non-tectonic sources. The most prominent of these appear to be related to hydrological processes in the region, including throughout the irrigated zone along the Karakum Canal parallel to the MKDF and from takyrs in the Karakum Desert. The Karakum Canal diverts water across the Karakum desert, with a total length of >1400 km. The canal sources water from the Amu Darya River, the main downstream drainage system of the Pamir mountains far to the east along the border with Tajikistan and Afghanistan. The majority of Turkmenistan's 5.85

million population lives along, and is dependent on, this irrigated zone for agriculture and economically important exports. The thin strip of land, 5–25 km wide, is located at the distinct change in topographic gradient between the foothills of the Köpetdag and the low-relief expanse of the Karakum Desert to the north.

The short wavelength signals have a negative sign in both the ascending and descending LOS which implies subsidence, and is also high-magnitude in comparison to the tectonic signals; the subsidence is typically >10 mm/yr (Figure 3.10) in the LOS and exceeds 50 mm/yr in localised parts of the irrigated zone. We have also confirmed that this signal is not the result of time-series bias. At the margins of the irrigated zone there is also uplift with a comparable, if not slightly lower, magnitude. Agricultural subsidence is commonly observed with InSAR and is typically attributed to groundwater pumping. However, in this region agricultural subsidence is somewhat surprising as we expected that most of the water for agriculture to be sourced directly from the Karakum Canal. This suggests that a large fraction of the agricultural water budget is instead sourced from the local water table. Nevertheless this demonstrates the potential for Sentinel-1 time-series to be used for the remote observation of water management in agricultural settings, which is especially valuable in such an arid region with major concerns about water mismanagement (*O'Hara*, 1997).

The general uplift of takyrs, clay basins with diameters of 10s km scattered across the Karakum Desert, is generally observed to be 1–5 mm/yr in the LOS (the pock-marked areas to the north of the MKDF in Figure 3.10). Takyrs are small depressions (≈10 m deep) in the desert surface, that form natural rain water catchment areas and have traditionally been used for rain water harvesting in the arid environment (*Fleskens et al.*, 2007; *Maman et al.*, 2011). The takyrs are large enough to remain stable features over the observation period and generally have excellent spatial and temporal coherence. We are unable to explore the mechanism

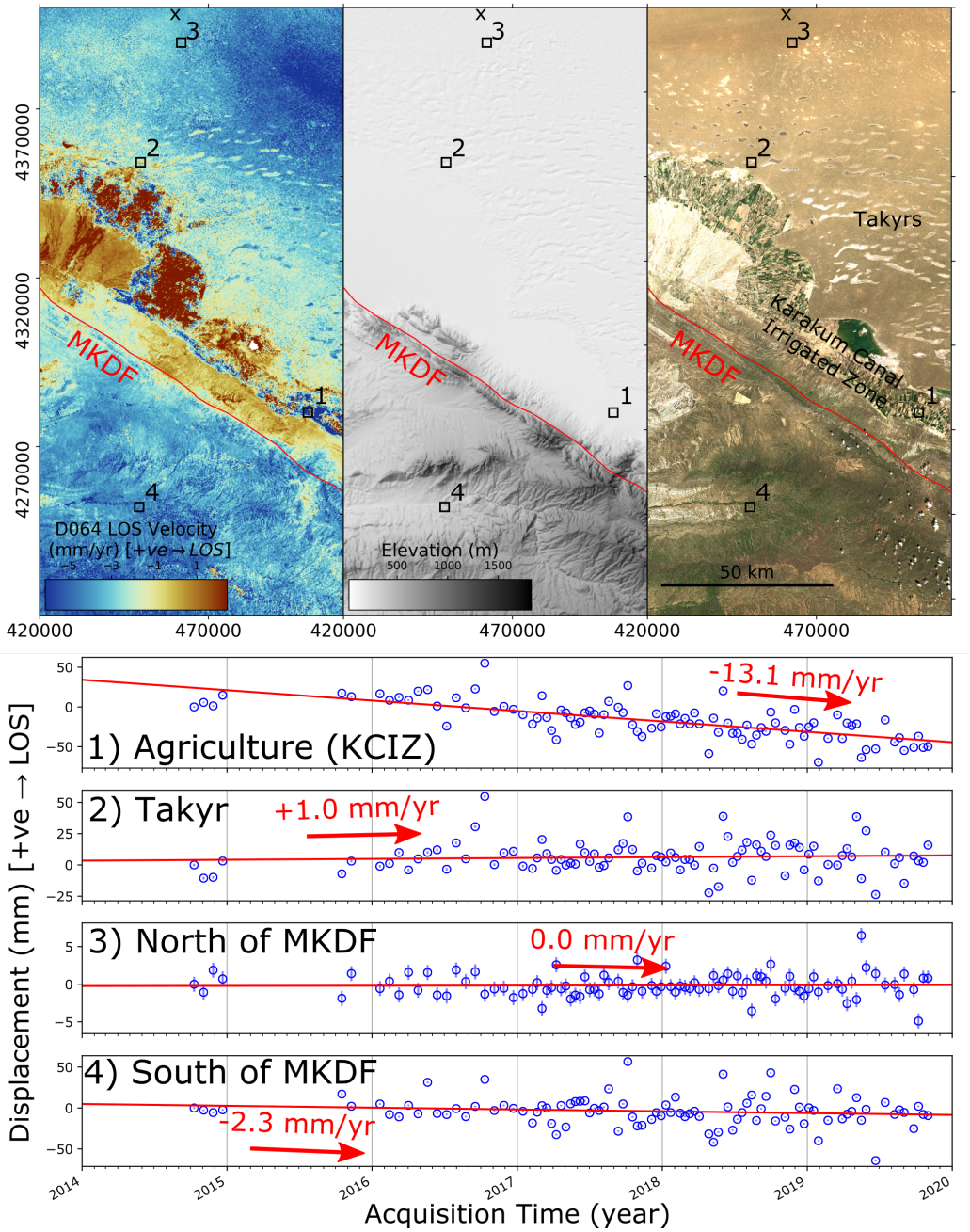


Figure 3.10: Upper map panels, from left to right: the time-series inversion from descending track 064 at the resolution of the unwrapped IFGs; elevation and hillshade of this same area across the MKDF; Sentinel-2 optical imagery, with both takyrs (mottled pits in the desert region to the North) and agriculture within the Karakum Canal irrigated zone clearly visible. The lower panels are the cumulative displacement time-series of points 1–4 (displayed as labelled square markers in the upper panels; agriculture, takyr, north of the MKDF, south of the MKDF) from 2014–2019, relative to the "X" marker in the far North of the figure. Displacements are averaged over a 10 × 10 pixel zone, with the reference zone 100 × 100 pixels in an area chosen to be in a relatively undeforming region in the far-field of the MKDF. The linear fit in the time-series inversion for each labelled point is shown by the red line; no obvious seasonal trends are evident in any of the displacements.

for the general uplift, but suggest that it is associated with hydrological processes possibly related to salt-precipitation or clay-sedimentary processes at the surface. Similar behaviour has been observed in salars, small salt pans in desert environments, which uplift due to accretion from saline sedimentary processes, and have been proposed to be used as monitoring indicators for water resource evolution in arid environments (e.g. *Ruch et al.*, 2012). *Fleskens et al.* (2007) also suggest that sustainable management of takyrs in Turkmenistan with traditional methods of fresh water harvesting present a viable water resource for future development and reducing the dependence on the Karakum Canal.

3.4.3 The rate of interseismic motion and evidence for strain partitioning along the MKDF

Combining the results from the profiles modelled (MKD5–7) by taking the weighted mean gives an estimate of the rate of right-lateral motion along the MKDF. The weighted mean, taking into account the standard deviation (σ) of multiple measurements ($x_1, \ldots x_i$), is $\hat{\mu} = \frac{\sum \frac{x_i}{\sigma_i^2}}{\sum \frac{1}{\sigma_i^2}}$. We use the range of uncertainty on all of the models to provide a conservative measure of the error on this measurement. This constrains the fault parallel slip-rate to 7.2 ± 2.4 mm/yr, and, using the same method, a rate of shortening of 4.3 ± 1.5 mm/yr. The fault-parallel slip-rate is comparable within error to the GPS-derived estimate from *Mousavi et al.* (2013), the Envisat-InSAR derived geodetic measurement from *Walters et al.* (2013), and the geologic slip-rate from *Walker et al.* (2021). From the inversion of the surface deformation, the locking depth of the MKDF is estimated to be ≈6 km; which is at the lower end of previous modelling of the MKDF by *Walters et al.* (2013), and relatively shallow for a continental strike-slip fault.

In comparison to the descending LOS derived slip-rate from *Walters et al.* (2013), our measurement is benefited by the inclusion of the ascending LOS which we use to

constrain the uplift to the north of the MKDF. In the MERIS-corrected descending LOS rate profile from *Walters et al.* (2013), there is evidence for a signal with positive range towards the LOS that extends with a wavelength of ≈60 km to the north of the MKDF. However without the accompanying ascending LOS, their model interprets this as an enhanced rate of fault parallel motion. InSAR-derived measurements using a single LOS with additive fault parallel and vertical signals on one side of a fault might over-estimate the slip-rate in this structural geometry. Similarly the profiles in *Walters et al.* (2013) also show long wavelength signals in the far field (at distances >150 km). This demonstrates the challenges when choosing the profile lengths (explored in Supplementary Figure 3.23), and that simply extending them to excessive perpendicular distances from the fault is not the solution as there is a possibility of intersecting additional signals.

We also explored the effect of introducing further complexity when modelling the LOS velocity fields. In Supplementary Figure 3.25, we solve for the position of the vertical strike-slip fault. However the model geometry consistently shifts towards the higher topography adjacent to the south of the fault, driven by a very short wavelength reversal in the ascending LOS. This also neglects the mapped position of the fault trace at the surface. Similarly solving for the dip of the strike-slip fault is possible, as explored in *Walters et al.* (2013), however a vertically dipping fault at the near surface in outcrop exposures of the MKDF (see field photograph in Supplementary Figure 3.27) and the linear fault trace cutting through topography is indicative of a vertical fault, and this would also neglect any rheological differences either side of the MKDF.

Another observation is vertical motion along the strike-slip fault itself (see profiles in Figures 3.6 and 3.7). Geomorphological analysis of a paleo-rupture scarp along the MKDF also presents localised evidence for vertical motion during the most recent earthquake along the MKDF (*Dodds et al.*, 2021). To model this, following the

approach of *Daout et al.* (2016a), we conserve the motion along the frontal thrust (see Supplementary Figure 3.26). This allows for the deep-seated convergence across the fault system to be partitioned between dip-slip motion on the frontal thrust fault and the strike-slip fault, such that the velocities are controlled by the geometry of the fault system and represent long-term deformation rates. This fits the deformation resolved in the LOS well, however the additional structural complexity does not significantly change the posterior distribution of parameters.

As mentioned above, introducing structural complexity into models without accounting for expected rheological heterogeneity either side of the MKDF is potentially risky. The proposed rapid slip-rate combined with a remarkably linear fault trace suggests that the MKDF is representative of the localisation to strain adjacent to a heterogeneity in crustal strength, observed elsewhere in continental settings (e.g. *Molnar and Dayem*, 2010). The MKDF separates the heavily deformed Iranian Plateau from the stable continental interior of the Turan Platform. The mechanical properties of these two regions are expected to be very different, which is reflected in the distribution of seismicity, topography and GPS velocities (e.g. *Jackson et al.*, 2002; *Copley and Jackson*, 2006). The widespread folding and faulting in the Iranian Plateau suggests that it is comprised of material with much lower rigidity in comparison to the Turan Platform (e.g. *Maggi et al.*, 2000; *Maggi and Priestley*, 2005). This is supported by differences in the propagation of seismic waves from large earthquakes in the region. (*Ambraseys*, 1997) states that throughout the historical record, earthquakes in this region have shown an asymmetry in their shaking intensity and damage distribution that extends far to the north but is limited to the south, possibly due to the difference in the elastic properties between the Köpetdag and Turan Platform.

Asymmetry in InSAR observations of surface deformation on continental strike-slip faults can be used to probe rheological heterogeneity in the crust (e.g.

Jolivet et al., 2011), with deformation concentrating on the more compliant side of the fault (e.g. *Segall*, 2005). This was previously explored in *Walters et al.* (2013), which concluded that including a rigidity contrast in their models of the MKDF supported a strong contrast however doing so did not result in considerable differences when estimating the locking depth (*Savage and Burford*, 1973). In the LOS velocity fields presented here, the combination of inferred vertical deformation to the north of the MKDF, anthropogenic degradation along the Karakum Canal, and a suggestion of residual topographically-correlated signals in the near-field will potentially obscure concentrations of deformation near to the fault.

The suggestion that the broad uplift to the north of the MKDF results from shortening across frontal thrust faults has implications from both a seismic hazard and regional tectonics perspective. The frontal thrusts run parallel to the irrigated zone along the Karakum Canal. The models in Figures 3.8 and 3.9 suggest they might extend directly beneath this region. The uplift in the LOS observations is supported by geomorphological evidence from the broad anticlines to the north of the main strike-slip fault and mapped reverse faulting paleo-rupture scarps in *Walker et al.* (2021).

Using the posterior distributions of model geometries, the dip angle of these thrust faults is estimated to range from 21–42°. From this geometry and the modelled rate of shortening we calculate a rate of uplift along the frontal thrusts of 2.5 mm/yr, although taking into account the broad range of uncertainties gives a possible range from 1.1–5.2 mm/yr. The rate of shortening is consistent with the projected motion of GPS station MAVT that *Mousavi et al.* (2013) use to estimate that 3.5 ± 1.0 mm/yr of shortening must be accommodated between the SCB block and the Turan Platform. Another consideration is reconciling this rate of shortening with the 0.3 mm/yr of shortening along the frontal thrust scarps measured by *Walker et al.* (2021). This measurement is derived from IRSL dating of an alluvial fan surface displaced

by the thrust scarp, and *Walker et al.* (2021) states that this measurement likely represents a minimum value for the rate of shortening. The LOS velocity fields also suggest that the frontal thrust systems possibly extend further to the north than this rupture scarp, in which case the rupture scarps could possibly represent a splay fault from the frontal thrust. However, again this is difficult to resolve with InSAR due to the overprinting of the tectonic signal by the subsidence along the Karakum Canal.

3.4.4 Kinematics of the South Caspian Basin

This geodetic fault parallel slip-rate and the recent geologic slip-rate of 9.1 ± 1.3 mm/yr (*Walker et al.*, 2021) are comparable within error. This implies the present rate of interseismic motion is consistent with the longer term Quaternary rate. Taking the weighted mean of the geodetic and geologic slip-rate, with an error $\sigma^2(\hat{\mu}) = \frac{1}{\sum \frac{1}{\sigma_i^2}}$, constrains the fault-parallel motion along the MKDF to 8.7 ± 1.1 mm/yr.

Walker et al. (2021) revised an Iran-Eurasia-SCB velocity triangle from *Copley and Jackson* (2006) (after *Jackson et al.*, 2002), assuming that the relative motion of the blocks can be represented by two-dimensional vectors (i.e. ignoring rotations and vertical motions). This estimates that the SCB is moving 10.4 ± 1.1 mm/yr relative to Eurasia, in a direction 333° ± 5°. The motion is calculated by assuming that the conjugate strike-slip motion along the MKDF and SFZ accommodate the range-parallel component of motion of the SCB. For the motion of Iran relative to stable Eurasia they use permanent GPS stations (KHUR and MOBK) in Central Iran from (*Khorrami et al.*, 2019), which constrains 11.9 ± 0.4 mm/yr in a direction of 358.5°. The range-parallel motion along the SFZ is 4.8 ± 0.8 mm/yr (striking 244°) derived from ascending and descending Envisat-InSAR time-series *Mousavi et al.* (2015); this rate is consistent with GPS velocities from *Mousavi et al.* (2013) and

the summed left-lateral late Quarternary rates across the Abr and Khuj segments of the SFZ (*Javidfakhr et al.*, 2011). *Walker et al.* (2021) infer that because the eastern Alborz is accommodating shortening perpendicular to the SFZ, the Caspian vertex lies towards the centre of the triangle relative to this vector. Similarly, assuming the Köpetdag accommodates shortening perpendicular to the MKDF, the Caspian vertex must lie towards the interior of the triangle relative to this vector. The overlapping region between these represents the plausible velocity for the SCB (*Walker et al.*, 2021).

We can revise this velocity triangle again, including the updated constraints of the motion accommodated by the MKDF. Instead of a pure right-lateral motion along the MKDF, we resolve a vector defined by the addition of the combined measurement for the strike-slip component from the geologic and geodetic slip-rates, and our inverted range for the fault perpendicular shortening. This gives a vector of 9.7 ± 1.8 mm/yr in a direction of 329 ± 9 °. Instead of using the Envisat InSAR-derived rate from *Mousavi et al.* (2015) along the SFZ, we use the relative motion of permanent GPS stations straddling the SFZ; BIAJ (V_E 1.11 ± 0.28 mm/yr, V_N 8.66 ± 0.22 mm/yr) and MAVT (V_E -4.80 ± 0.34 mm/yr, V_N 5.78 ± 0.16 mm/yr) (*Mousavi et al.*, 2013). This returns a purely left-lateral vector across the fault zone of 6.6 mm/yr in the direction 244° (also parallel to the fault strike modelled in *Mousavi et al.* (2015)). For the Iran-Eurasia motion, we also use GPS station KHUR (at 55.1°E) from *Khorrami et al.* (2019), which has a velocity relative to stable Eurasia of 11.5 ± 0.1 mm/yr in a direction of 001°. The velocity triangle is presented in Figure 3.11, with all of the defined vectors referenced to stable Eurasia.

The velocity triangle in Figure 3.11 supports the rates and direction of motion for the SCB from *Walker et al.* (2021) (after *Copley and Jackson* (2006)), approximately aligning with SCB-Eurasia vector from *Walker et al.* (2021) (10.4 ± 1.1 mm/yr in a direction of 333 ± 5 °). However, the main difference is that the overlapping zones of

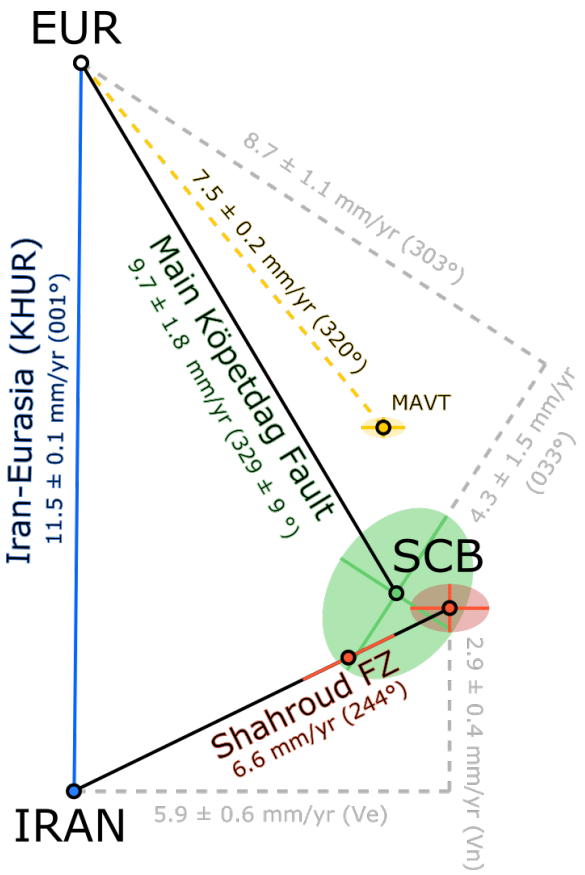


Figure 3.11: Velocity triangle constructed following the approach of *Walker et al.* (2021) for the motion of the South Caspian Basin, Eurasia and Iran. We resolve a vector for the MKDF from the combined measurement for strike-slip and our inverted range of fault perpendicular shortening across the fault system; 9.3 mm/yr in a direction of 330° (green, with error given by the ellipse). The relative motion of permanent GPS stations located either side of the the Shahroud fault zone is used to constrain the overall motion across the distributed network of faults (red; the highlighted zone on the vector also shows the InSAR-derived rate from *Mousavi et al.* (2013)); BIAJ (V_E 1.11 ± 0.28 mm/yr, V_N 8.66 ± 0.22 mm/yr) and MAVT (V_E -4.80 ± 0.34 mm/yr, V_N 5.78 ± 0.16 mm/yr; also plotted in yellow) (*Mousavi et al.*, 2013). We use the GPS station KHUR (blue, 11.5 ± 0.1 mm/yr, 001°; *Khorrami et al.* (2019)) for the vector of the Iran-Eurasia convergence at this longitude.

the error ellipses from motion along the conjugate MKDF-SFZ faults suggests that motion along these faults can accommodate the motion of the SCB without requiring additional deformation within the East Caspian Lowlands or at the margins of the block in the eastern Alborz. The geodetic measurements along the MKDF can also be considered relative to the GPS velocity of station MAVT in the East Caspian Lowlands (see Figure 3.11). Assuming the velocity of MAVT is correct, the fault

perpendicular shortening modelled from the LOS velocity fields possibly slightly over-estimates the rate of shortening along the frontal thrust faults. This is possible as explained previously due to the overprinting of the tectonic signal by deformation associated with irrigation adjacent to the Karakum Canal. However the observation of >1 mm/yr of uplift to the north of the MKDF does correlate with the GPS velocity, and would suggest that the convergence measured by MAVT is transferred to the frontal thrusts, rather than being distributed along structures in the Köpetdag interior or East Caspian Lowlands. Furthermore the assumption that the velocity of a GPS station at 55°E is representative of the Iran-Eurasia convergence across the conjugate system is possibly inaccurate, as GPS velocities show an eastward reduction in the rate of convergence of ≈-1.2 mm/yr/°E between 52–60° E (e.g. *Khorrami et al.*, 2019).

3.5 Conclusion

We model the interseismic motion along the MKDF from descending and ascending Sentinel-1 InSAR time-series. We implement a processing strategy for the correction and performance analysis of tropospheric models, which suggests a 25–40% under-estimation in the amplitude of the tropospheric path delay in this region. We model the rate of fault-parallel motion across the MKDF and combine this with the geological rate determined in *Walker et al.* (2021) to constrain 8.7 ± 1.1 mm/yr right-lateral motion, and a shallow locking depth of ≈6 km. We resolve broad uplift immediately to the north of the MKDF, which we interpret as resulting from fault-perpendicular motion along frontal thrusts to the MKDF. Modelling the uplift observed in the LOS estimates 4.3 ± 1.5 mm/yr of shortening across these frontal thrusts. This implies that most of the convergence measured with GPS in the East Caspian Lowlands (*Mousavi et al.*, 2013) is transferred to the frontal thrusts to the north of the MKDF. Revising velocity triangles from *Walker et al.* (2021) supports

the rate of motion of the SCB (10.4 ± 1.1 mm/yr in a direction of 333 ± 5 °), however we suggest that motion along the conjugate MKDF-SFZ is representative of the motion of the SCB. Reconciling the modelled rate of shortening resolved in the LOS velocity fields with GPS velocities (*Mousavi et al.*, 2013), suggests that this rate is possibly over-estimated slightly probably due to overprinting of the tectonic signal by deformation along the irrigated zone adjacent to the Karakum Canal. However the interpretation of >1 mm/yr of uplift resulting from deformation along frontal thrusts to the north of the MKDF is compatible with GPS velocities, and suggests that at this latitude remaining Iran-Eurasia convergence is accommodated along these frontal thrusts to the MKDF.

3.6 Acknowledgments

This research is supported by the UK National Environmental Research Council (NERC; Doctoral Training Partnership in Environmental Research; NE/L002612/1), the NERC-funded Centre for Observation and Modelling of Earthquakes, Volcanoes and Tectonics (COMET), the NERC grant 'Looking into the Continents from Space' (LiCS; NE/K011006/1), the NERC-ESRC Increasing Resilience to Natural Hazards program 'Earthquakes without Frontiers (EwF)' (NE/J02001X/1), by the Leverhulme Trust Research Project Grant 'EROICA' (RPG-2018-371), and the Global Challenge Research Fund (Internal Oxford QR allocation). InSAR data is provided by the ESA Copernicus Sentinel-1 Satellite Missions. InSAR time-series processing and analysis uses the NSBAS processing chain. Tropospheric path-delay corrections are provided by the Generic Atmospheric Correction Online Service for InSAR (GACOS), with data from the European Centre for Medium-Range Weather Forecasts (ECMWF; operational high-resolution tropospheric products). Worldview-2 satellite imagery is provided courtesy of the DigitalGlobe Foundation. We thank the President of Turkmenistan and the National Academy of Sciences

of Turkmenistan for the ongoing support of this joint UK-Turkmenistan scientific collaboration.

Supplementary Material

Table 3.1: Previous estimates of the rate of interseismic strain accumulatiom on the MKDF from a variety of methods (GPS, plate closure models, InSAR, geological). The slip-rate estimates are highly variable and inconsistent within uncertainty bounds (with uncertainty bounds where available).

	Fault Parallel (mm/yr)	**Convergence (mm/yr)**	**Method**
Lyberis and Manby (1999)	5 ±2	-	Cross-section restoration
Copley and Jackson (2006)	9.3 ± 2	5.8 ± 2	Plate closure model
Masson et al. (2007)	3 ± 1	-	GPS (SHIR)
Hollingsworth et al. (2008)	3 ± 2	2 ± 2	GPS (SHIR)
Djamour et al. (2010)	3 ± 2	1 ± 2	GPS (block model)
Mousavi et al. (2013)	6.7 ± 0.5	3.4 ± 1.0	GPS (MAR2/MAVT)
Walters et al. (2013)	8.5 ± 3.5	0	InSAR (Envisat)
Walker et al. (2021)	9.1 ± 1.3	0.3	Geological (IRSL)
This paper	7.2 ± 2.4	4.3 ± 1.5	InSAR (Sentinel-1)

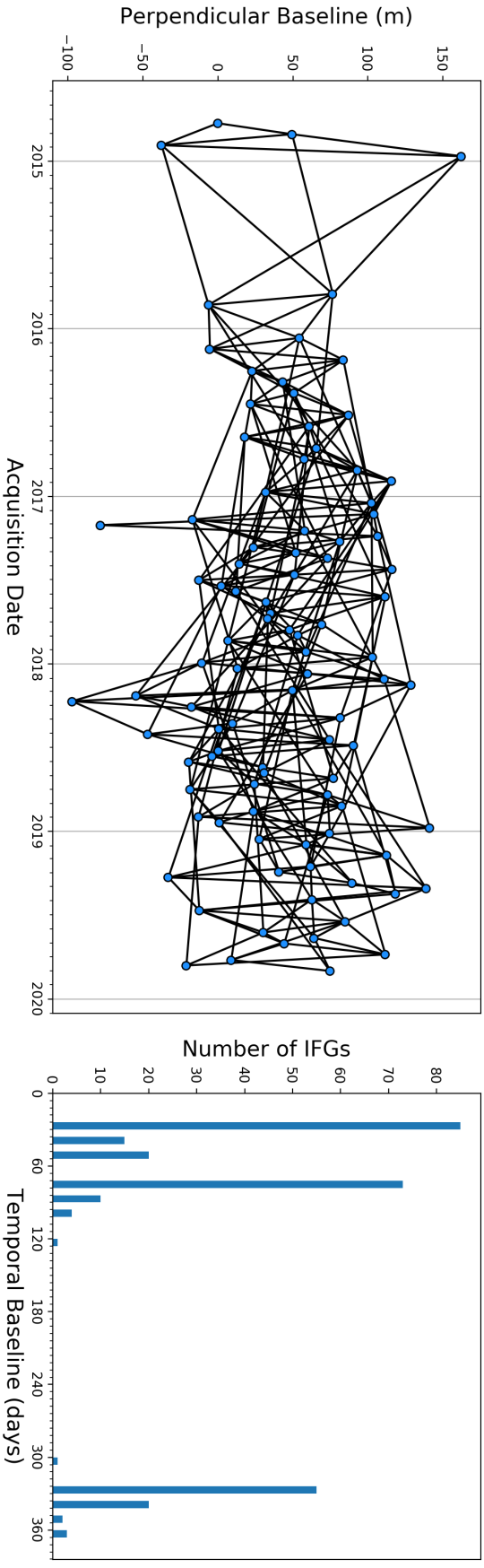


Figure 3.12: Descending track D064 perpendicular baseline versus temporal baseline plot. This InSAR time-series consists of 290 IFGs from 96 acquisitions.

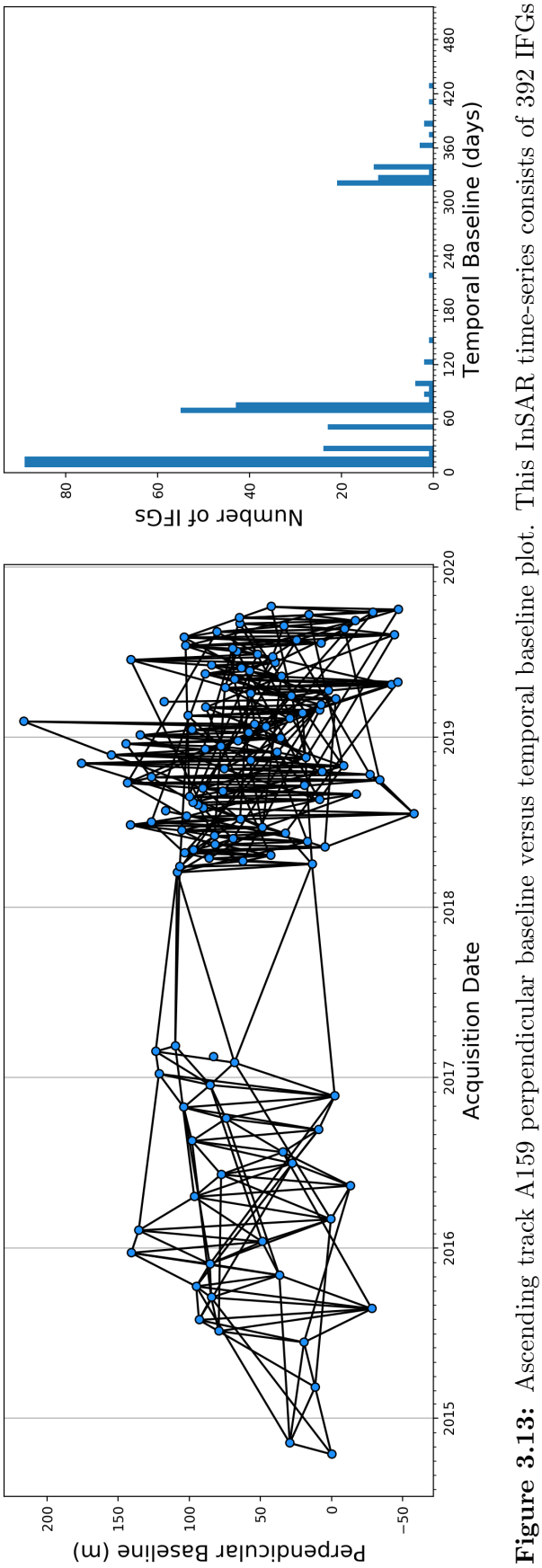


Figure 3.13: Ascending track A159 perpendicular baseline versus temporal baseline plot. This InSAR time-series consists of 392 IFGs from 126 acquisitions; note the approximately year long acquisition gap from 10/03/2017 – 17/03/2018.

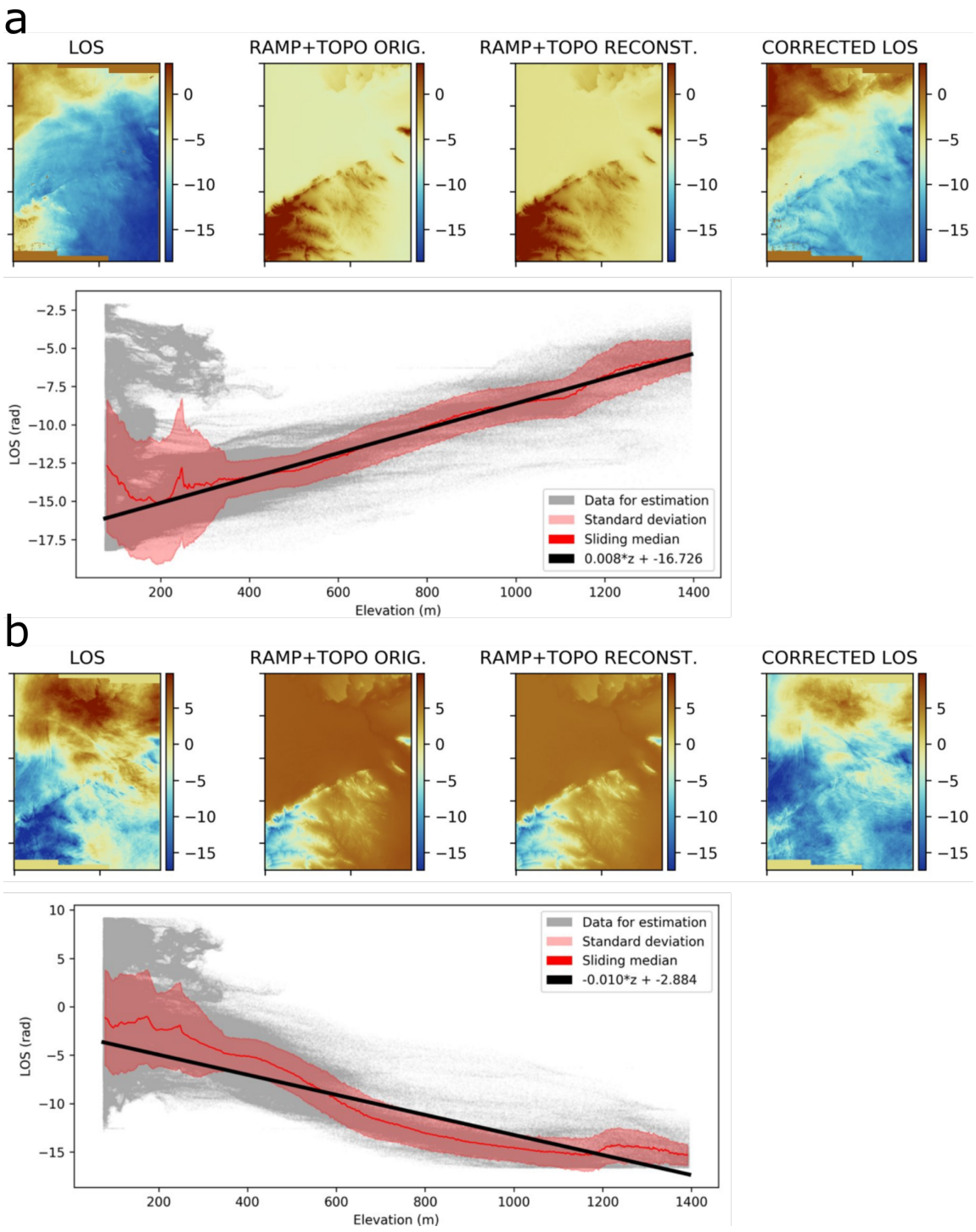


Figure 3.14: Correcting IFGs with an empirical phase-elevation relationship (a) 20141127-20150207, b) 20150619-20150713; from descending track D064, with all LOS scales in radians). The phase-elevation correction is good at capturing the relationship with topography in the lower right of both IFGS; however in both cases large turbulent stratospheric delays in the low elevation region to the north remain after the correction and dominate the corrected IFG.

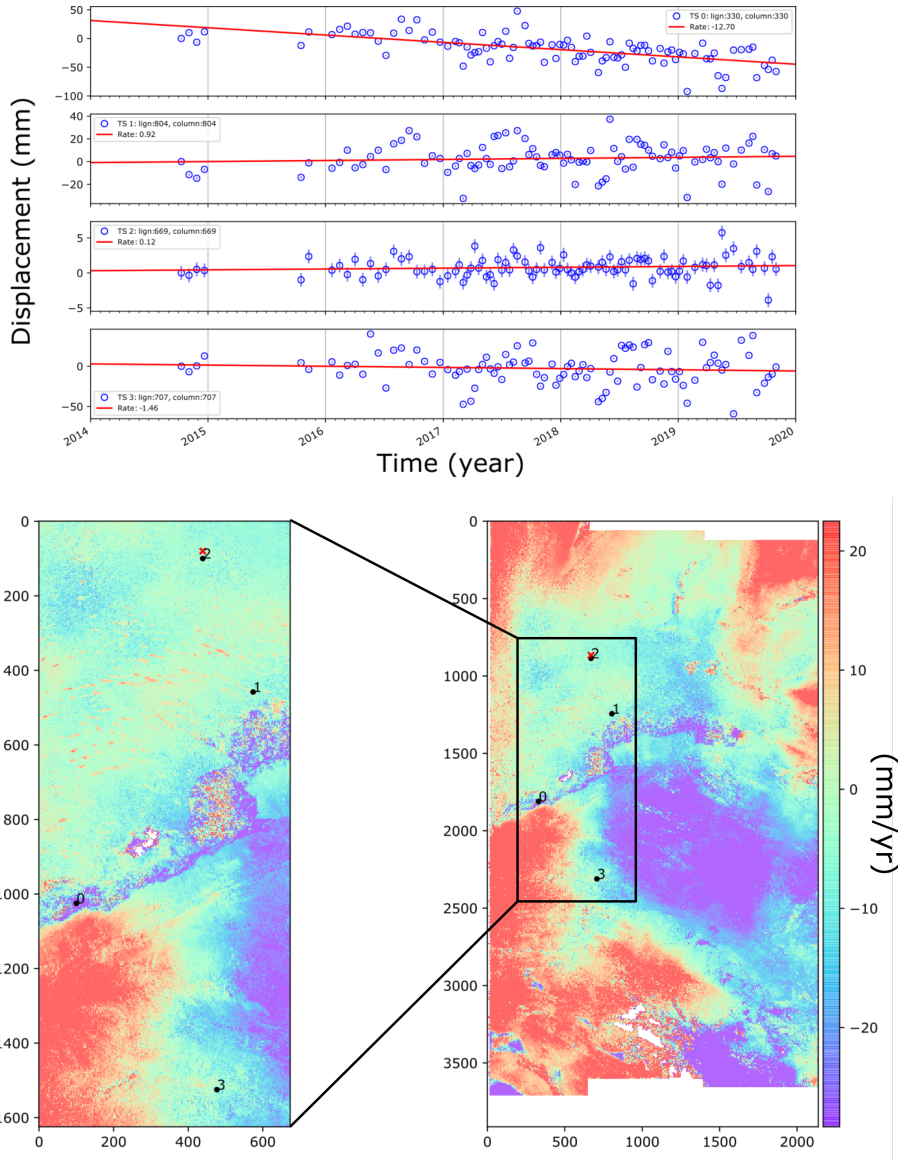


Figure 3.15: InSAR time-series for descending track 064 without atmospheric corrections (processed using time-series ramp estimation method from *Maubant et al.* (2020)). Red cross to the north is the reference area (100 × 100 pixels), chosen to be in the far field from the fault at low elevation. The displacement time-series of numbered pixels 0–3 (averaging across 20 × 20 pixels) are shown below, with the red lines showing the decomposed linear trend for the velocity maps. These aim to capture different areas in the time-series to resolve possible seasonality in the time-series: 0) Karakum Canal irrigated zone, 1) takyrs, 2) low elevation, and 3) high elevation. We are unable to solve for a robust seasonal signal in the time-series maps. This is due to the influence of turbulent signals dominating the time-series which results in high perturbances from any seasonal trend in the time-series.

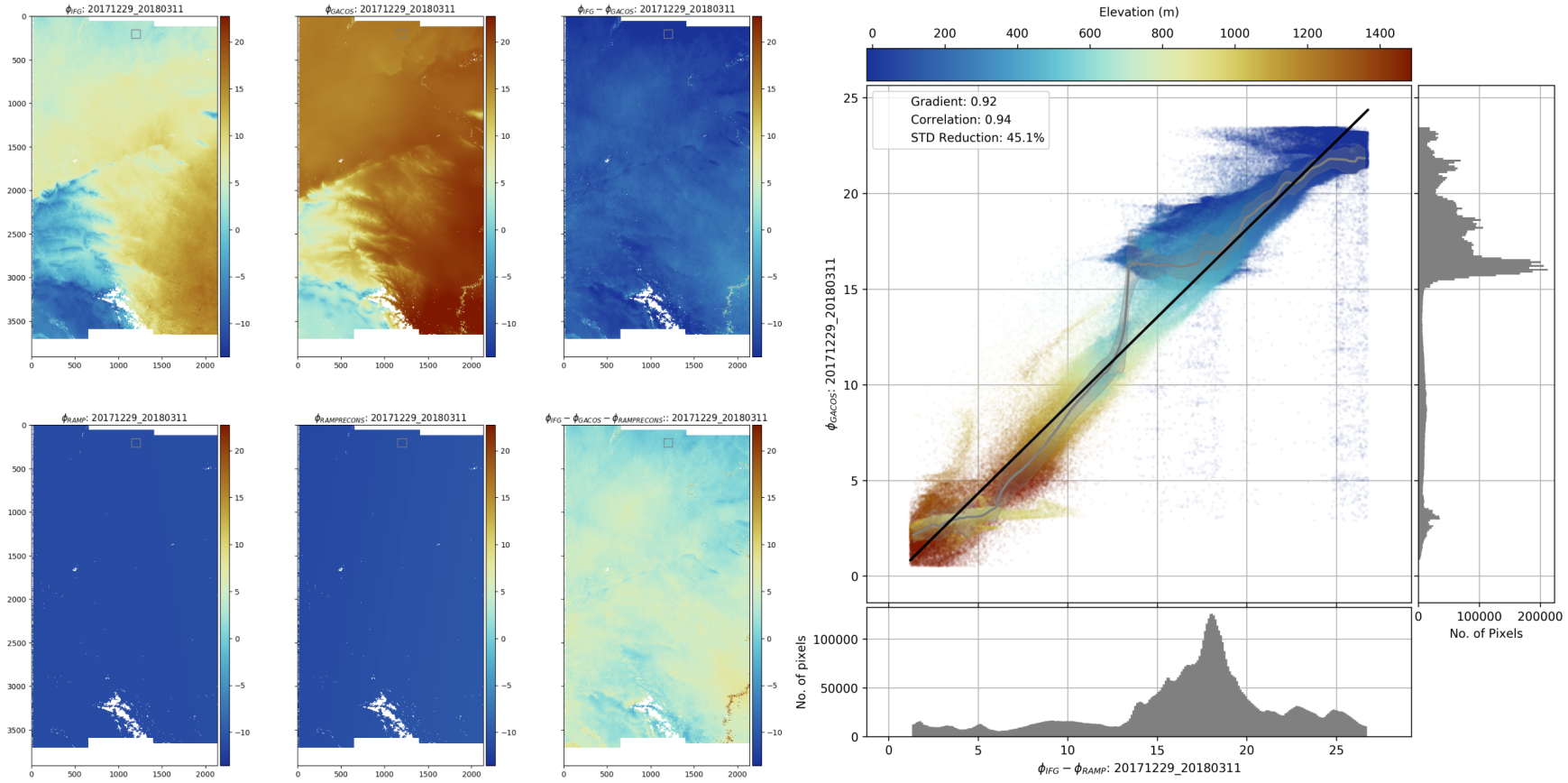


Figure 3.16: Left) Tropospheric path-delay correction with GACOS for IFG 20171229-20180311, with the processing strategy presented above (units for all θ in mm/yr). Right) ϕ_{GACOS} vs. $\phi_{IFG} - \phi_{RAMP}$ plot, coloured by elevation. This demonstrates an example where the GACOS model corresponds to the IFG phase excellently. The statistical metrics reflect this observation. Both the gradient of the ϕ_{GACOS} vs. $\phi_{IFG} - \phi_{RAMP}$ are very close to 1; the correction results in standard deviation reduction of $\approx 45\%$.

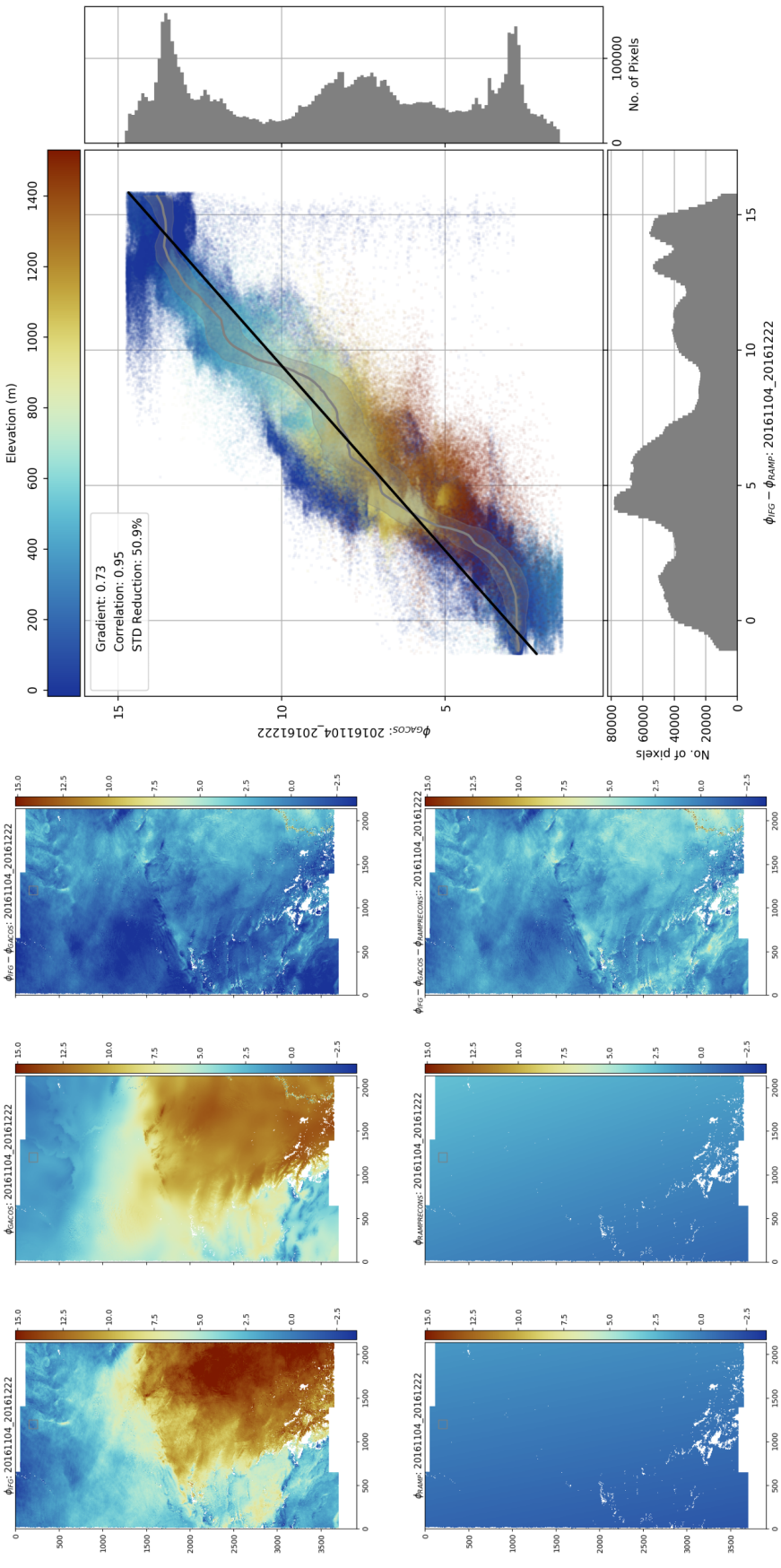


Figure 3.17: Left) Tropospheric path-delay correction with GACOS for IFG 20161104-2016122, with the processing strategy presented above (units for all θ in mm/yr). Right) ϕ_{GACOS} vs. $\phi_{IFG} - \phi_{RAMP}$ plot, coloured by elevation. This is an interesting example that relates to the histogram results for the entire time-series. The distribution of the ϕ_{GACOS} vs. $\phi_{IFG} - \phi_{RAMP}$ plot remains linear however the gradient is only 0.73. This contrasts with the correlation, which is excellent (> 0.9). These observations suggest that the spatial characteristics of the corrections are excellent, however the amplitude of the corrections is significantly underestimating the phase-delay by $> 25\%$.

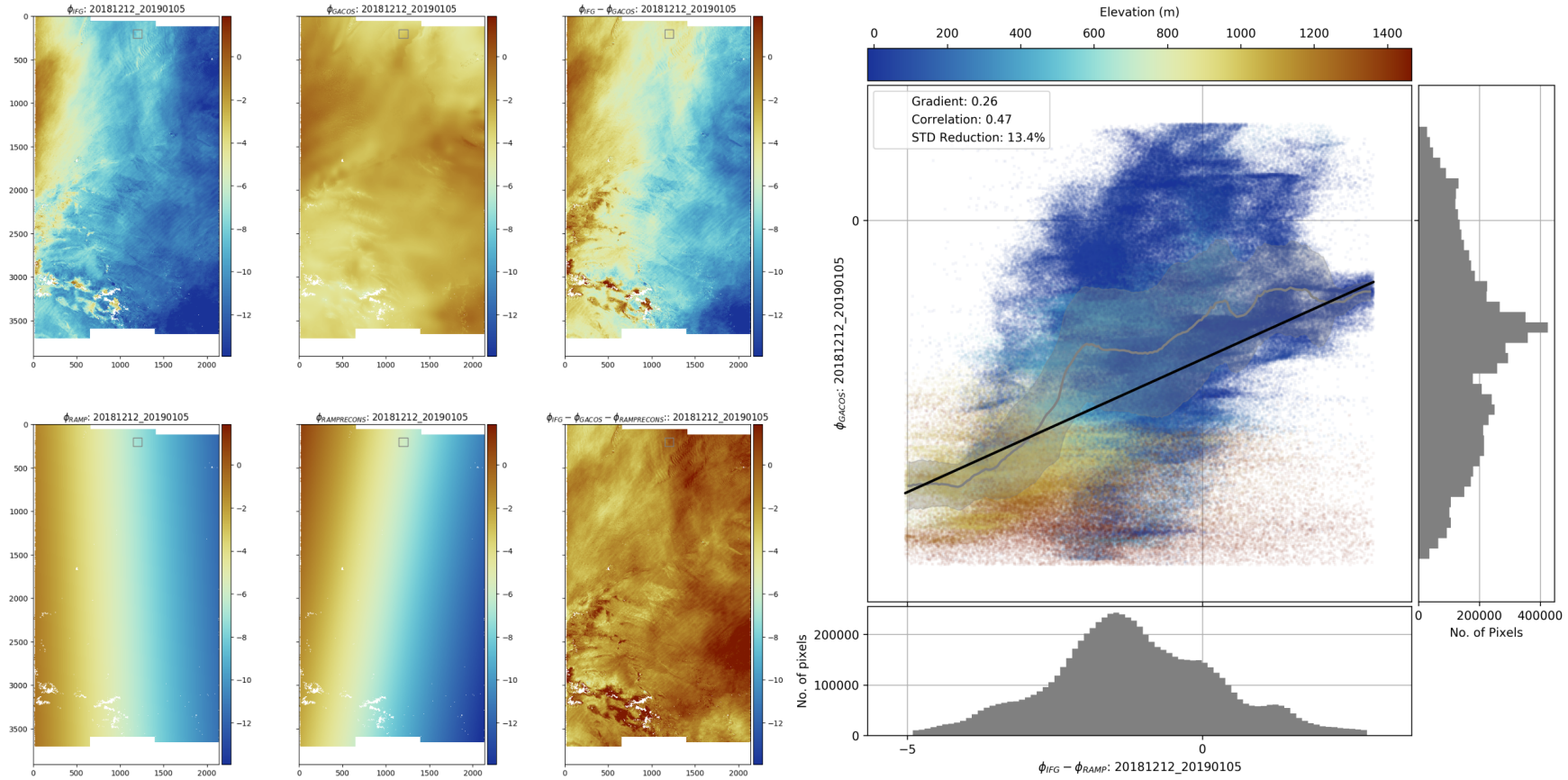


Figure 3.18: Left) Tropospheric path-delay correction with GACOS for IFG 20181212-20190105, with the processing strategy presented above (units for all θ in mm/yr). Right) ϕ_{GACOS} vs. $\phi_{IFG} - \phi_{RAMP}$ plot, coloured by elevation. This IFG corrections presents an example where the GACOS correction is not performing well. This is highlighted by the low performance in all three statistical metrics. In addition, this example reinforces the benefit of the simultaneous ramp estimation between the IFG phase and the model phase. Furthermore the ramp and reconstructed ramp panels present the necessary strategy to invert the individual ramp parameter across the time-series network to maintain phase closure. Despite the difficulty with turbulent tropospheric signals, the corrected IFG still has a reduced variance when compared with the uncorrected IFG.

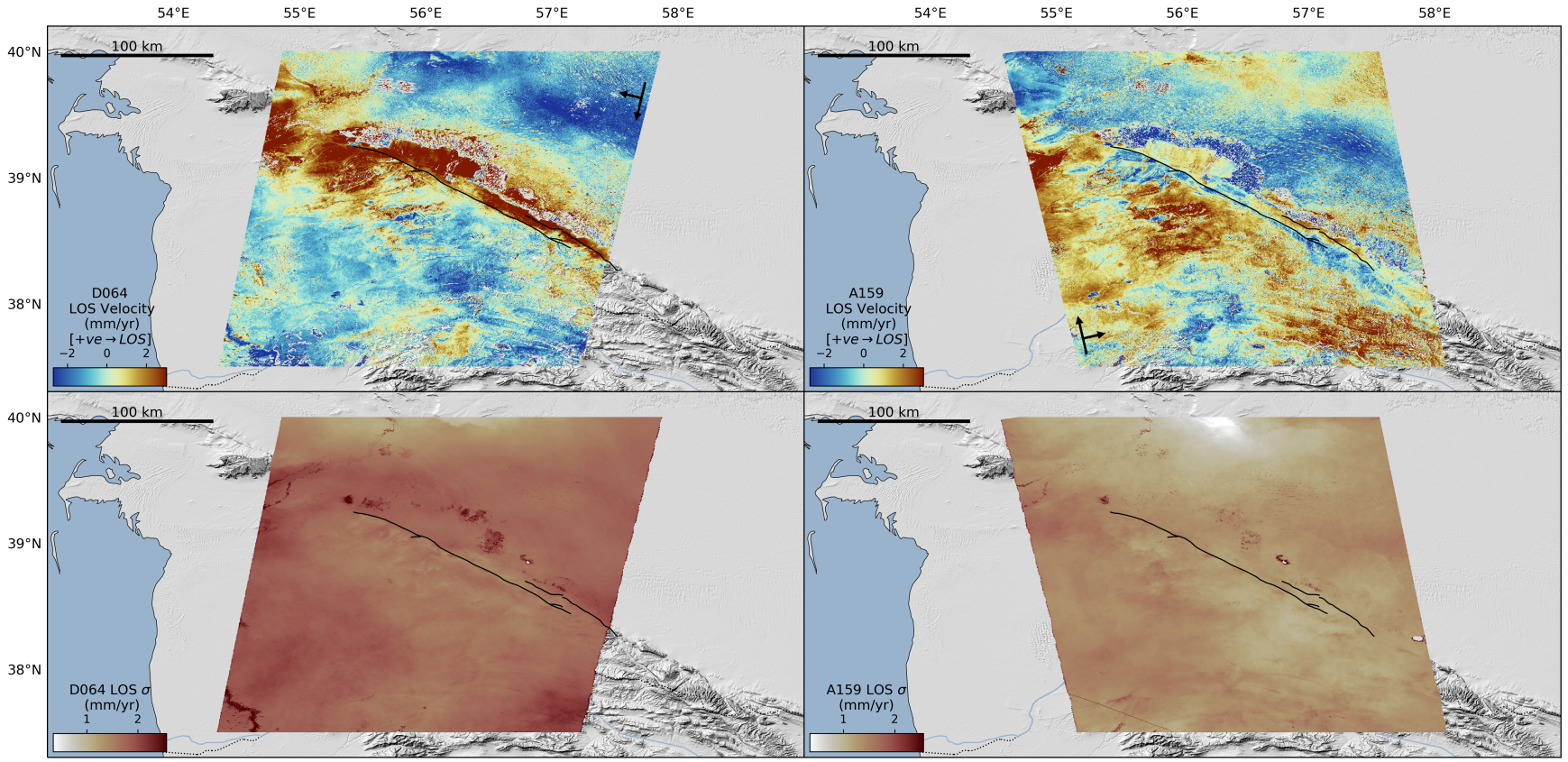


Figure 3.19: Top row: LOS velocity rate-maps from time-series inversion for the descending (left, D064) and ascending (right, A159) tracks; LOS velocity in mm/yr, with positive motion towards the LOS direction of the satellite. MKDF is delineated by a solid black line, striking WNW-ESE. Bottom row: the corresponding 1σ uncertainty (in mm/yr) maps from the time-series inversion for D064 (left) and A159 (right).

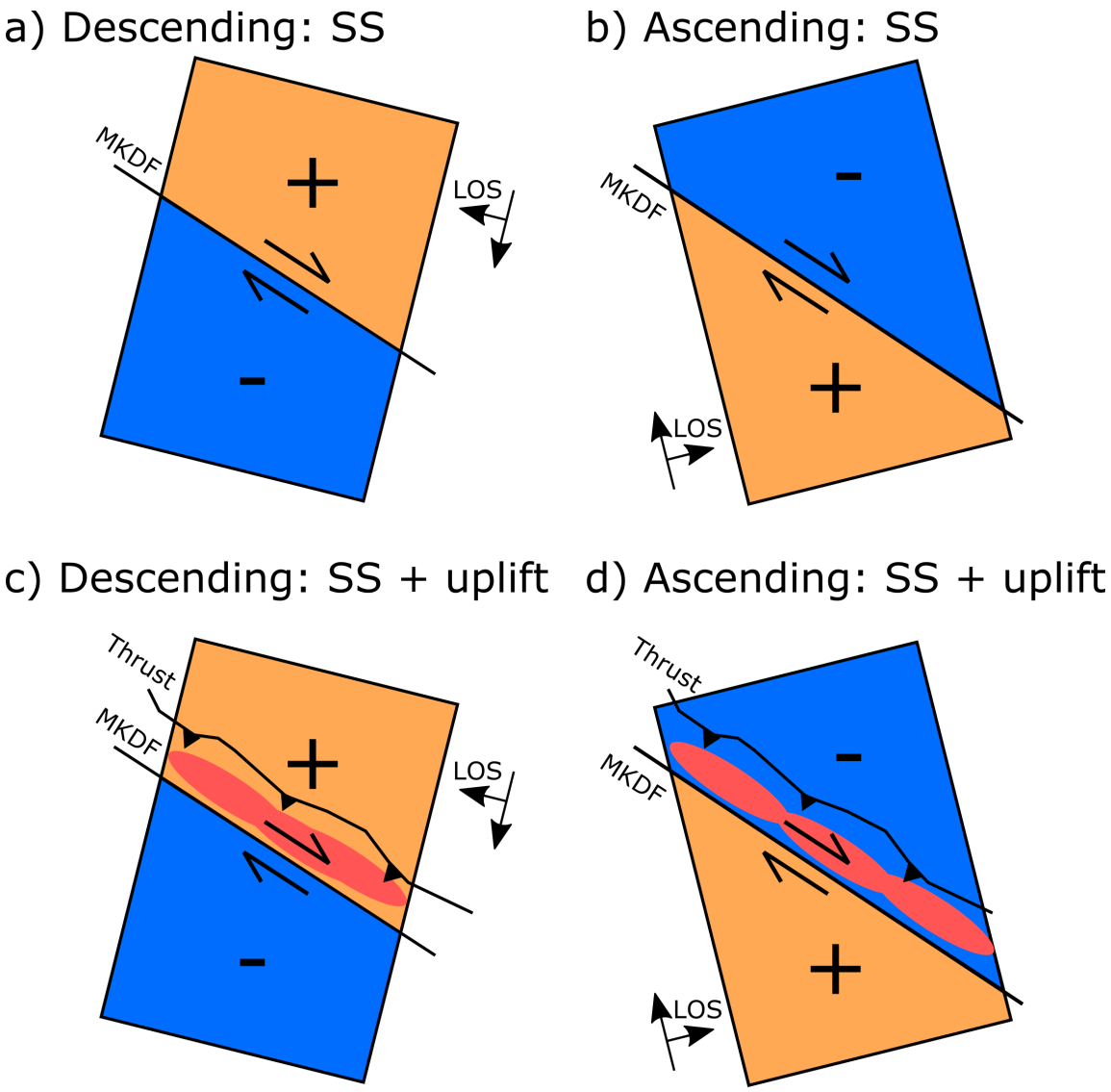


Figure 3.20: Simplified expected LOS observations from dextral motion on the MKDF, observed from the descending and ascending LOS geometry; red/orange colours represent motion of the ground towards the satellite LOS, blue away from the satellite LOS. a) Descending LOS; b) Ascending LOS. c) and d) are the same as the panels above, except for the addition of a thrust fault to the north of the MKDF. This structure results in uplift between the two mapped faults, which is difficult to distinguish in the descending LOS as the signal is additive. However in the ascending LOS, the uplift signal opposes this motion and is very obvious in the LOS velocity maps.

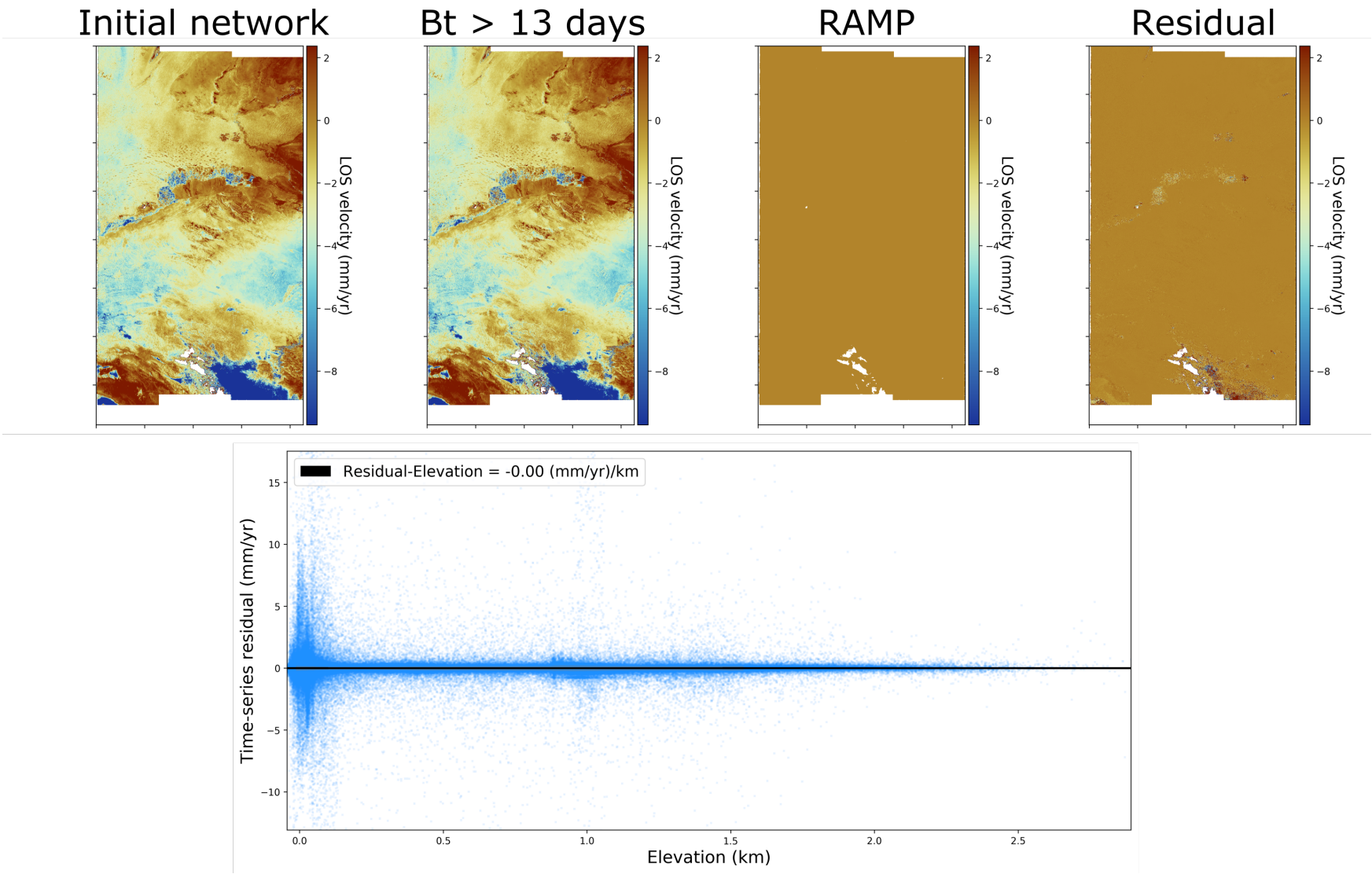


Figure 3.21: Investigating the potential effects of short baseline interferogram biases on the results of the time-series inversion with comparison maps for descending track D064. Top row, from left to right: including IFGs with short baselines; excluding IFGs with temporal baselines <13 days (the eventual network used for analysis in this paper); the best-fitting ramp and offset ($ax + by + c$) to the difference of the two time-series rate-maps; the residual difference of the time-series after removal of the estimated ramp. No short baseline biases that would affect the interpretation of tectonic signals are observed for this region of the Köpetdag. Bottom row: There is no observable phase-elevation relationship within this descending track (D064) over this area of Turkmenistan/NE Iran, albeit with relatively muted topography. The main differences are restricted to low elevation regions associated with agricultural/hydrological signals.

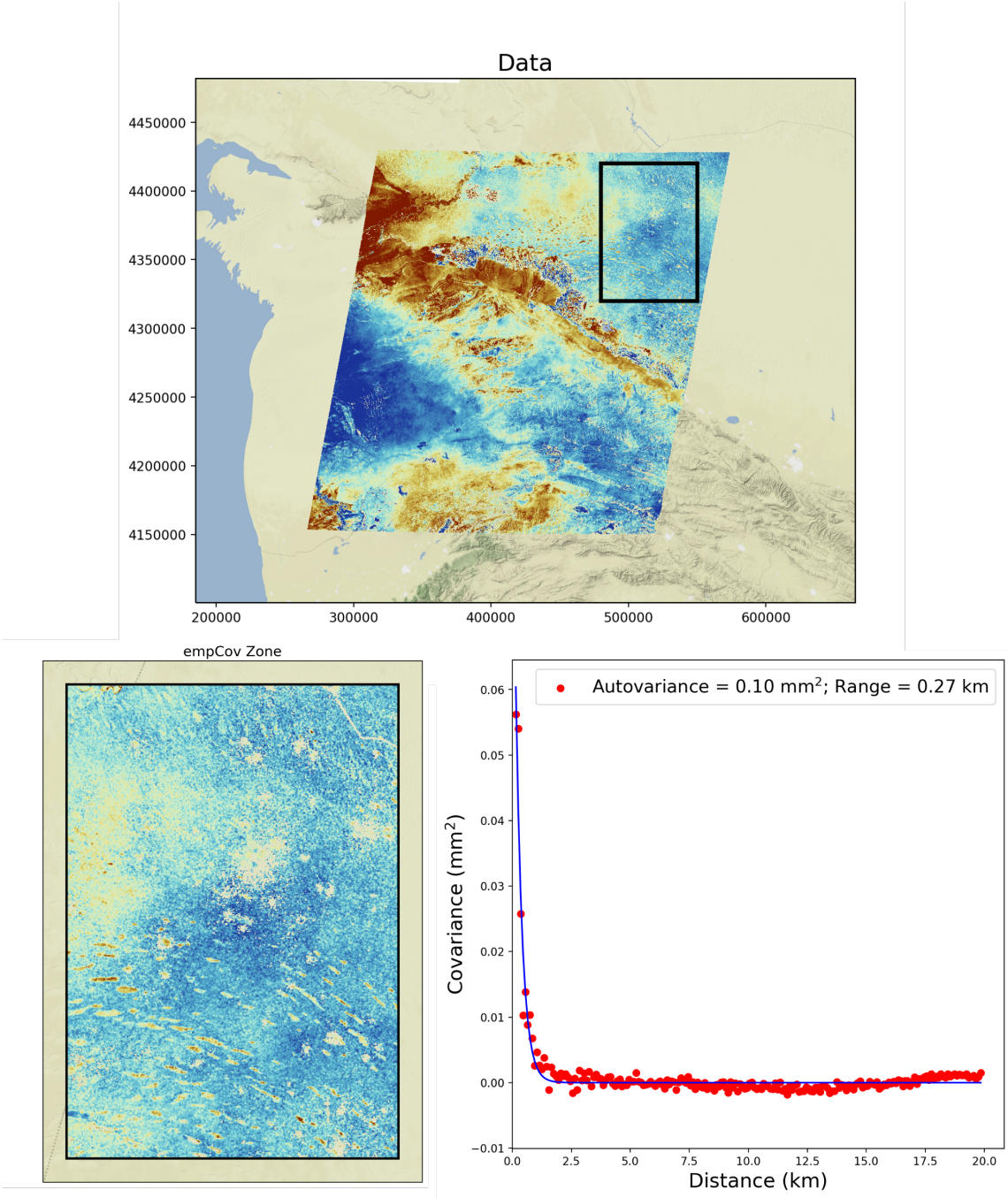


Figure 3.22: Empirical covariance estimation for the descending LOS (D064) time-series inversion following the method of Sudhaus and Jonsson (2009). Estimation uses the functional form $b\exp(\frac{-h}{a})$. The autovariance (b) is approximately 0.10 mm^2 and e-folding decay length scale (a) is approximately 270 m.

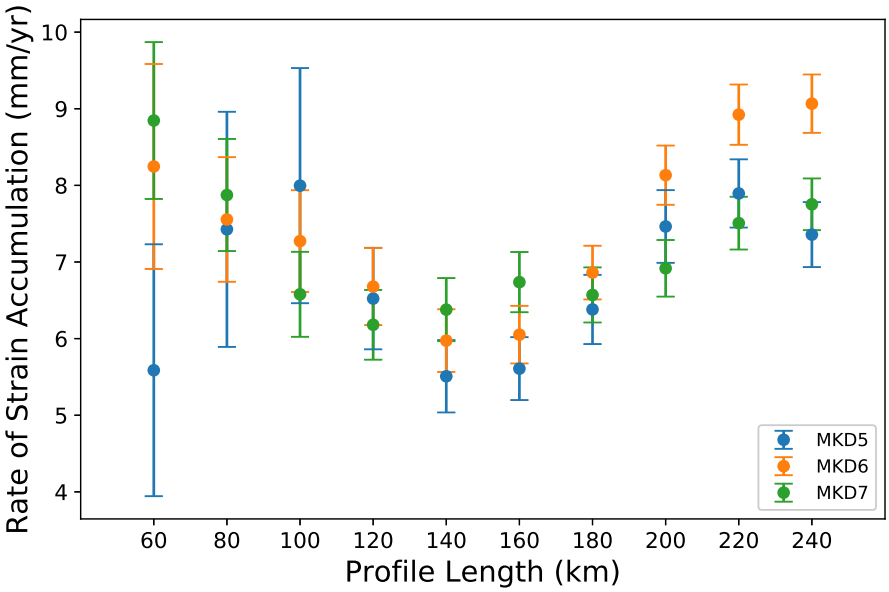


Figure 3.23: Modelling the descending LOS time-series data from three profiles (MKD5–7) yields variable results for the rate of strike-slip strain accumulation on the MKDF. At profile lengths ≤100 km, the wavelength of the apparent thrusting-generated uplift constructively interferes with the descending LOS and increases the modelled geodetic slip-rate. At very long profile lengths (>160 km), the modelled geodetic rate also increases; these signals are beyond the typical wavelength of deformation surrounding a continental strike-slip fault. Therefore in our modelling strategy, we confine our analysis to profile lengths of 120 – 160 km.

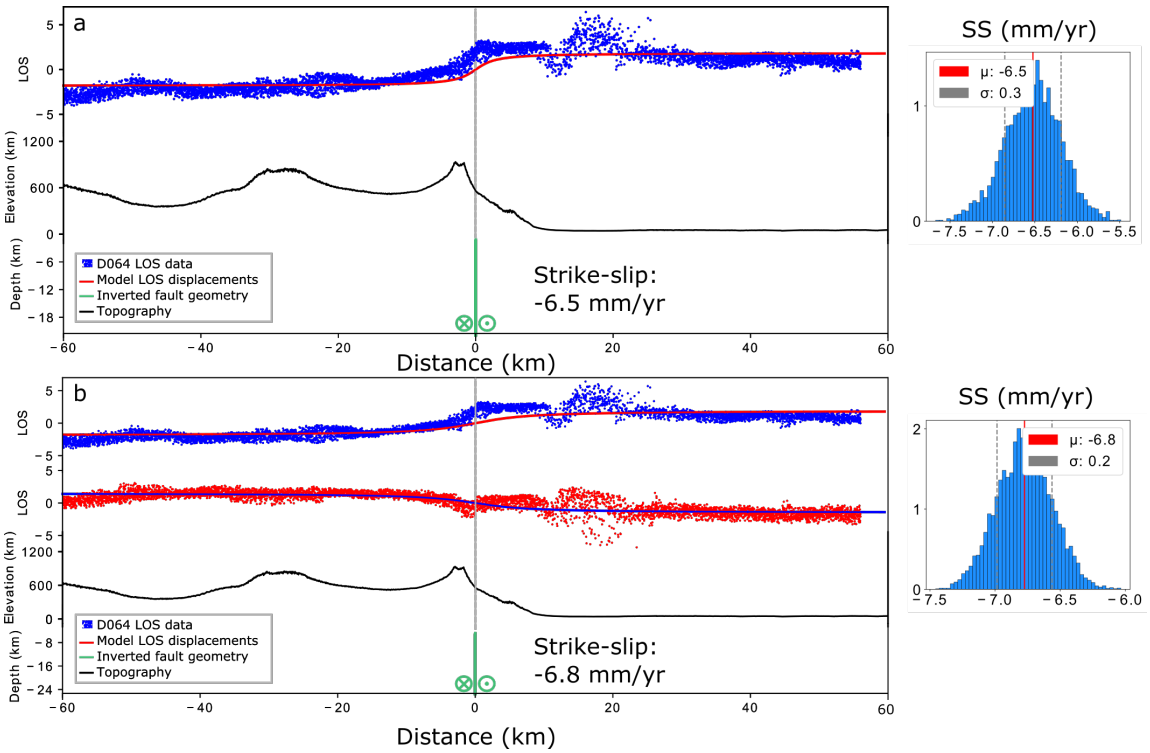


Figure 3.24: Modelling the surface deformation in profile MKD5 (120 km length, 20 km width). a) Inverting the surface deformation in only the descending LOS. b) Inverting the surface deformation in both the descending and ascending LOS. We are unable to model the surface deformation with a more complex geometry (see Figures 3.8 and 3.9) to probe the uplift to the north of the MKDF in this profile due to the wide zone of overprinting by the Karakum Canal irrigated zone.

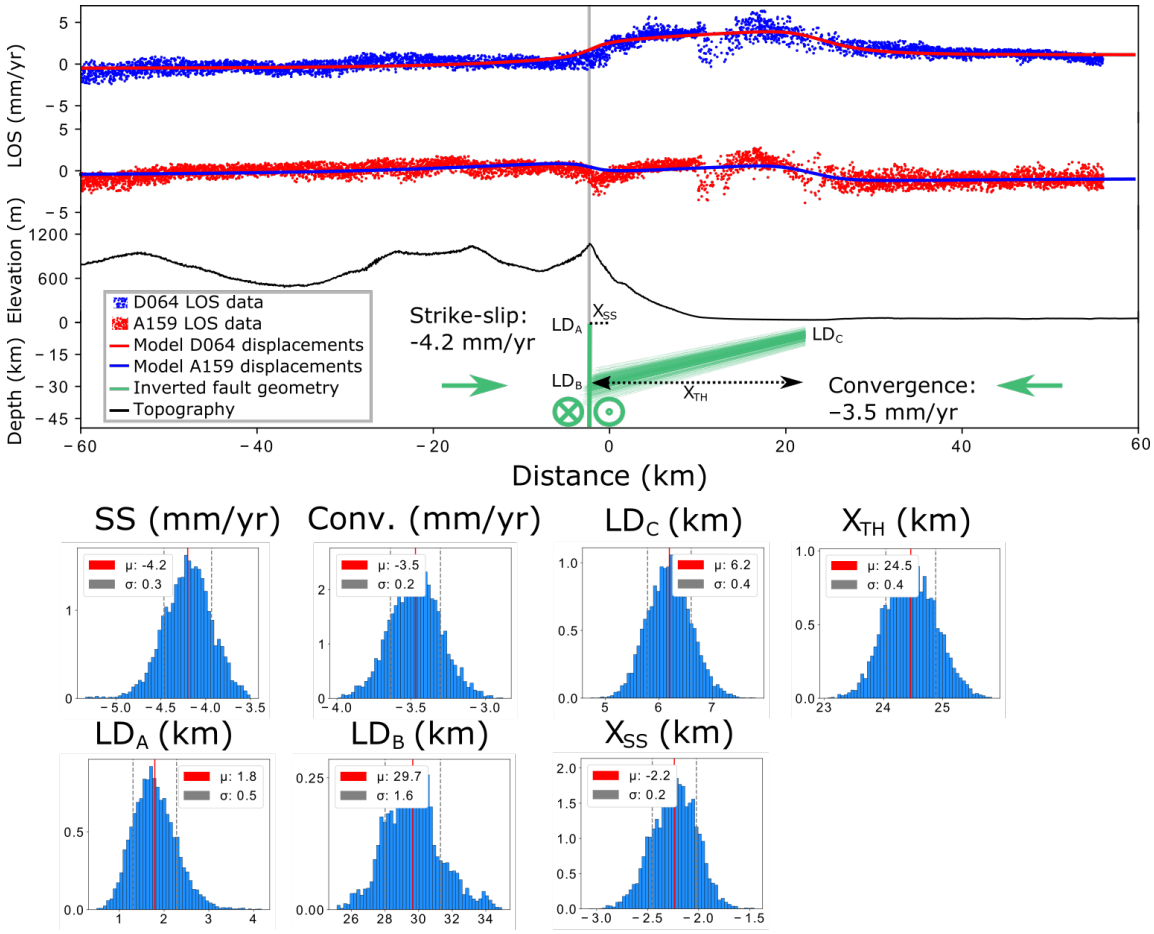


Figure 3.25: Introducing an additional free parameter to the inversion, the location of the primary strike-slip fault (X_{SS}). The topography shown is a sliding median of the topography with a window size of < 1 km. The topographic ridge (the northernmost in the Köpetdag) is aligned with the strike of the MKDF, although offset by 1–5 km to the south. Interpreting the near-field signals with this model is very difficult due the variability along strike of both the position of the MKDF and the ridge itself within a profile, both of which can have a variation of several kilometres within each profile swath. There is also the potential for residual topographically-correlated deformation signals and this neglects the well-mapped fault trace; therefore we discard the results from this model.

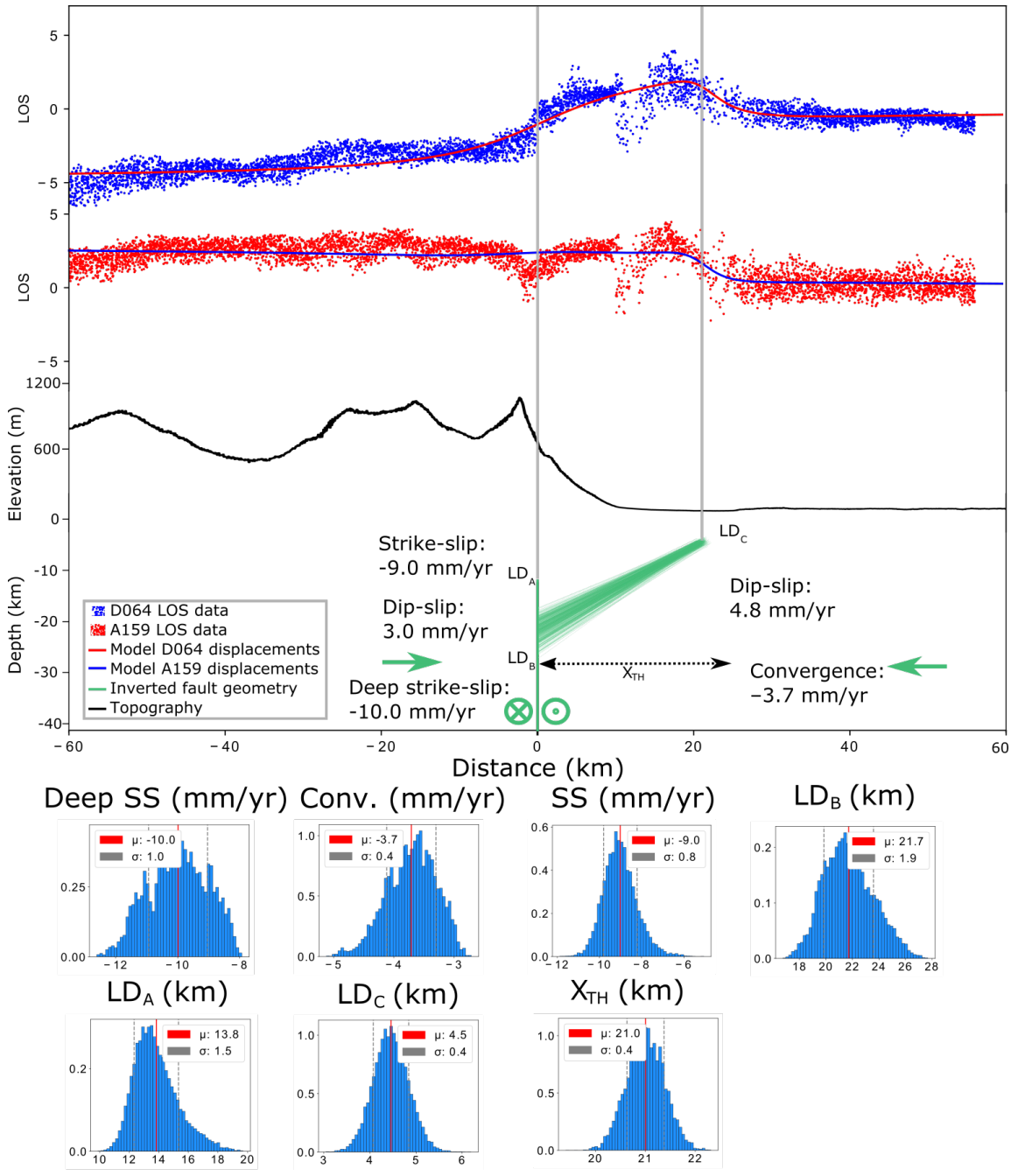


Figure 3.26: Modelling the surface deformation with a fixed position strike-slip fault and thrust fault extending northward, with the addition of the conservation of motion on the frontal thrust. This results in vertical motion directly along the strike-slip fault. There is evidence along the Central Segment for localised vertical motion, although this model neglects the permanent inelastic deformation along anticlines between the structures.

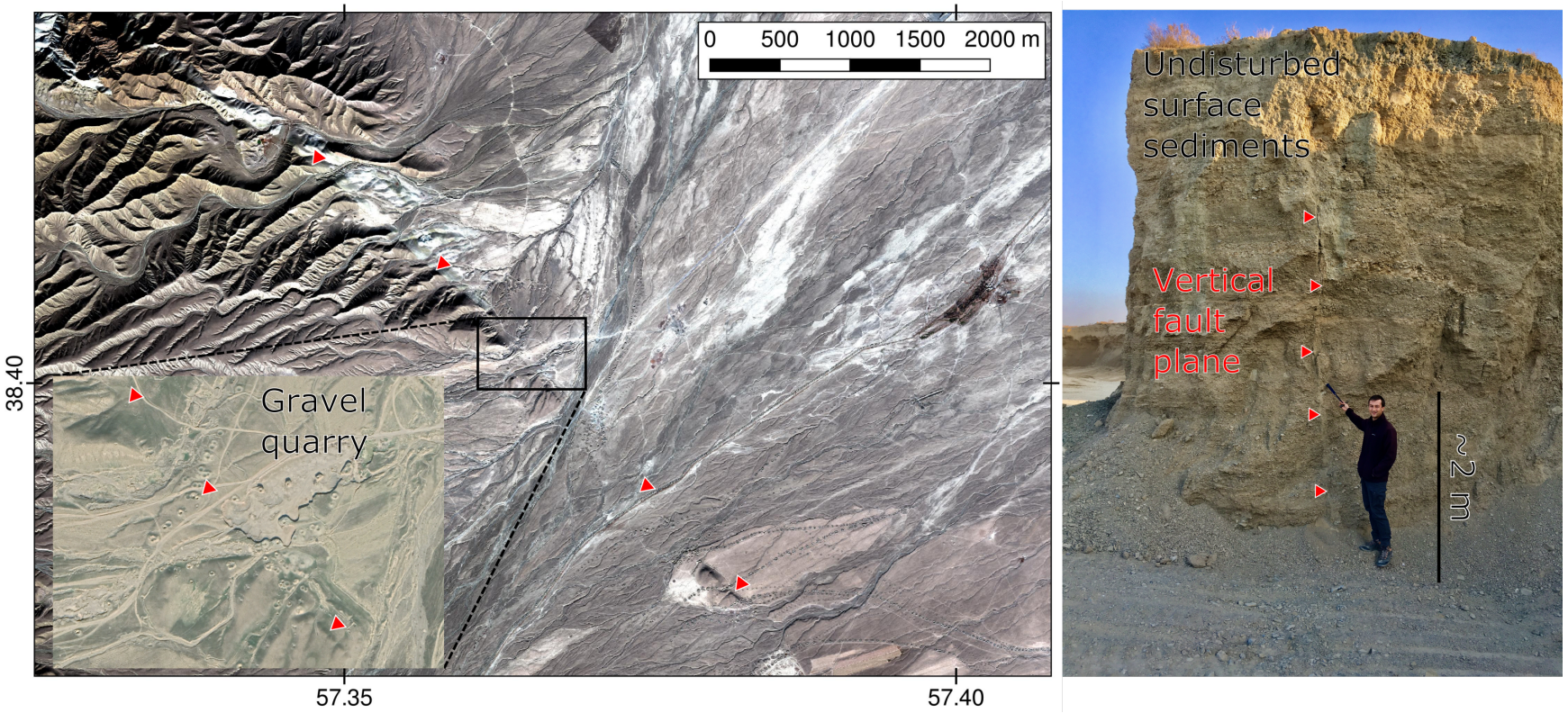


Figure 3.27: Fault cross-section exposure from a gravel quarry that has recently excavated across the fault (location: 38.40091° N, 57.36005° E), photographed during a field campaign to Turkmenistan in November, 2019. The near-surface fault exposure (≈5 m) is dipping vertically, as expected for this relatively mature, predominantly strike-slip fault. This provides evidence to reinforce our modelling strategy, with the primary segment of the MKDF as a vertical structure with additional structures branching of this main fault.

Chapter 4

Towards strain-rate mapping with Sentinel-1 InSAR time-series through the Köpetdag and Eastern Alborz

Nicholas Dodds[1], Simon Daout[2,1], Barry Parsons[1], Richard Walker[1], Marie-Pierre Doin[2]

[1]COMET, Department of Earth Sciences, Oxford University, Oxford, OX1 3AN, UK.
[2]Institut des Sciences de la Terre (ISTerre), Université Grenoble Alpes, Grenoble, France.

Abstract

The extrusion of the South Caspian Basin (SCB), an aseismic block moving independently of its surroundings, is facilitated by conjugate strike-slip motion along the Main Köpetdag Fault (MKDF), Turkmenistan, and the Shahroud Fault Zone (SFZ) in the the Eastern Alborz, NE Iran. However whether strain is accommodated

only by motion along the two major strike-slip faults in the conjugate system, or is partitioned on to other structures inside (i.e. through the East Caspian Lowlands, Köpetdag, or Eastern Alborz) and outside the conjugate system (both to the north of the MKDF, and to the south of the SFZ) remains an important question in establishing the motion of the SCB. To resolve this, we derive regional velocity fields in both the ascending and descending LOS, covering 600 km × 600 km of the region; and decompose these into the east-west (V_E) and sub-vertical (V_{UN}) components. We present a spatially-continuous image of the lateral extrusion of the SCB, with the westward component observed to start abruptly at the Bäherden-Quchan Fault Zone (BQFZ). The extrusion is facilitated by strike-slip motion along the MKDF and SFZ, which have distinct velocity steps resolved in the V_E component of 4–4.5 mm/yr and 5.5–6 mm/yr mm/yr respectively. Projecting this velocity-step to fault parallel motion provides lower-bound fault parallel slip-rates along these faults of 4.8–5.4 mm/yr along the MKDF and 6.0–6.6 mm/yr along the SFZ. However the velocity fields suggest the interior of the SCB is moving faster than this, with ≈-8 mm/yr resolved in the V_E component relative to the Turan platform. We explore the differences in the distribution of deformation across the MKDF and SFZ, and suggest this relates to the rheology of the crust surrounding these fault zones. Furthermore we observe interseismic deformation across numerous structures through the Köpetdag and Eastern Alborz, including distributed deformation across the BQFZ, parallel fault segments in the SFZ, frontal thrusts to the MKDF, and reverse faults in the eastern Köpetdag.

4.1 Introduction

The European Space Agency and European Commission policy on data availability means that Sentinel-1 data is freely available to any type of user. The ≈250 km swath width of the interferometric wide-swath (IW) mode of Sentinel-1, combined with ever-increasing computational power and storage capacity to process the abundance of data captured by the six to twelve-day repeat time, has resulted in recent InSAR-derived geodetic studies investigating tectonics at greater spatial scales (e.g. *Weiss et al.*, 2020). These studies have demonstrated the capability of InSAR satellites to image and measure strain accumulation across, not only, large fault systems, but also the interaction of structures over large tectonic domains. The aim of these projects currently in development is to have spatially and temporally continuous geodetic measurements across whole orogenic belts, even entire continents (e.g. COMET-LiCS, *Lazecký et al.* (2020); FLATSIM, *Durand et al.* (2019)), which can then be integrated with other geophysical and geological data-sets.

Following on from Chapter 3, we expand our InSAR processing footprint over the Köpetdag and the eastern Alborz to cover the entire onshore extent of the South Caspian Basin (SCB) (see Figure 4.1); with three ascending (A057, A159, A086) and three descending tracks (D137, D064, D166) (see Figure 4.2 and 4.3). The longitudinal extent of 51–61° E starts at the Caspian Sea shoreline in the west and continues eastward across the range front of the Köpetdag. This region has a maximum latitudinal extent from 35–41° N, covering greater than 600 km by 600 km of the East Caspian Lowlands, Köpetdag and Eastern Alborz. The size of area is chosen in order to retain the finer-scale details resolved in traditional single-fault focused InSAR studies (e.g. *Walters et al.*, 2013; *Mousavi et al.*, 2015), whilst bridging the gap towards orogen-scale InSAR processing projects currently in development (e.g. *Lazecký et al.*, 2020; *Durand et al.*, 2019).

The primary target within this InSAR coverage is the conjugate fault system

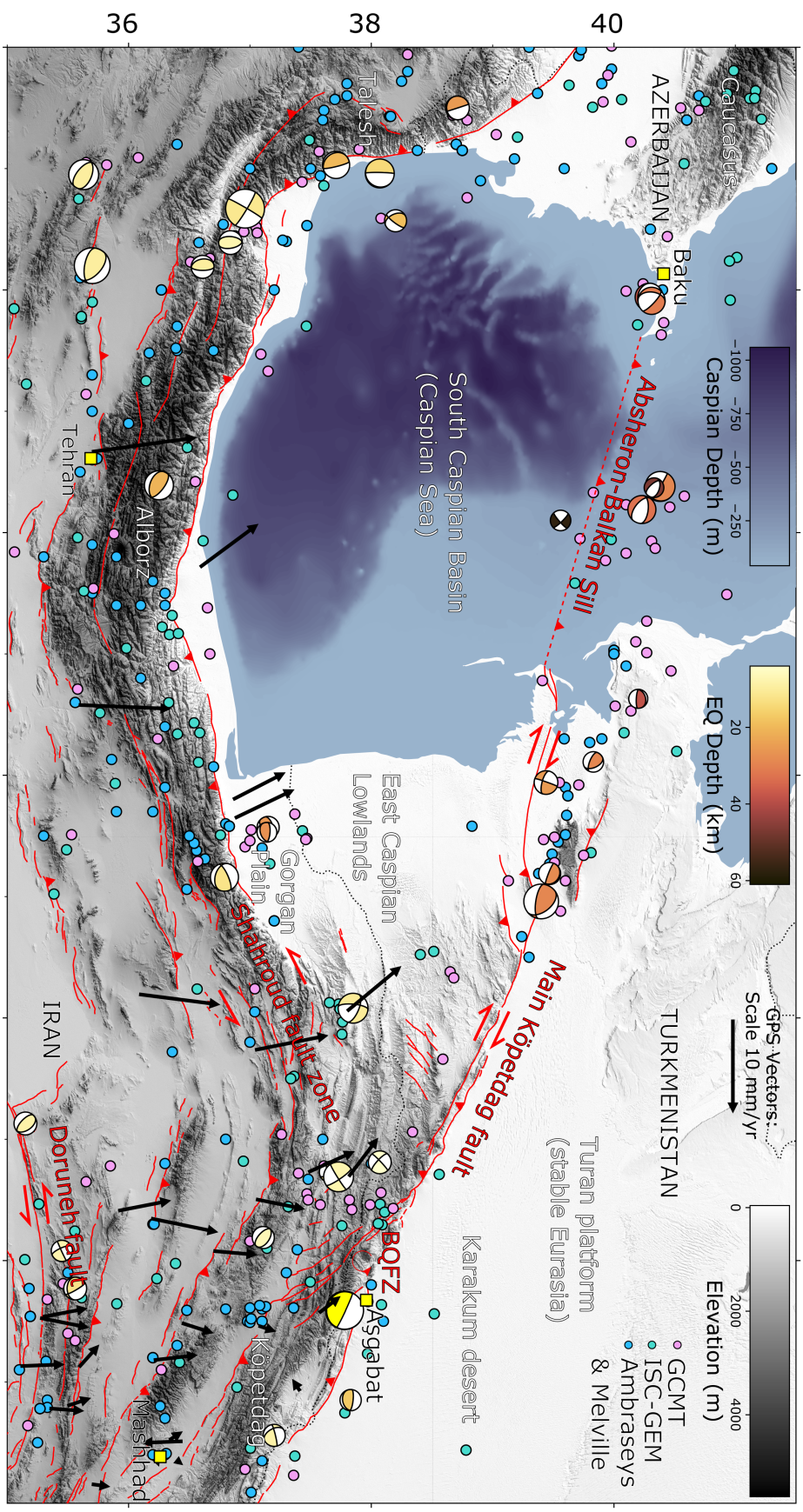


Figure 4.1: An overview of the active tectonics surrounding the South Caspian Basin. The active faults and zones of deformation surrounding the rigid interior of the basin are labeled in red (updated from *Walker et al.* (2021)). Earthquake focal mechanisms and depths are from the Global Waveform Catalogue (*Wimpenny*, 2020); with the addition of the 1948 M 7.3 Aşgabat from *McKenzie* (1972) in yellow. Also shown are earthquake locations from the historical catalogue (3000 BC–1905; in light blue) of *Ambraseys and Melville* (2005), and the instrumental catalogues from ISC-GEM (1906–1975; in light green) and GCMT (1976–2020; in pink). GPS velocities from *Mousavi et al.* (2013) are shown by black arrows. South Caspian bathymetry is from the General Bathymetric Chart of the Oceans (GEBCO; *Weatherall et al.* (2015)). The grey-scaled rendered elevation-hillshade background is from the Shuttle Radar Topography Mission (SRTM).

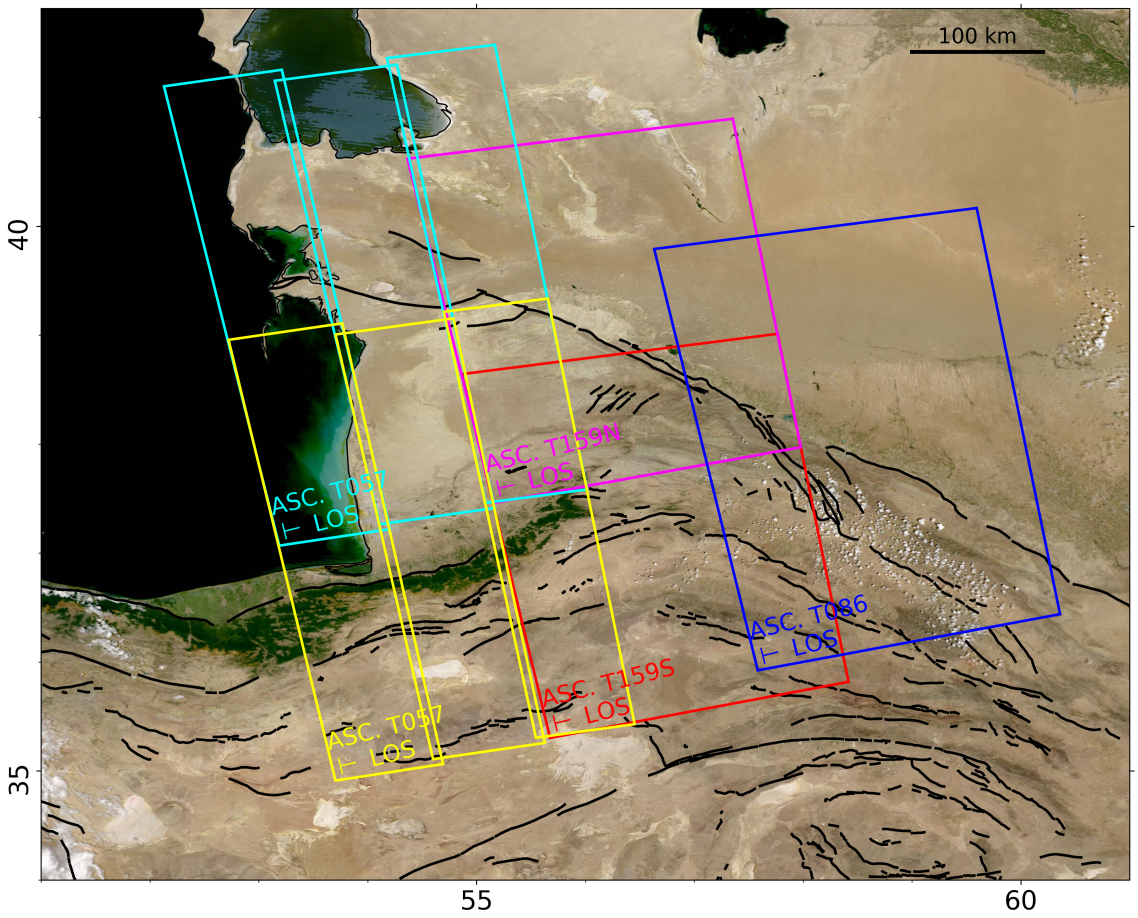


Figure 4.2: Ascending Sentinel-1 InSAR track coverage across the Köpetdag and eastern Alborz (subswath outlines are shown for track 057 adjacent to the Caspian due to processing issues detailed in Section 4.3.2). Track and frame outlines are labelled in colour, including the along-track frame overlaps. Active faults across NE Iran are delineated by black lines (updated from *Walker et al.* (2021)). The background image is low cloud-cover MODIS Terra optical imagery.

defined by the right-lateral MKDF and left-lateral Shahroud Fault Zone (SFZ) (see Figure 4.1). These conjugate faults facilitate the extrusion of the SCB to the northwest (e.g. *Jackson et al.*, 2002; *Copley and Jackson*, 2006; *Walker et al.*, 2021), which is an aseismic block moving independently of its surroundings (e.g. *Jackson et al.*, 2002; *Djamour et al.*, 2010). Previous geodetic (e.g. *Walters et al.*, 2013; *Mousavi et al.*, 2013, 2015; *Djamour et al.*, 2010) and geological (e.g. *Walker et al.*, 2021; *Javidfakhr et al.*, 2011) investigations have attempted to resolve the motion of the SCB by measuring the motion across the bounding faults (MKDF

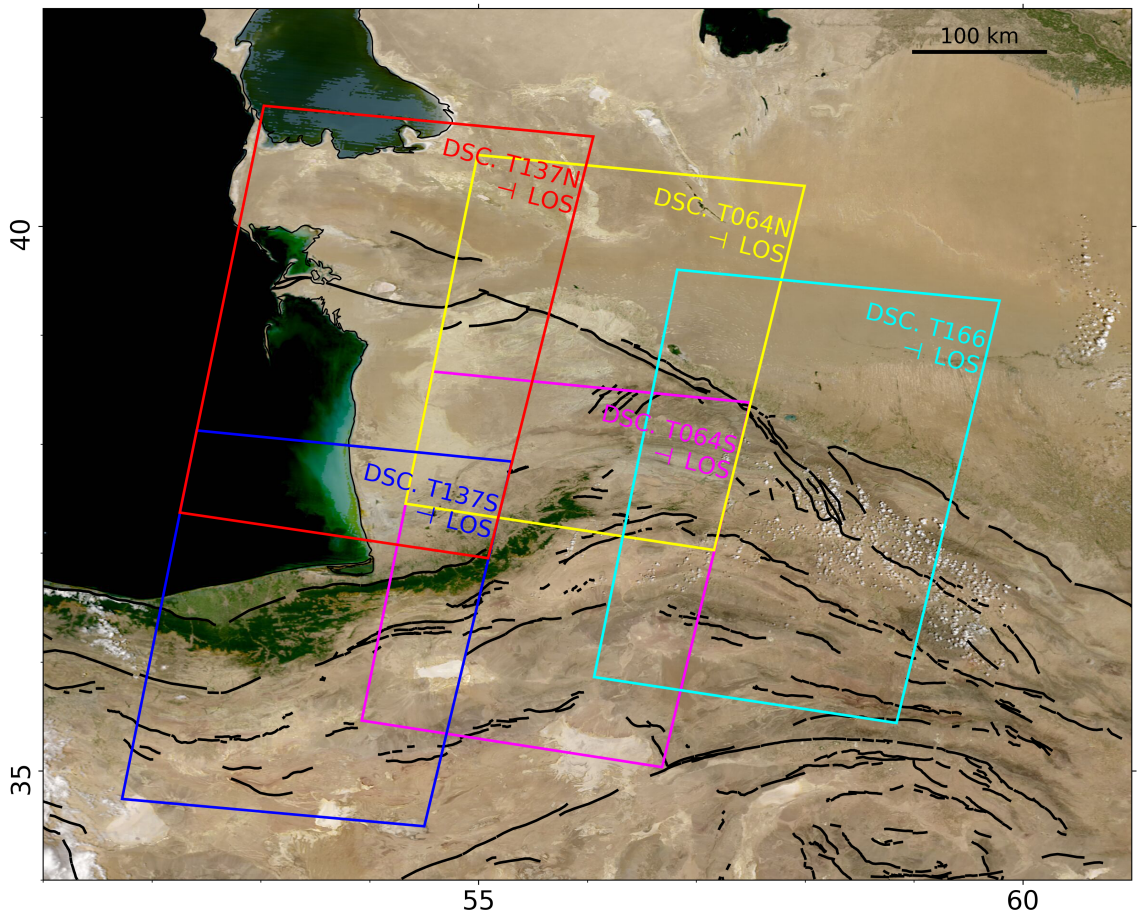


Figure 4.3: Descending Sentinel-1 InSAR track coverage across the Köpetdag and eastern Alborz. Track and frame outlines are labelled in colour, including the along-track frame overlaps. Active faults across NE Iran are delineated by black lines (updated from *Walker et al.* (2021)). The background image is low cloud-cover MODIS Terra optical imagery.

and SFZ), and projecting the motion onto the SCB (e.g. *Walker et al.*, 2021; *Copley and Jackson*, 2006; *Jackson et al.*, 2002; *Mousavi et al.*, 2013). However whether strain is accommodated only by motion along the two major strike-slip faults in the conjugate system, or is partitioned on to other structures inside (i.e. through the East Caspian Lowlands, Köpetdag, or Eastern Alborz) and outside the conjugate system (both to the north of the MKDF, and to the south of the SFZ) remains an important question (e.g. *Jackson et al.*, 2002; *Mousavi et al.*, 2013). This information is required to establish the direction, rate of motion and pole of rotation of the SCB. Therefore we derive regional-scale velocity maps from Sentinel-1 InSAR time-series

to resolve the distribution of deformation across the conjugate fault system.

In addition there are numerous other active tectonic structures within the InSAR coverage, which present a significant seismic hazard to NE Iran and Turkmenistan. These include the westward extension of the MKDF through to the Absheron-Balkan Sill in the Caspian Sea, where dextral shallow-crustal strike-slip faulting connects to the deeper subduction-style kinematics proposed at the northern boundary of the SCB (*Jackson et al.*, 2002); the Bäherden-Quchan fault zone (BQFZ in Figure 4.1), a distributed network of strike-slip faults within the Köpetdag interior that transfers strain by vertical-axis rotation along parallel faults and along-strike extension (*Hollingsworth et al.*, 2006); and numerous active thrust fault systems in the eastern Köpetdag that have hosted historically devastating earthquakes (*Hollingsworth et al.*, 2006).

4.2 InSAR processing and time-series generation

We process Synthetic Aperture Radar (SAR) data from the ESA Sentinel-1 data archive using the New Small Baseline Subset (NSBAS; *Doin et al.* (2011, 2015); *Grandin* (2015); *Grandin et al.* (2016)) processing chain (which uses the ROI_PAC software; *Rosen et al.* (2004)). As mentioned above, three ascending (A057, A159, A086) and three descending tracks (D137, D064, D166) are processed. Tracks are processed in interferometric wide-swath (IW) mode, with a swath width of 250 km (in the range direction). Tracks with high latitudinal extents (>3.5°) are divided into overlapping frames along track due to computational processing and storage limitations, ensuring that frame overlaps are greater than 1° (≈110 km).

The interferometric networks span the entire Sentinel-1 archive (October, 2014–December, 2020) for each track, although there are instances in which networks are cropped due to acquisition gaps, data corruption, or poor quality data. For each frame, interferograms are generated with 40 looks in range and 8 looks in the

azimuth direction (resulting in a horizontal resolution of 160 m × 120 m for each pixel). The range of perpendicular baselines for Sentinel-1 data is generally very low, with an RMS orbital tube of ≈100 m. Initially the interferometric network contains a wide range of temporal baselines from 6 days to >1 year, although subsequently short temporal baseline interferograms (<13 days) are removed during an iterative network refinement strategy during the time-series inversion detailed below. The interferograms generally have excellent spatial and temporal coherence, which contributes to the very high fraction of pixels successfully unwrapped in each frame in the next stage of processing.

Unwrapping is performed using a specific routine within the NSBAS processing chain, following *Grandin et al.* (2012) and *Daout et al.* (2020). The unwrapping procedure is as follows: 1) Prior to unwrapping, we remove the ERA5 model tropospheric phase-delay from interferograms to reduce the phase variability in interferograms (subsequently this removed phase-delay is reintroduced after unwrapping); 2) The amplitude of the interferograms is replaced by the phase-colinearity, as defined by *Pinel-Puysségur et al.* (2012); 3) We use a coherence-dependent filter in triangular sliding windows, calculated by the weighted average of the complex phase by the colinearity (*Doin et al.*, 2011); 4) We impose an unwrapping path that goes from high to low coherence areas (*Grandin et al.*, 2012); 5) Following this, we compute the phase difference between the unwrapped phase and a set of IFGs obtained with the Goldstein-Werner filter (*Goldstein and Werner*, 1998) that filters less heavily. The residual is assumed to be between $-\pi$ and π, and added back to the unwrapped phase (*López-Quiroz et al.*, 2009; *Chen et al.*, 2015). 6) Re-introduce the phase variability removed using the ERA5 tropospheric models prior to time-series inversion (*Daout et al.*, 2020).

4.2.1 Time-series inversion, interferometric network refinement and tropospheric phase-delay corrections

We perform an iterative time-series inversion and network refinement procedure to improve the quality of the tectonic deformation signals, and reduce the effect of time-series biases, atmospheric signals and phase-misclosure on our output LOS velocity time-series rate-maps (the final interferometric networks for each frame are shown in Supplementary Figures 4.39 to 4.45). At each stage of the refinement procedure, we ensure that the interferometric network remains connected prior to time-series inversion. The time-series of LOS displacements is reconstructed using the NSBAS method (*Doin et al.*, 2015), which inverts the phase delays of unwrapped IFGs, pixel by pixel, to solve for the incremental phase delay of each date relative to the preceding date, with the total phase delay then obtained by adding incremental phase delays relative to the first acquisition (which is set to zero). Regularisation allows for an adjustment of disrupted sections of the time-series for pixels where the inversion is under-determined. However very few pixels are affected, permitting the use of a very low smoothing coefficient due to the temporal sampling ensured by the Sentinel-1 acquisition frequency and excellent unwrapping coverage. The inversion is temporally referenced to the earliest date in the time-series and spatially referenced to a stable non-deforming zone, located far away from any known active faults or deformation sources associated with anthropogenic disruption. Following this we compute the average pixel velocity in the LOS with a linear regularization function of the form $\phi_i = V \times t_i$, where ϕ_i is the pixel phase change between time t_i and the first epoch, and V is the best estimate of the pixel velocity in the LOS.

The first iteration of the time-series inversion procedure uses the approach of *López-Quiroz et al.* (2009) to map inconsistencies in the interferometric network using the root-mean-square (RMS) misclosure of individual pixels in the time-series. This provides a method to check for unwrapping errors, with problematic interferograms

or epochs discarded or corrected, depending on the network connectivity. The next time-series inversion iteration re-runs the inversion using this refined network, with only low RMS-misclosure (<2.0 mm) interferograms retained in the network. Following this, another time-series inversion iteration removes short-baseline interferograms from the network (in this case excluding temporal baselines of <13 days) to minimise possible biases associated with short temporal baselines. This follows recent observations that asymmetrical cyclical surface deformation cycles, combined with systematic decorrelation of the radar phase in specific portions of these cycles, introduces biases in the LOS velocity time-series inversion (*Ansari et al.*, 2020; *Daout et al.*, 2020).

The next stage implements tropospheric phase-delay corrections. These phase propagation delays through the troposphere are the main limiting factor for measuring millimetric displacements of ground motion when deriving estimates of interseismic strain accumulation with InSAR (*Doin et al.*, 2009). For all the frames processed, the application of GACOS corrections (derived from HRES-ECMWF atmospheric models; *Yu et al.* (2017, 2018b,a)) and ERA5 corrections within the NSBAS processing chain (methods in *Doin et al.* (2009); *Jolivet et al.* (2011)) are tested separately using the methods described in Chapter 3. The final iteration uses performance analysis metrics (also described in Chapter 3) to further refine the interferometric network. We remove interferograms and epochs with poor performance from the networks, defined as: a negative gradient when computing a linear regression to the interferometric phase versus the tropospheric phase-delay correction; negative correlation (Pearson's R coefficient) between the interferometric phase and the tropospheric model; or a significant increase in the standard deviation of the phase variability introduced by the tropospheric model correction.

The resulting products used for subsequent analysis are spatial maps of the average surface LOS velocity in mm/yr (all individual frames are presented

in Supplementary Figures 4.46 to 4.53). Uncertainty maps (in mm/yr) are also computed during the iterative time-series decomposition, equal to the root-mean-square of the misfit of the cumulative displacements in the time-series to the linear fit. Prior to subsequent analysis, the output time-series LOS velocity maps are masked using the final evaluation of the RMS misclosure of individual pixels in the time-series. For this we use a pixel masking threshold of 2.5 mm/yr, calculated for all interferograms as the RMS of the observed phase and the reconstructed phase from inverted successive phase delays (*López-Quiroz et al.*, 2009).

4.2.2 Whether to remove tropospheric phase-delay model corrections from time-series analysis?

Previous InSAR studies in this region noted difficulty with tropospheric delays estimated from atmospheric models; *Walters et al.* (2013) used Envisat's Medium-Resolution Imaging Spectrometer (MERIS) instrument to provide a direct measurement of the water vapour content in each epoch of their InSAR time-series, stating that the proximity to the Caspian Sea was the probable cause of the high magnitude of tropospheric path-delays. The aim of tropospheric phase-delay corrections is to mitigate noise in the displacement time-series introduced by phase propagation delays through the troposphere. At a pixel level, these model corrections aim to reduce the scatter in the displacement time-series to improve the estimation of the linear trend (the LOS velocity) and associated variance. From a scene or frame-scale perspective, we analyse the performance of these corrections on the time-series using the metrics detailed previously. At both these scales, both tropospheric model corrections (GACOS and ERA5) in this region performed satisfactorily with regard to the gradient and correlation metrics, although some corrections on the descending tracks resulted in an increase in standard deviation (Supplementary Figures 4.54 and 4.55). Both GACOS and ERA5 performed very

similarly for all tracks (an example is presented in Supplementary Figure 4.56). However, when examining the overlap region across tracks in the tropospheric-model corrected LOS time-series, we noticed differences in the LOS time-series at an intermediate scale.

These differences are observed in several settings within the time-series velocity maps. In Figures 4.4d and 4.5d we present several examples; these include difference along topographic features, such as the Köpetdag range front, and also long-wavelength effects in low relief areas, including the East Caspian Lowlands and the Karakum Desert. In some scenes the tropospheric model corrections increase the correlation of the LOS time-series velocity with topography, and introduced distinct phase-elevation relationships that did not exist in the data prior to correction (Figures 4.4 and 4.5, b and c). These effects are, to a degree, expected with tropospheric model correction (e.g. changes to velocity-elevation relationships). However we observe opposite behaviour and inconsistency within across-track overlaps, which do not exist prior to correction (Figure 4.6). These signals are in proximity to structures of interest, and also assumed non-deforming regions, and so we decided to use non-model corrected time-series in the subsequent analysis. These above effects could possibly reflect the remoteness of the region and limited data input into global weather models, as well as previously noted difficulty with water vapour from the adjacent Caspian Sea (*Walters et al.*, 2013). There are examples of track overlaps where the GACOS corrections do not introduce different signals (Figure 4.7), however the inconsistency in the behaviour of the corrections we observe across the entire processing region means that we decided not to use tropospheric model-corrected time-series for subsequent analysis. The implicit cost in not using these tropospheric corrections will be a possible small increase in the RMS uncertainty in the linear time-series fits.

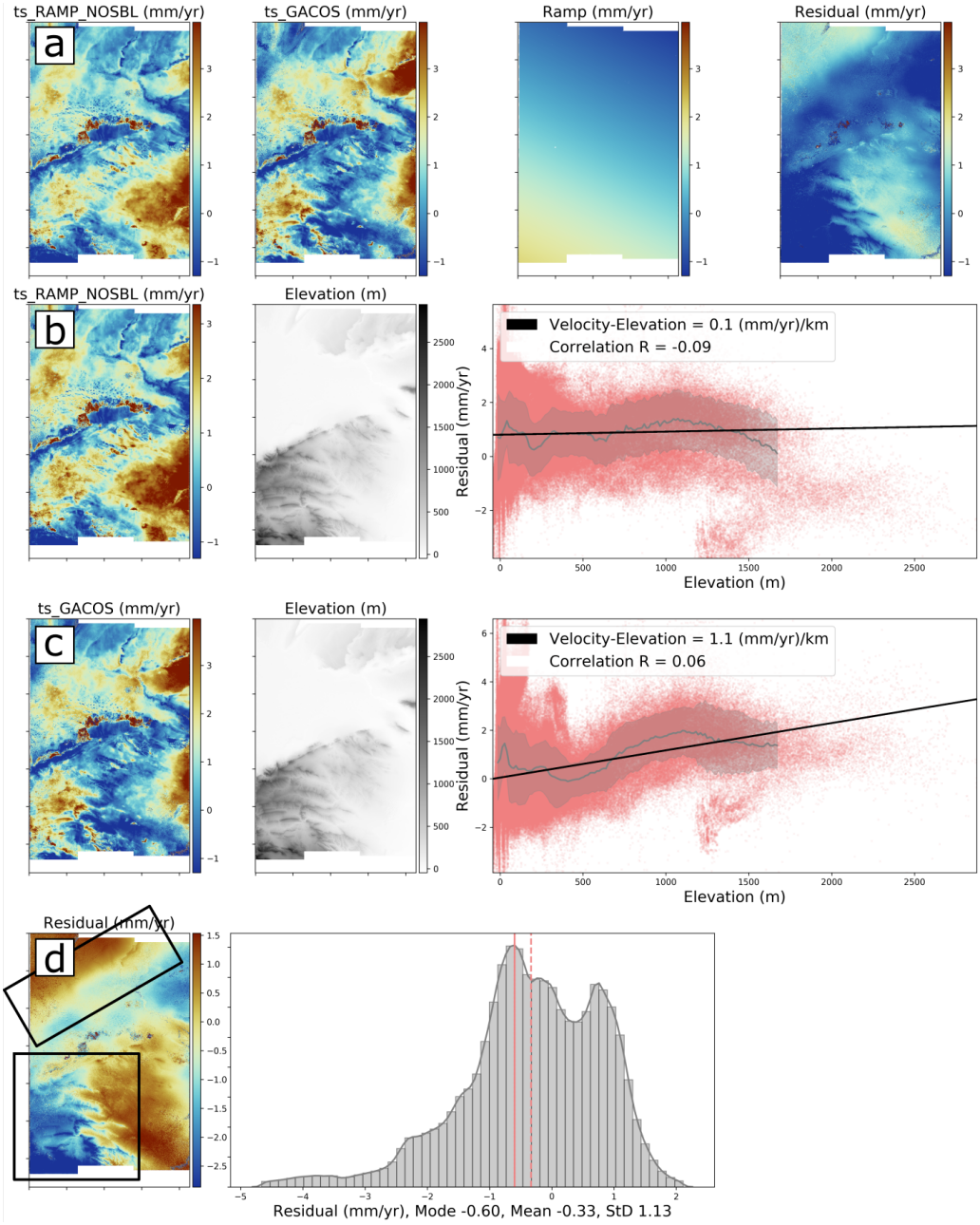


Figure 4.4: Comparison of uncorrected and GACOS corrected time-series velocity maps for D064N in radar geometry. a) The output time-series for D064 for the uncorrected (not including short baseline IFGs), the GACOS corrected time-series, a ramp estimated to tie these time-series together, and the residual of the overlap. b) and c) are the output uncorrected and GACOS corrected time-series plotted against elevation; note the positive velocity-elevation relationship introduced by the GACOS correction. d) The residuals (note the colour scale limits are compressed versus the top row) show differences introduced by the tropospheric corrections with boxes showing a phase-elevation correlated signal (lower left), and an unexplained abrupt velocity gradient in the Karakum Desert (upper), with a normalised frequency histogram of the residuals also shown.

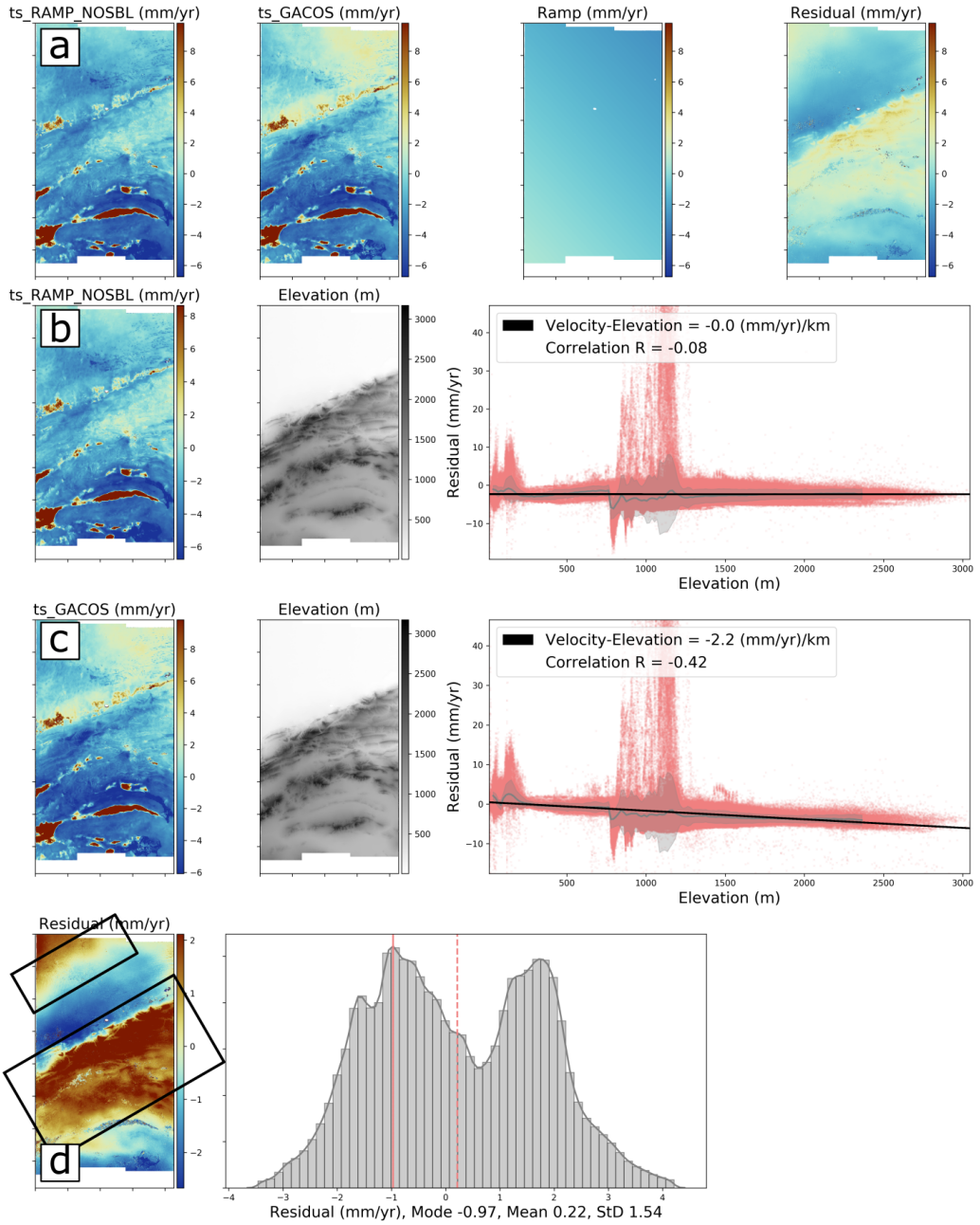


Figure 4.5: Comparison of uncorrected and GACOS corrected time-series velocity maps for D166 in radar geometry. a) The output time-series for D166 for the uncorrected (not including short baseline IFGs), the GACOS corrected time-series, a ramp estimated to tie these time-series together, and the residual of the overlap. b) and c) are the output uncorrected and GACOS corrected time-series plotted against elevation; note the positive velocity-elevation relationship introduced by the GACOS correction, although with a different sign (negative) to the relationship in the adjacent track in Figure 4.4 (note both time-series are spatially reference to the far north of the image). d) The residuals show differences introduced by the tropospheric corrections with boxes showing a phase-elevation correlated signal (lower), and an unexplained abrupt velocity gradient in the Karakum Desert (upper).

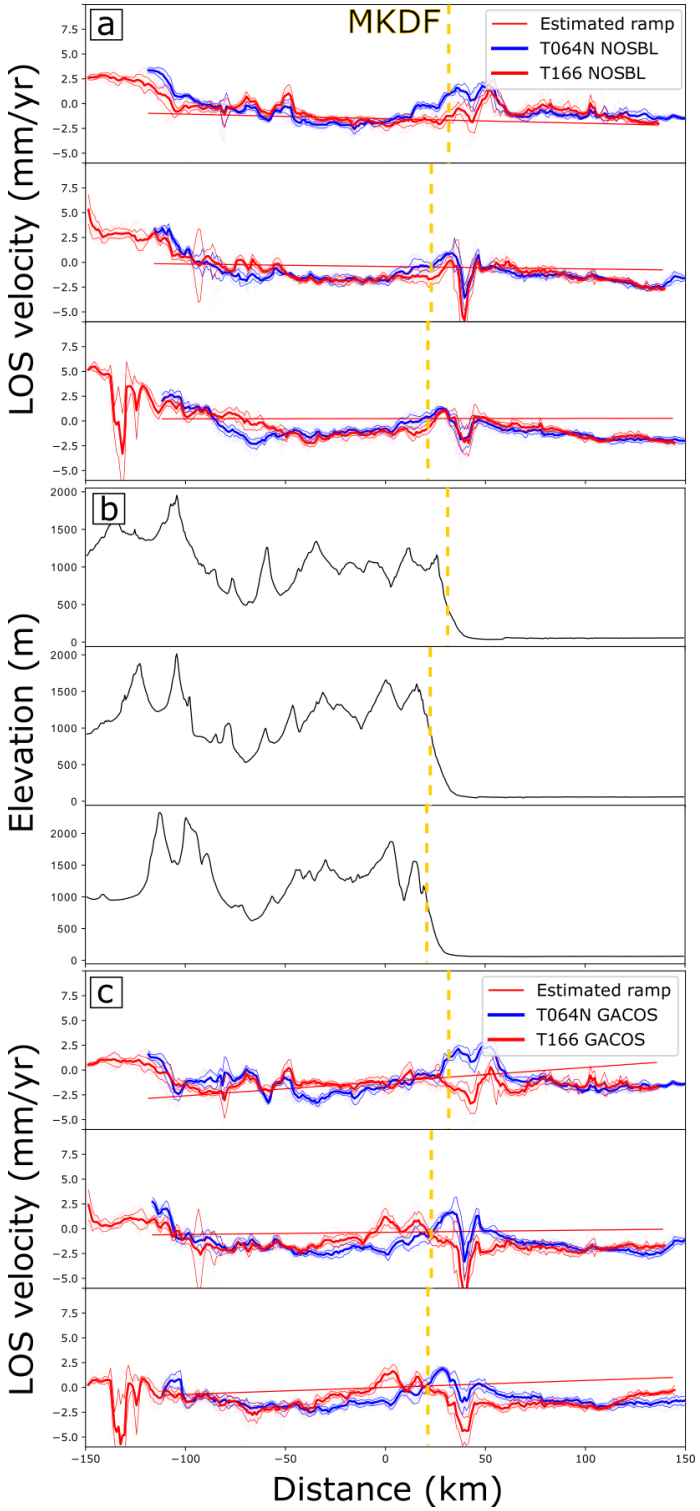


Figure 4.6: Across-track overlap profiles for D064-D166 before and after GACOS correction. Three profiles are shown, all 300 km in the azimuth direction with a swath width of 20 km; D064 LOS data in blue, D166 LOS data in red (red line shows the linear trend removed for the profile comparison). a) LOS time-series prior to GACOS correction shows good agreement in all profiles. b) Topography in each swath shown in black (sliding median). c) LOS time-series after GACOS correction has divergence of the profiles in several location, most notably along the Köpetdag range front (with location of the MKDF shown by the orange dashed line).

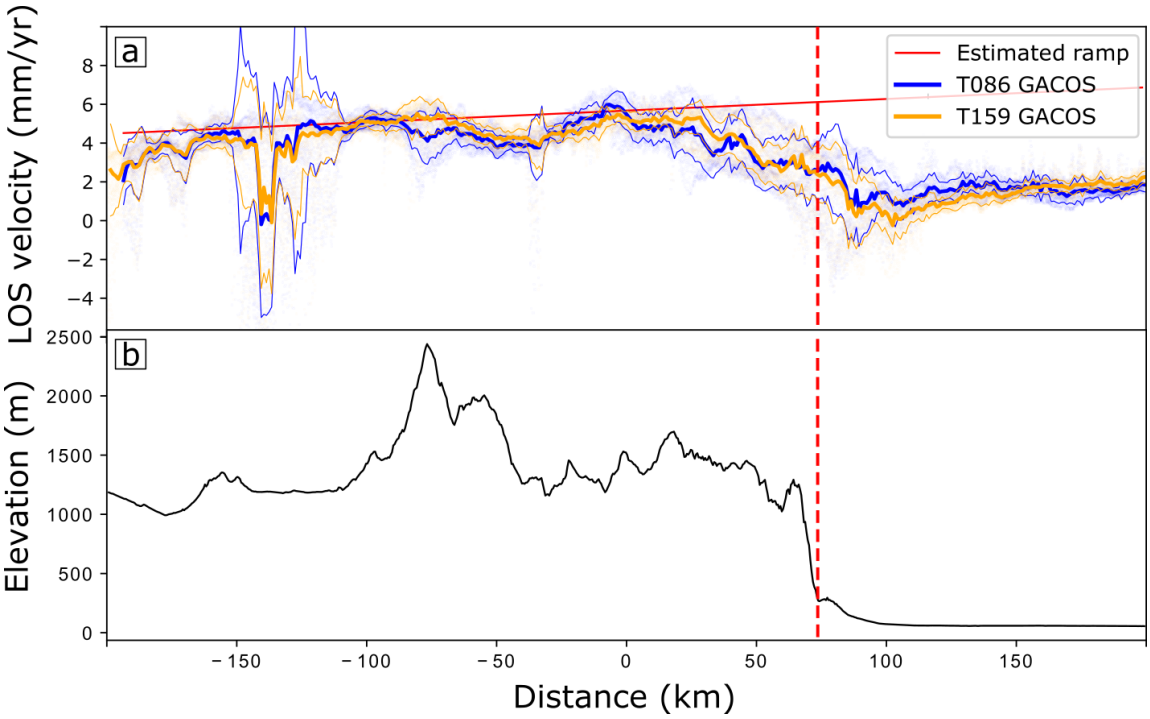


Figure 4.7: Across-track overlap profile for A159-A086 with GACOS correction. The profile is 400 km in the azimuth direction with a swath width of 40 km; A159 LOS data in orange, D166 LOS data in blue (red line shows the linear trend removed for the profile comparison). a) the LOS velocity fields in these tracks show excellent agreement after GACOS correction (in contrast to Figure 4.6), b) topography in the profile swath; the red dashed line shows the location of the MKDF in the overlap region.

4.3 Generating a regional-scale velocity field

4.3.1 Combining frames along-track using overlaps

When designing the frame-based division of our InSAR processing, we ensured that frame overlaps are >1°. This is much greater than automatic frame-based processors such as LiCSAR, which uses single burst overlaps ≈20 km (*Lazecký et al.*, 2020). This decision was made to maximise the fidelity of the merging of frames along track, particularly to ensure the reduction of "hinging" along the frame overlap zone, which propagates erroneous ramps predominantly in the azimuth direction. This was also based on the prior knowledge of the sparsity and poor distribution of GPS stations within our footprint. There are no GPS stations north of the

Iranian-Turkmen border, which made it unlikely that we could use to help in referencing the individual frames. Horizontal and vertical GPS velocities can be used through interpolated fields to reference InSAR LOS velocity fields both along and across tracks to a common, known reference frame (e.g. *Weiss et al.*, 2020). Prior to merging, any extreme positive or negative velocity in the frames are masked to mitigate biasing during the ramp inversion. This employs a strategy to crop severely skewed distributions, which calculates a histogram of the LOS and crops the distribution to the closest value to the mode of either the 1st/99th percentile or the mode $\pm 2\sigma$.

To merge frames along-track, we solve for the best-fitting offset and planar tilt that ties the southernmost frame to the adjacent northern frame. This calculates the residual between the along-track frame overlaps and inverts for a planar tilt and offset of the form $ax + by + c$; with a pixel weighting equal to the square root of the sum of the squares of the uncertainty in the overlap region for each frame. We analyse the histogram distribution of the residual in the overlap zone after removing this planar tilt. This planar tilt is then extrapolated to "tie" the southernmost track to the northern frame. Inside the overlap region itself, we use a linear fade-weighting for the LOS velocity of pixels by calculating their proximity in the azimuth direction to the overlap boundaries (see illustration in Figure 4.9). This mitigates the introduction of velocity steps in the LOS along the frame boundaries in the merged velocity fields. This process is shown for descending track D064 and ascending track A159 in Figures 4.8 and 4.9. The histogram of the residuals after the planar tilt is applied shows that the merging performs excellently on the large along-track overlap regions, with the residuals below the noise level ($\approx$1 mm/yr) of the LOS time-series data.

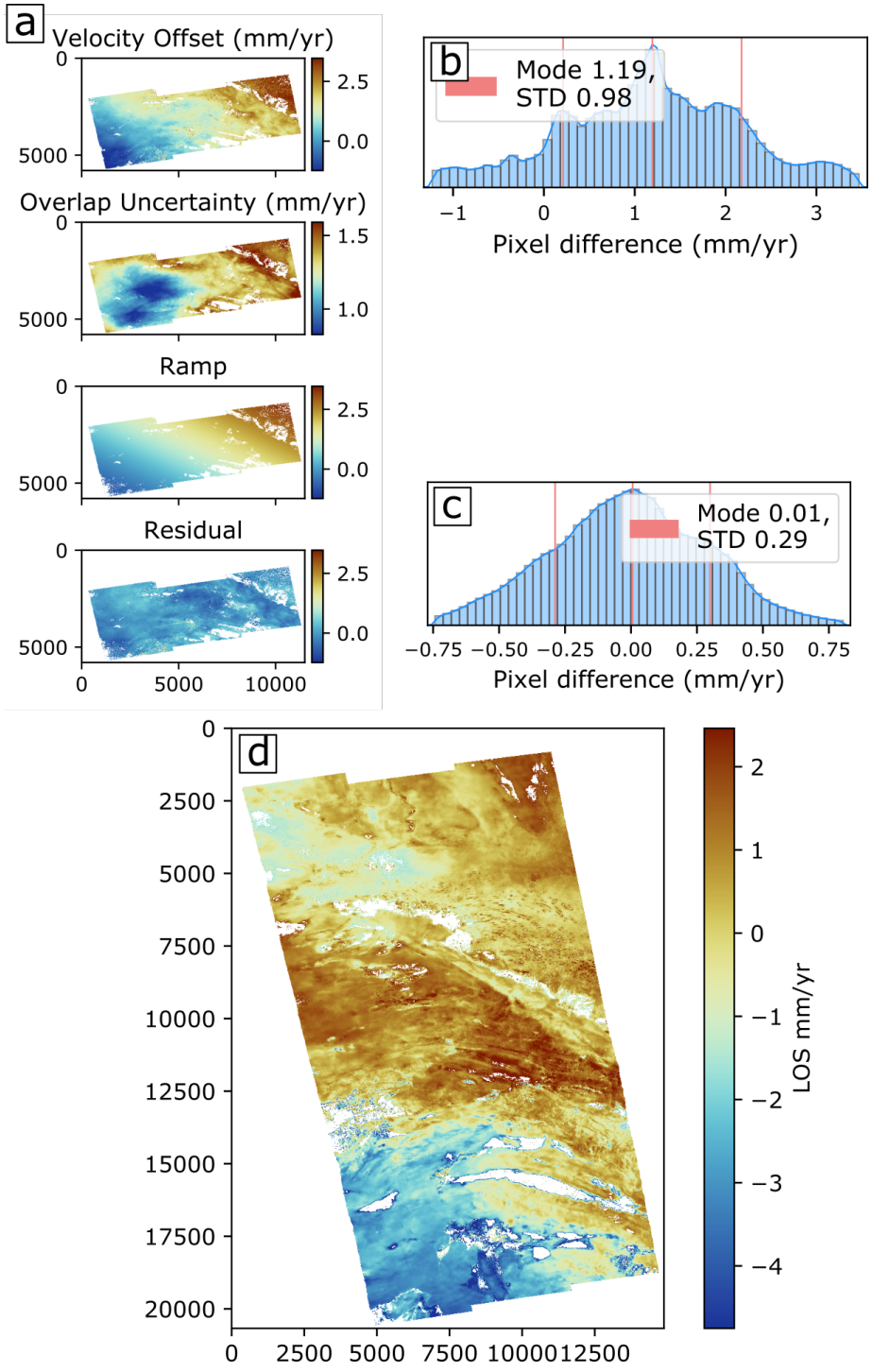


Figure 4.8: Along-track frame merging strategy and results for ascending track 159. a) The overlap residual is calculated in the overlap region of the two adjacent frames, to which a planar ramp is estimated, and subsequently removed from the data to tie the southern frame to the northern frame. b) and c) are the histograms of the residuals prior to and after the ramp estimation. d) The final frame-merging result, with no obvious steps in the LOS velocity along frame boundaries.

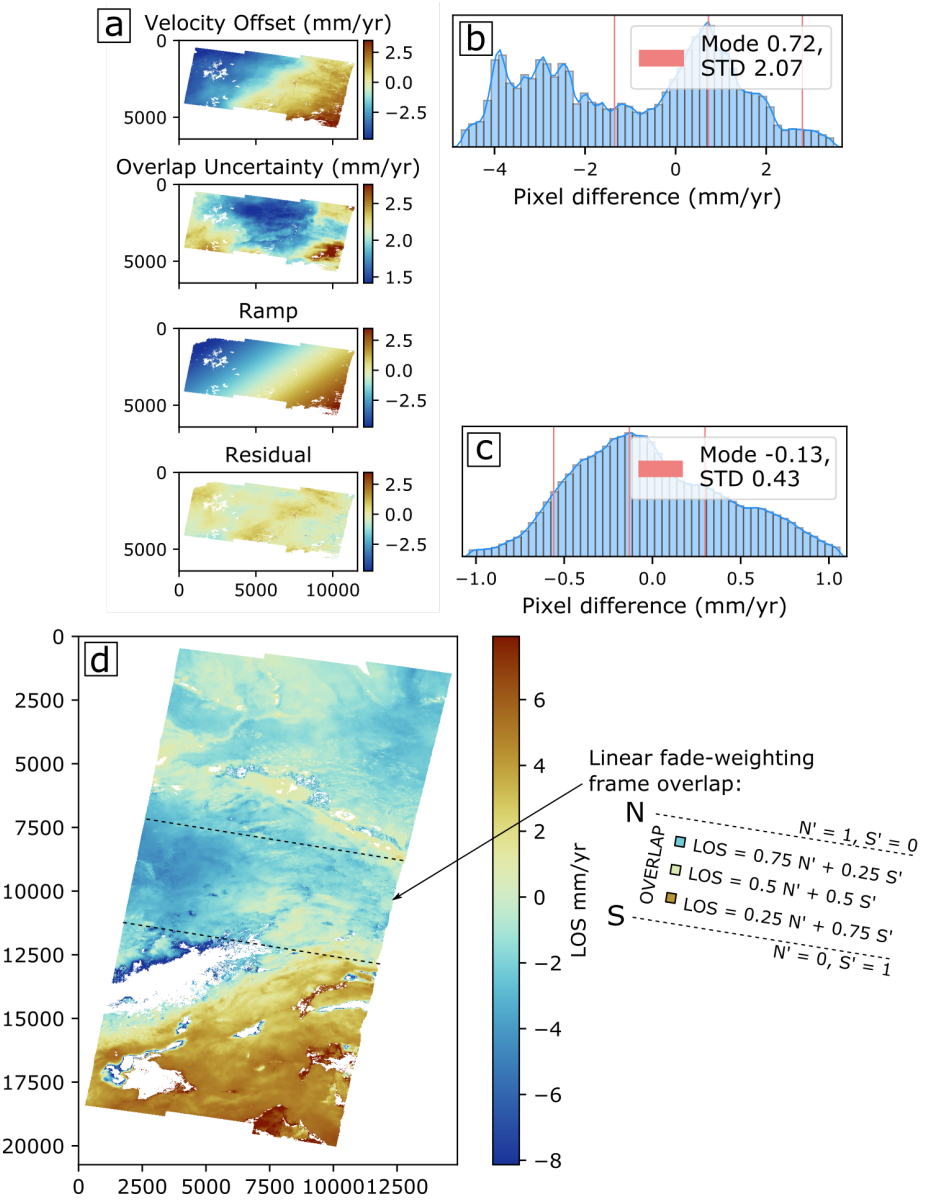


Figure 4.9: Along-track frame merging strategy and results for descending track 064. a) The overlap residual is calculated in the overlap region of the two adjacent frames, to which a planar ramp is estimated, and subsequently removed from the data to tie the southern frame to the northern frame. b) and c) are the histograms of the residuals prior to and after the ramp estimation. d) The final frame-merging result, with no obvious steps in the LOS velocity along frame boundaries.

4.3.2 Reduction of frame extent along the Caspian Sea

For the ascending (A057) and descending (D137) tracks adjacent to the Caspian Sea, it was very difficult to both generate time-series and subsequently reference

the velocity fields to a common, known reference frame. Therefore at this stage, we decide to continue our analysis without the southernmost frame of track D137 (D137S; unwrapping and referencing issues) and track A057 (time-series generation issues). These tracks cover the highest topography in the Eastern Alborz; adjacent to this is a humid, densely vegetated forested region along the northern margin of the topography between the mountain range and the Caspian Sea (the Caspian Sea is noted to be a problematic source of tropospheric water vapour observed by *Walters et al.* (2013)); and finally surrounding the southeastern corner of the Caspian Sea is the Dasht-e Gorgan (Gorgan Plain), an intensely farmed agricultural region.

The combination of the high topography, dense vegetation and agriculture are destructive to signals observed with InSAR. There is an east-west band defined by these adjacent features that has very low coherence. We attempted to manage this by restricting the time-series to times when both satellites in the Sentinel-1 constellation were acquiring data (2017–present). This allowed us to generate a time-series with a high-density of short-baseline IFGs to initially check for unwrapping errors. However, unwrapping paths have to find a continuous route through the east-west band of topography, vegetation and agriculture, often along narrow valleys. With D137S, we successfully managed to generate a time-series and unwrap using this strategy, however the subsequent frame merging procedure becomes increasingly difficult.

The along-track frame merging with the tracks adjacent to the Caspian Sea, especially so with D137, relies on a very small along-track frame overlap region (approximately 100 km by 100 km; see Figure 4.3). This is because the southeastern corner of the Caspian Sea cuts across two subswaths, only leaving the easternmost part of the track to merge with. In addition, part of the frame overlap region contains the rapidly subsiding Gorgan Plain (subsiding at >60 mm/yr in the LOS; GPS station location GRGN in the Gorgan Plain in Figure 4.1 is subsiding at ≈ 70 mm/yr, personal communications with Dr. Z. Mousavi), which biases the ramp

estimation unless we remove the data. The result of this is that the frame-merging here is susceptible to introducing erroneous tilts in both the azimuth and range direction (see Figure 4.10). Nevertheless in future research, we aim to integrate the full extent of tracks A057 and D137. These contain the deformation within the East Caspian Lowlands and the westernmost part of the onshore extension of the SCB (i.e. closest to the basin interior).

4.3.3 Comparison of across-track overlaps

The comparison of across-track overlaps is a more complicated process than along-track frame overlaps. The IW acquisition mode of Sentinel-1 captures three sub-swaths using the TOPSAR (Terrain Observation with Progressive Scans SAR) mode. This combines steering the beam in both the range direction (ScanSAR), and also backward to forward in the azimuth direction. The ScanSAR steering results in a variation in incidence angle from 29.1°– 46.0° across the 250 km wide swath. Therefore there is a difference in the LOS vector from the change in incidence angle, θ, in across-track overlaps (the difference is 8–11°; in comparison, the variation in heading angle, ϕ, is only ≈0.1° over the same length scale). The across-track overlap extent is approximately the same width as a single Sentinel-1 subswath (≈110 km).

Examining the definition of the projection of the velocity into the LOS, V_{LOS}, of a pixel moving in Cartesian reference frame ($V_{E,N,U}$ are the pixel's velocity in the east-west, north-south and vertical directions respectively),

$$V_{LOS} = -V_E \cos\phi \sin\theta + V_N \sin\phi \sin\theta + V_U \cos\theta\,, \tag{4.1}$$

we can explore the effect of the difference of incidence (θ) and heading angle (ϕ) on the LOS velocity in the overlap region. In the higher incidence overlap (where θ approaches 46.0°), the LOS is increasingly sensitive to east-west horizontal

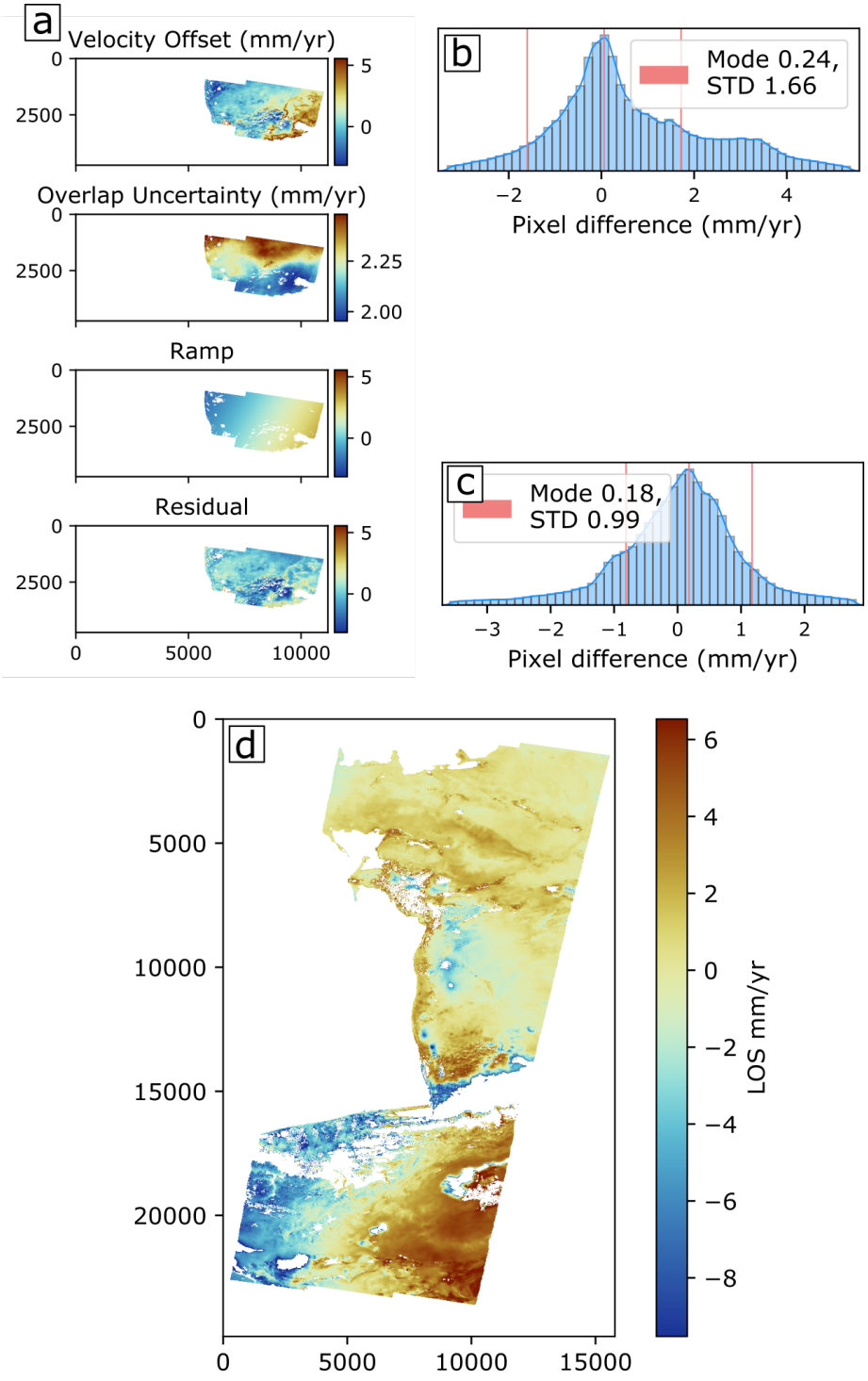


Figure 4.10: Along-track frame merging strategy and unsuccessful results for descending track 137 which borders the Caspian Sea. a) The overlap residual is calculated in the overlap region of the two adjacent frames, to which a planar ramp is estimated, and subsequently removed from the data to tie the southern frame to the northern frame. b) and c) are the histograms of the residuals prior to and after the ramp estimation. d) The final frame-merging result, showing a distinct ramp in the range-direction in the southern frame. For D137 this process is erroneous primarily due to the small overlap region (approximately 4,000×2,000 pixels, in comparison to 10,000×5,000 pixels in Figures 4.9 and 4.8, and also rapid subsidence in the overlap region.

displacements ($\sin\theta$ term in the V_E component of V_{LOS}). Whilst in the lower incidence overlap (29.1°), the LOS is increasingly sensitive to vertical displacements ($\cos\theta$ term in the V_U component of V_{LOS}). Note the sensitivity of the V_{LOS} to the V_N component is very low (due to the $\sin\phi\sin\theta$ term being very small) in both overlaps so we can ignore this effect. Therefore for any pixel located in an across-track overlap region, there is an expected but unknown change in the LOS velocity within each track depending on the true velocity of the pixel. However without external control from GPS velocity fields, it is difficult to correct for this expected variation (some methods exploration is provided in Appendix A).

Despite these differences, directly comparing the LOS velocity fields in across-track overlaps (without accounting for differences in incidence angles) provides useful information. To evaluate the LOS variability in the overlap region, we perform a similar procedure to the along-track frame merging process. We invert for a planar ramp in the across-track overlap residual and remove this trend, before analysing the histogram distribution of the residuals. Primarily we use these to confirm fidelity of the along-track frame-merging, which can introduce tilts in the azimuth direction, with the results shown in Figures 4.11, 4.12 and 4.13. This shows that for the central and eastern across-track overlaps for both ascending and descending frames, the phase variability is <1 mm/yr which is at approximately the noise threshold of the LOS velocity maps. The across-track overlaps are also used to evaluate changes to the LOS velocity maps at each stage of the network refinement procedure, as well as showing expected differences in the LOS along strike-slip structures (see Figure 4.11). Prior to referencing to a known reference frame, the LOS velocity maps for each LOS can be displayed in an approximate common reference using the across-track overlap comparison (Figures 4.14 and 4.15; without accounting for the difference in incidence angle). Despite not being referenced to a known reference frame, we begin to observe the regional scale tectonic configuration with the westward extrusion of a wedge of

material in Figures 4.11 and 4.13.

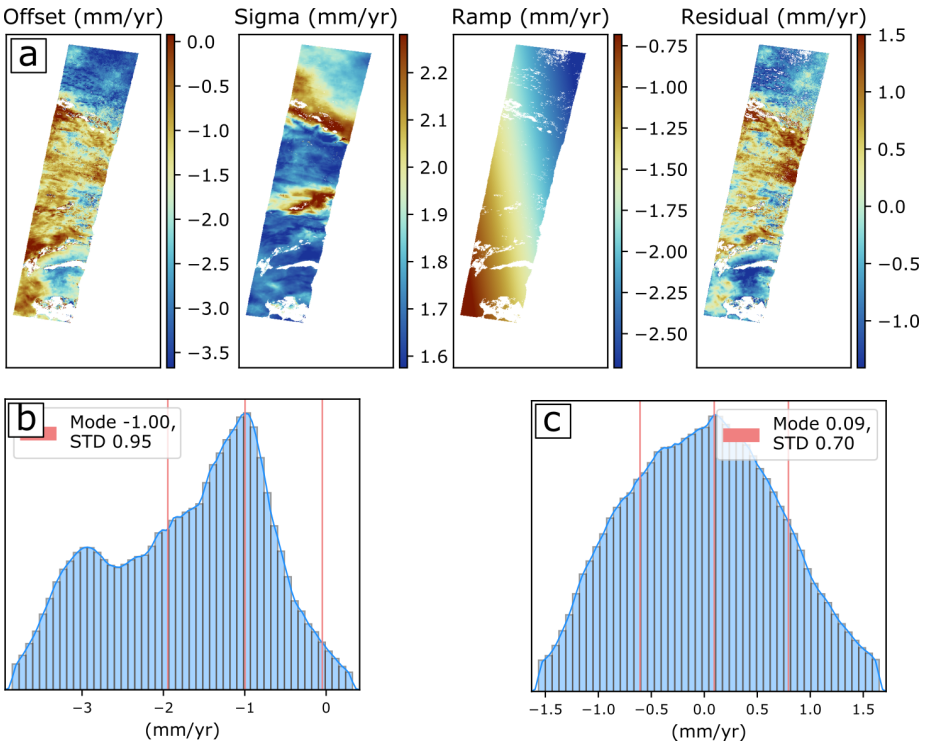


Figure 4.11: Across-track overlap comparison for D064-D166. a) Estimation of the planar trend and removal from the across-track residual. b) Histogram of overlap residuals prior to planar trend removal. c) Histogram of overlap residual after removal of a planar trend. Shear along both the MKDF and SFZ is visible in the residual of the across-track overlap; this is expected due to the difference in incidence angle of the LOS observing a different component of the motion along these faults.

4.3.4 Referencing LOS velocity fields to a stable Eurasia reference frame

The next step is to reference all the LOS velocity fields (now in merged track form) to a common, known reference frame. This aims to produce a regional velocity field in both the ascending and descending LOS. These can then be used to estimate other velocity components, e.g. east-west, with further steps required subsequently to derive measurements of strain across the region (e.g. *Weiss et al.*, 2020). Typically this involves referencing the LOS velocity fields with GPS data (e.g. *Hussain et al.*,

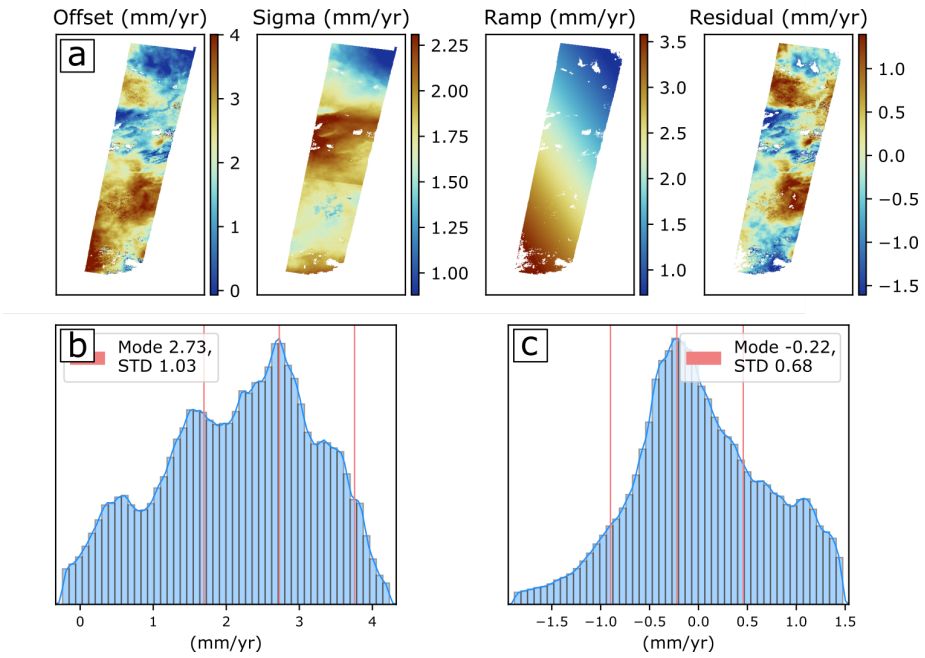


Figure 4.12: Across-track overlap comparison for D137-D064. a) Estimation of the planar trend and removal from the across-track residual. b) Histogram of overlap residuals prior to planar trend removal. c) Histogram of overlap residual after removal of a planar trend.

2016), which ties the LOS velocity fields to a GPS reference. The difficulty in this region is that the distribution of published GPS data (*Mousavi et al.*, 2013) is only within Iran (thus limited to the southern portion of our velocity fields, see Figure 4.1), and only has the horizontal (two-dimensional) velocity components. In addition the total number of stations is relatively low, which means, as well as a poor distribution of GPS stations within each track, the number of constraints to reference the LOS data is sparse. The number of stations is limited further by the location of some GPS stations within rapidly subsiding agricultural zones (e.g. around the Gorgan Plain, moving at a rate an order of magnitude higher than the tectonic signals; personal communications with Dr. Z. Mousavi) and cannot therefore be used (visible in the LOS velocity fields in Figures 4.11 and 4.13).

Therefore we implement a referencing strategy that incorporates regional geological information to provide further referencing constraints. When designing the spatial extent of this study, we deliberately extended our InSAR footprint into

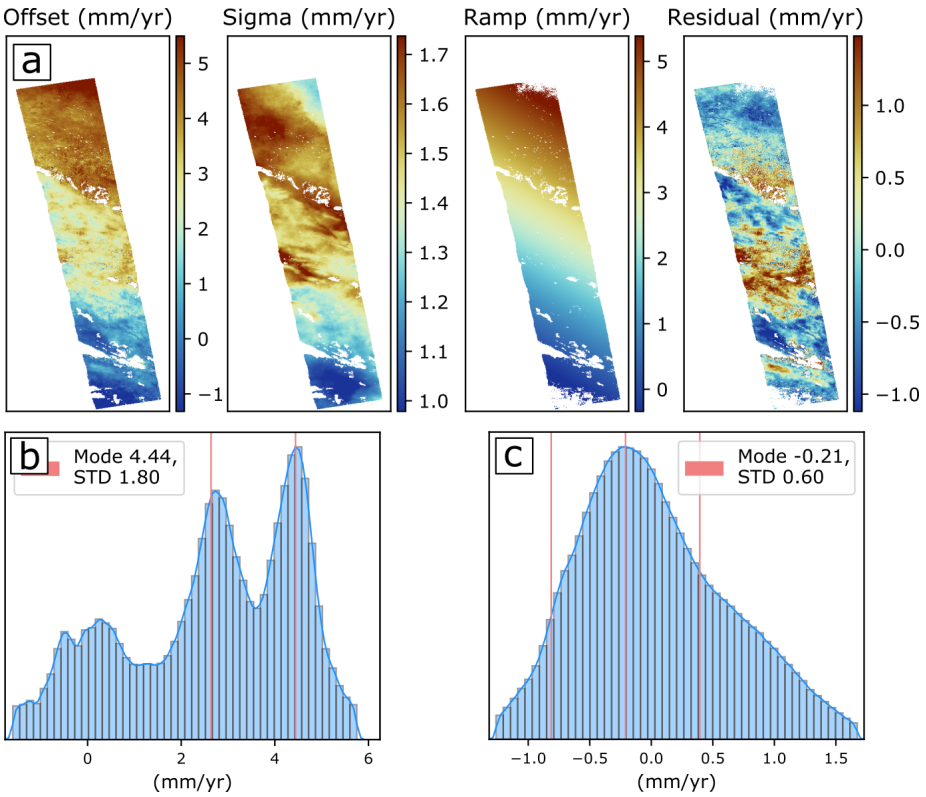


Figure 4.13: Across-track overlap comparison for A159-A086. a) Estimation of the planar trend and removal from the across-track residual. b) Histogram of overlap residuals prior to planar trend removal. c) Histogram of overlap residual after removal of a planar trend.

the Turan platform by >200 km for each track. The Turan platform is assumed to represent stable Eurasia (e.g. *Jackson et al.*, 2002), and so should have a velocity that reflects this (i.e. near zero within a stable Eurasia reference frame). Therefore to generate "dummy" GPS stations, we randomly sample the portion of the InSAR tracks that intersect the Turan platform ensuring these are located away from any mapped active structures.

When sampling the Turan platform, we ensure that the dummy GPS stations have a consistent velocity across an expanding window, to avoid sampling localised velocity outliers or pixels on the edges of masked/no data regions. The expanding window samples the LOS velocity field at a random location, with the window starting at a minimum number of pixels ($n_{pixels} = 5$). The window samples n pixels in in each direction (so a $2n \times 2n$ window). This grows until the fraction of pixels within

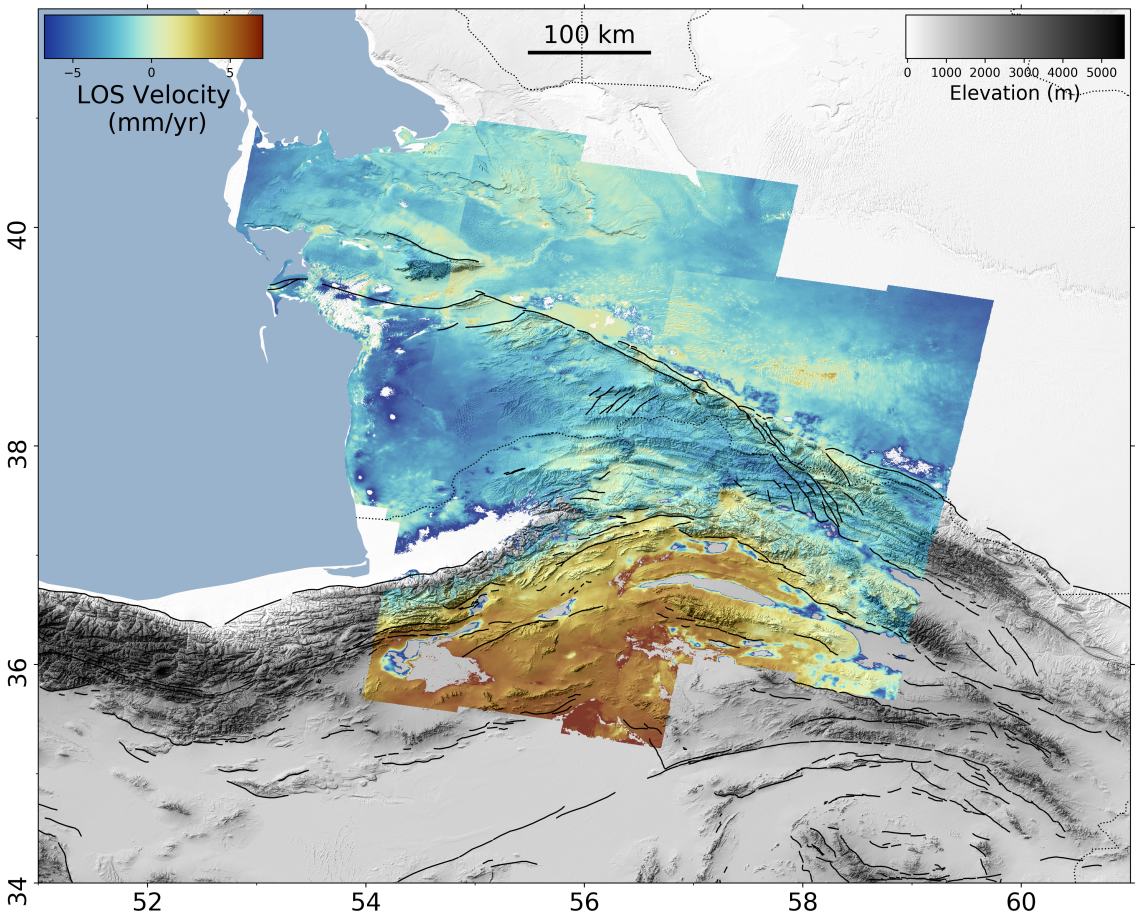


Figure 4.14: Descending LOS velocity maps presented in a common, unknown reference frame using across-track overlap comparisons to tie the tracks together. Black lines are mapped faults from *Walker et al.* (2021).

the sliding window is >50% the total window size (unless a maximum window size, $n = 20$ is reached with insufficient data, in which case another sample location is taken). The size of the sliding window range is chosen to reflect the range of correlation distances (in number of pixels) determined through empirical covariance estimates of non-deforming regions in the LOS velocity fields (see Figure 3.22 in Chapter 3). The LOS velocity at the sample location is calculated as the mean of the LOS velocity of the pixels in the sliding window weighted by the standard error,

$$V_{LOS_{2n\times 2n}} = \frac{\sum_{i=1}^{n} \frac{V_{LOS_i}}{\sigma^2_{LOS_i}}}{\sum_{i=1}^{n} \frac{1}{\sigma^2_{LOS_i}}}, \tag{4.2}$$

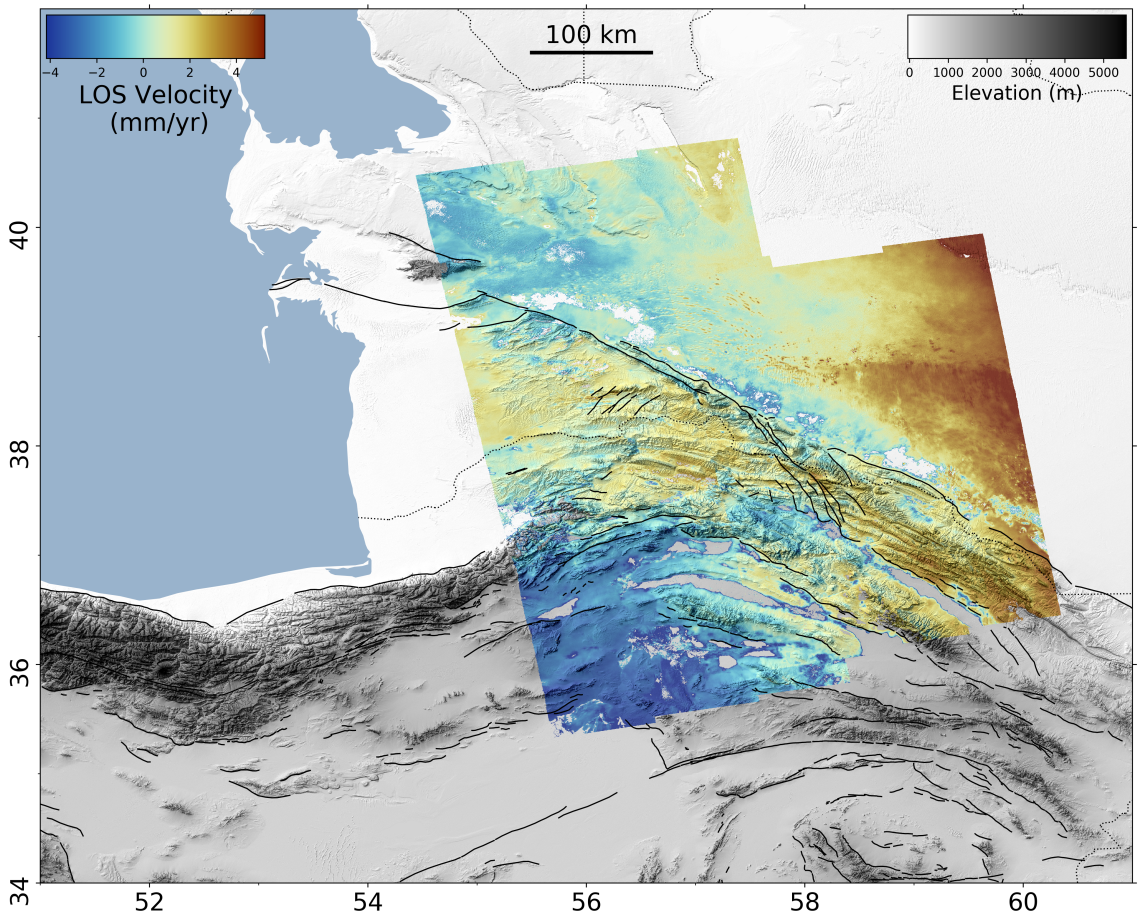


Figure 4.15: Ascending LOS velocity maps presented in a common, unknown reference frame using across-track overlap comparisons to tie the tracks together. Black lines are mapped faults from *Walker et al.* (2021).

with standard error equal to,

$$\sigma_{LOS_{2n\times 2n}} = \sqrt{\frac{1}{\sum_{i=1}^{n} \frac{1}{\sigma^2_{LOS_i}}}}. \tag{4.3}$$

When generating the dummy GPS stations, sample locations with high uncertainty (using a threshold of 0.1 mm/yr) are discarded. For each track we generate eight dummy GPS stations in the northern portion that covers the Turan platform, with the number chosen to be comparable to the number of GPS stations that are co-located with the LOS time-series in NE Iran.

Combining the NE Iran 2D GPS stations and our dummy GPS stations provides

sufficient constraints to quasi-reference the LOS velocity field to a stable Eurasia reference frame. To do this we project the GPS velocity components into the LOS (and the same with the standard error for each station). This step requires further assumptions for the components of the input data. To project the NE Iran GPS stations to the LOS, we use the horizontal velocities from *Mousavi et al.* (2013) and set their vertical velocity to zero. This assumption for the vertical velocity of these stations is balanced by attaching a high standard error, in comparison to the other velocity components, of 3 mm/yr (exceeding the standard error of vertical components determined through campaign GPS; personal communication with Dr. Z. Mousavi). Similarly for the dummy GPS stations, both horizontal and the vertical velocity components are set to zero. To these, we attach a standard error for the GPS velocity projected into the LOS comparable to the moderate to high standard error stations from the Iranian network (1.5 mm/yr).

Following this, we make the assumption that the LOS velocity field can be tied to the GPS velocity field by the addition of a planar ramp,

$$V_{GPS} = V_{LOS} + (ax + by + c)\,. \tag{4.4}$$

We solve for the best-fitting planar ramp and offset to $ax + by + c = V_{GPS} - V_{LOS}$, using a sequential least squares optimization weighted by the data errors. The ramp and offset is then added to the LOS velocity field to tie it to the GPS data, which is an approximate stable Eurasia reference. An example of this procedure is presented in Figure 4.16. This shows the combined NE Iran and dummy GPS-velocity fields projected into the LOS and their uncertainty; the ramp estimation on the residuals between the GPS projected into the LOS and the InSAR time-series LOS velocity at the same location; and finally the GPS-tied quasi-referenced velocity fields with the distribution of the GPS velocity residuals.

This is repeated for all tracks (Supplementary, Figures 4.57 to 4.60), at which

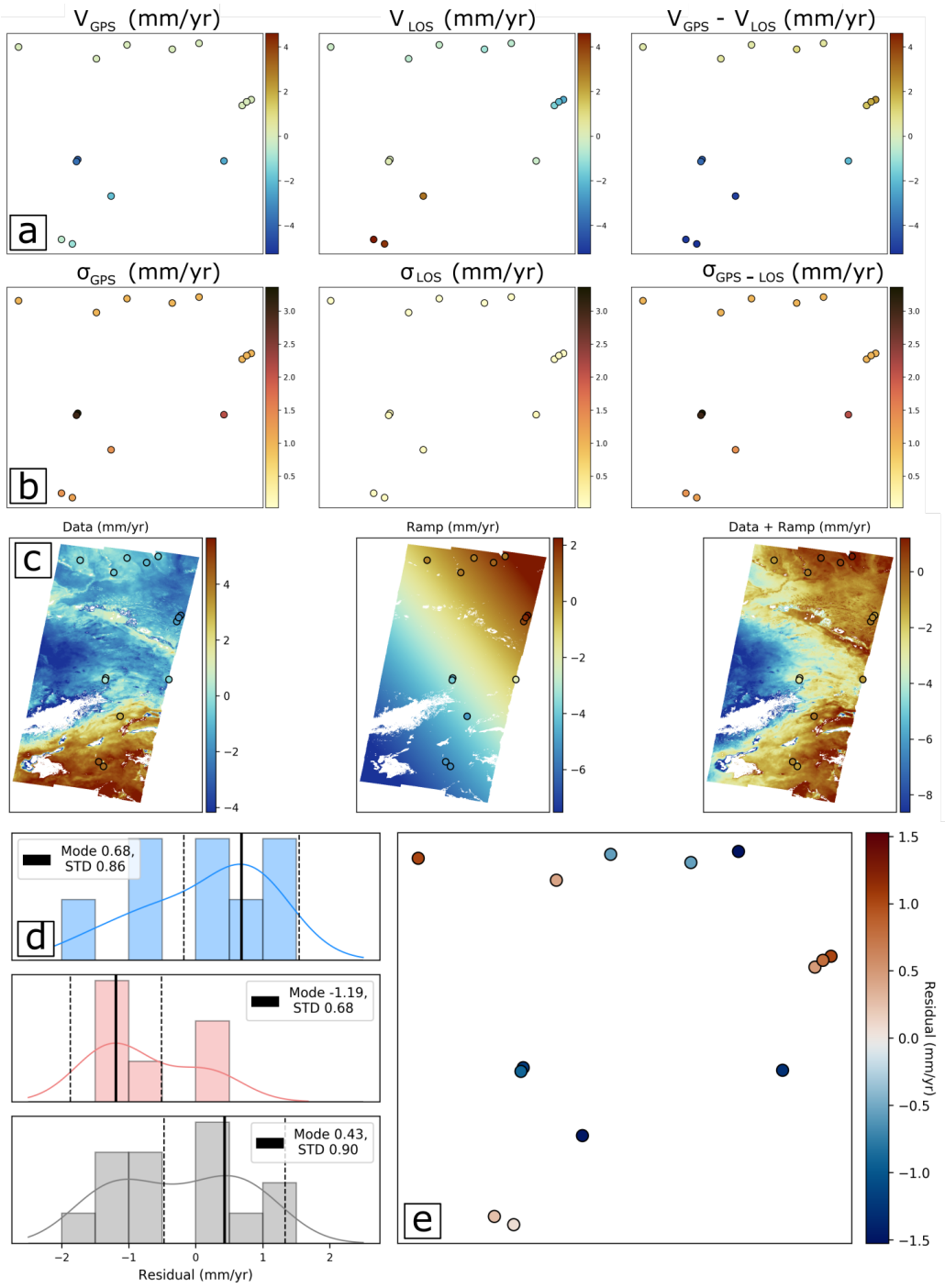


Figure 4.16: Referencing the LOS velocity field for D064 with GPS (approximate stable Eurasia reference frame). Distribution of GPS stations from the NE Iran network (*Mousavi et al.*, 2013) comprise the southern stations, and "dummy" Turan GPS stations the southern stations, that overlap the LOS velocity field with their (a) velocity and (b) standard error projected into the LOS; also shown are the extracted LOS values at the same point, and the residuals between the GPS values and the LOS. c) Shows the GPS ramp estimation and tying procedure, which applies a planar tilt and offset to bring the LOS into the stable Eurasia reference frame of the GPS data. d) and e) show the residuals of this ramp estimation procedure, with the histograms divided to show the different networks (blue is the "dummy" Turan, red is the "real" NE Iran, grey is combined GPS networks).

point we can reanalyse the across-track overlaps, this time without ramp estimation as the LOS data is regarded as tied to a common, known reference frame. The histograms of the across-track overlap residuals from the GPS-referenced LOS velocity maps are presented in Figures 4.17 to 4.19. For the central and eastern tracks, in both the ascending and descending LOS, the histograms of the residuals indicate that the GPS referencing has performed satisfactorily within the noise threshold of the LOS time-series. There is an issue however with the referencing of track D137 (see Supplementary Figure 4.58). For this track, there are no GPS stations from within the Iranian network included in the referencing. To include D137 in subsequent analysis, we instead employ a different approach. We use the residual in the across-track overlap region with the central track (D064), and using the ramp-estimation approach detailed in Section 4.3.3 to tie D137 to the same reference frame as the GPS-tied central track (D064). The histogram of the residuals is greatly improved (Figure 4.19a), with a distribution within the noise levels of the LOS time-series and no obvious systematic bias in the output.

4.3.5 Decomposing the ascending and descending LOS into V_E and V_{UN}

At this stage, we have all the ascending and descending LOS velocity maps quasi-referenced to a stable-Eurasia reference frame (Figures 4.20 and 4.21). The combination of the ascending and descending LOS allows for two velocity components to be resolved. Following the approach of Lin Shen at the University of Leeds (personal communication), it is possible to decompose the ascending and descending LOS velocity (V_{LOS}) into an east-west (V_E) and sub-vertical component (V_{UN}).

$$V_{LOS} = -V_E \cos\phi \sin\theta + V_{UN} \cos\alpha \,, \tag{4.5}$$

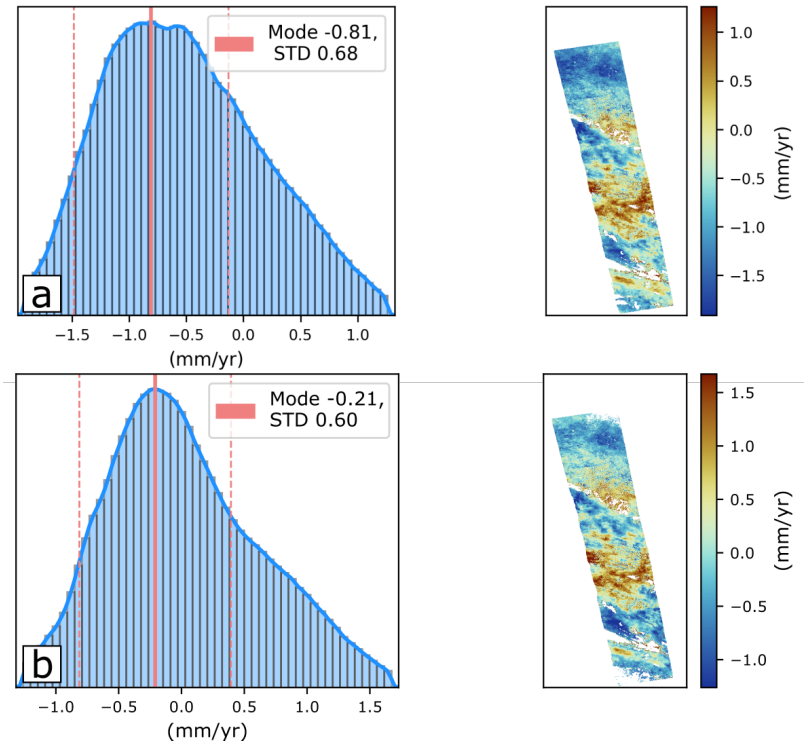


Figure 4.17: Track overlap histogram comparison of (a) GPS-tying, vs. (b) ramp-tying the LOS velocity fields for A159-A086. The overlap offset is still below the noise level of the LOS time-series. Despite the modal offset appearing skewed, this possibly results motion occurring (e.g. along faults) within the overlap region viewed from a different LOS.

where α is the angle between the LOS vector and the V_{UN} plane (Figure A.1).

Through further inspection, the geometry of the LOS vector can be used to express $\cos\alpha$ in terms of θ and ϕ. Recognising that $AB = OA\sin\alpha$, and $AB = AC\sin\beta = OA\sin\theta\sin\beta$, can be combined to give, $\sin\alpha = \sin\theta\sin\beta$. Following this, making use of $\sin^2\beta = \cos^2\phi$ (and the trigonometric identity $\cos^2\alpha = 1-\sin^2\alpha$) is used to show that,

$$\cos\alpha = \sqrt{1-\sin^2\theta\sin^2\beta} = \sqrt{1-\sin^2\theta\cos^2\phi}\,. \tag{4.6}$$

The resulting expression decomposes V_{LOS} into V_E and V_{UN}, importantly expressed

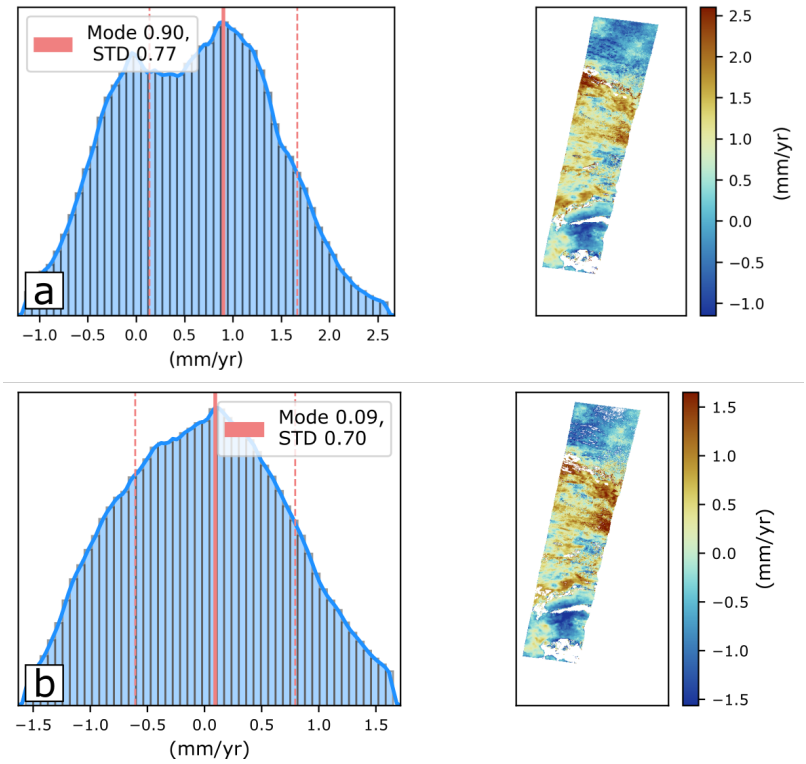


Figure 4.18: Track overlap histogram comparison of (a) GPS-tying, vs. (b) ramp-tying the LOS velocity fields for D064-D166. The overlap offset is still below the noise level of the LOS time-series. Despite the modal offset appearing skewed, this possibly results motion occurring (e.g. along faults) within the overlap region viewed from a different LOS.

using only the known values for the incidence, θ, and heading, ϕ,

$$V_{LOS} = -V_E \cos\phi \sin\theta + V_{UN}\sqrt{1 - \sin^2\theta \cos^2\phi}\,. \tag{4.7}$$

The major assumption in this decomposition, is that the angle α is the same for any LOS vector. However this is not the case predominantly due to the variation in incidence angle of Sentinel-1 (29.1°–46.0°), and to a lesser effect the variation in heading angle ($\approx \pm 0.1°$ over an equivalent length scale). The possible variation in $\cos(\alpha)$ is $\approx 0.8 \pm 0.09$. To quantify the sources of error due to this assumption, we define the angle γ between the projection of the LOS vector in the V_{UN} plane and

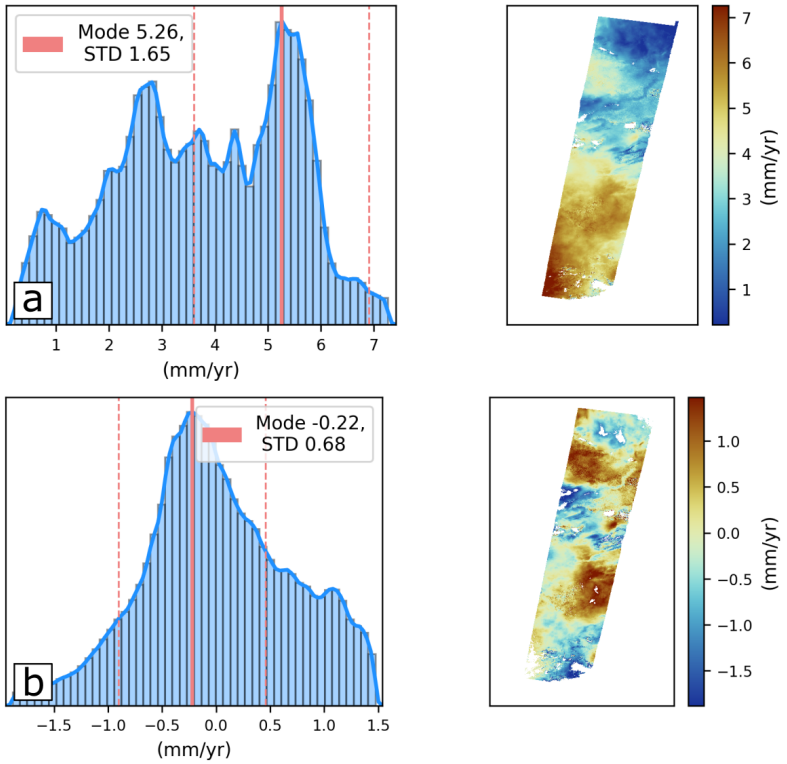


Figure 4.19: Track overlap histogram comparison of (a) GPS-tying, vs. (b) ramp-tying LOS velocity fields for D137-D064. In this case the GPS-tying does not perform adequately, possibly due to the lack of "real" GPS stations that overlap this track. An alternative referencing approach is required, instead making use of the ramp-tying overlap results to tie D137 to the GPS-tied D064.

the vertical axis ($\angle COB$ in Figure A.1). Therefore by equating,

$$V_{UN} = \frac{V_N \sin\phi \sin\theta + V_U \cos\theta}{\sqrt{1 - \sin^2\theta \cos^2\phi}}\,, \tag{4.8}$$

and,

$$V_{UN} = -V_N \sin\gamma + V_U \cos\gamma\,, \tag{4.9}$$

to isolate equations for $\sin(\gamma)$ and $\cos(\gamma)$, we can define (by using $\tan(\gamma) = \frac{\sin(\gamma)}{\cos(\gamma)}$),

$$\tan(\gamma) = \frac{-\sin(\phi)\sin(\theta)}{\cos(\theta)} \tag{4.10}$$

$$\gamma = \tan^{-1}\left(-\sin(\phi)\tan(\theta)\right)\,. \tag{4.11}$$

Using the range of incidence angles for Sentinel-1, the range of values for γ is from 7–13°. Therefore it is possible to establish the main source of error in V_{UN} is from V_N, as the range of $\sin(\gamma)$ is $\approx 0.17 \pm 0.05$. In contrast, with respect to V_U the range of $\cos(\gamma)$ is $\approx 0.98 \pm 0.01$. Returning to V_N as the principle source of error in the decomposition, the magnitude or error (5%) will be below that of the LOS velocity maps ($\approx$1 mm/yr) unless the rate of V_N exceeds $\approx$20 mm/yr. This is well below the rate of north-south motion relative to a Eurasia reference expected at the northern margins of the Iranian Plateau.

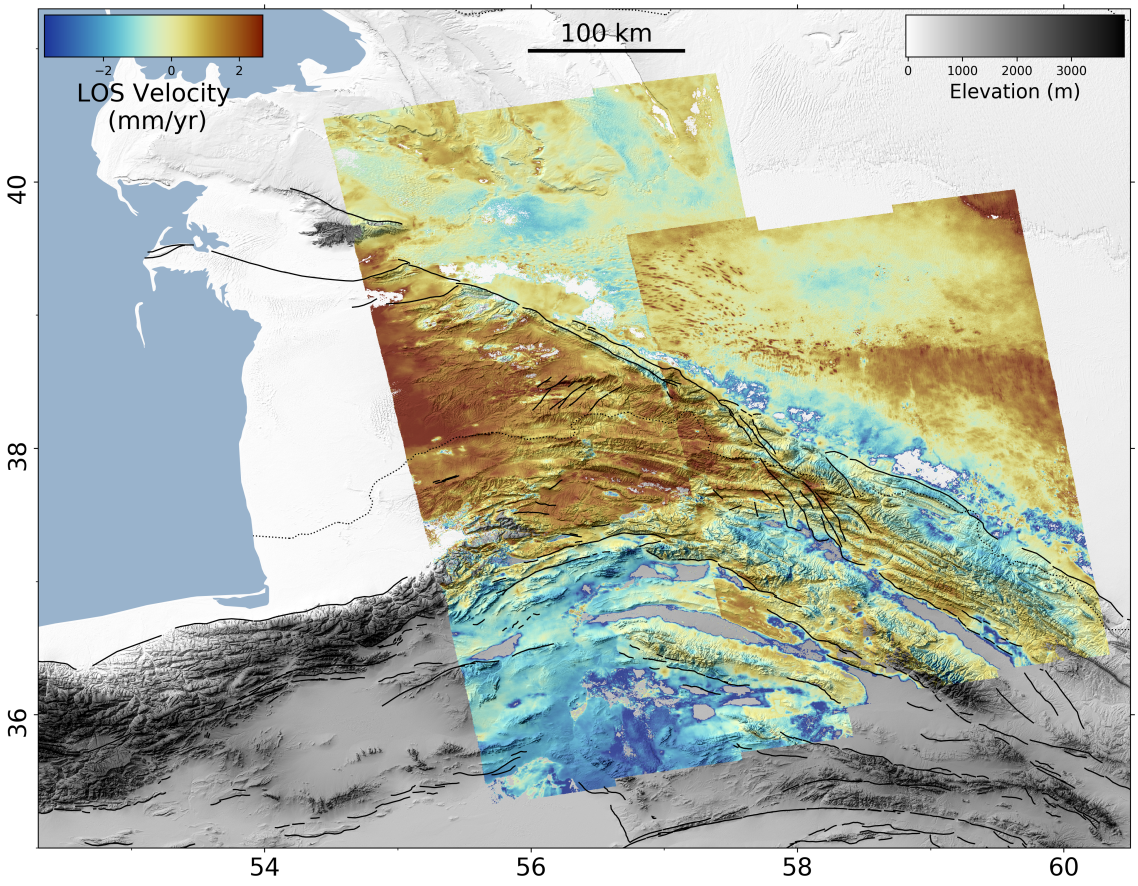


Figure 4.20: GPS-referenced ascending LOS tracks (A159, A086). The step in the LOS velocity fields across track is expected from the difference in incidence angle of the LOS whilst observing motion along a strike-slip fault. Black lines show mapped faults from *Walker et al.* (2021).

For the extent covered by both ascending and descending time-series, we compute

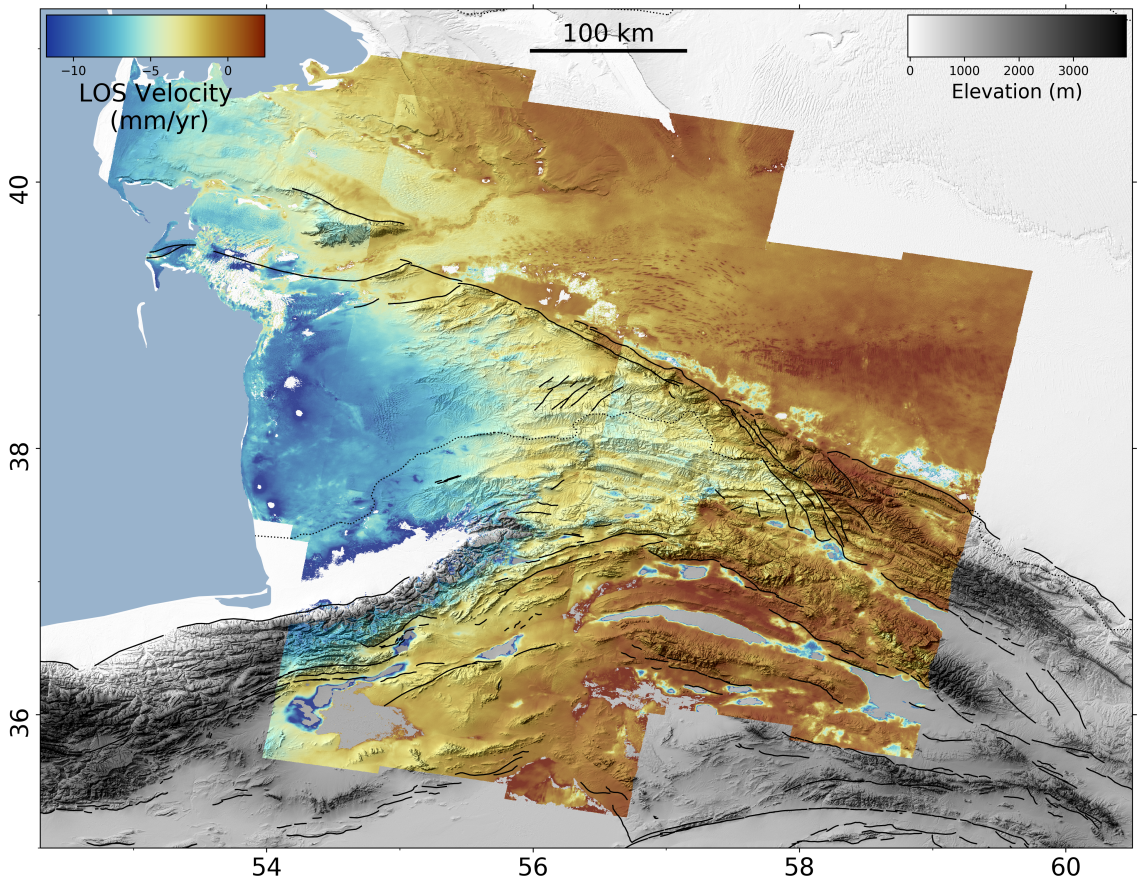


Figure 4.21: GPS-referenced descending LOS tracks (D137, D064, D166). The step in the LOS velocity fields across track is expected from the difference in incidence angle of the LOS whilst observing motion along a strike-slip fault. Black lines show mapped faults from *Walker et al.* (2021).

a least-squares solution for V_E and V_{UN}. For pixels within ascending or descending track overlaps, or in some instances both, this computation becomes over-determined (see Figure 4.22 for a visual representation of the input data to this calculation). Prior to the calculation the ascending and descending LOS velocity fields must be re-sampled to a spatially consistent grid, which we do using a bi-linear interpolation to a 250 m grid-spacing. The final results of this decomposition are shown in Figures 4.23 and 4.24, noting that positive V_{UN} is from either southward or upwards motion. The east-west velocity field has much lower spatial variability than the sub-vertical velocity field. This is because localised sources of noise from short wavelength vertical

deformation, typically from hydrological signals, decompose into the V_{UN} component. In contrast, the smooth deformation observed in the V_E component is predominantly from tectonic signals.

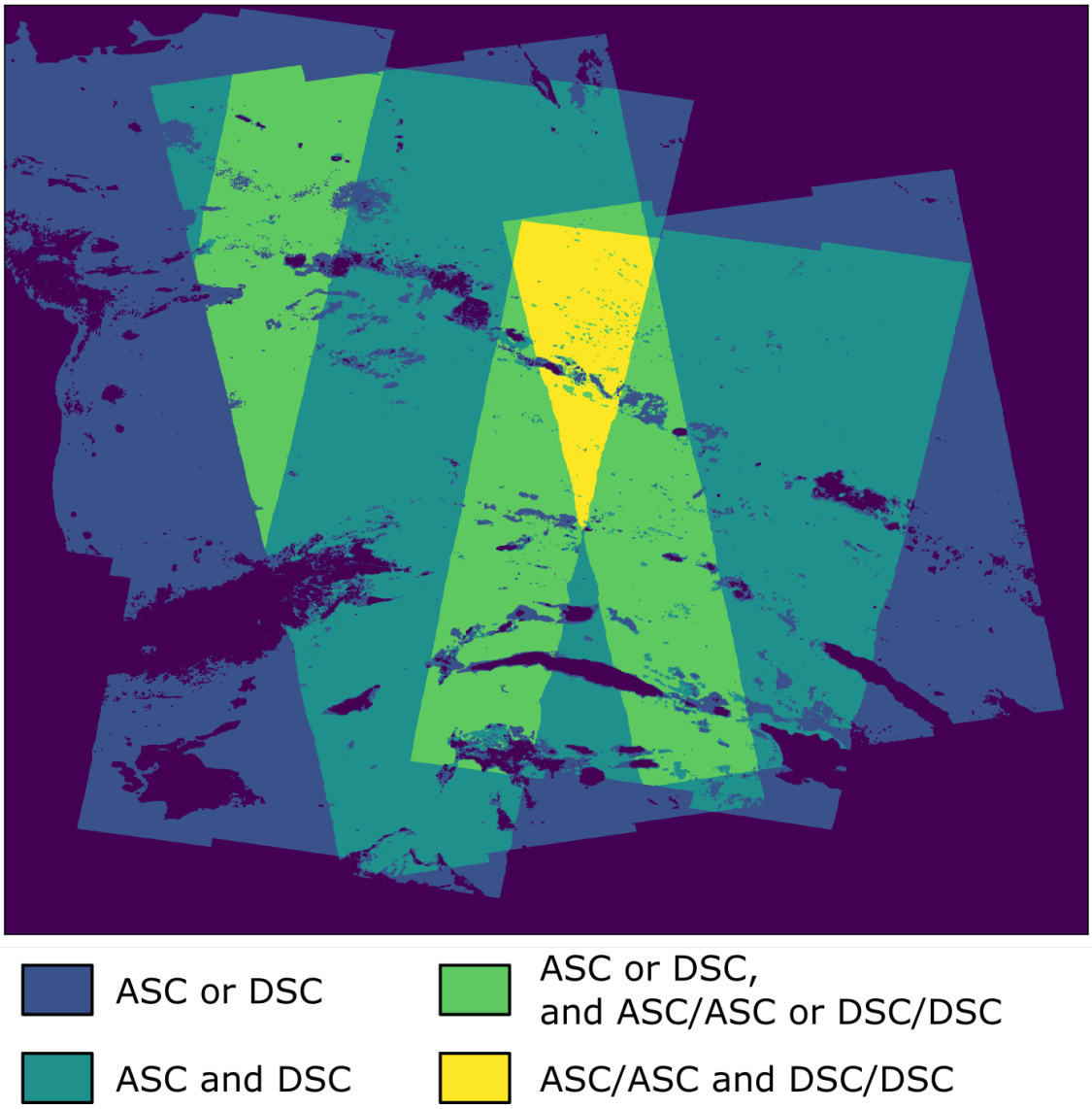


Figure 4.22: Visualisation of the spatial extent of the LOS velocity fields used for the computation of V_E and V_{UN}. This can only be calculated on pixels with ascending and descending LOS data (teal, green, yellow), therefore the dark blue (no data) and medium blue (only descending or ascending LOS data available) shaded regions are excluded from the calculation. The decomposition becomes over-determined for track-overlap regions (green and yellow).

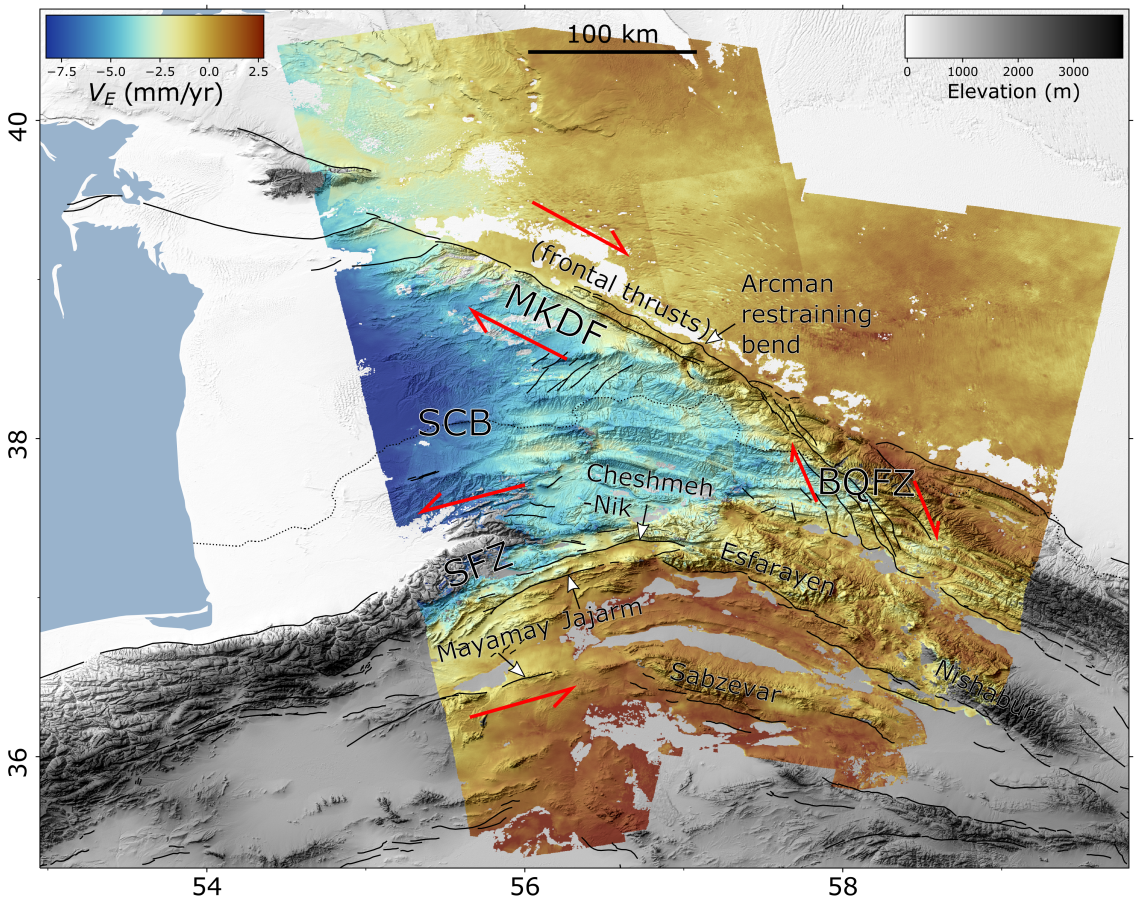


Figure 4.23: Hillshade-rendered map of the V_E component from decomposition into east-west and sub-vertical component. Active faults are delineated by black lines, from *Walker et al.* (2021).

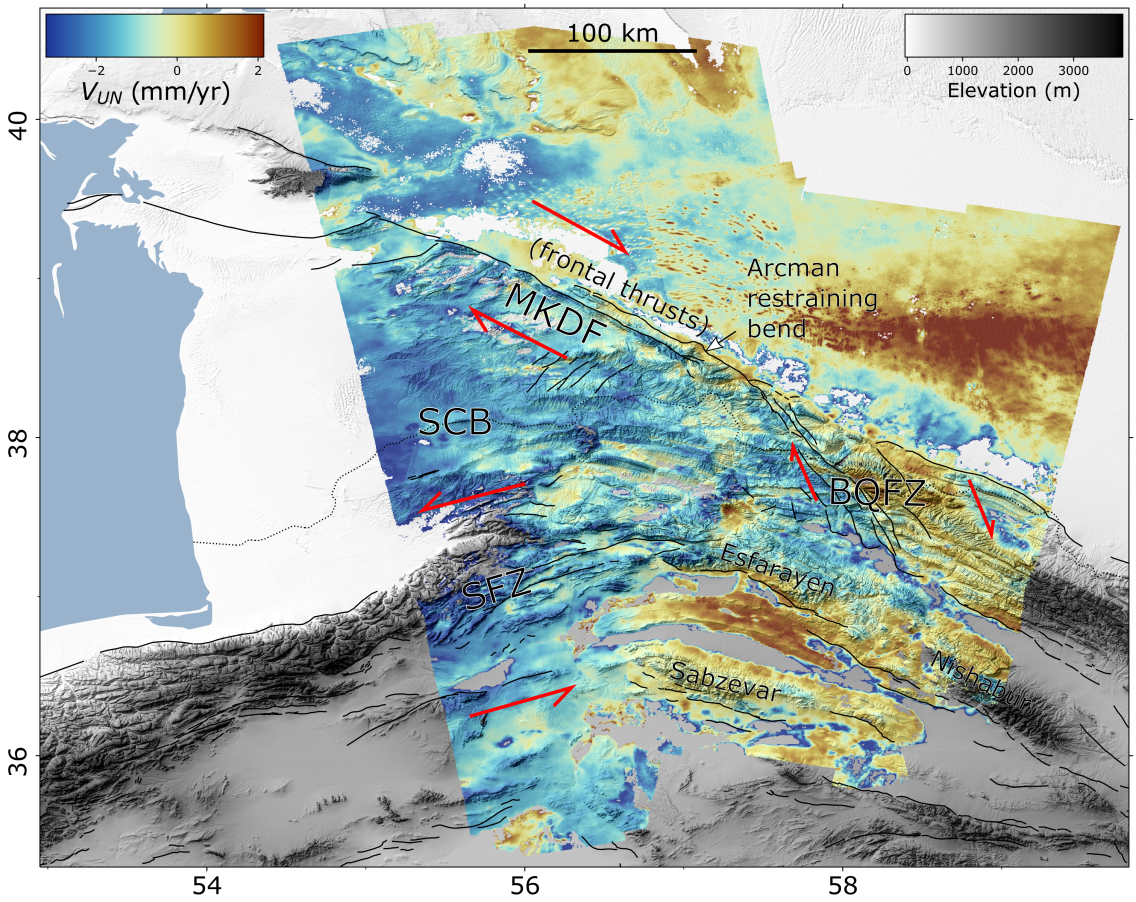


Figure 4.24: Hillshade-rendered map of the V_{UN} component from decomposition into east-west and subvertical component. Positive V_{UN} (red) corresponds to upwards or southwards motion resolved in the LOS, and negative (blue) corresponds to either downwards or northward motion. Active faults are delineated by black lines, from *Walker et al.* (2021).

4.4 Imaging the extrusion of the South Caspian Basin

The V_E component in Figure 4.23 presents a spatially-continuous image that we can interpret from a tectonic perspective. The velocity gradients are concentrated along the MKDF and SFZ, which together form a conjugate fault system facilitating the westward extrusion of the blue wedge of material in Figure 4.23. We interpret the motion of this wedge of material as an image of the extrusion of the SCB, correlating with previous geological (e.g. *Walker et al.*, 2021; *Hollingsworth et al.*, 2008; *Ritz et al.*, 2006), geodetic (e.g. *Mousavi et al.*, 2013, 2015; *Walters et al.*, 2013; *Djamour et al.*, 2010) and seismological (e.g. *Jackson et al.*, 2002; *Jackson and McKenzie*, 1984; *Copley and Jackson*, 2006) interpretations of the kinematics in this region.

Profiles through the respective velocity fields from the V_E and V_{UN} decomposition and the ascending and descending LOS, provide quantitative constraints on the rates of deformation. In Figure 4.25, we present north-south oriented profiles of the V_E through the wedge of SCB material. The velocity-steps (resolved in the east-west component) across the MKDF and SFZ are 4–6 mm/yr and 4.5–6.5 mm/yr respectively, and the wedge of SCB material narrows towards the apex of the conjugate system. There is a suggestion in the SCB wedge of a negative V_{UN} component relative to outside the conjugate system, which can either be explained by northwards motion of the SCB relative to Eurasia and Iran (e.g. *Jackson et al.*, 2002), subsidence of the basin (e.g. *Green et al.*, 2009), or a combination of the two resolved in the V_{UN} component. Another observation in Figure 4.25 is the difference in the distribution of the deformation between the MKDF and SFZ (see orange shaded regions). The velocity gradient across the SFZ is distributed across a fault zone with numerous parallel segments (e.g. *Hollingsworth et al.*, 2010; *Mousavi et al.*, 2015), in comparison to the MKDF which is concentrated along a single strand (e.g.

Walker et al., 2021).

Another important observation to address in the V_E component in Figure 4.23, is an apparent negative gradient (increasingly negative velocity in the west direction) within the East Caspian Lowlands. Figure 4.26 presents an east-west oriented profile through this velocity gradient towards the apex of the SCB wedge. The profile through the V_E field shows this gradient, which appears to be a relatively abrupt change at 56° E (at -100 km profile distance). The V_{UN} profile suggests there is a subtle negative gradient, although this could be the result of few constraints on the referencing of the easternmost LOS velocity fields. Unfortunately the data extent of the ascending velocity field constrains the western limit of the decomposition and so does not provide any further insight to this apparent gradient. However the descending profile extends to the shoreline of the Caspian Sea. The limit of this velocity gradient is evident in the profile through the descending LOS in both D064 and D137, which appears to level out at 55° E (-175 km profile distance) to ≈-8 mm/yr in the descending LOS.

Without the inclusion of another ascending track adjacent to the Caspian Sea, we are unable to provide any conclusive interpretation of what this signal represents. The gradient observed in V_E could result from an Euler rotation of the SCB around a pole of rotation relatively nearby to the northwest, as modelled with GPS (*Djamour et al.*, 2010; *Mousavi et al.*, 2013). However if the gradient is defined over a finite length-scale in the wedge of material, as is possibly suggested by the descending LOS velocity profile in Figure 4.26, this can not be the case. This alternative example suggests the velocity of the interior of the SCB is moving faster than easternmost part of the wedge adjacent to the conjugate faults. In which case the SFZ and MKDF are not truly representative of the motion of the block. However this would require either extension and subsidence in the East Caspian Lowlands, significant internal deformation within the East Caspian Lowlands, or increasing

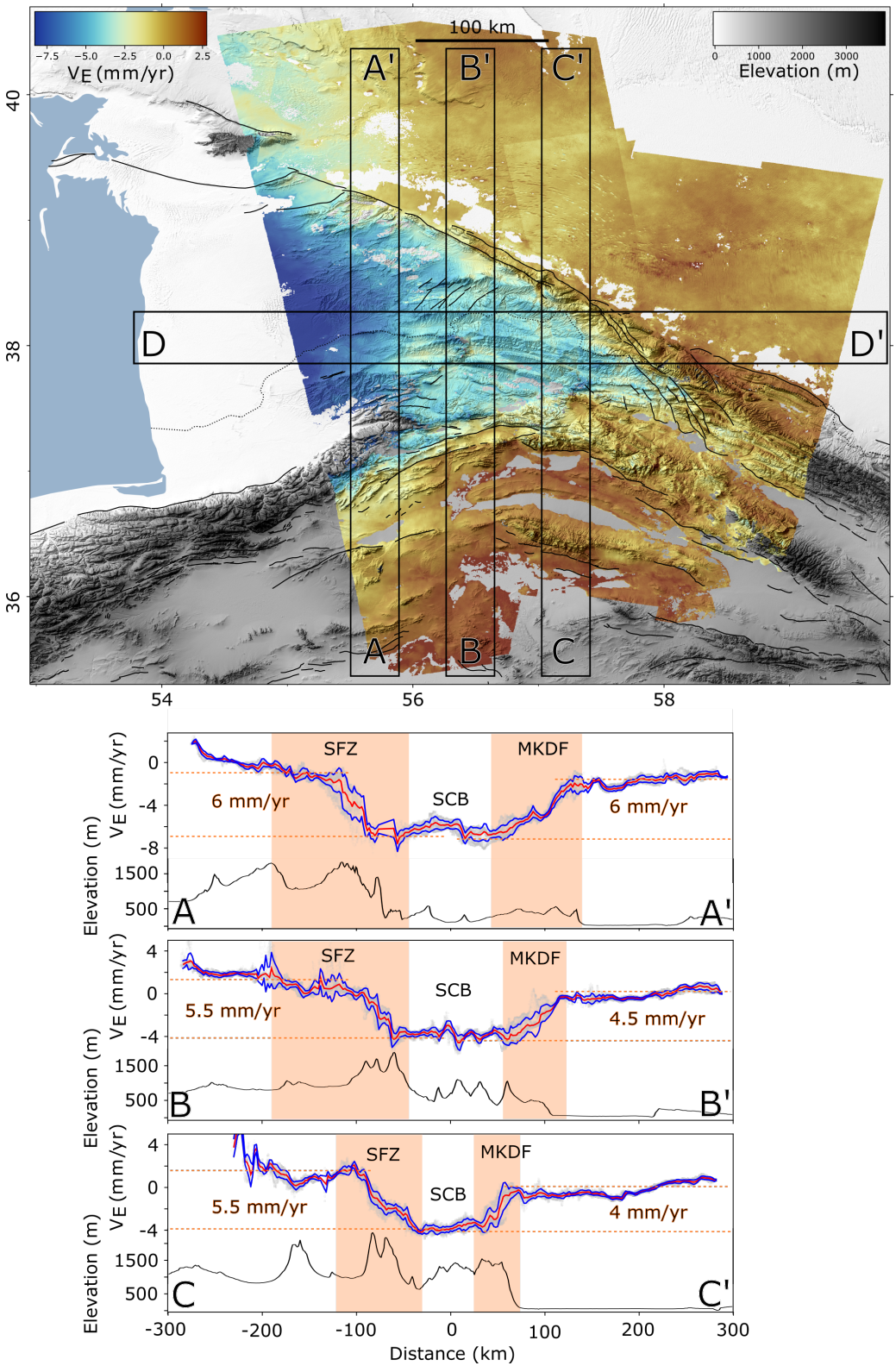


Figure 4.25: North-south oriented profiles of V_E, across the wedge of extruding SCB material. The profiles A-A', B-B' and C-C' have a length of 600 km and a swath width of 30 km (D-D' is shown in Figure 4.26). The orange zones highlight the deformation associated with the SFZ and MKDF in each profile; note the much greater width of the SFZ from distributed deformation across a network of faults.

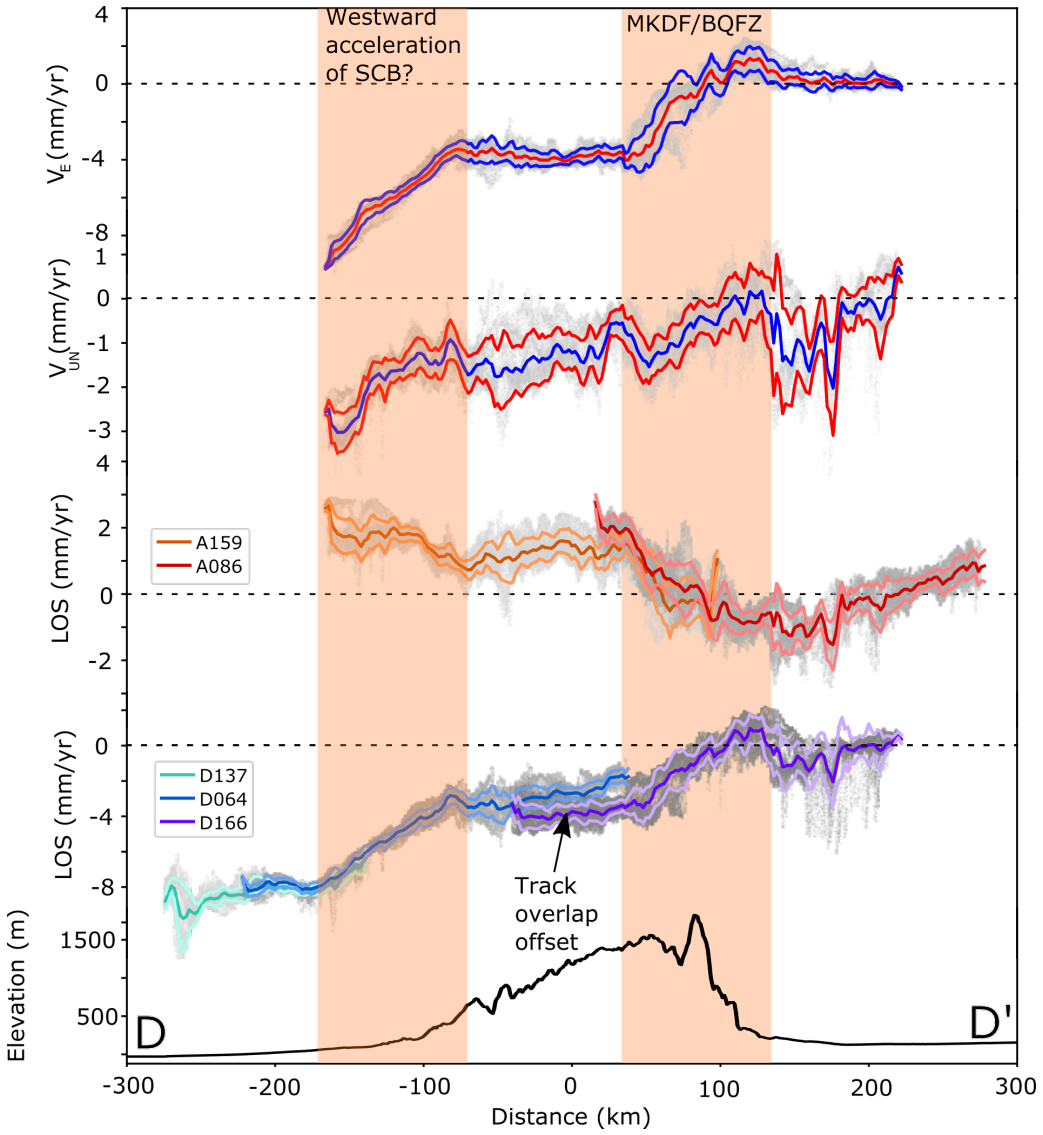


Figure 4.26: East-West oriented profile across the apex of the wedge of extruding SCB material (location of D-D' is shown in Figure 4.25). From top to bottom: V_E, V_{UN}, ascending LOS, and descending LOS. The orange zones highlight the intersection with the MKDF/BQFZ, and an unexpected signal or possible higher velocity within the East Caspian Lowlands.

north-south convergence towards the Caspian Sea to counteract the divergence. An alternative explanation is that the conjugate motion resolved along the MDKF and SFZ is representative of the South Caspian motion, and this velocity gradient is non-tectonic in origin. A possible explanation here is that this is an observation of the gravitational collapse of the thick sediment pile in the East Caspian Lowlands

into the basin. The total thickness of the sediment pile in the South Caspian is >25 km, with 5 km of post-miocene sediments (*Jackson et al.*, 2002). The signal is unlikely to represent sediment compaction as the deformation is predominantly resolved in the horizontal component, although this could contribute to a negative vertical component resolved in V_{UN}.

As well as this insight into the kinematics of the extrusion of the SCB, the velocity fields present further observations of tectonic deformation along numerous structures throughout the region. These observations are summarised in Figures 4.27 and 4.28 (including examples of hydrological and anthropogenic deformation/noise decomposed into the sub-vertical component). The following sections present quantitative analysis and interpretation of the deformation across these fault systems, and discuss their contribution to the kinematic understanding of the tectonics in this region.

4.4.1 The Main Köpetdag fault - a plate-boundary type fault?

Figure 4.29 shows profiles of the V_E component across the MKDF. These show the expected right-lateral motion across the fault. Between 56° E and 58° E the right-lateral motion is relatively constant, with a velocity step of 4–4.5 mm/yr. Assuming that the westward component resolves only fault parallel deformation, this corresponds to a slip-rate of 4.8–5.4 mm/yr across the MKDF; a lower bound on the true slip-rate. However the westernmost profile (A–A') constrains significantly greater deformation, with a rate exceeding 7 mm/yr in V_E. This is because the profile intersects further into the East Caspian Lowlands, and into the apparently faster-moving deformation resolved within the interior. An additional observation of the westernmost profile is that the deformation is distributed across either a longer-wavelength or an additional linear trend. A longer wavelength hints at a

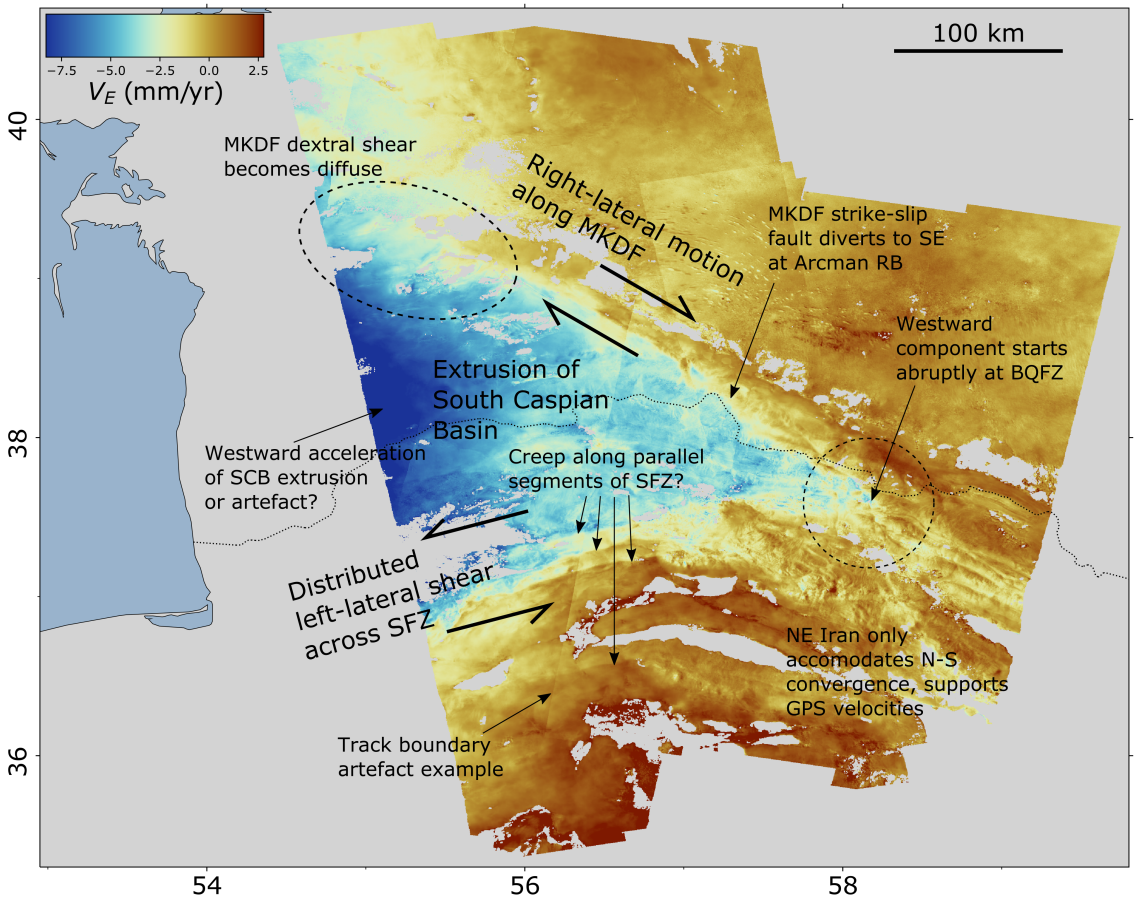


Figure 4.27: Annotated map of the V_E component of the decomposition of the LOS time-series velocity maps into V_E and V_{UN}, primarily showing the extrusion of the SCB by the right-lateral MKDF and left-lateral SFZ.

change in character along the western segment, possibly related to the kinematic linkage to the Absheron-Balkan Sill offshore. Whereas a linear trend might relate to the motion or rotation of the interior of the SCB discussed in the section above.

Figure 4.30 presents profiles of V_{UN} across the MKDF. The signal in these profiles is much noisier due to short-wavelength hydrological and topographically correlated residuals that partition into the sub-vertical component. However these profiles present evidence for deformation to the north of the MKDF, which supports the modelling of deformation along frontal thrusts to the MKDF in Chapter 3. The magnitude of the signal is on the order of 1–1.5 mm.yr (resolved in the subvertical

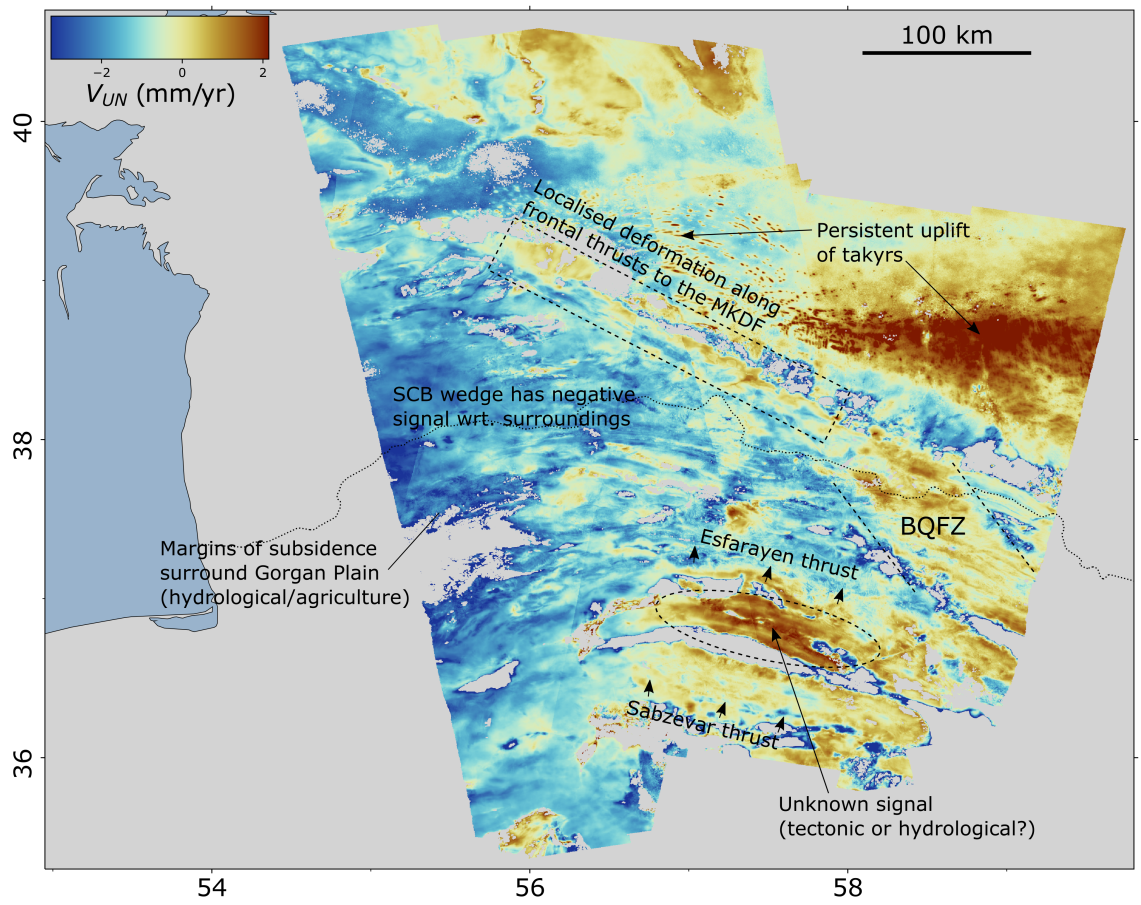


Figure 4.28: Annotated map of the V_{UN} component of the decomposition of the LOS time-series velocity maps into V_E and V_{UN}.

component). Generally this signal is constrained to the adjacent 20 km to the north of the main strike-slip fault, however the extent is hidden by subsidence along the Karakum Canal irrigated zone (see orange and blue shading in Figure 4.30). It is very difficult to conclude decisively that this signal has no relationship to the hydrological subsidence along this zone, however there are several pieces of evidence that suggest it is tectonic in origin. The concentration of deformation begins immediately to the north of the MKDF and is observed within the badlands between the MKDF and mapped frontal thrust scarps. This area has a moderate topographic gradient (approximately 500 m over the 10 km), and is comprised of incised alluvial fan terraces. The badlands are composed of coarse fan deposits and are not able

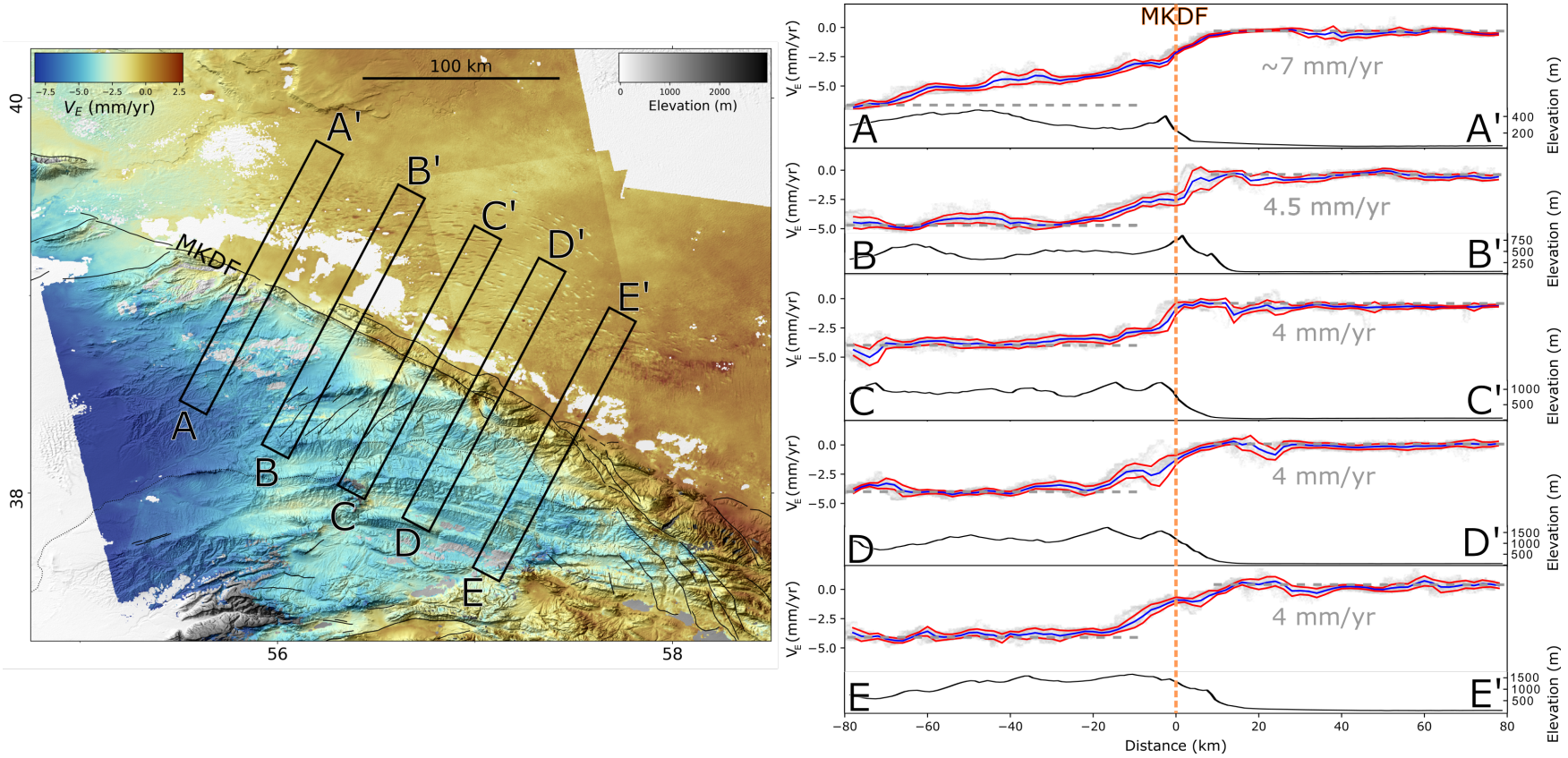


Figure 4.29: Fault-perpendicular profiles of V_E across the MKDF. Profile swaths are 160 km in length, with a width of 20km (striking 123°). Most of the profiles show a consistent velocity step of 4–4.5 mm/yr. The westernmost profile intersects the apparently faster moving interior of the South Caspian block.

to support agriculture; therefore we are unable to attribute the source of this deformation to similar mechanisms to the high-magnitude agricultural/hydrological subsidence signals immediately to the north. In addition, there appears to be concentrations around structural features such as the Arçman restraining bend and eastern segment of the MKDF (where a reverse component becomes progressively more dominant in the geomorphology; *Walker et al.* (2021)).

The interseismic motion along the MKDF appears to be representative of a plate-boundary type fault. The fault parallel motion is concentrated on a single, linear (for >200 km), vertical strike-slip fault, which is accumulating strain at a relatively fast rate for a continental interior setting. Long, linear strike-slip faults have been suggested to represent concentrations of strain along lateral rheological contrasts in the lithosphere (*Molnar and Dayem*, 2010, e.g.). A rheological contrast is possibly expected at the norther border of the Iranian Plateau with the Turan platform, and correlates to the change in geomorphological expression of deformation and distribution of seismicity (see Figure 1.3). Furthermore the suggestion that the MKDF is representative of a plate boundary supports paleoseismological evidence for the character of earthquake ruptures along the fault in Chapter 2, with large-magnitude, long-recurrence interval earthquakes.

4.4.2 Distributed deformation through the Shahroud Fault Zone

Similar to the MKDF, the fault parallel motion along the SFZ is well resolved in the V_E component in Figure 4.31. The velocity step in the V_E component is 5.5–6 mm/yr across the SFZ, although the motion appears to be distributed across a network of closely-spaced parallel faults. Figure 4.32 presents a zoomed in perspective of this distributed deformation, focusing on an area across the mapped Jajarm and Cheshmeh-Nik fault segments, and an additional segment to the north. There also

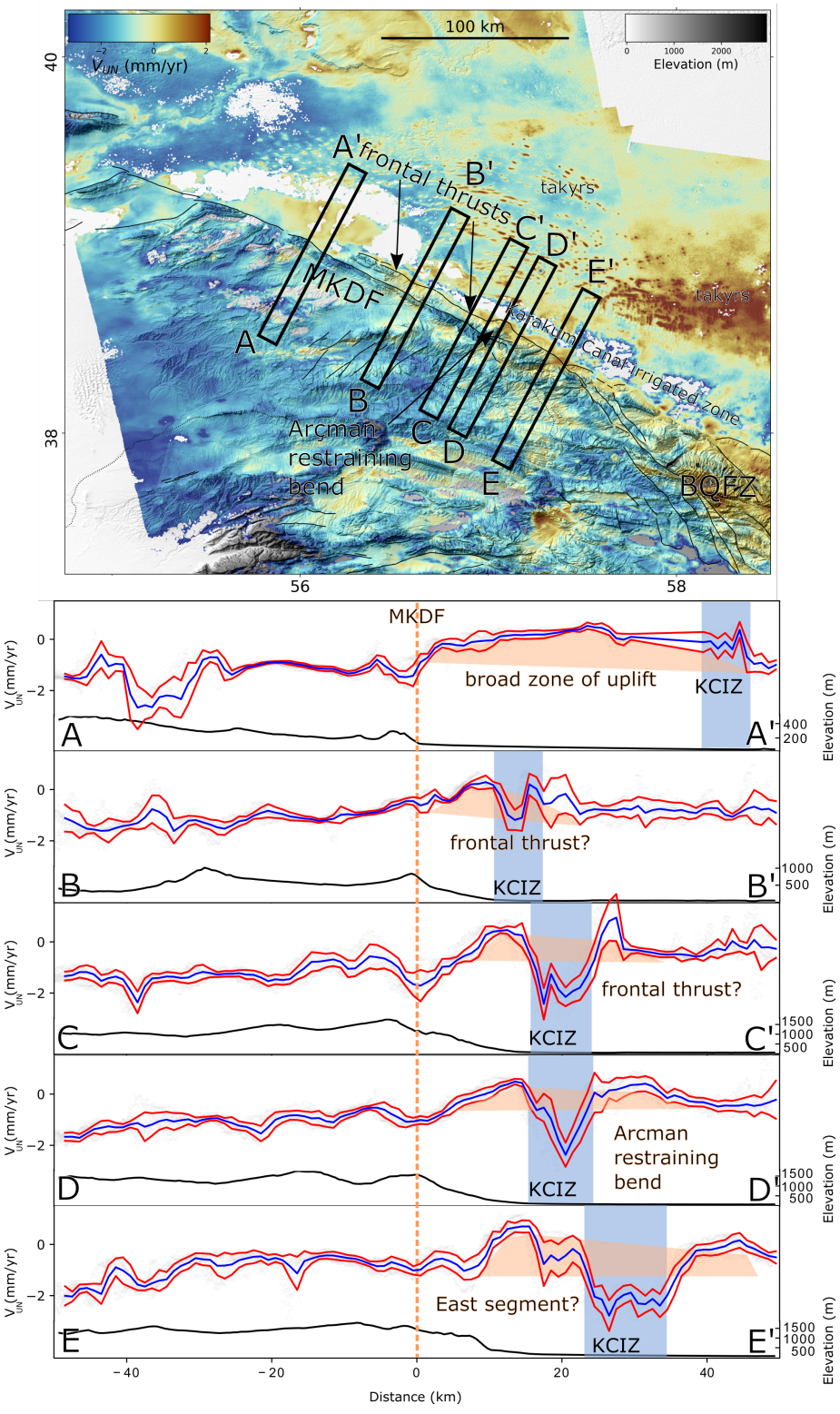


Figure 4.30: Fault-perpendicular profiles of V_{UN} across the MKDF. The orange shading represents the uplift modelled as motion at depth across the frontal thrusts in Chapter 3, and the blue is the intersection with the Karakum Canal irrigated zone (KCIZ). Profile swaths are 100 km long and 10 km wide.

appears to be a small component of the left-lateral motion being accommodated across the Mayamar segment further south. The V_E component suggests that these faults have very shallow locking depths, however evidence for surface creep is inconclusive within the LOS velocity fields (Figure 4.32). Unfortunately due to the spatial extent of the ascending data, we are unable to resolve the velocity across the westernmost onshore segments of the SFZ.

In contrast to the MKDF, the distributed deformation across the SFZ possibly reflects the differences in rheologogical contrasts across the two fault zones; with no evidence for any significant contrast in rheology across the SFZ. The distributed network of faults that comprise the SFZ defines a fault zone >100 km wide (perpendicular to strike). Assuming V_E resolves only fault parallel motion across the SFZ, the total velocity step corresponds to 6.0–6.6 mm/yr (using a fault strike of 246°). This supports the most recent GPS estimates across the SFZ of 4–6 mm/yr (*Mousavi et al.*, 2013), although is slightly higher than the previous Envisat-InSAR derived estimate (4.75±0.8 mm/yr across the Jajarm and Abr segments) from *Mousavi et al.* (2015). The SFZ also has evidence of hosting large earthquakes with long recurrence intervals (*Hollingsworth et al.*, 2010). How segmentation controls earthquake ruptures along the SFZ remains unknown, and whether these closely-spaced parallel segments are capable of hosting multi-segment ruptures is an important consideration from a seismic hazard perspective.

4.4.3 The Bäherden-Quchan Fault Zone and its role in tectonic models of NE Iran

The observations across the BQFZ provide insight into both the faulting at a local-scale and the kinematics through the Köpetdag and NE Iran. In Figure 4.33, we present east-west profiles across the BQFZ showing the LOS velocity fields and the decomposition into the V_E and V_{UN} components. The NNW-SSE

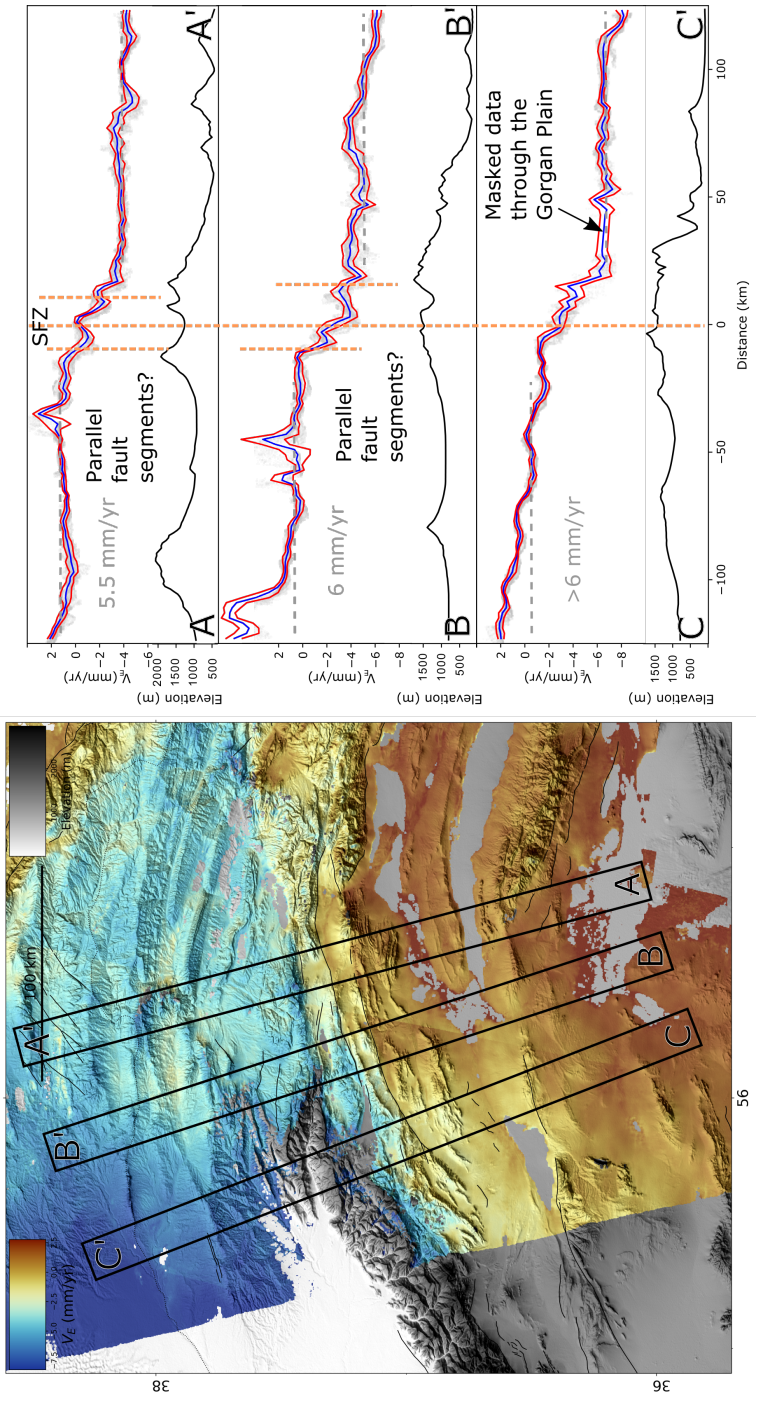


Figure 4.31: Fault-zone perpendicular V_E profiles across the SFZ, showing a velocity step of 5.5–6 mm/yr across the fault zone. Profile swaths have lengths of 250km, with widths of 20 km, and variable strikes from 68–70°.

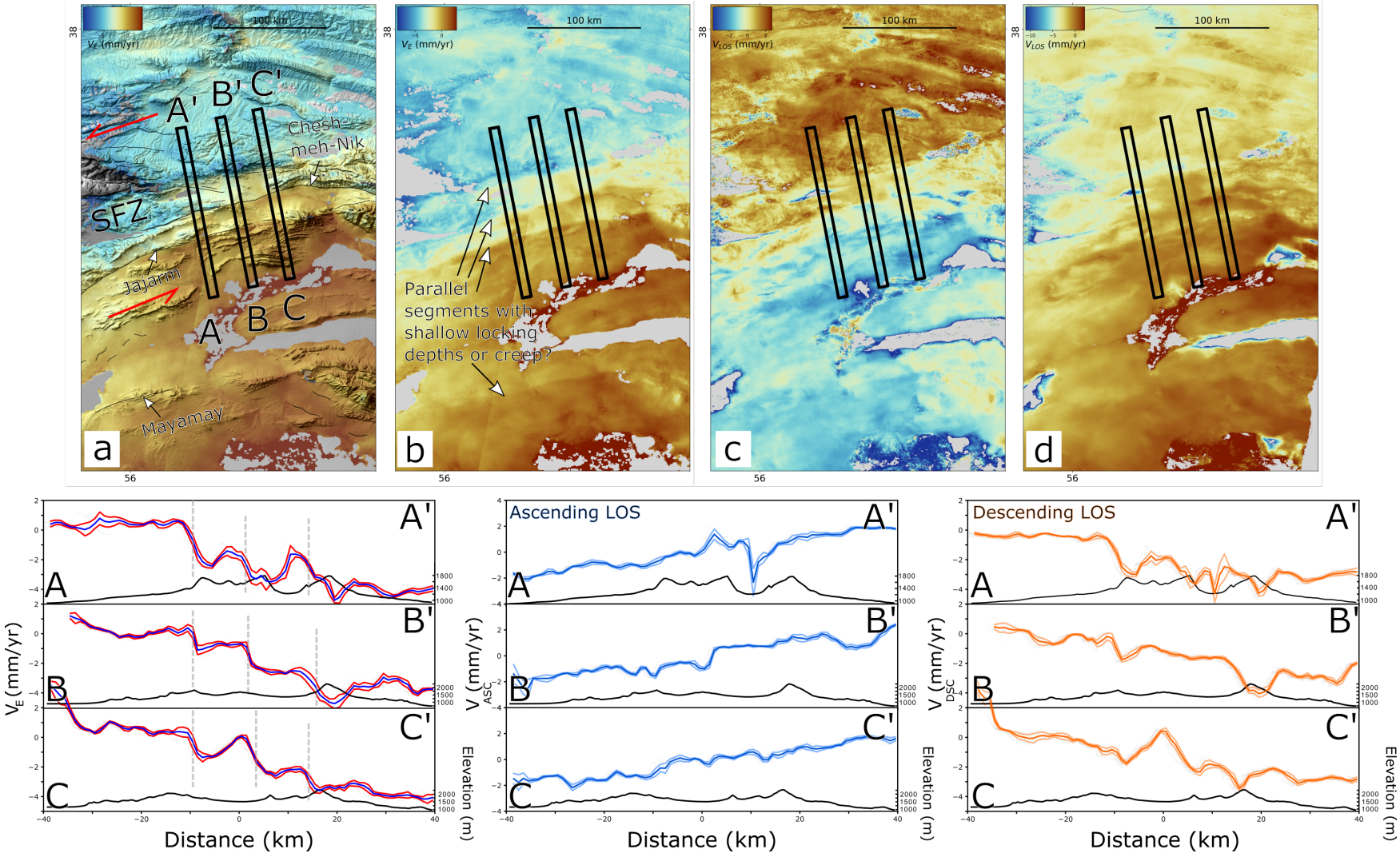


Figure 4.32: Fault-perpendicular profiles across the SFZ, concentrating on the region with evidence for distributed parallel strike-slip motion across a series of faults (including the Jajarm and Cheshmeh-Nik segments). Map panels are: a) V_E with hillshade render, b) V_E, c) ascending LOS, d) descending LOS. In the V_E maps, there is a suggestion that the faults are possibly creeping at the surface or locked at a very shallow depth along previously mapped fault segments (fault map from *Walker et al.* (2021)). However the LOS profiles do not show any conclusive evidence for surface creep.

oriented predominantly strike-slip faults in the BQFZ are not optimally-oriented to be observed in the LOS. However the deformation across the BQFZ is visible in the V_E and V_{UN} components. The westward component of deformation within the SCB wedge of material starts abruptly at the BQFZ, whilst the subvertical component shows that deformation within the BQFZ is constrained by mapped faults in the west and possibly an additional parallel structure in the east (see Figure 4.33d).

From a local seismic hazard perspective, the observed deformation correlates well with the historical seismicity concentrated across the fault zone; which includes the Quchan earthquake sequence (1851, 1871–1872, 1893 and 1895), 1929 Baghan and 1997 Bojnurd earthquakes (*Hollingsworth et al.*, 2006). The BQFZ accommodates ≈5 mm/yr resolved in the V_E component. This appears to predominantly be taken up in the narrow zone of through-going faults mapped by *Hollingsworth et al.* (2006). There is an additional >2 mm/yr resolved in V_{UN}, which could be either from the NNW-SSE oriented strike-slip faults or vertical deformation along accompanying reverse faults. Through examination of the terms in $V_{UN} = -V_N \sin\gamma + V_U \cos\gamma$, V_{UN} is ≈5.75 more sensitive to V_U than V_N. Although there is likely to be variation in V_N across the fault zone.

From a regional tectonic perspective, the observation of westward velocity of the SCB starting abruptly at the BQFZ has implications for proposed regional tectonic and kinematic models through the Köpetdag and NE Iran. There are two broadly competing models presented in Figure 4.34 ((b) *Shabanian et al.* (2009), and (d) *Hollingsworth et al.* (2008) after *McKenzie and Jackson* (1986)). The above observations can only support the model of *Hollingsworth et al.* (2008) as there is no through-going right-lateral shear in the eastern Köpetdag, required in the model from *Shabanian et al.* (2009). This also reinforces the idea proposed by *Jackson et al.* (2002) that the SCB is moving independently from its surroundings, as is not kinematically connected to the faults within eastern Iran (i.e. the *Shabanian et al.*

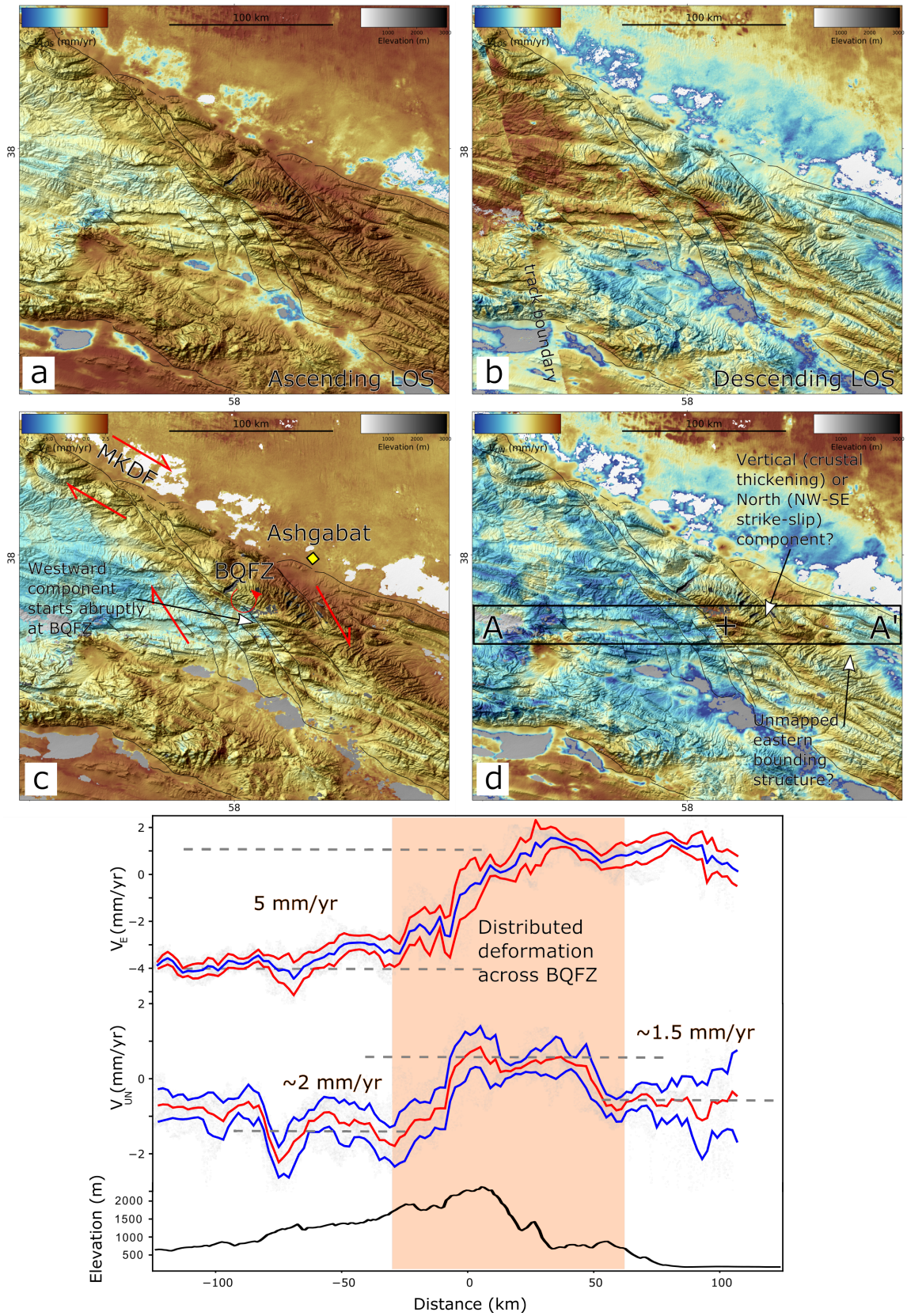


Figure 4.33: East-west profile through the BQFZ (profile length is 250 km, and width is 20 km. Map panels show: a) ascending LOS, b) descending LOS, c) V_E, and d) V_{UN}. The westward component of motion of the SCB starts abruptly at the BQFZ with no evidence for through-going shear. There is a defined signal in the sub-vertical component (d) which is difficult to attribute separately to either vertical or northward motion across the fault zone.

(2009) model).

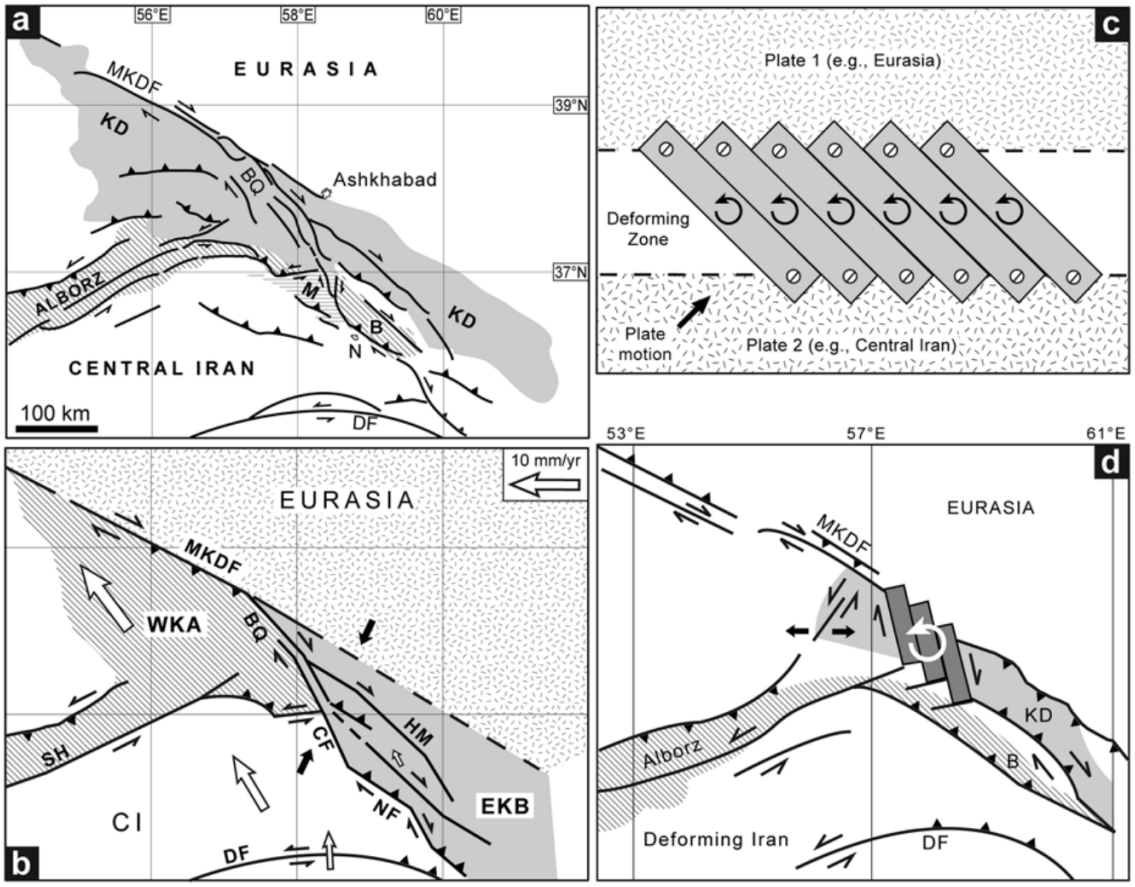


Figure 4.34: From *Shabanian et al.* (2009), competing tectonic kinematic models through the Köpetdag and NE Iran (BQ is BQFZ). a) Fault map of the Köpetdag; b) kinematic model of *Shabanian et al.* (2009); c) vertical axis rotation of pinned tectonic blocks after *McKenzie and Jackson* (1986); and d) the kinematic model of *Hollingsworth et al.* (2008). Note that (b) requires through-going right-lateral shear in the Köpetdag, which *Shabanian et al.* (2009) connects through to the Doruneh fault (DF) and the major N-S oriented strike-slip faults in eastern Iran.

4.4.4 Accommodation of convergence through the eastern Köpetdag

Throughout the eastern Köpetdag, seismicity (e.g. *Ambraseys and Melville*, 2005; *Jackson et al.*, 2002), geomorphology (e.g. *Hollingsworth et al.*, 2006) and GPS velocities (4.5 ± 0.5 mm/yr at 59° E; *Mousavi et al.* (2013)) indicate that north-south

convergence is accommodated along numerous thrust faults. Many of the mapped thrusts faults are from historical earthquake ruptures and now correspond to the location of GPS stations in *Mousavi et al.* (2013), including Neyshabur, Esfarayen and Sabzevar. A section of the V_{UN} component in the velocity decomposition intersects these three thrust systems, shown in Figure 4.35. A broad zone (50–75 km wide) of positive sub-vertical deformation is located between the mapped Sabzevar and Esfarayen thrust faults, instead aligning with two smaller anticlinal ridges inside the valley. The magnitude of this signal is 2–3 mm/yr (V_{UN}). Also located within the anticline-bound valley is a zone of intense agricultural subsidence, however the broad wavelength of this signal outside of this narrow zone presents convincing evidence it is tectonic in origin. It is also not possible to say whether this represents active deformation beneath a younger generation of anticlines or connects kinematically to the mapped reverse faults. However we do not observe any resolvable motion directly across any of the mapped fault systems.

4.4.5 The kinematics of conjugate fault systems and mechanics of lateral extrusion

By projecting the strike-slip components resolved in V_E to fault parallel motion along the MKDF (5.1 ± 0.3 mm/yr, 303°) and SFZ (6.3 ± 0.3 mm/yr, 246°), we can construct a velocity triangle to constrain the kinematics accommodated by the conjugate system. This follows a similar approach to *Walker et al.* (2021) (after *Copley and Jackson* (2006)) and to Chapter 3. However as we do not observe any internal deformation, we assume that the strike-slip motion across the MKDF and SFZ is representative of the motion of the SCB. This yields lower rates to previous studies with the results shown in Figure 4.36. It is important to note that the estimated rate neglects shortening across the frontal thrusts to the MKDF, as this convergence is transferred outside of the conjugate system (shaded area in

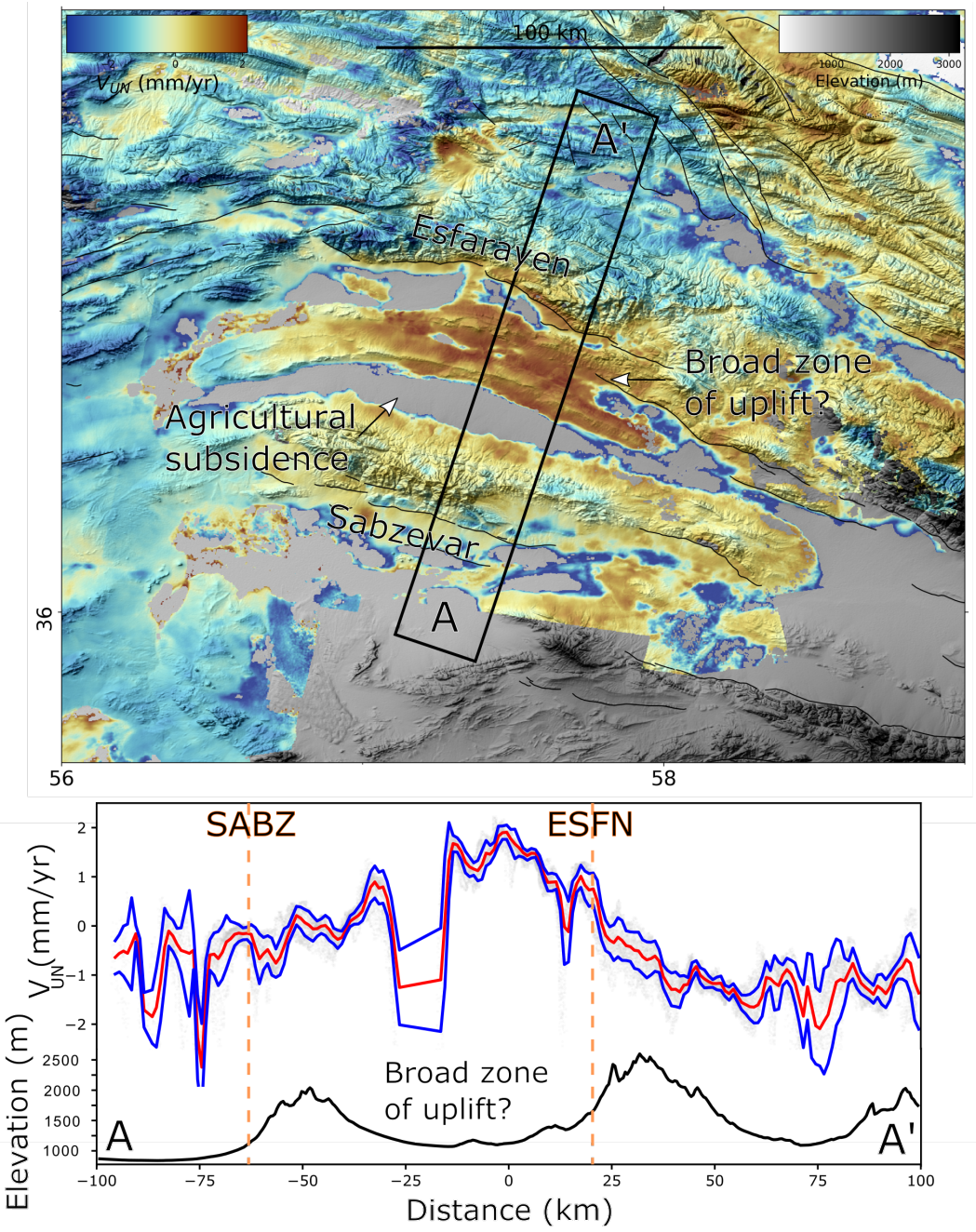


Figure 4.35: V_{UN} profile (length 200km, swath width 20 km) through the Sabzevar and Esfarayen reverse fault systems. There is a broad positive sub-vertical signal (2–3 mm/yr) in the valley between these faults.

Figure 4.36). The component of Arabia-Eurasia convergence accommodated by the MKDF-SFZ is resolved to be 5.6 ± 0.5 mm/yr at 15°. This suggests that much of the Arabia-Eurasia convergence must be accommodated outside of the conjugate system, especially to the south of the SFZ. Th convergence at station KHUR at 55° E is 11.5 ± 0.1 mm/yr in a direction 001° (*Khorrami et al.*, 2019), although it is important to account for the eastward reduction in this rate which has a convergence gradient of ≈-1.2 mm/yr/°E.

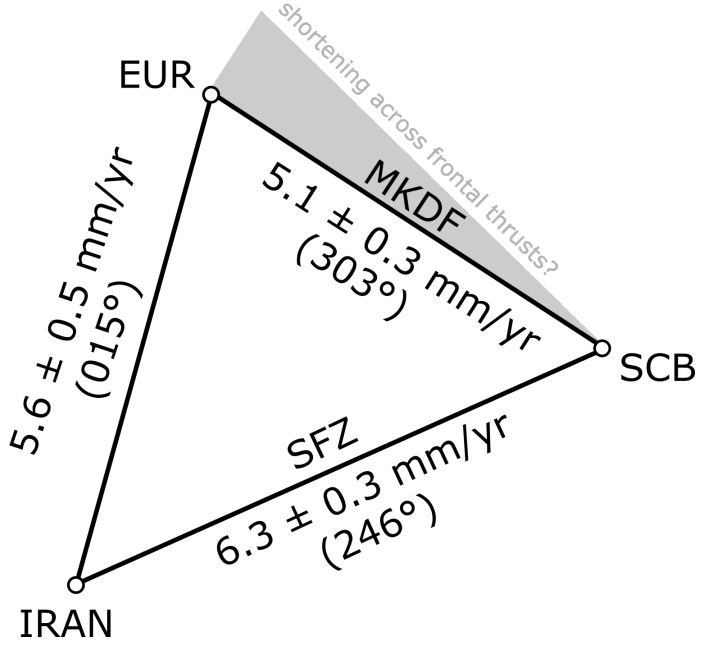


Figure 4.36: By projecting the strike-slip components resolved in V_E to fault parallel motion along the MKDF (5.1 ± 0.3 mm/yr, 303°) and SFZ (6.3 ± 0.3 mm/yr, 246°), we can construct a velocity triangle to constrain the kinematics accommodated by the conjugate MKDF-SFZ system.

The combined motion across the MKDF and SFZ is comparable to other examples of continental conjugate strike-slip fault systems. Comparison of these fault systems could be used in future to probe the rheology within conjugate fault systems and the mechanics of lateral extrusion in the continents. The best resolved of these is the conjugate North Anatolian and East Anatolian fault systems (NAF and EAF), which facilitate the westward extrusion of Anatolia also within the Arabia-Eurasia

collision (e.g. *Weiss et al.*, 2020; *Hussain et al.*, 2016). Similar to the MKDF-SFZ, the NAF-EAF is a conjugate set of predominantly strike-slip faults with opposing slip-directions, resulting in lateral extrusion of the material between them. Likewise the NAF and EAF have near-linear fault traces, which extend for approximately 1500 km and 500 km respectively, and the internal angle of the conjugate is very comparable to the MKDF-SFZ. The extrusion of the Anatolia block is at 20-25 mm/yr (e.g. *Weiss et al.*, 2020; *Floyd et al.*, 2010), which is two to three times the proposed rate of motion for the SCB (e.g. *Copley and Jackson*, 2006; *Mousavi et al.*, 2013). However in comparison to the MKDF-SFZ which we show to have approximately equal rates of motion across them (Figure 4.26), strain is predominantly accommodated along the NAF (e.g. *Weiss et al.*, 2020; *Cavalié and Jónsson*, 2014) (see Figure 4.37). This difference could be explained by differences in boundary conditions surrounding the Anatolian plate and SCB, internal variations in gravitational potential energy driving lateral extrusion, and the rheology of the lithosphere in these regions (e.g. *England et al.*, 2016).

Another continental conjugate fault comparison can be made with the Vakhsh fault and the Darvaz fault, which meet to the NE of the Tajik depression and to the NW of the Pamir (see Figure 4.38). These faults act as a conjugate system which laterally extrude material from the Pamir Plateau into the Tajik Depression to the southwest (e.g. *Ratschbacher et al.*, 1991; *Ischuk et al.*, 2013). However the interaction of these fault systems between the western Pamir and southwestern Tien Shan, which confine the NE narrowing Tajik Basin, appears more complex than that of the MKDF-SFZ. Instead the Vakhsh fault zone is a dextral-transpressive fault (e.g. *Trifonov*, 1978), and the opposing Darvaz fault (N-NE striking) has been shown to have sinistral-transtensional motion (*Metzger et al.*, 2020). The rates of motion are also highly variable along these faults in both the fault-parallel and fault-perpendicular components (see Figure 4.38),

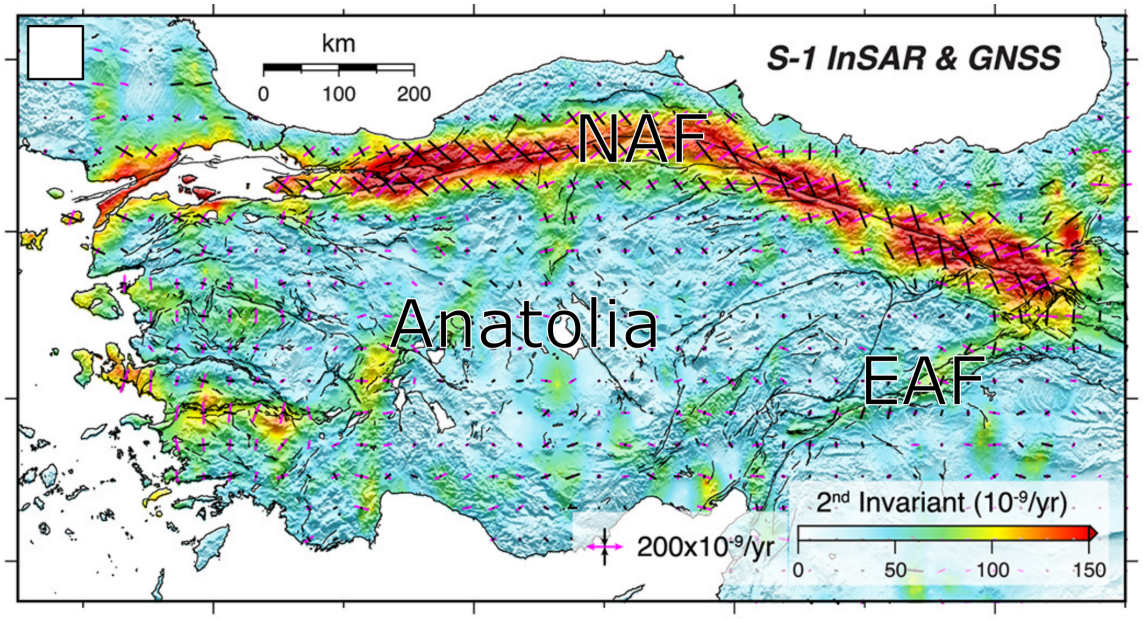


Figure 4.37: From *Weiss et al.* (2020), strain rate map showing the second invariant of the stress tensor, or the magnitude of horizontal strains, from the joint inversion of GPS and Sentinel-1 velocities in Anatolia, with strain predominantly accommodated along the North Anatolian Fault (NAF), and also along the East Anatolian Fault (EAF) to the southeast.

which is possibly a reflection of their variable orientation along strike; especially when compared to the linearity in both the MKDF-SFZ and NAF-EAF conjugate systems. Similarly the internal angle between the conjugate faults here is much narrower than that of either the MKDF-SFZ or NAF-EAF conjugate systems. The mechanics of lateral extrusion here are evidently different, and the contrasts possibly reflect the complexity along the block boundaries of the Tajik Depression and the uncertain boundary conditions along the western margin (personal communications with Roberta Wilkinson, University of Oxford; 2021). In the case of both the South Caspian and Anatolia there is a rigid block immediately to the north, whereas the Tajik Basin is adjacent to the Tien Shan mountain range, and so it might be rheological contrasts that control these differences. Similarly the rheology of the block inside the conjugate fault systems may be controlling the geometry; in the Tajik Basin there is evidently significant internal deformation with a fold and thrust

belt, whereas in the case of the South Caspian it seems to be more rigid.

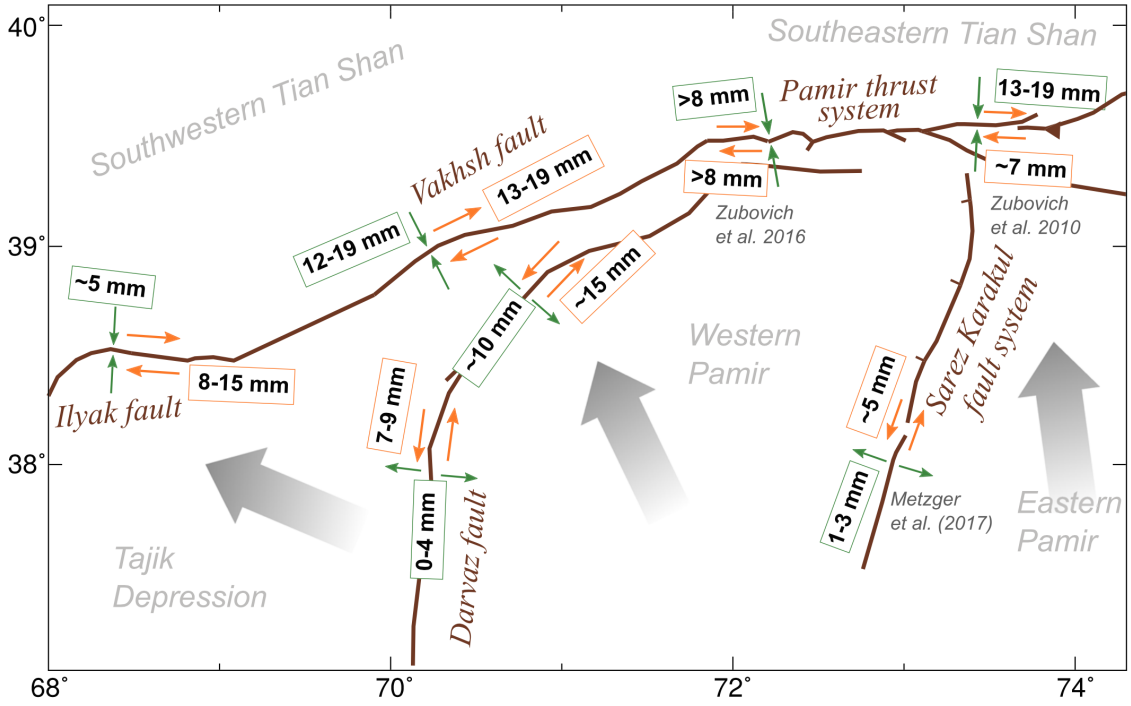


Figure 4.38: Kinematics of the Tajik depression from *Metzger et al.* (2020). The Vakhsh fault and the Darvaz fault comprise a complex conjugate fault system, with dextral-transpressive motion (*Metzger et al.*, 2020) and sinistral-transtensional motion (e.g. *Trifonov*, 1978) respectively.

4.5 Conclusion

We present velocity fields derived from Sentinel-1 InSAR time-series from both ascending and descending LOS, and decompose these into the V_E and V_{UN} components, covering a 600 km × 600 km region of the onshore extension of the SCB, Köpetdag interior and eastern Alborz. The LOS velocity fields are referenced to a stable Eurasia reference field using GPS stations within NE Iran and the assumption that the velocity of the Turan platform is zero within the same reference frame. This provides a spatially-continuous image of the westward extrusion of the SCB.

The extrusion is facilitated by strike-slip motion along the MKDF and SFZ, which

have distinct velocity steps resolved in the V_E component of 4–4.5 mm/yr and 5.5–6 mm/yr respectively. Projecting this velocity-step to fault parallel motion provides lower-bound fault parallel slip-rates along these faults of 4.8–5.4 mm/yr along the MKDF and 6.0–6.6 mm/yr along the SFZ. However the velocity fields suggest the interior of the SCB may be moving faster than this, ≈-8 mm/yr in the V_E component relative to the Turan platform. This is reflected in the westernmost profiles across the conjugate faults, which resolve faster V_E velocity steps of >7 mm/yr along the MKDF and >6.5 mm/yr along the SFZ, although we note this signal might be non-tectonic in origin. The velocity of the faster-moving interior appears to stabilise from the descending LOS, and the future inclusion of an additional ascending LOS track (A057) through the East Caspian Lowlands will be used to confirm this observation. We compare the observed kinematic behaviour across the MKDF-SFZ conjugate fault system to other continental conjugate fault systems, which we suggest could be used in future to probe the rheology within conjugate fault systems and the mechanics of lateral extrusion in the continents.

In addition, we resolve deformation along numerous tectonic structures within the Köpetdag and Eastern Alborz, which we interpret as resulting from interseismic deformation at depth. Along the MKDF, the V_{UN} component supports LOS observations in Chapter 3 for greater than 1 mm/yr of uplift from deformation extending beneath the mapped frontal thrust faults from *Walker et al.* (2021), and concentrating around structural barriers to rupture identified in Chapter 2. We also suggest the MKDF is a plate-boundary type fault, supporting evidence presented in Chapter 2. We observe distributed deformation through the SFZ across a network of parallel faults, with the Jajarm, Cheshmeh-Nik, Mayamar segments (and an additional previously unmapped segment to the north) suggested to be locked at very shallow depths. The westward component of deformation in the SCB wedge starts abruptly at the BQFZ, which accommodates ≈5 mm/yr resolved in the V_E

component, and 1.5–2 mm/yr resolved in V_{UN}. This provides evidence that supports the tectonic model proposed for the region by *Hollingsworth et al.* (2008), but not that proposed by *Shabanian et al.* (2009) which requires through-going right-lateral shear in the eastern Köpetdag. Finally we observe a strong (2–3 mm/yr) subvertical component in the eastern Köpetdag in close proximity to the Neyshabur, Esfarayen and Sabzevar thrust fault systems; all of which have historically-recorded earthquake ruptures (e.g. *Hollingsworth et al.*, 2006). However the signal we observe is not aligned with any of these structures, and is instead aligned to two lower-relief anticlinal ridges located within a valley bounded by the Esfarayen and Sabzevar thrusts.

Supplementary

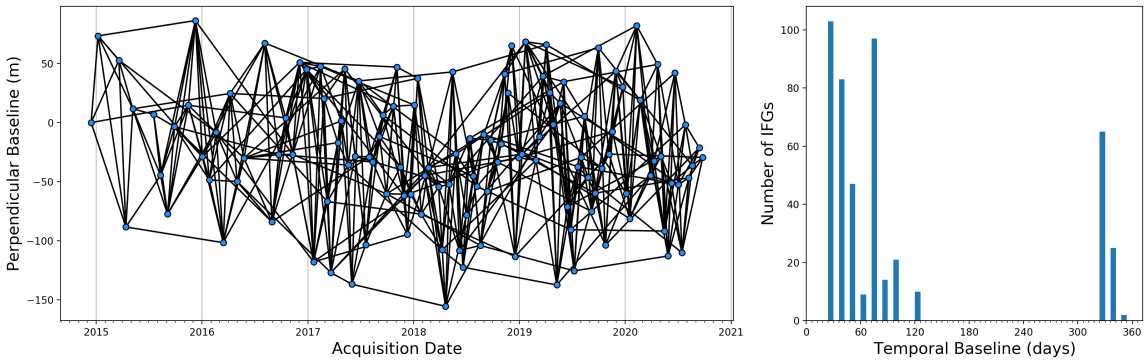


Figure 4.39: Perpendicular baseline versus temporal baseline plots for track D137N after the removal of IFGs with short temporal baselines from the network, with a histogram of temporal baselines also shown.

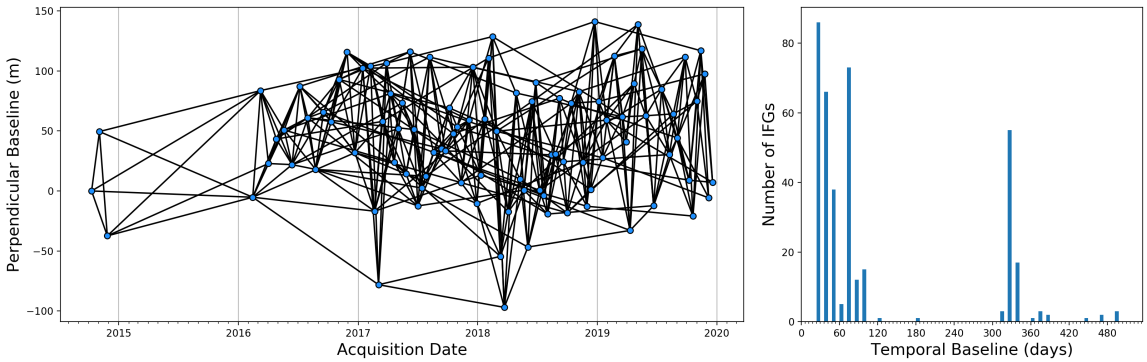


Figure 4.40: Perpendicular baseline versus temporal baseline plots for track D064N after the removal of IFGs with short temporal baselines from the network, with a histogram of temporal baselines also shown.

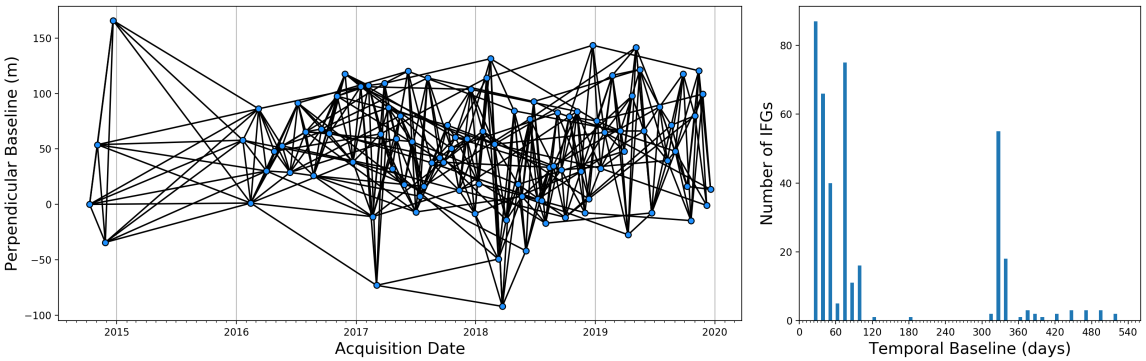


Figure 4.41: Perpendicular baseline versus temporal baseline plots for track D064S after the removal of IFGs with short temporal baselines from the network, with a histogram of temporal baselines also shown.

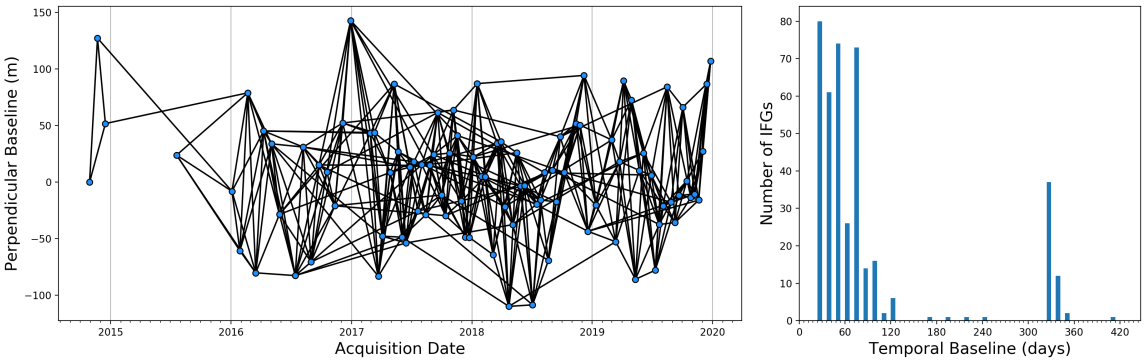


Figure 4.42: Perpendicular baseline versus temporal baseline plots for track D166 after the removal of IFGs with short temporal baselines from the network, with a histogram of temporal baselines also shown.

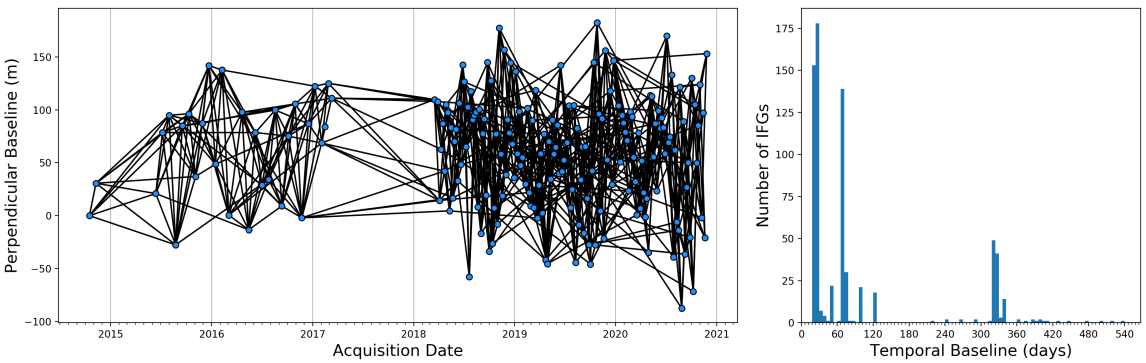


Figure 4.43: Perpendicular baseline versus temporal baseline plots for track A159N after the removal of IFGs with short temporal baselines from the network, with a histogram of temporal baselines also shown.

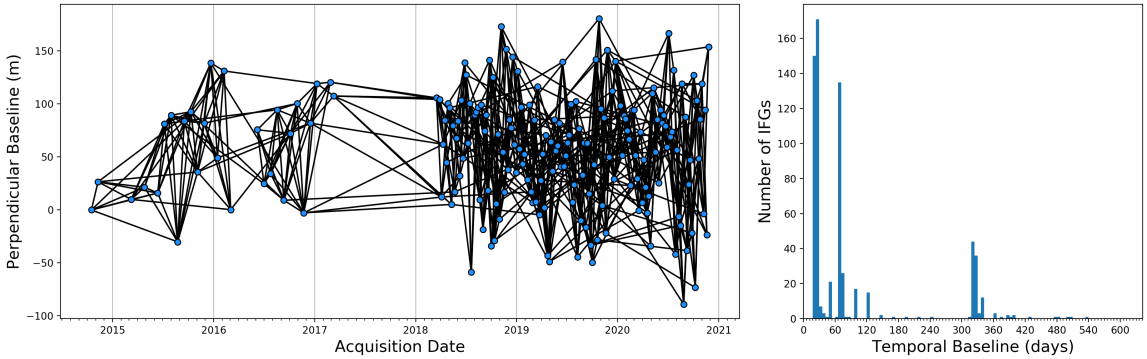


Figure 4.44: Perpendicular baseline versus temporal baseline plots for track A159S after the removal of IFGs with short temporal baselines from the network, with a histogram of temporal baselines also shown.

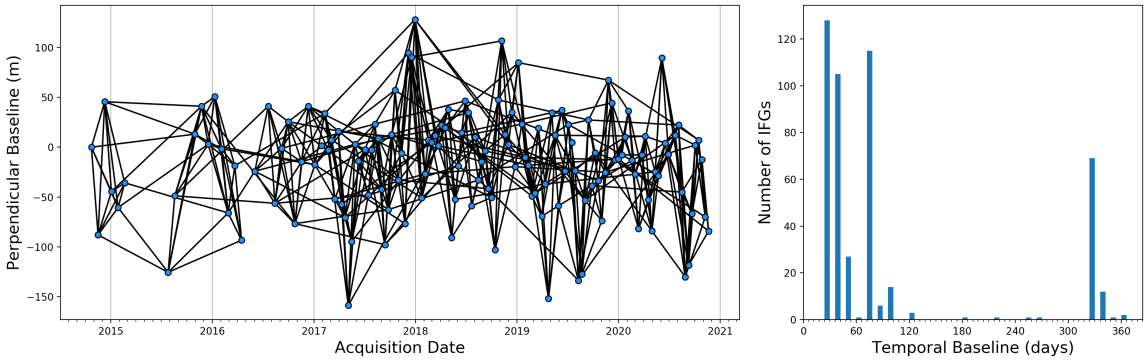


Figure 4.45: Perpendicular baseline versus temporal baseline plots for track A086 after the removal of IFGs with short temporal baselines from the network, with a histogram of temporal baselines also shown.

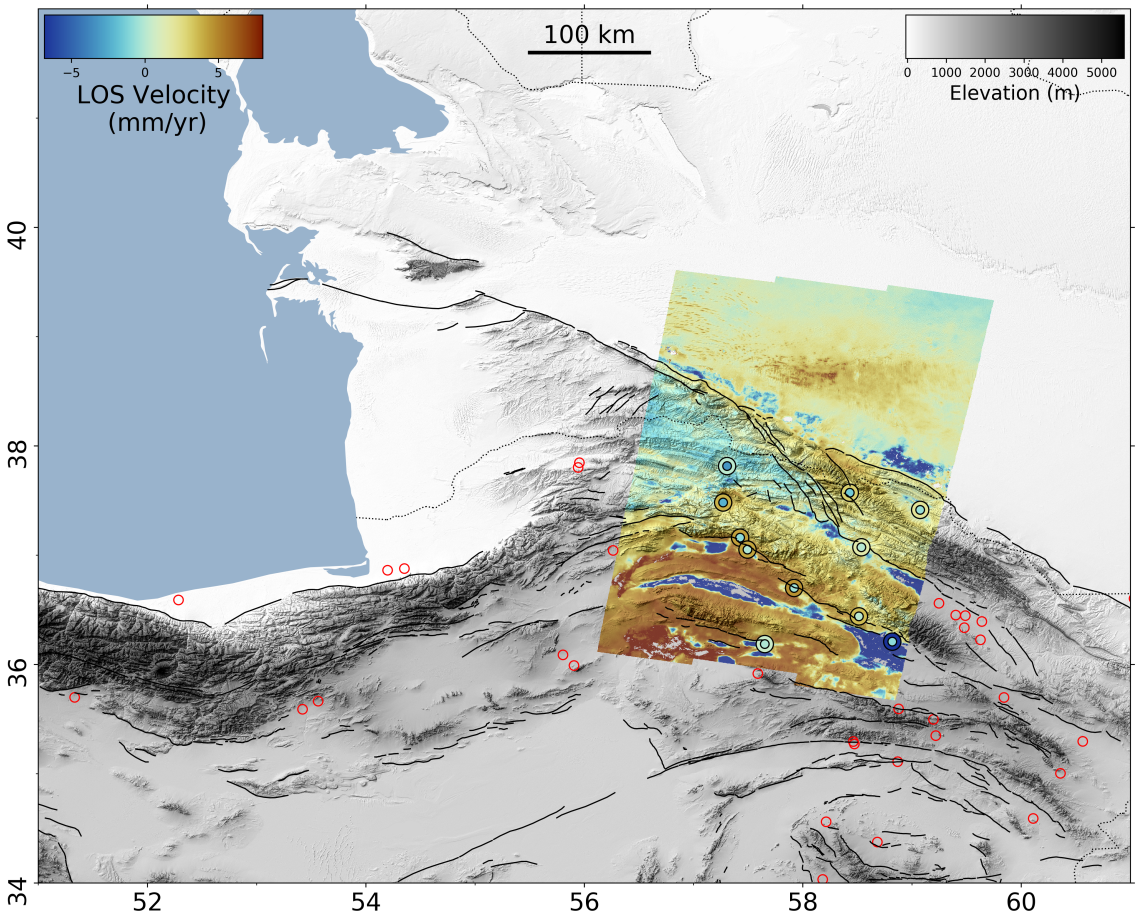


Figure 4.46: LOS velocity field for frame D166. Also shown are the distribution of GPS stations from *Mousavi et al.* (2013) (red circles), with the inside circle showing the GPS velocity projected into the LOS and the outside circle the InSAR LOS velocity at the same location (prior to referencing).

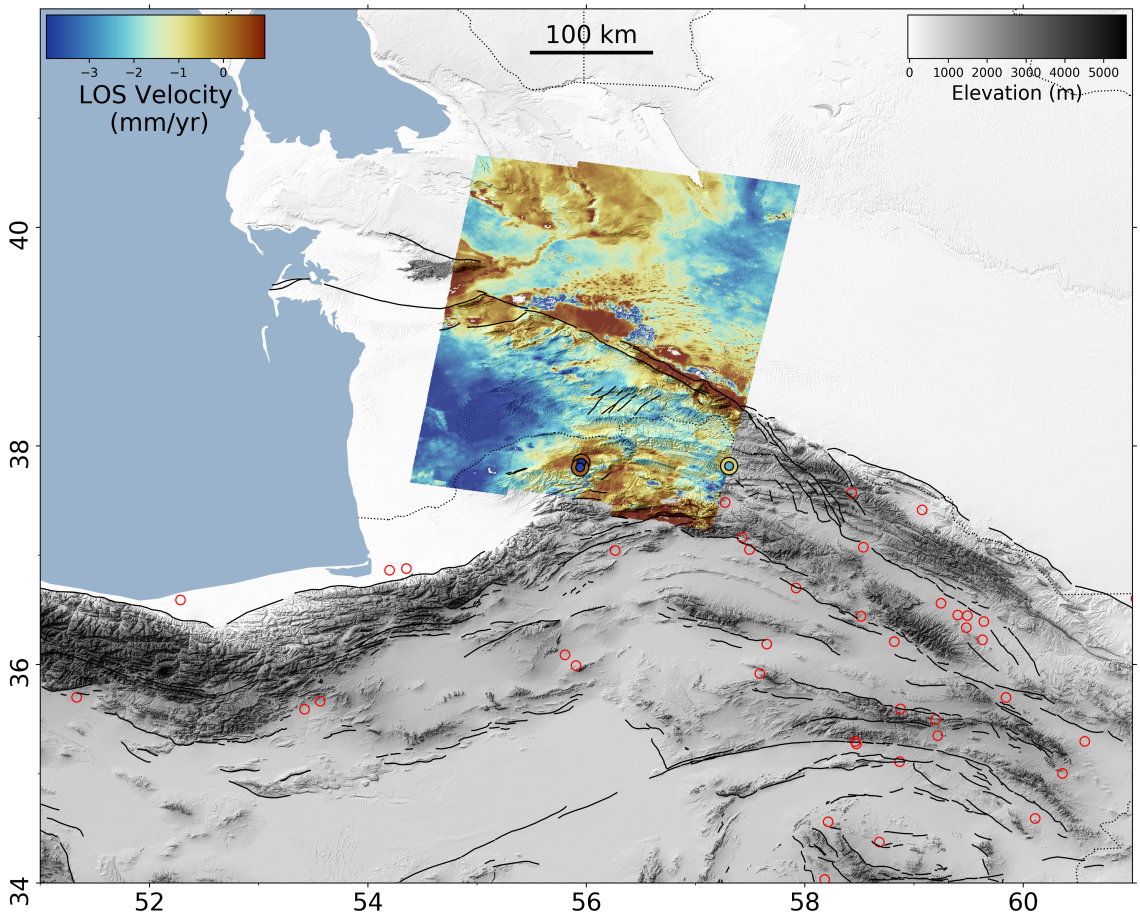


Figure 4.47: LOS velocity field for frame D064N. Also shown are the distribution of GPS stations from *Mousavi et al.* (2013) (red circles), with the inside circle showing the GPS velocity projected into the LOS and the outside circle the InSAR LOS velocity at the same location (prior to referencing).

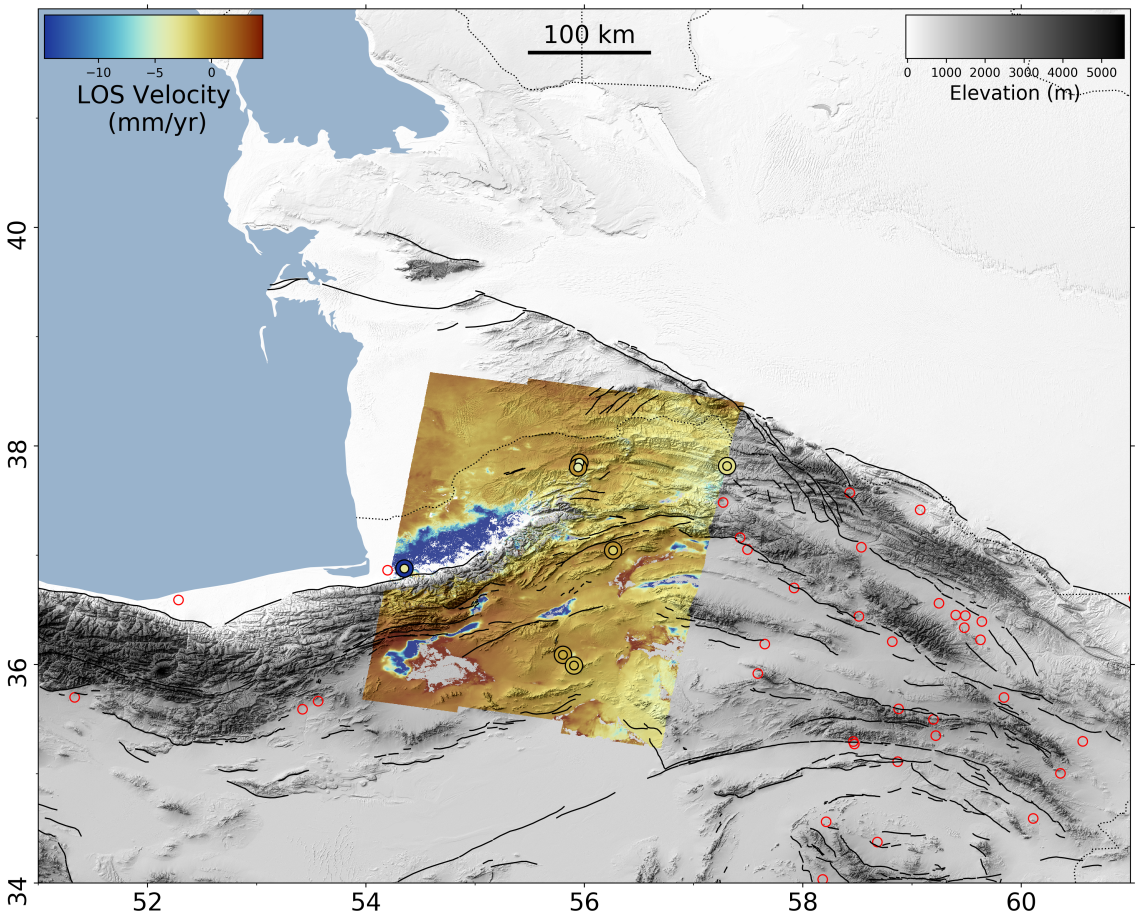


Figure 4.48: LOS velocity field for frame D064S. Also shown are the distribution of GPS stations from *Mousavi et al.* (2013) (red circles), with the inside circle showing the GPS velocity projected into the LOS and the outside circle the InSAR LOS velocity at the same location (prior to referencing).

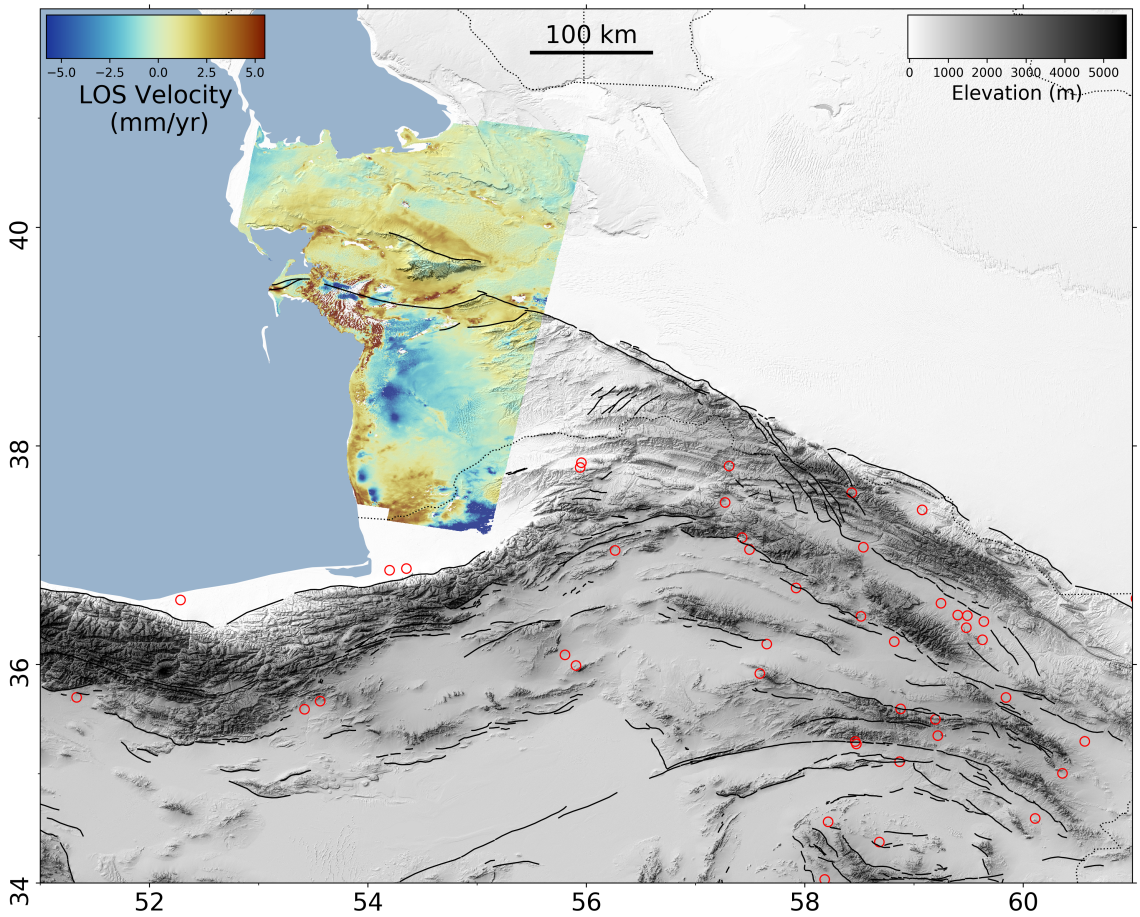


Figure 4.49: LOS velocity field for frame D137N. Also shown are the distribution of GPS stations from *Mousavi et al.* (2013) (red circles), with the inside circle showing the GPS velocity projected into the LOS and the outside circle the InSAR LOS velocity at the same location (prior to referencing).

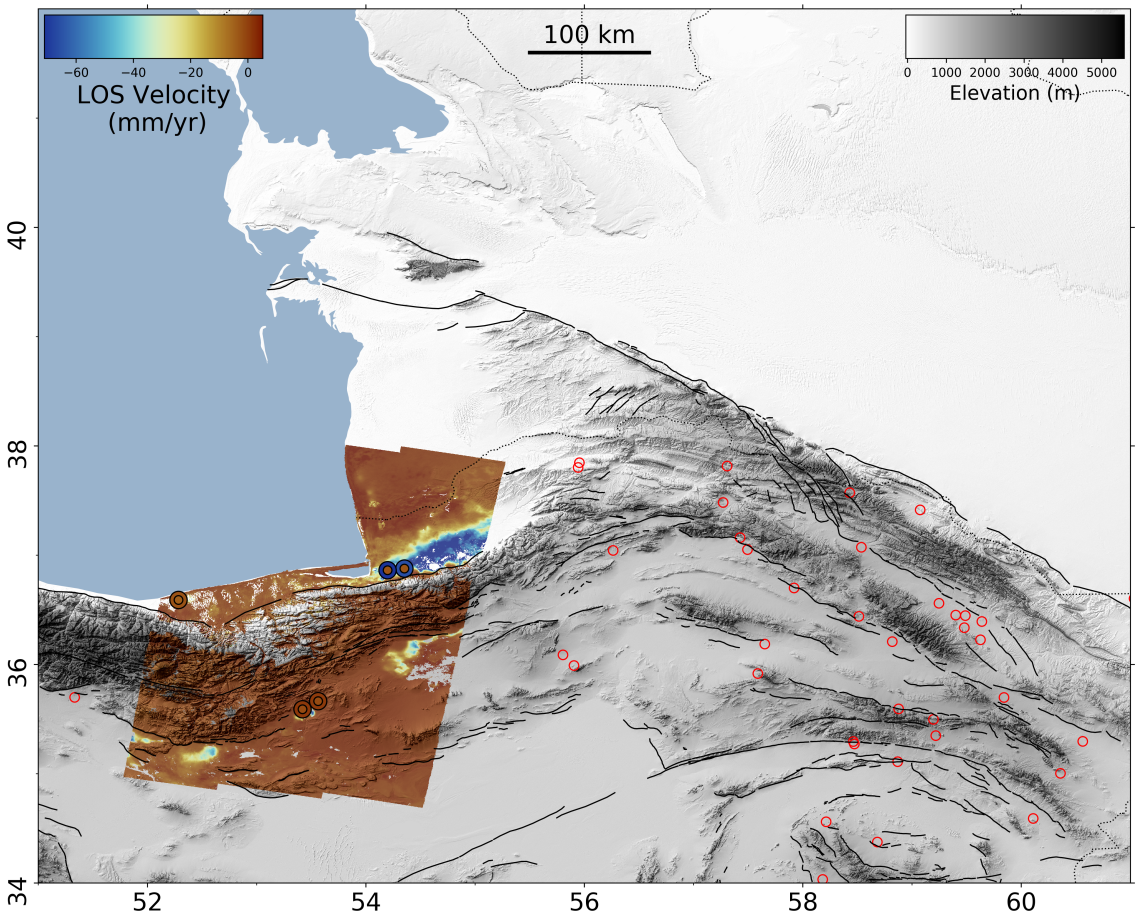


Figure 4.50: LOS velocity field for frame D137S. Also shown are the distribution of GPS stations from *Mousavi et al.* (2013) (red circles), with the inside circle showing the GPS velocity projected into the LOS and the outside circle the InSAR LOS velocity at the same location (prior to referencing).

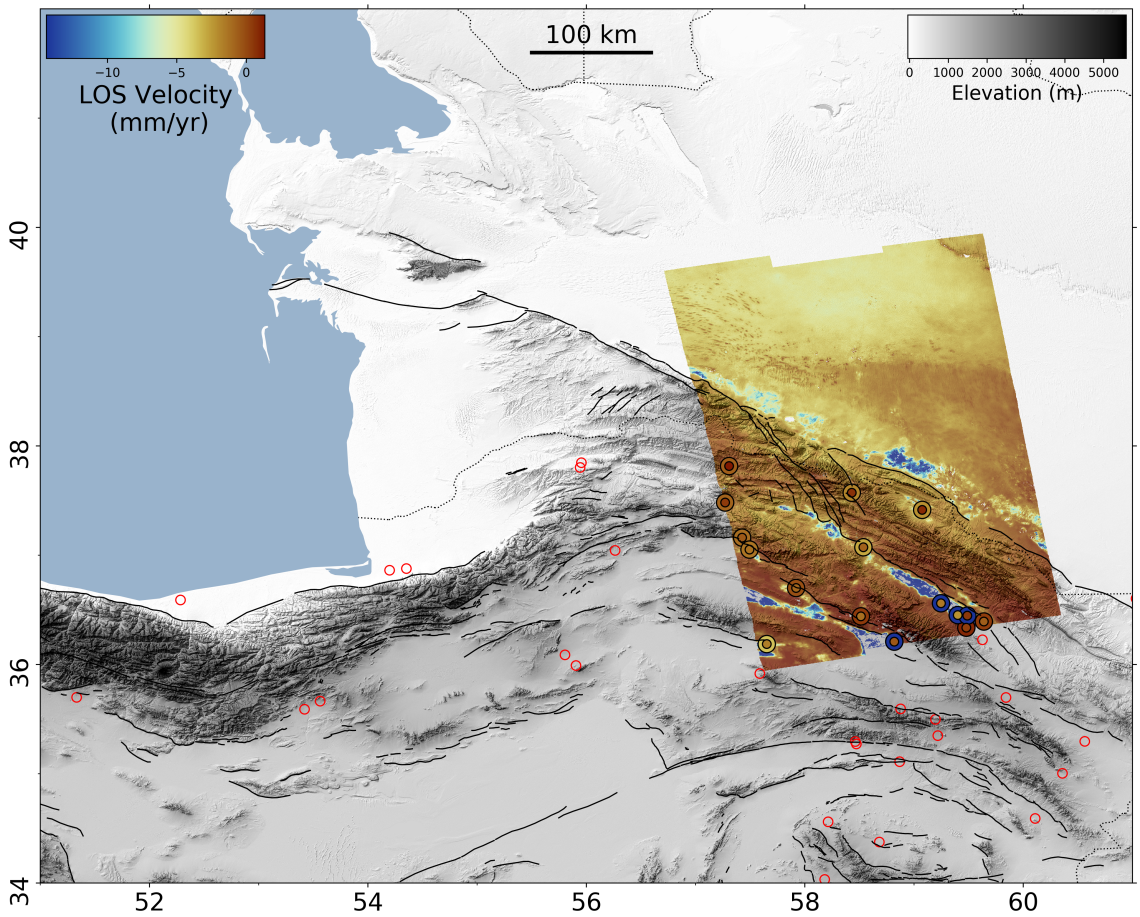


Figure 4.51: LOS velocity field for frame A086. Also shown are the distribution of GPS stations from *Mousavi et al.* (2013) (red circles), with the inside circle showing the GPS velocity projected into the LOS and the outside circle the InSAR LOS velocity at the same location (prior to referencing).

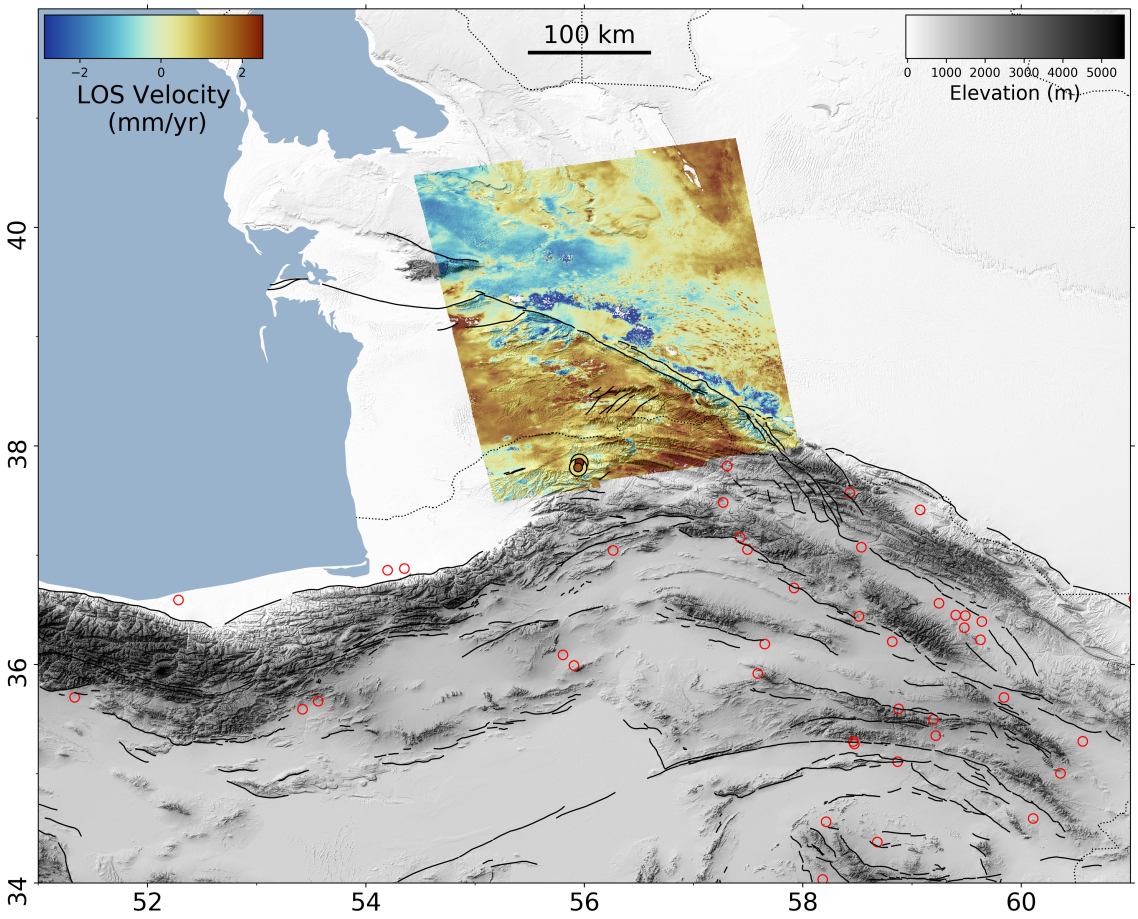


Figure 4.52: LOS velocity field for frame A159N. Also shown are the distribution of GPS stations from *Mousavi et al.* (2013) (red circles), with the inside circle showing the GPS velocity projected into the LOS and the outside circle the InSAR LOS velocity at the same location (prior to referencing).

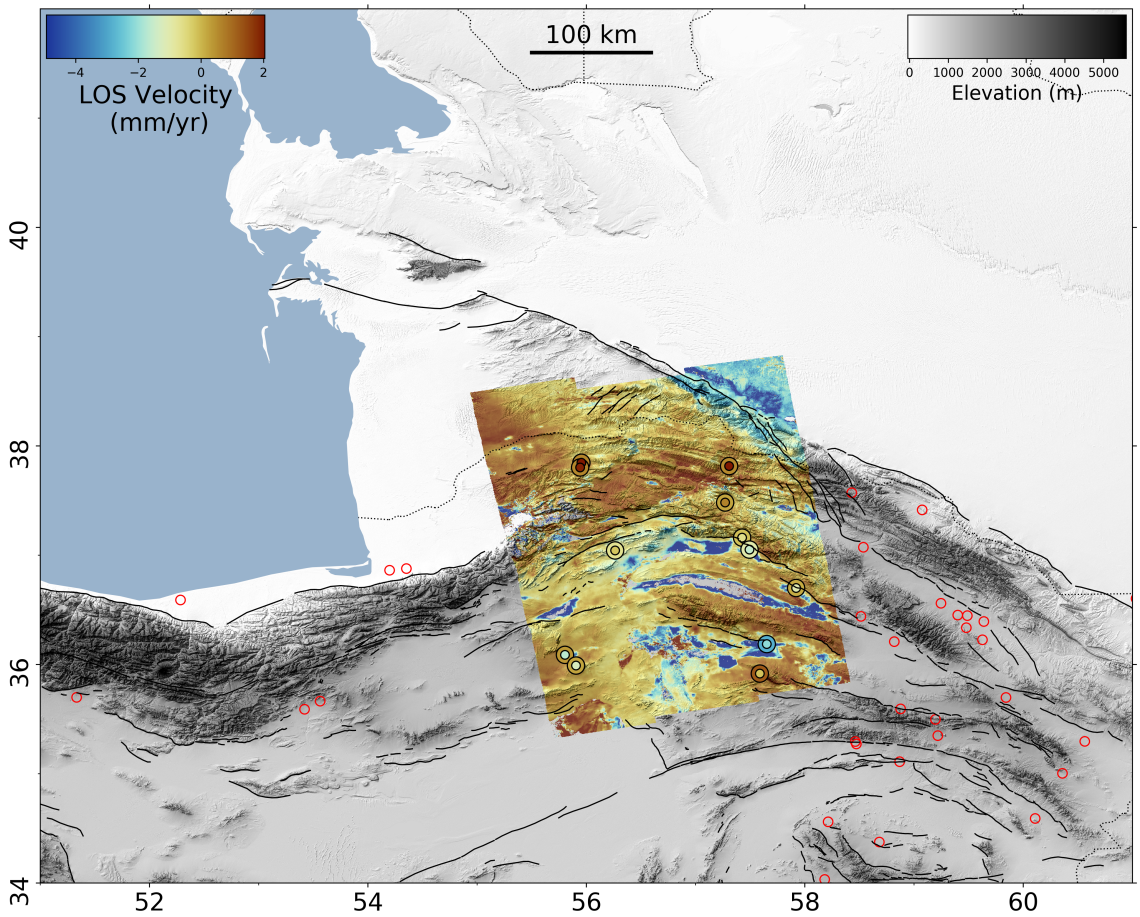


Figure 4.53: LOS velocity field for frame A159S. Also shown are the distribution of GPS stations from *Mousavi et al.* (2013) (red circles), with the inside circle showing the GPS velocity projected into the LOS and the outside circle the InSAR LOS velocity at the same location (prior to referencing).

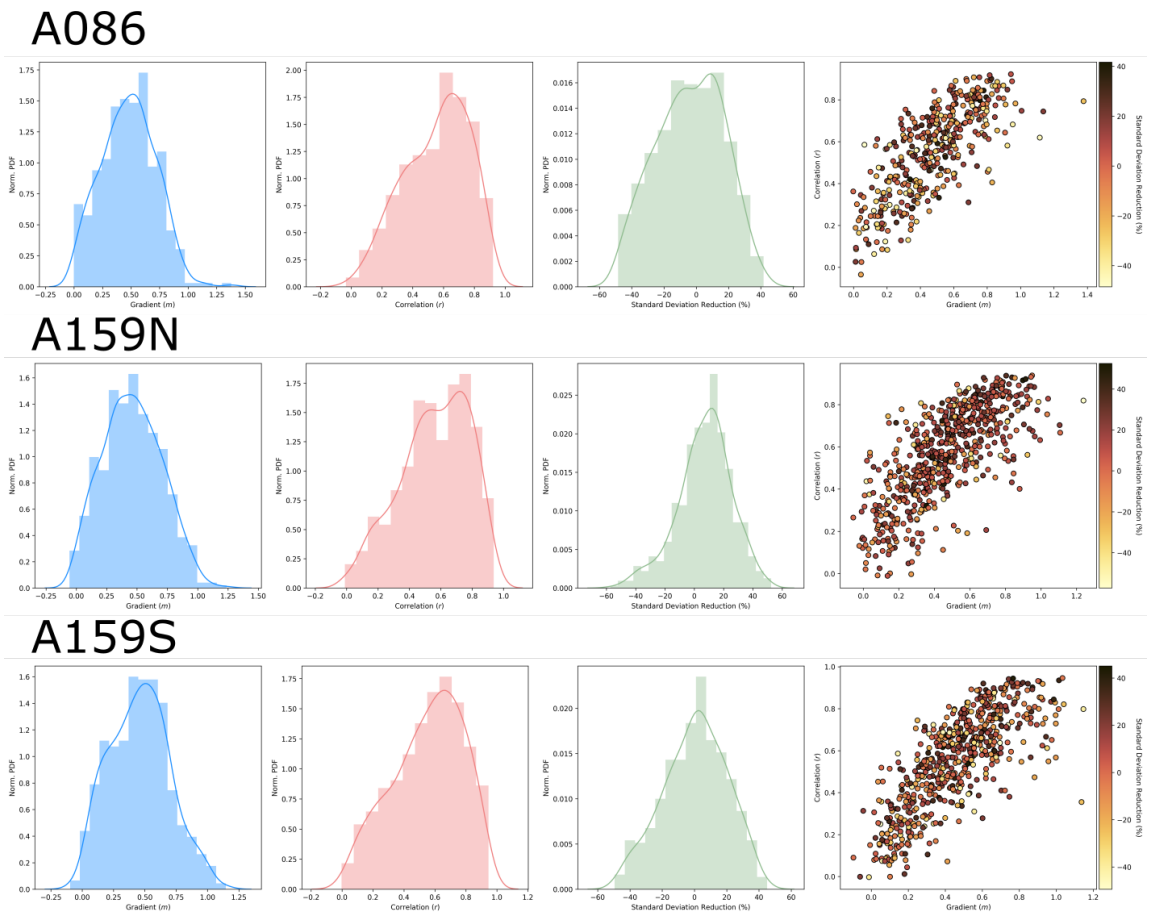


Figure 4.54: Ascending frames performance metrics for GACOS corrections on interferograms in each frame network. Performance metrics are explained in detail in Chapter 3.

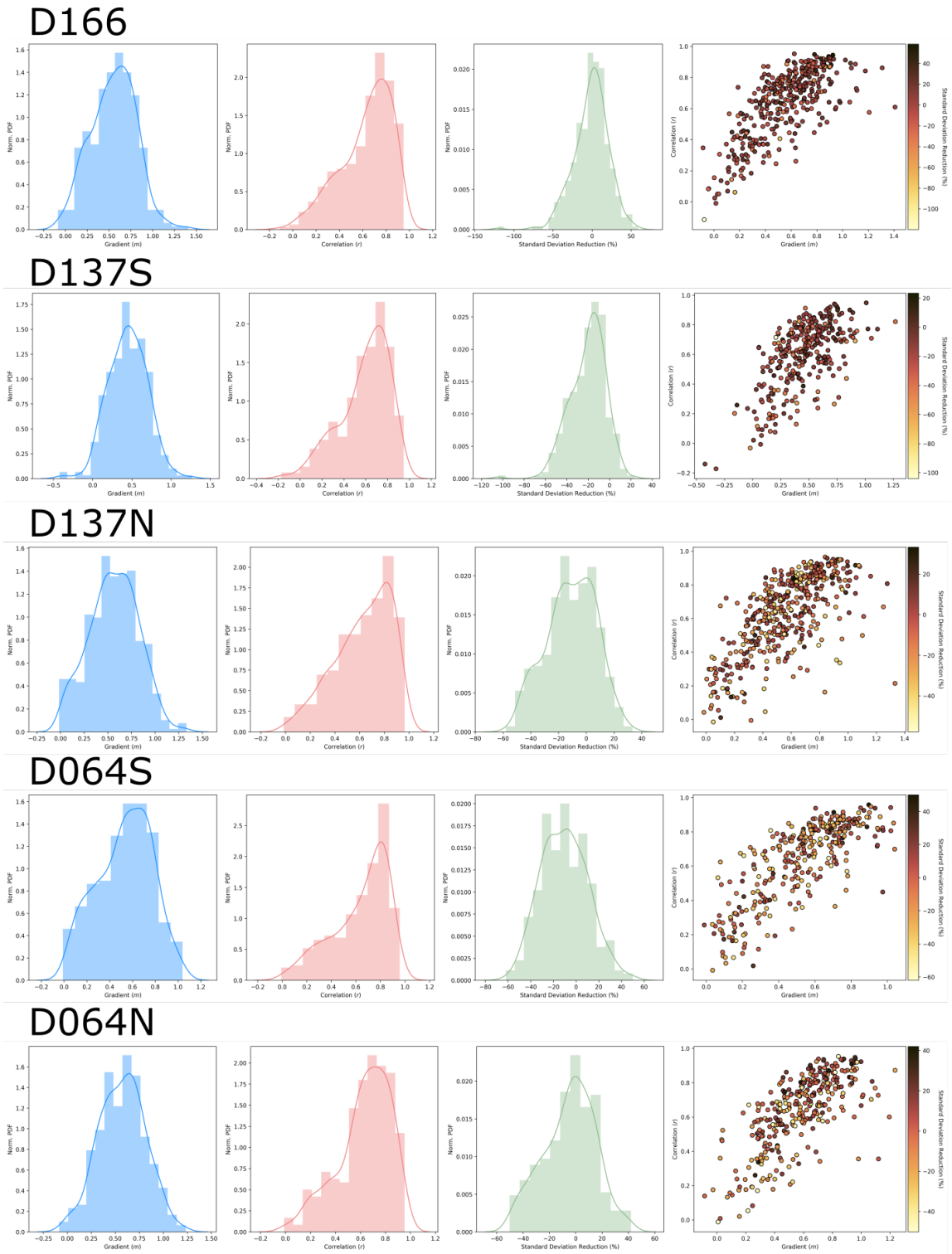


Figure 4.55: Descending frames performance metrics for GACOS corrections on interferograms in each frame network. Performance metrics are explained in detail in Chapter 3.

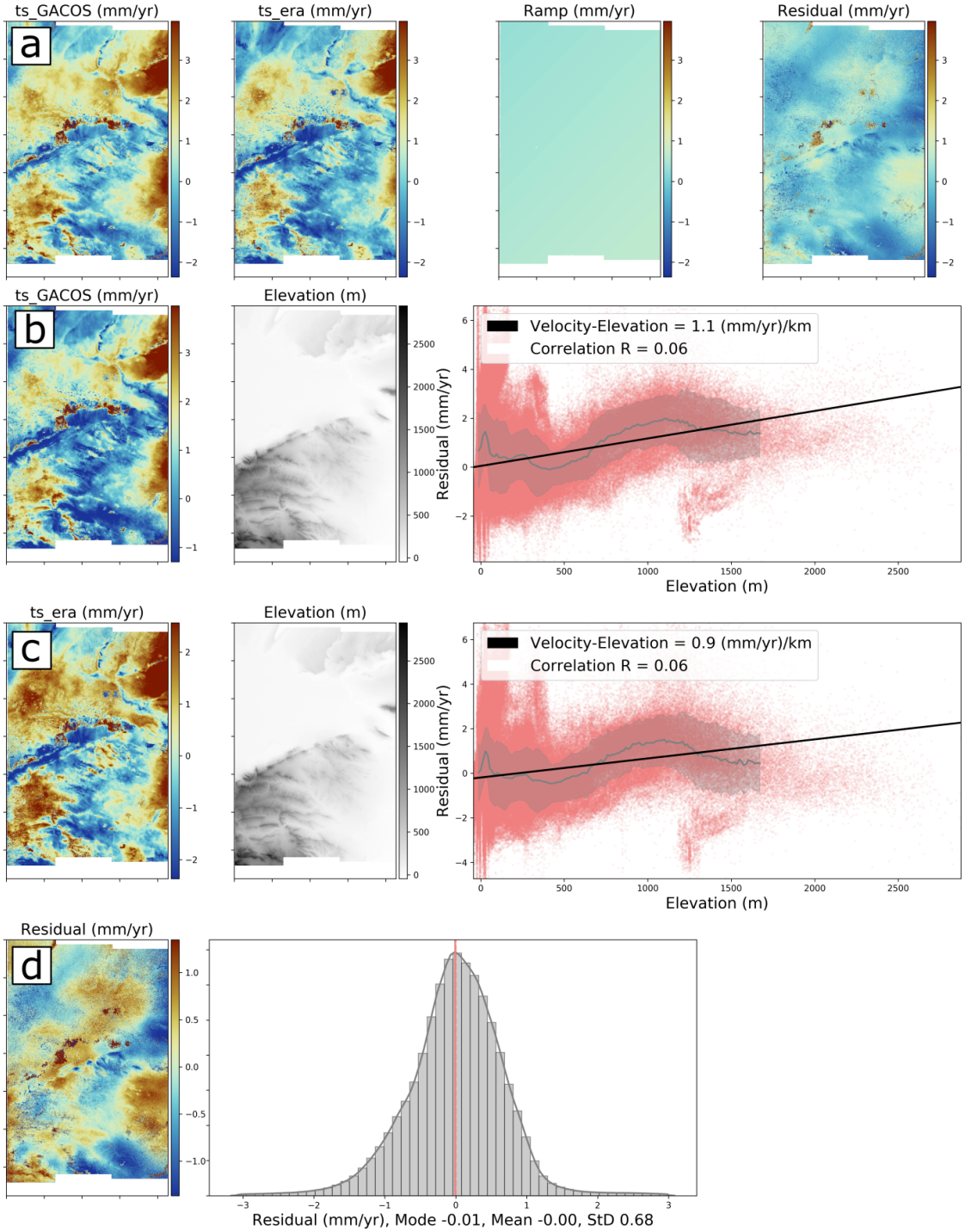


Figure 4.56: Comparison of GACOS corrected and ERA5 corrected time-series for D064N in radar geometry. a) The output time-series for D064 for the GACOS corrected time-series, the ERA5 corrected timeseries, a ramp estimated to tie these time-series together, and the residual of the overlap. b) and c) are the GACOS corrected and ERA5 corrected time-series plotted against elevation. d) The residuals (note the colour scale limits are compressed versus the top row) show differences introduced by the different tropospheric correction models.

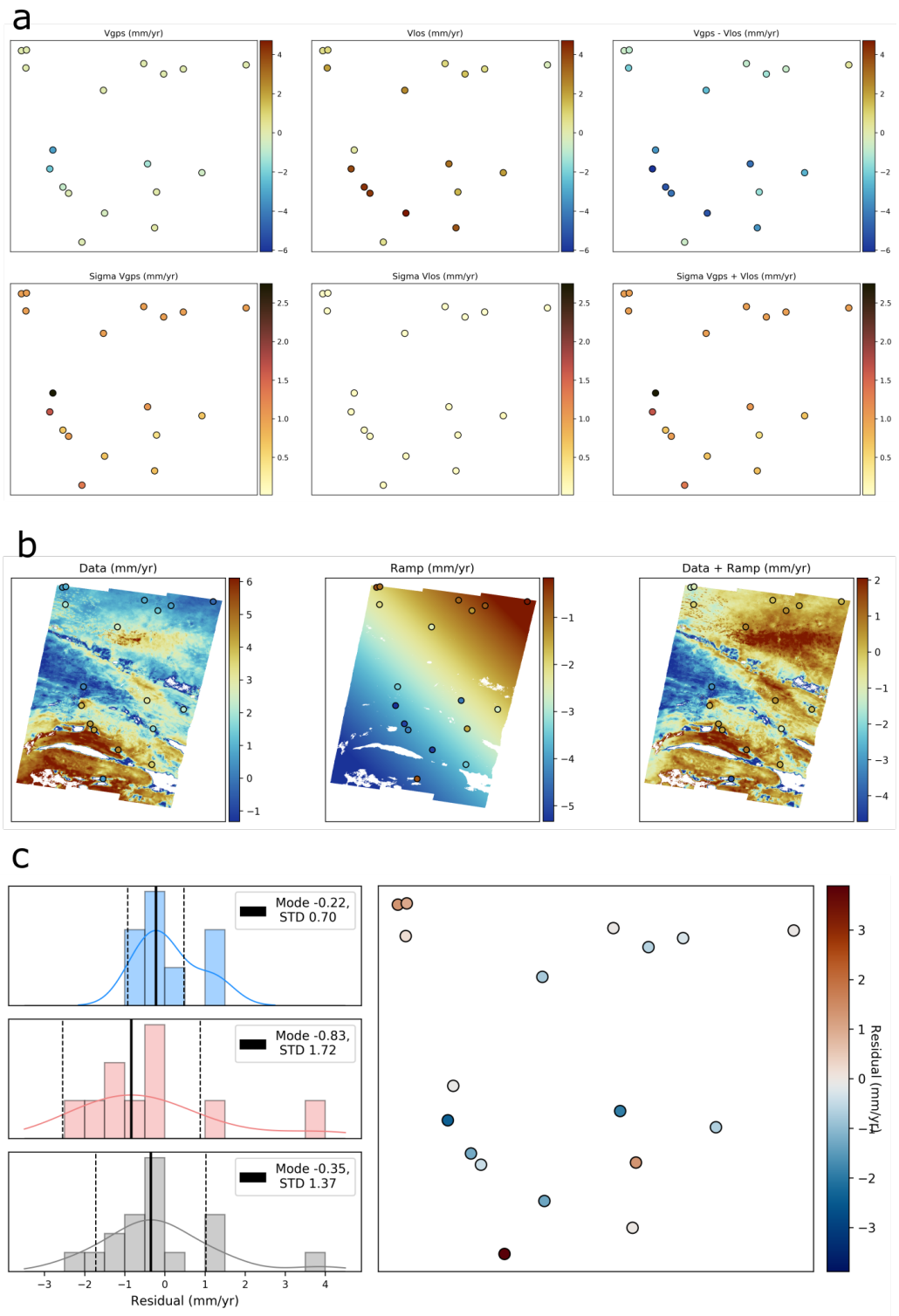


Figure 4.57: Referencing the LOS velocity field for D166 with GPS (approximate stable Eurasia reference frame). a) Distribution of GPS stations from the NE Iran network (*Mousavi et al.*, 2013) comprise the southern stations, and "dummy" Turan GPS stations the southern stations, that overlap the LOS velocity field with their velocity and standard error projected into the LOS; also shown are the extracted LOS values at the same point, and the residuals between the GPS values and the LOS. b) Shows the GPS ramp estimation and tying procedure, which applies a linear tilt to bring the LOS into the stable Eurasia reference frame of the GPS data. c) The residuals of this ramp estimation procedure, with the histograms divided to show the different networks (blue is Turan, red is NE Iran, grey is combined).

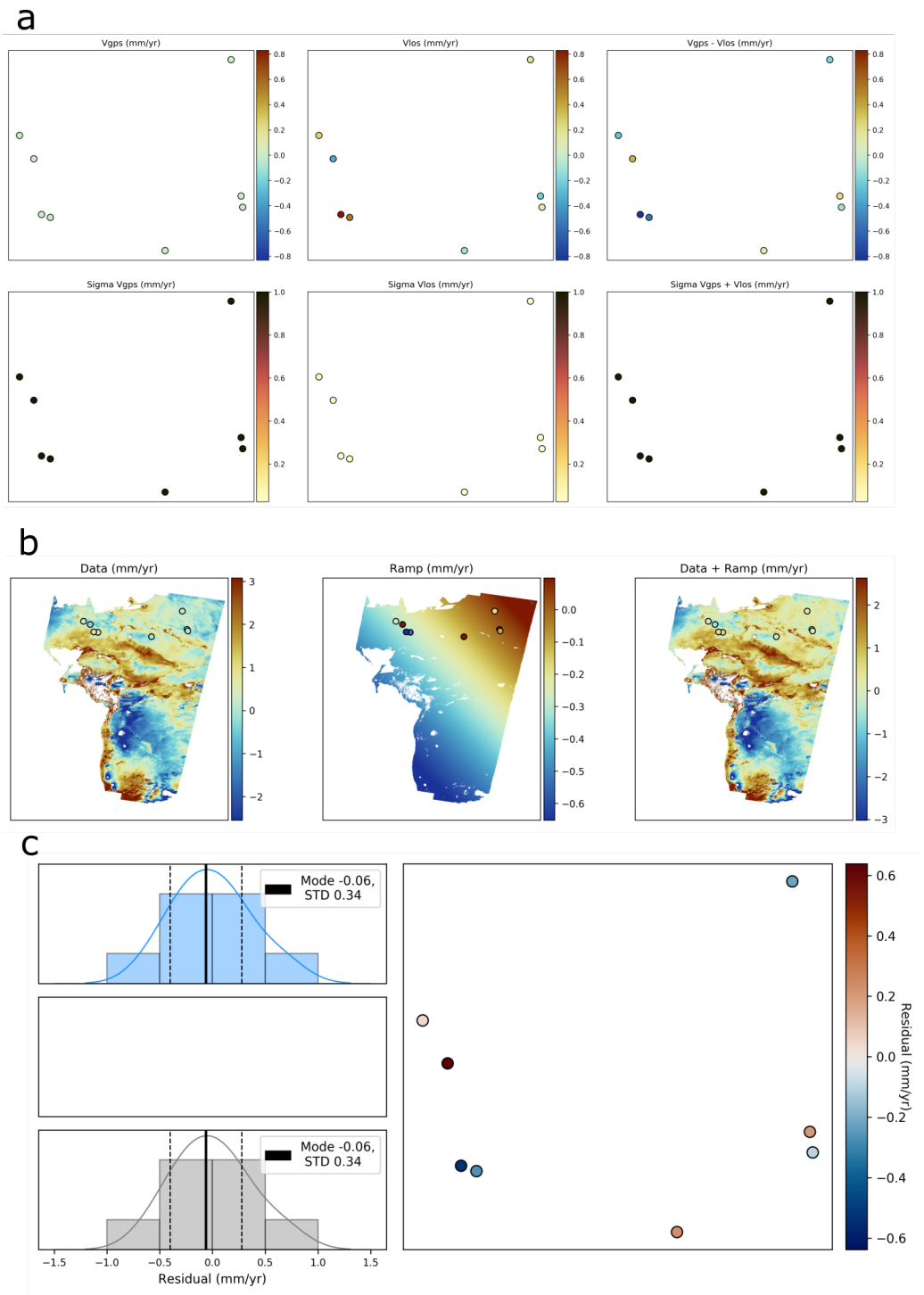


Figure 4.58: Referencing the LOS velocity field for D137 with GPS, using the same strategy as Figure 4.57. Note in this track, the extent does not overlap with any stations in the NE Iran network and so the referencing is only using dummy GPS stations.

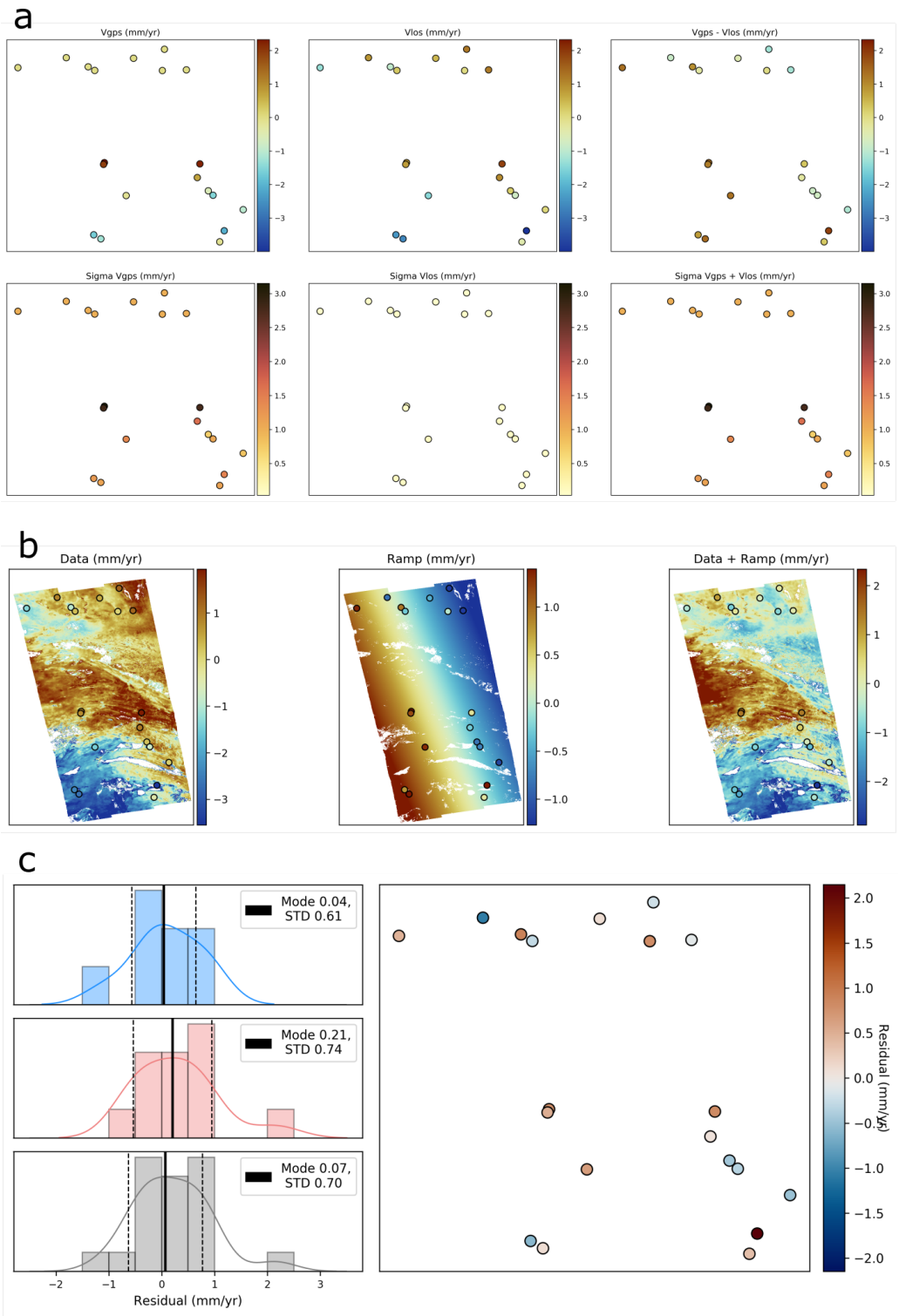


Figure 4.59: Referencing the LOS velocity field for A159 with GPS, using the same strategy as Figure 4.57.

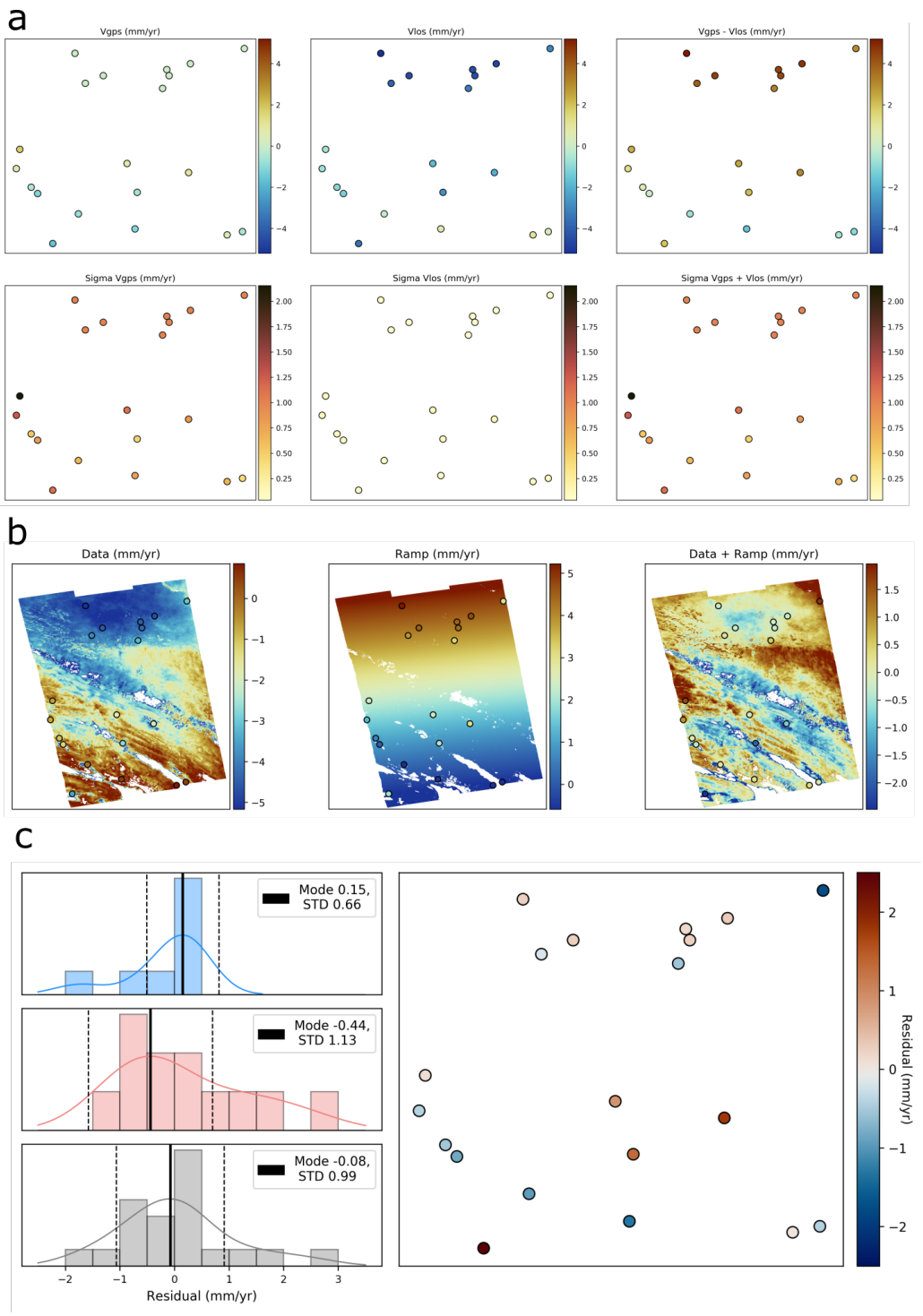


Figure 4.60: Referencing the LOS velocity field for A086 with GPS, using the same strategy as Figure 4.57.

Chapter 5

Concluding remarks

The research chapters within this thesis are focused on characterising deformation surrounding the South Caspian Basin (SCB), an aseismic block moving independently of its surroundings (*Jackson et al.*, 2002), along the northern margins of the Iranian Plateau. Fault zones surrounding the basin are in proximity to numerous urban agglomerations, which have a combined population exceeding 15 million. Motivated by characterising the seismic hazard posed by faults surrounding the basin, this research aims to improve our understanding of the motion of the basin with respect to its surroundings. I measure how the motion of the SCB is accommodated and strain is distributed through fault zones along its boundaries, predominantly using InSAR time-series methods. I also characterise how the resulting strain is released from earthquake ruptures preserved in the geological record. Within each chapter there are detailed conclusions which are not repeated here; instead this section aims to reflect on the previous chapters, providing a broader discussion of the results presented in this thesis and remarks on direction for future research.

Chapters 2 and 3 focus specifically on the Main Köpetdag fault (MKDF), Turkmenistan, with Chapter 4 providing additional observations along the fault system. From a seismic hazard perspective, these chapters demonstrate the value

in promoting a multidisciplinary approach to characterise seismic hazard along faults. The MKDF is one of the two major strike-slip faults in the conjugate system that facilitates the motion of the SCB. The MKDF had previously been recognised as a major component in the kinematic evolution of the SCB from seismological (e.g. *Jackson et al.*, 2002; *Jackson and McKenzie*, 1984) and geodetic (e.g. *Hollingsworth et al.*, 2008; *Djamour et al.*, 2010; *Mousavi et al.*, 2013; *Walters et al.*, 2013) observations, however very little was know about its capability to generate earthquakes (e.g. *Walker et al.*, 2021). The research presented in this thesis has improved our characterisation of seismic hazard along the MKDF, which requires accurately quantifying both sides of the strain accumulation-strain release balance. These provide the necessary components to begin to develop integrated seismicity and geodetic earthquake likelihood models for local seismic hazard assessments (e.g. *Rollins and Avouac*, 2019).

Chapter 2 presents the first evidence of paleo-earthquakes along the MKDF, the only evidence of strain release along this fault. This research shows that the MKDF is capable of rupturing in high-magnitude surface rupturing events, which are comparable in magnitude to the largest earthquakes in the Arabia-Eurasia collision zone (e.g. *Hollingsworth et al.*, 2010). There are a plethora of additional research questions arising from this initial study which will require additional field investigations of the MKDF, predominantly related to the role that along strike segmentation has played in previous ruptures along the fault (e.g. *Wesnousky*, 2006). This chapter reinforces the limitations of seismological records to fully characterise the distribution of faults because of their limited temporal extent, especially in the slow-moving continental interiors. Historical records, even in regions with exceptional records of earthquakes over thousands of years such as Persia and China, have levels of completeness that vary through space and time. It will never be clear whether seismic gaps within deforming zones are due to incompleteness of

the historical record (e.g. *Ambraseys and Melville*, 2005). However by combining the geomorphological signature of previous earthquakes on the landscape with paleoseismological techniques, we can begin to fill in the gaps in these records. This is evidently the case with the MKDF but is also applicable to comparable structures around the world, especially to those that have distinct geomorphic expressions yet apparently seismically-quiescent pasts.

Advances in the spatial and temporal resolution of InSAR satellite acquisitions, combined with ever-increasing computational processing and data storage means that the InSAR time-series presented in Chapters 3 and 4 contain over an order of magnitude higher-quality IFGs than previous studies in this region (e.g. *Walters et al.*, 2013; *Mousavi et al.*, 2015). These advances have improved the resolution and quality of the InSAR time-series derived measurements, with noise levels in these measurements now below 1 mm/yr. In addition, generating time-series from both ascending and descending LOS has provided insight into additional deformation signals, such as the inferred strain partitioning along the MKDF. Aside from these improvements, it is possible to compare the capability of InSAR time-series observations at different spatial scales to characterise deformation. Chapter 3 highlights the the importance of maximising the resolution of the data, with localised observations providing valuable insight into deformation along individual structures. The finer-scale products present observations of structural complexity, distributed deformation, and interactions between various deformation mechanisms. Similarly the time-series presented in Chapter 4 retains sufficient resolution to characterise distributed deformation along parallel segments in the SFZ, which are an important consideration from a seismic hazard perspective if they host multi-segment ruptures (e.g. *Hamling et al.*, 2017). In comparison, at a broader scale Chapter 4 demonstrates the potential of continental-scale InSAR-processing projects in development (e.g. *Lazecký et al.*, 2020; *Durand et al.*, 2019) to, in future, provide insight into the

broader-scale mechanics of continental deformation.

Finally, a recurring reflection from this thesis is that geodetic observations of deformation will always need to be accompanied by geological knowledge. From an InSAR perspective, this includes in separating tectonic signals from sources of non-tectonic deformation (e.g. hydrological or anthropogenic in Chapter 3). However the most important aspect to recognise is that geology initially guides geodetic research, and subsequently provides direction throughout the subsequent interpretation and modelling of the observations.

5.1 Directions for future research

There are numerous directions for future research that will build on the research in Chapters 2 to 4, as well as directions for methods developments that will advance the capability of the techniques used in this thesis.

The mechanics of lateral extrusion facilitated by strike-slip faulting dominates the geodetic observations presented in Chapters 3 and 4. Similarly the shorter-term geomorphological expression presented in Chapter 2 is focused predominantly on the major strike-slip fault. To improve the characterisation of seismic hazard in the region, future research could focus on improving our understanding of other structures in the region. This is particularly the case with strain-partitioning secondary structures to the major strike-slip faults, but also other faults within the Köpetdag and Eastern Alborz presented in Chapter 4. For example, future research should aim to better resolve deformation along the frontal thrusts presented in Chapter 3 with geodetic methods, and also to characterise the strain release along the thrust scarps mapped out in *Walker et al.* (2021). These additional structures have the potential to significantly increase the seismic hazard posed by faults in the region, yet these faults remain poorly characterised. This requires more extensive paleoseismological investigations of faults in the region, which should also target

constraining the role of along strike segmentation on ruptures.

Questions remain as to the role that north-south convergence within the Arabia-Eurasia collision is playing in the motion of the SCB. This is difficult to constrain with the methods used in Chapters 3 and 4 as a result of the insensitivity of the InSAR LOS to north-south motion. The integration of additional GPS data into the analysis presented in this thesis would provide better constraints on this motion. This should primarily target a deployment of GPS stations within Turkmenistan, and also densification of the GPS network in northeast Iran. If the high costs associated with seafloor geodesy become less prohibitive in the near future, much of the uncertainty with regards to the motion of the SCB would be resolved by directly measuring the motion of the basin interior. A lower cost, remote alternative to constrain the north-south component, would be to utilise burst overlap interferometry with Sentinel-1 (e.g. *Grandin et al.*, 2016; *Li et al.*, 2021). This might also provide insight into the enigmatic kinematic role of the Absheron-Balkan Sill, which is proposed to be a subduction interface (e.g. *Jackson et al.*, 2002). Constraining the north-south motion should then also allow us to compute the vertical component from the sub-vertical component in the decomposition results presented in Chapter 4, which can also be compared to vertical motions constrained by GPS velocities. Along both the MKDF and SFZ, topography across these fault zones indicates that shortening has played an important longer-term role in the kinematics of the region.

The lifetime of Sentinel-1 is expected to be 7–12 years, and so we are currently in the middle of the expected operational period of the satellite. There is an abundance of data to process, with observations advancing our understanding of surface deformation across numerous scientific fields. With the present length of InSAR time-series observations, the level of uncertainty on the measurements is $\approx$1 mm/yr. As the length of the time-series observations increases, this level

should reduce further enabling more precise observations of surface deformation. In addition, the proposed launch of the auxiliary Harmony mission, comprised of two companion satellites to the Sentinel-1 constellation, should provide even higher precision in measuring surface deformation. To mitigate the effects of tropospheric signals, the greatest source of uncertainty when measuring interseismic motion with InSAR time-series, improvements are required in the accuracy of global atmospheric models as demonstrated in Chapter 4 in remote regions. Methods exist to integrate GNSS data of tropospheric path delays into these models (e.g. *Yu et al.*, 2017, 2018b), however at present this is not always possible due to the sparse distribution of continuous stations. Another source of error is the ionosphere, the probable cause of long-wavelength residuals in interferograms. The mitigation of ionospheric signals requires advances in the development of ionospheric path-delay models and their application to InSAR time-series with Sentinel-1 (e.g. *Liang et al.*, 2019). Alternatively in the near future, the dual-frequency NISAR mission (NASA/ISRO, USA/India) will allow for the removal of ionospheric signals, by combining L and S-band radar.

The research presented in this thesis has improved our understanding of the motion of the SCB. This research has resolved the rate and distribution of strain accumulation on faults facilitating the motion of the basin, and also determined the character of earthquake ruptures which release the strain. The measurements and observations presented will provide invaluable contributions to accurately characterise the seismic hazard posed by faults surrounding the basin. Research questions still remain with numerous directions suggested for future research in this region. However, the greatest challenge will be to effectively communicate the seismic hazard posed by faults in the region. This will allow this knowledge to be integrated into societal awareness and infrastructure developments in the rapidly growing economies in this part of the modern Silk Roads. This will hopefully in

future enable the mitigation of the devastating hazards posed by earthquakes along the northern margins of the Iranian Plateau.

Bibliography

Ainscoe, E. A., K. E. Abdrakhmatov, S. Baikulov, A. S. Carr, A. J. Elliott, C. Grützner, and R. T. Walker (2019), Variability in surface rupture between successive earthquakes on the Suusamyr Fault, Kyrgyz Tien Shan: implications for palaeoseismology, *Geophysical Journal International*, *216*(1), 703–725, doi:10.1093/gji/ggy457. 1.3

Allen, M., J. Jackson, and R. Walker (2004), Late Cenozoic reorganization of the Arabia-Eurasia collision and the comparison of short-term and long-term deformation rates, *Tectonics*, *23*(2), doi:https://doi.org/10.1029/2003TC001530. 1.4

Allen, M. B., and H. A. Armstrong (2008), Arabia–Eurasia collision and the forcing of mid-Cenozoic global cooling, *Palaeogeography, Palaeoclimatology, Palaeoecology*, *265*(1), 52–58, doi:https://doi.org/10.1016/j.palaeo.2008.04.021. 1.4

Ambraseys, N. N. (1997), The Krasnovodsk (Turkmenistan) Earthquake of 8 July 1895, *Journal of Earthquake Engineering*, *1*(2), 293–317, doi:10.1080/13632469708962370. 2.2.2, 3.4.3

Ambraseys, N. N., and C. P. Melville (1982), A History of Persian earthquakes, *Earthquake Engineering & Structural Dynamics*, *11*(4), 591, doi:https://doi.org/10.1002/eqe.4290110412. 2.1, 2.2.2, 2.5

Ambraseys, N. N., and C. P. Melville (2005), *A History of Persian Earthquakes*, Cambridge University Press. 1.3, 1.4, 1.3, 1.4, 2.2, 2.2.2, 3.1, 3.1, 4.1, 4.4.4, 5

Ansari, H., F. De Zan, and A. Parizzi (2020), Study of Systematic Bias in Measuring Surface Deformation With SAR Interferometry, *IEEE Transactions on Geoscience and Remote Sensing*, doi:10.1109/tgrs.2020.3003421. 3.2, 3.2.3, 4.2.1

Avouac, J.-P. (2015), From Geodetic Imaging of Seismic and Aseismic Fault Slip to Dynamic Modeling of the Seismic Cycle, *Annual Review of Earth and Planetary Sciences*, *43*(1), 150223150959,000, doi:10.1146/annurev-earth-060614-105302. 1.3

Bayhaqī, A. i. Z., and A. Bahmanyār (1938), Tārīkh-i BayhaqTehran, *Tehran: Bungāh-i Dānish*. 2.5

Becker, T. W., and H. Schmeling (1998), Earthquake recurrence-time variations with and without fault-zone interactions, *Geophysical Journal International*, *135*(1), 165–176, doi:10.1046/j.1365-246X.1998.00624.x. 1.2

Béjar-Pizarro, M., A. Socquet, R. Armijo, D. Carrizo, J. Genrich, and M. Simons (2013), Andean structural control on interseismic coupling in the North Chile subduction zone, *Nature Geoscience*, doi:10.1038/ngeo1802. 3.1, 3.2.1

Bekaert, D. P., A. Hooper, and T. J. Wright (2015), A spatially variable power law tropospheric correction technique for InSAR data, *Journal of Geophysical Research: Solid Earth*, doi:10.1002/2014JB011558. 3.1, 3.2.1

Berberian, M. (1976), *Contribution to the Seismotectonics of Iran, part II, 518p.* 2.5

Berberian, M. (2014), *Earthquakes and Coseismic Surface Faulting on the Iranian Plateau.* 1.4, 2.1, 2.2.2, 2.5

Berberian, M., and R. S. Yeats (1999), Patterns of historical earthquake rupture in the Iranian Plateau, *Bulletin of the Seismological Society of America*, *89*(1), 120–139, doi:10.1785/BSSA0890010120. 2.1, 2.2.2

Berberian, M., and R. S. Yeats (2001), Contribution of archaeological data to studies of earthquake history in the Iranian Plateau, *Journal of Structural Geology*, *23*(2-3), 563–584, doi:10.1016/S0191-8141(00)00115-2. 2.2.2

Bilham, R. (2009), The seismic future of cities, *Bulletin of Earthquake Engineering*, *7*(4), 839, doi:10.1007/s10518-009-9147-0. 1.1

Bird, P. (2003), An updated digital model of plate boundaries, *Geochemistry, Geophysics, Geosystems*, doi:10.1029/2001GC000252. 1.1

Cavalié, O., and S. Jónsson (2014), Block-like plate movements in eastern Anatolia observed by InSAR, *Geophysical Research Letters*, *41*(1), 26–31, doi:https://doi.org/10.1002/2013GL058170. 4.4.5

Chen, J., H. A. Zebker, and R. Knight (2015), A persistent scatterer interpolation for retrieving accurate ground deformation over InSAR-decorrelated agricultural fields, *Geophysical Research Letters*, doi:10.1002/2015GL065031. 3.2, 4.2

Chen, K. H., and R. Bürgmann (2017), Creeping faults: Good news, bad news?, *Reviews of Geophysics*, *55*(2), 282–286, doi:10.1002/2017RG000565. 1.3

Copley, A., and J. Jackson (2006), Active tectonics of the Turkish-Iranian Plateau, *Tectonics*, *25*(6), 1–19, doi:10.1029/2005TC001906. 1.4, 2.2.1, 3.1, 3.4.3, 3.4.4, 3.4.4, 3.1, 4.1, 4.4, 4.4.5, 4.4.5

Copley, A., and R. Jolivet (2016), Fault rheology in an aseismic fold-thrust belt (Shahdad, eastern Iran), *Journal of Geophysical Research: Solid Earth*, *121*(1), 412–431, doi:https://doi.org/10.1002/2015JB012431. 1.3

Copley, A., O. Weller, P. Cawood, and C. Warren (2021), Understanding earthquakes using the geological record: an introduction, *Philosophical Transactions of the Royal Society A: Mathematical, Physical and Engineering Sciences*, *379*(2193), 20190,410, doi:10.1098/rsta.2019.0410. 1.1

Daout, S., S. Barbot, G. Peltzer, M. P. Doin, Z. Liu, and R. Jolivet (2016a), Constraining the kinematics of metropolitan Los Angeles faults with a slip-partitioning model, *Geophysical Research Letters*, doi:10.1002/2016GL071061. 3.3, 3.4.3

Daout, S., R. Jolivet, C. Lasserre, M. P. Doin, S. Barbot, P. Tapponnier, G. Peltzer, A. Socquet, and J. Sun (2016b), Along-strike variations of the partitioning of convergence across the Haiyuan fault system detected by InSAR, *Geophysical Journal International*, doi:10.1093/gji/ggw028. 3.3

Daout, S., M. P. Doin, G. Peltzer, A. Socquet, and C. Lasserre (2017), Large-scale InSAR monitoring of permafrost freeze-thaw cycles on the Tibetan Plateau, *Geophysical Research Letters*, doi:10.1002/2016GL070781. 3.2.2

Daout, S., M. P. Doin, G. Peltzer, C. Lasserre, A. Socquet, M. Volat, and H. Sudhaus (2018), Strain Partitioning and Present-Day Fault Kinematics in NW Tibet From Envisat SAR Interferometry, *Journal of Geophysical Research: Solid Earth*, *123*(3), 2462–2483, doi:10.1002/2017JB015020. 3.1, 3.2.1, 3.2.2

Daout, S., H. Sudhaus, T. Kausch, A. Steinberg, and B. Dini (2019), Interseismic and Postseismic Shallow Creep of the North Qaidam Thrust Faults Detected with a Multitemporal InSAR Analysis, *Journal of Geophysical Research: Solid Earth*, *124*(7), 7259–7279, doi:10.1029/2019JB017692. 1.2

Daout, S., B. Dini, W. Haeberli, M. P. Doin, and B. Parsons (2020), Ice loss in the Northeastern Tibetan Plateau permafrost as seen by 16 yr of ESA SAR missions, *Earth and Planetary Science Letters*, doi:10.1016/j.epsl.2020.116404. 3.2.3, 4.2, 4.2.1

Davidovich, A. (1951), Report on the 1947 Excavations in the Area of the Square Hall of Old Nisa, Ashgabat., in *Proceedings of the South Turkmenistan Archaeological Complex Expedition*, pp. 108–42. 2.2.2, 3.1

Djamour, Y., P. Vernant, R. Bayer, H. R. Nankali, J. F. Ritz, J. Hinderer, Y. Hatam, B. Luck, N. Le Moigne, M. Sedighi, and F. Khorrami (2010), GPS and gravity constraints on continental deformation in the Alborz mountain range, Iran, *Geophysical Journal International*, *183*(3), 1287–1301, doi:10.1111/j.1365-246X.2010.04811.x. 1.4, 2.2.1, 3.1, 3.1, 4.1, 4.4, 4.4, 5

Dodds, N., G. Begenjev, Y. Bezmenov, C. Gruetzner, R. Mirzin, E. Rhodes, R. Walker, and P. Wordsworth (2021), A large-magnitude Medieval earthquake on the Main Köpetdag (Kopeh Dagh) fault, Turkmenistan, *Manuscript submitted for publication*. 3.1, 3.4.3

Doin, M. P., C. Lasserre, G. Peltzer, O. Cavalié, and C. Doubre (2009), Corrections of stratified tropospheric delays in SAR interferometry: Validation with global atmospheric models, *Journal of Applied Geophysics*, *69*(1), 35–50, doi:10.1016/j.jappgeo.2009.03.010. 3.1, 3.2.1, 4.2.1

Doin, M.-P., F. Lodge, S. Guillaso, R. Jolivet, C. Lasserre, G. Ducret, R. Grandin, E. Pathier, and V. Pinel (2011), Presentation of the small baseline NSBAS processing chain on a case example: the Etna deformation monitoring from 2003 to 2010 using Envisat data, *Proceedings of the ESA 'Fringe 2011 Workshop', Frascati, Italy, (19-23 September 2011)*. 3.2, 4.2

Doin, M. P., C. Twardzik, G. Ducret, C. Lasserre, S. Guillaso, and S. Jianbao (2015), InSAR measurement of the deformation around Siling Co Lake: Inferences on the lower crust viscosity in central Tibet, *Journal of Geophysical Research: Solid Earth*, doi:10.1002/2014JB011768. 3.2, 3.2.2, 4.2, 4.2.1

Dolan, J., D. Bowman, and C. Sammis (2004), Long-range and long-term fault interactions in Southern California, *Geology*, *35*, 855–858. 1.2

Dolan, J. F., L. J. McAuliffe, E. J. Rhodes, S. F. McGill, and R. Zinke (2016), Extreme multi-millennial slip rate variations on the Garlock fault, California: Strain super-cycles, potentially time-variable fault strength, and implications for system-level earthquake occurrence, *Earth and Planetary Science Letters*, *446*, 123–136, doi:https://doi.org/10.1016/j.epsl.2016.04.011. 1.2

Durand, P., J. Donadieu, C. Proy, C. Dominique, R. Grandin, E. Ostanciaux, E. Pointal, C. Lasserre, M.-P. Doin, E. Pathier, F. Thollard, and C. Laurent (2019), FLATSIM Form@ter LArge-scale multi-Temporal Sentinel-1 Interferometry processing chain in MUSCATE, in *MDIS Workshop La Petite Pierre*. 1.2, 4.1, 5

Elliott, A. J., M. E. Oskin, J. Liu-Zeng, and Y. Shao (2015), Rupture termination at restraining bends: The last great earthquake on the Altyn Tagh Fault, *Geophysical Research Letters*, *42*(7), 2164–2170, doi:https://doi.org/10.1002/2015GL063107. 2.5

Elliott, J. R., R. J. Walters, and T. J. Wright (2016), The role of space-based observation in understanding and responding to active tectonics and earthquakes, *Nature Communications*, *7*, 1–16, doi:10.1038/ncomms13844. 3.1

England, P., and J. Jackson (2011), Uncharted seismic risk, *Nature Geoscience*, *4*(6), 348–349, doi:10.1038/ngeo1168. 1.1, 1.1, 1.2

England, P., G. Houseman, and J.-M. Nocquet (2016), Constraints from GPS measurements on the dynamics of deformation in Anatolia and the Aegean, *Journal of Geophysical Research: Solid Earth*, *121*(12), 8888–8916, doi:https://doi.org/10.1002/2016JB013382. 4.4.5

Eshagh, M., R. Tenzer, and M. Eshagh (2020), Elastic thickness of the Iranian lithosphere from gravity and seismic data, *Tectonophysics*, *774*(February 2019), 228,186, doi:10.1016/j.tecto.2019.228186. 2.5

Fagereng, Å., and A. Beall (2021), Is complex fault zone behaviour a reflection of rheological heterogeneity?, *Philosophical Transactions of the Royal Society A: Mathematical, Physical and Engineering Sciences*, *379*(2193), 20190,421, doi:10.1098/rsta.2019.0421. 1.1

Fleskens, L., A. Ataev, B. Mamedov, and W. P. Spaan (2007), Desert water harvesting from takyr surfaces: Assessing the potential of traditional and experimental technologies in the Karakum, *Land Degradation and Development*, *18*(1), 17–39, doi:10.1002/ldr.759. 3.4.2

Floyd, M. A., H. Billiris, D. Paradissis, G. Veis, A. Avallone, P. Briole, S. McClusky, J.-M. Nocquet, K. Palamartchouk, B. Parsons, and P. C. England (2010), A new velocity field for Greece: Implications for the kinematics and dynamics of the Aegean, *Journal of Geophysical Research: Solid Earth*, *115*(B10), doi:https://doi.org/10.1029/2009JB007040. 4.4.5

Ghassemi, M. R., and E. Garzanti (2019), Geology and geomorphology of Turkmenistan: A review, *Geopersia*, *9*(1), 125–140, doi:10.22059/GEOPE.2018.265613.648416. 2.4.1

Gold, R. D., E. Cowgill, J. R. Arrowsmith, J. Gosse, X. Chen, and X.-F. Wang (2009), Riser diachroneity, lateral erosion, and uncertainty in rates of strike-slip faulting: A case study from Tuzidun along the Altyn Tagh Fault, NW China, *Journal of Geophysical Research: Solid Earth*, *114*(B4), doi:https://doi.org/10.1029/2008JB005913. 1.2

Gold, R. D., E. Cowgill, J. R. Arrowsmith, and A. M. Friedrich (2017), Pulsed strain release on the Altyn Tagh fault, northwest China, *Earth and Planetary Science Letters*, *459*, 291–300, doi:https://doi.org/10.1016/j.epsl.2016.11.024. 1.3

Goldfinger, C., Y. Ikeda, R. S. Yeats, and J. Ren (2013), Superquakes and Supercycles, *Seismological Research Letters*, *84*(1), 24–32, doi:10.1785/0220110135. 1.3

Goldstein, R. M., and C. L. Werner (1998), Radar interferogram filtering for geophysical applications, *Geophysical Research Letters*, doi:10.1029/1998GL900033. 3.2, 4.2

Grandin, R. (2015), Interferometric processing of SLC Sentinel-1 TOPS data, in *European Space Agency, (Special Publication) ESA SP*, doi:10.5270/fringe2015.pp116. 3.2, 4.2

Grandin, R., M. P. Doin, L. Bollinger, B. Pinel-Puysségur, G. Ducret, R. Jolivet, and S. N. Sapkota (2012), Long-term growth of the Himalaya inferred from interseismic InSAR measurement, *Geology*, doi:10.1130/G33154.1. 1.2, 3.2, 4.2

Grandin, R., E. Klein, M. Métois, and C. Vigny (2016), Three-dimensional displacement field of the 2015 Mw8.3 Illapel earthquake (Chile) from across- and along-track Sentinel-1 TOPS interferometry, *Geophysical Research Letters*, doi:10.1002/2016GL067954. 3.2, 4.2, 5.1

Grant, L. B., and K. Sieh (1994), Paleoseismic evidence of clustered earthquakes on the San Andreas Fault in the Carrizo Plain, California, *Journal of Geophysical Research: Solid Earth*, *99*(B4), 6819–6841, doi:https://doi.org/10.1029/94JB00125. 1.3

Green, T., N. Abdullayev, J. Hossack, G. Riley, and A. M. Roberts (2009), Sedimentation and subsidence in the South Caspian Basin, Azerbaijan, *Geological Society Special Publication*, doi:10.1144/SP312.12. 1.4, 4.4

Gutenberg, B., and C. F. Richter (1950), Seismicity of the Earth and Associated Phenomena, *Tellus*, *2*(1), 68, doi:https://doi.org/10.1111/j.2153-3490.1950.tb00313.x. 1.3

Hamling, I. J., S. Hreinsdóttir, K. Clark, J. Elliott, C. Liang, E. Fielding, N. Litchfield, P. Villamor, L. Wallace, T. J. Wright, E. D'Anastasio, S. Bannister, D. Burbidge, P. Denys, P. Gentle, J. Howarth, C. Mueller, N. Palmer, C. Pearson, W. Power, P. Barnes, D. J. A. Barrell, R. Van Dissen, R. Langridge, T. Little, A. Nicol, J. Pettinga, J. Rowland, and M. Stirling (2017), Complex multifault rupture during the 2016 M_w 7.8 Kaikōura earthquake, New Zealand, *Science*. 5

Hanks, T. C., and H. Kanamori (1979), A moment magnitude scale, in *Journal of Geophysical Research B: Solid Earth*, doi:10.1029/JB084iB05p02348. 2.5

Hanssen, R. F. (2001), *Radar Interferometry: Data Interpretation and Error Analysis (Remote Sensing and Digital Image Processing)*. 3.2.1

Harris, R. A. (2017), Large earthquakes and creeping faults, *Reviews of Geophysics*, *55*(1), 169–198, doi:10.1002/2016RG000539. 1.3

Hollingsworth, J., J. Jackson, R. Walker, M. R. Gheitanchi, and M. J. Bolourchi (2006), Strike-slip faulting, rotation, and along-strike elongation in the Kopeh Dagh mountains, NE Iran, *Geophysical Journal International*, *166*, 1161–1177, doi:10.1111/j.1365-246X.2006.02983.x. 2.2.1, 2.2.2, 3.1, 3.1, 4.1, 4.4.3, 4.4.4, 4.5

Hollingsworth, J., J. Jackson, R. Walker, and H. Nazari (2008), Extrusion tectonics and subduction in the easter South Caspian region since 10 Ma, *Geology*, *36*(10), 763–766, doi:10.1130/G25008A.1. 1.4, 1.4, 2.2, 2.2.1, 2.4.1, 2.4.2, 3.1, 3.1, 3.2.2, 3.1, 4.4, 4.4.3, 4.34, 4.5, 5

Hollingsworth, J., H. Nazari, J. F. Ritz, R. Salamati, M. Talebian, A. Bahroudi, R. T. Walker, M. Rizza, and J. Jackson (2010), Active tectonics of the east Alborz mountains, NE Iran: Rupture of the left-lateral Astaneh fault system during the

great 856 A.D. Qumis earthquake, *Journal of Geophysical Research: Solid Earth*, *115*(12), 1–19, doi:10.1029/2009JB007185. 1.4, 2.1, 2.2.1, 2.2.1, 2.2.2, 2.5, 3.1, 4.4, 4.4.2, 5

Hussain, E., A. Hooper, T. J. Wright, R. J. Walters, and D. P. S. Bekaert (2016), Interseismic strain accumulation across the central North Anatolian Fault from iteratively unwrapped InSAR measurements, *Journal of Geophysical Research: Solid Earth*, *121*(12), 9000–9019, doi:https://doi.org/10.1002/2016JB013108. 1.2, 4.3.4, 4.4.5

Ischuk, A., R. Bendick, A. Rybin, P. Molnar, S. F. Khan, S. Kuzikov, S. Mohadjer, U. Saydullaev, Z. Ilyasova, G. Schelochkov, and A. V. Zubovich (2013), Kinematics of the Pamir and Hindu Kush regions from GPS geodesy, *Journal of Geophysical Research: Solid Earth*, *118*(5), 2408–2416, doi:https://doi.org/10.1002/jgrb.50185. 4.4.5

Jackson, J. (2001), Living with earthquakes: know your faults, *Journal of Earthquake Engineering*, *05*, 5–123, doi:10.1142/S1363246901000431. 1.1

Jackson, J., and G. R. Conway (2006), Fatal attraction: Living with earthquakes, the growth of villages into megacities, and earthquake vulnerability in the modern world, *Philosophical Transactions of the Royal Society A: Mathematical, Physical and Engineering Sciences*, *364*(1845), 1911–1925, doi:10.1098/rsta.2006.1805. 1.1

Jackson, J., and D. McKenzie (1984), Active tectonics of the Alpine-Himalayan Belt between western Turkey and Pakistan, *Geophysical Journal of the Royal Astronomical Society*, *77*(1), 185–264. 1.1, 1.4, 1.4, 2.1, 4.4, 5

Jackson, J., and D. McKenzie (1988), The relationship between plate motions and seismic moment tensors, and the rates of active deformation in the Mediterranean and Middle East, *Geophysical Journal International*, *93*(1), 45–73, doi:10.1111/j.1365-246X.1988.tb01387.x. 1.1

Jackson, J., K. Priestley, M. Allen, and M. Berberian (2002), Active tectonics of the South Caspian Basin, *Geophysical Journal International*, *148*, 214–245. (document), 1.4, 1.3, 1.4, 1.4, 2.1, 2.2.1, 2.2.2, 3.1, 3.1, 3.3.2, 3.4.3, 3.4.4, 4.1, 4.3.4, 4.4, 4.4, 4.4.3, 4.4.4, 5, 5.1

Jackson, J. A., J. Gagnepain, G. Houseman, G. C. P. King, P. Papadimitriou, C. Soufleris, and J. Virieux (1982), Seismicity, normal faulting, and the geomorphological development of the Gulf of Corinth (Greece): the Corinth earthquakes of February and March 1981, *Earth and Planetary Science Letters*, *57*(2), 377–397, doi:https://doi.org/10.1016/0012-821X(82)90158-3. 1.3

Javidfakhr, B., O. Bellier, E. Shabanian, L. Siame, L. Léanni, D. Bourlès, and S. Ahmadian (2011), Fault kinematics and active tectonics at the southeastern boundary of the eastern Alborz (Abr and Khij fault zones): Geodynamic implications for NNE Iran, *Journal of Geodynamics*, *52*(3), 290–303, doi:https://doi.org/10.1016/j.jog.2011.02.005. 2.2.1, 3.1, 3.4.4, 4.1

Johnson, K. M. (2013), Slip rates and off-fault deformation in Southern California inferred from GPS data and models, *Journal of Geophysical Research: Solid Earth*, *118*(10), 5643–5664, doi:10.1002/jgrb.50365. 1.2

Jolivet, R., R. Cattin, N. Chamot-Rooke, C. Lasserre, and G. Peltzer (2008), Thin-plate modeling of interseismic deformation and asymmetry across the Altyn Tagh fault zone, *Geophysical Research Letters*, *35*(2), 1–5, doi:10.1029/2007GL031511. 1.2

Jolivet, R., R. Grandin, C. Lasserre, M. P. Doin, and G. Peltzer (2011), Systematic InSAR tropospheric phase delay corrections from global meteorological reanalysis data, *Geophysical Research Letters*, *38*(17), 1–6, doi:10.1029/2011GL048757. 3.1, 3.2.1, 3.4.3, 4.2.1

Khorrami, F., P. Vernant, F. Masson, F. Nilfouroushan, Z. Mousavi, H. Nankali, S. A. Saadat, A. Walpersdorf, S. Hosseini, P. Tavakoli, A. Aghamohammadi, and M. Alijanzade (2019), An up-to-date crustal deformation map of Iran using integrated campaign-mode and permanent GPS velocities, *Geophysical Journal International*, doi:10.1093/gji/ggz045. 1.4, 1.3, 1.4, 2.2.1, 3.1, 3.4.4, 3.11, 3.4.4, 4.4.5

Klinger, Y., J. P. Avouac, L. Dorbath, N. A. Karaki, and N. Tisnerat (2000), Seismic behaviour of the Dead Sea fault along Araba valley, Jordan, *Geophysical Journal International*, *142*(3), 769–782, doi:10.1046/j.1365-246x.2000.00166.x. 2.1

Klinger, Y., X. Xu, P. Tapponnier, J. Van der Woerd, C. Lasserre, and G. King (2005), High-resolution satellite imagery mapping for the surface rupture and slip distribution of the Mw 7.8, 14 November 2001 Kokoxili earthquake, Kunlun fault, northern Tibet, China, *Bulletin of the Seismological Society of America*, *95*(5), 1970–1987, doi:10.1785/0120040233. 2.5

Klinger, Y., M. Etchebes, P. Tapponnier, and C. Narteau (2011), Characteristic slip for five great earthquakes along the Fuyun fault in China, *Nature Geoscience*, *4*(6), 389–392, doi:10.1038/ngeo1158. 1.3, 2.4.3, 2.5

Kondorskaia, N., and N. Shebalin (1977), A New Catalogue of Strong Earthquakes in the Territory of the USSR from Ancient Times until 1975 ., *Moscow: Izdatel'stvo 'Nauka'*. 2.5

Kostrov, V., and V. Riznichenko (1974), Seismic moment and energy of earthquakes and seismic flow of rock, *Physics of the Solid Earth*, (1), 13–21. 1.3

Kreemer, C., G. Blewitt, and E. C. Klein (2014), A geodetic plate motion and Global Strain Rate Model, *Geochemistry, Geophysics, Geosystems*, *15*(10), 3849–3889, doi:https://doi.org/10.1002/2014GC005407. 1.2

Kurtz, R., Y. Klinger, M. Ferry, and J. Ritz (2018), Horizontal surface-slip distribution through several seismic cycles: The Eastern Bogd

fault, Gobi-Altai, Mongolia, *Tectonophysics*, *734-735*(March), 167–182, doi:10.1016/j.tecto.2018.03.011. 2.3, 2.4.3, 2.9, B.1

Lasserre, C., G. Peltzer, F. Crampé, Y. Klinger, J. Van der Woerd, and P. Tapponnier (2005), Coseismic deformation of the 2001 Mw = 7.8 Kokoxili earthquake in Tibet, measured by synthetic aperture radar interferometry, *Journal of Geophysical Research: Solid Earth*, *110*(B12), doi:https://doi.org/10.1029/2004JB003500. 2.5

Lazecký, M., K. Spaans, P. J. González, Y. Maghsoudi, Y. Morishita, F. Albino, J. Elliott, N. Greenall, E. Hatton, A. Hooper, D. Juncu, A. McDougall, R. J. Walters, C. S. Watson, J. R. Weiss, and T. J. Wright (2020), LiCSAR: An Automatic InSAR Tool for Measuring and Monitoring Tectonic and Volcanic Activity, doi:10.3390/rs12152430. 1.2, 4.1, 4.3.1, 5

Li, X., S. Jónsson, and Y. Cao (2021), Interseismic deformation from Sentinel-1 burst-overlap interferometry: Application to the southern Dead Sea fault, *Earth and Space Science Open Archive*. 5.1

Liang, C., P. Agram, M. Simons, and E. J. Fielding (2019), Ionospheric Correction of InSAR Time Series Analysis of C-band Sentinel-1 TOPS Data, *IEEE Transactions on Geoscience and Remote Sensing*, *57*(9), 6755–6773, doi:10.1109/TGRS.2019.2908494. 5.1

Liapin, A. (2006), The Excavations of A.A. Marushchenko at Ak-Tepe, *Problems of History, Philology, Culture*, *16*(1), 267–92. 2.2.2, 3.1

Lin, Z., J. Liu-Zeng, R. J. Weldon, J. Tian, C. Ding, and Y. Du (2020), Modeling repeated coseismic slip to identify and characterize individual earthquakes from geomorphic offsets on strike-slip faults, *Earth and Planetary Science Letters*, doi:10.1016/j.epsl.2020.116313. 2.4.3

Litvinskiĭ, B. (1951), Report on the Work of the Archaeological Group of the 5th Division of IUTAKE in 1947, Ashgabat., *Tech. rep.* 2.5

López-Quiroz, P., M. P. Doin, F. Tupin, P. Briole, and J. M. Nicolas (2009), Time series analysis of Mexico City subsidence constrained by radar interferometry, *Journal of Applied Geophysics*, doi:10.1016/j.jappgeo.2009.02.006. 3.2, 3.2.2, 3.2.2, 3.2.2, 4.2, 4.2.1

Lu, Z., T. Wright, and C. Wicks (2003), Deformation of the 2002 Denali Fault Earthquakes, mapped by Radarsat-1 interferometry, *Eos, Transactions American Geophysical Union*, *84*(41), 425–431, doi:https://doi.org/10.1029/2003EO410002. 2.5

Lyberis, N., and G. Manby (1999), Oblique to Orthogonal Convergence across the Turan Block in the Post-Miocene, *AAPG Bulletin*, *83*(7), 1135–1160, doi:10.1306/E4FD2E97-1732-11D7-8645000102C1865D. 3.1

Mackenzie, D., J. R. Elliott, E. Altunel, R. T. Walker, Y. C. Kurban, J.-L. Schwenninger, and B. Parsons (2016), Seismotectonics and rupture process of the MW 7.1 2011 Van reverse-faulting earthquake, eastern Turkey, and implications for hazard in regions of distributed shortening, *Geophysical Journal International*, *206*(1), 501–524, doi:10.1093/gji/ggw158. 2.1

Maggi, A., and K. Priestley (2005), Surface waveform tomography of the Turkish-Iranian plateau, *Geophysical Journal International*, doi:10.1111/j.1365-246X.2005.02505.x. 3.4.3

Maggi, A., J. A. Jackson, D. McKenzie, and K. Priestley (2000), Earthquake focal depths, effective elastic thickness, and the strength of the continental lithosphere, *Geology*, doi:10.1130/0091-7613(2000)028¡0495:efdeet¿2.3.co;2. 3.4.3

Maman, S., L. Orlovsky, D. G. Blumberg, P. Berliner, and B. Mamedov (2011), A landcover change study of takyr surfaces in Turkmenistan, *Journal of Arid Environments*, *75*(9), 842–850, doi:10.1016/j.jaridenv.2011.04.002. 3.4.2

Mangino, S., and K. Priestley (1998), The crustal structure of the southern Caspian region, *Geophysical Journal International*, doi:10.1046/j.1365-246X.1998.00520.x. 1.4, 1.4

Marone, C. J., C. H. Scholtz, and R. Bilham (1991), On the mechanics of earthquake afterslip, *Journal of Geophysical Research: Solid Earth*, *96*(B5), 8441–8452, doi:https://doi.org/10.1029/91JB00275. 1.2

Masson, F., M. Anvari, Y. Djamour, A. Walpersdorf, F. Tavakoli, M. Daignières, H. Nankali, and S. Van Gorp (2007), Large-scale velocity field and strain tensor in Iran inferred from GPS measurements: New insight for the present-day deformation pattern within NE Iran, *Geophysical Journal International*, *170*(1), 436–440, doi:10.1111/j.1365-246X.2007.03477.x. 3.1, 3.1

Maubant, L., E. Pathier, S. Daout, M. Radiguet, M. P. Doin, E. Kazachkina, V. Kostoglodov, N. Cotte, and A. Walpersdorf (2020), Independent Component Analysis and Parametric Approach for Source Separation in InSAR Time Series at Regional Scale: Application to the 2017–2018 Slow Slip Event in Guerrero (Mexico), *Journal of Geophysical Research: Solid Earth*, *125*(3), 1–24, doi:10.1029/2019JB018187. 3.2.1, 3.15

McKenzie, D. (1972), Active Tectonics of the Mediterranean Region, *Geophysical Journal of the Royal Astronomical Society*, *30*(2), 109–185, doi:10.1111/j.1365-246X.1972.tb02351.x. 1.1, 1.3, 2.2.2, 3.1, 3.1, 4.1

McKenzie, D., and J. Jackson (1986), A block model of distributed deformation by faulting, *Journal of the Geological Society*, *143*(2), 349 LP – 353, doi:10.1144/gsjgs.143.2.0349. 4.4.3, 4.34

McKenzie, D. P., and R. L. Parker (1967), The North Pacific: an Example of Tectonics on a Sphere, *Nature*, *216*(5122), 1276–1280, doi:10.1038/2161276a0. 1.1

Metzger, S., A. Ischuk, Z. Deng, L. Ratschbacher, M. Perry, S. K. Kufner, R. Bendick, and M. Moreno (2020), Dense GNSS Profiles Across the Northwestern Tip of the India-Asia Collision Zone: Triggered Slip and Westward Flow of the Peter the First Range, Pamir, Into the Tajik Depression, *Tectonics*, *39*(2), 1–20, doi:10.1029/2019TC005797. (document), 4.4.5, 4.38

Molnar, P. (1979), Earthquake recurrence intervals and plate tectonics, *Bulletin of the Seismological Society of America*, *69*(1), 115–133. 1.3

Molnar, P. (1988), Continental tectonics in the aftermath of plate tectonics, *Nature*, *335*(6186), 131–137, doi:10.1038/335131a0. 1.1

Molnar, P., and K. E. Dayem (2010), Major intracontinental strike-slip faults and contrasts in lithospheric strength, *Geosphere*, *6*(4), 444–467, doi:10.1130/GES00519.1. 1.1, 3.4.3, 4.4.1

Molnar, P., and P. Tapponnier (1975), Cenozoic Tectonics of Asia: Effects of a Continental Collision, *Science*, *189*(4201), 419 LP – 426, doi:10.1126/science.189.4201.419. 1.1

Mousavi, Z., A. Walpersdorf, R. T. Walker, F. Tavakoli, E. Pathier, H. Nankali, F. Nilfouroushan, and Y. Djamour (2013), Global Positioning System constraints on the active tectonics of NE Iran and the South Caspian region, *Earth and Planetary Science Letters*, *377-378*, 287–298, doi:10.1016/j.epsl.2013.07.007. 1.4, 1.4, 2.2, 2.2.1, 3.1, 3.2, 3.1, 3.3.3, 3.4.3, 3.4.4, 3.11, 3.5, 3.1, 4.1, 4.1, 4.3.4, 4.3.4, 4.16, 4.4, 4.4, 4.4.2, 4.4.4, 4.4.5, 4.46, 4.47, 4.48, 4.49, 4.50, 4.51, 4.52, 4.53, 4.57, 5

Mousavi, Z., E. Pathier, R. T. Walker, A. Walpersdorf, F. Tavakoli, H. Nankali, M. Sedighi, and M. P. Doin (2015), Interseismic deformation of the Shahroud fault system (NE Iran) from space-borne radar interferometry measurements, *Geophysical Research Letters*, doi:10.1002/2015GL064440. 1.4, 1.4, 2.2.1, 3.1, 3.4.4, 4.1, 4.1, 4.4, 4.4.2, 5

Mousavi, Z., M. Fattahi, M. Khatib, M. Talebian, E. Pathier, A. Walpersdorf, R. A. Sloan, A. L. Thomas, E. Rhodes, F. Clive, N. Dodds, and R. T. Walker (2021), Constant slip-rate on the Doruneh strike-slip fault, Iran, averaged over Late Pleistocene, Holocene, and decadal timescales, *Tectonics*, *n/a*(n/a), e2020TC006,256, doi:https://doi.org/10.1029/2020TC006256. 1.2, 2.1

Murav'ëv, N. (1871), Journey to Khiva: Through the Turcoman Country. Translated by Philipp Strahl and W.S.A. Lockhart. Calcutta: Foreign Department Press. 2.5

Murray, K. D., D. P. Bekaert, and R. B. Lohman (2019), Tropospheric corrections for InSAR: Statistical assessments and applications to the Central United States and Mexico, *Remote Sensing of Environment*, *232*(July), 111,326, doi:10.1016/j.rse.2019.111326. 3.2.1

Munis, S. M. M., and M. R. M. Agahi (1999), Firdaws Al-Iqbāl: History of Khorezm, translated by Yuri Bregel., *Islamic History and Civilization: Studies and Texts*, *28*. 2.5

Narshakhī, A. B. M. i. J. (1954), *The History of Bukhara, translated by Richard N Frye*. 2.5

Nemati, M., J. Hollingsworth, Z. Zhan, M. Javad Bolourchi, and M. Talebian (2013), Microseismicity and seismotectonics of the south caspian lowlands, NE iran, *Geophysical Journal International*, doi:10.1093/gji/ggs114. 3.1

Nissen, E., A. Ghods, E. Karasözen, J. R. Elliott, W. D. Barnhart, E. A. Bergman, G. P. Hayes, M. Jamal-Reyhani, M. Nemati, and F. Tan (2019), The 12 November 2017 M w 7.3 Ezgeleh-Sarpolzahab (Iran) earthquake and active tectonics of the Lurestan Arc, *Journal of Geophysical Research: Solid Earth*, *124*(2), 2124–2152. 1.4, 2.1

O'Hara, S. L. (1997), Irrigation and land degradation: Implications for agriculture in Turkmenistan, central Asia, *Journal of Arid Environments*, *37*(1), 165–179, doi:10.1006/jare.1996.0238. 3.4.2

Okada, Y. (1992), Internal deformation due to shear and tensile faults in a half-space, *Bulletin of the Seismological Society of America*, *82*(2), 1018–1040. 1.2

Peltzer, G., F. Crampé, S. Hensley, and P. Rosen (2001), Transient strain accumulation and fault interaction in the eastern California shear zone, *Geology*, *29*, 975–978. 1.2

Pilipko, V. N. (2007), Some Results of the Archaeological Investigations at Old Nisa, *Rossiyskaya arkheologiya*, *1*, 150–58. 2.2.2, 3.1

Pinel-Puysségur, B., R. Michel, and J. P. Avouac (2012), Multi-link InSAR time series: Enhancement of a wrapped interferometric database, *IEEE Journal of Selected Topics in Applied Earth Observations and Remote Sensing*, doi:10.1109/JSTARS.2012.2196758. 3.2, 4.2

Pollitz, F. F. (1997), Gravitational viscoelastic postseismic relaxation on a layered spherical Earth, doi:10.1029/97jb01277. 1.2

Prescott, W. H., and A. Nur (1981), The accommodation of relative motion at depth on the San Andreas Fault System in California, *Journal of Geophysical Research: Solid Earth*, *86*(B2), 999–1004, doi:https://doi.org/10.1029/JB086iB02p00999. 1.2

Priestley, K., H. J. Patton, and C. A. Schultz (2001), Modeling anomalous surface-wave propagation across the Southern Caspian Basin, *Bulletin of the Seismological Society of America*, doi:10.1785/0120010118. 1.4, 1.4

Radfar, A., A. R. Chakdel, A. Nejati, M. Soleimani, and FaridTaati (2019), New insights into the structure of the South Caspian Basin from seismic reflection data, Gorgan Plain, Iran, *International Journal of Earth Sciences*, doi:10.1007/s00531-018-1659-x. 3.1

Ratschbacher, L., O. Merle, P. Davy, and P. Cobbold (1991), Lateral extrusion in the eastern Alps, Part 1: Boundary conditions and experiments scaled for gravity, *Tectonics*, *10*(2), 245–256, doi:https://doi.org/10.1029/90TC02622. 4.4.5

Reid, H. F. (1910), The mechanics of the earthquake, in The California Earthquake of April 18, 1906, *Tech. rep.* 1.2

Ritz, J. F., H. Nazari, A. Ghassemi, R. Salamati, A. Shafei, S. Solaymani, and P. Vernant (2006), Active transtension inside central Alborz: A new insight into northern Iran-southern Caspian geodynamics, *Geology*, doi:10.1130/G22319.1. 2.1, 4.4

Rizza, M., P. Vernant, J. F. Ritz, M. Peyret, H. Nankali, H. Nazari, Y. Djamour, R. Salamati, F. Tavakoli, J. Chéry, S. A. Mahan, and F. Masson (2013), Morphotectonic and geodetic evidence for a constant slip-rate over the last 45 kyr along the Tabriz fault (Iran), *Geophysical Journal International*, *193*(3), 1083–1094, doi:10.1093/gji/ggt041. 2.1

Rockwell, T. K., S. Lindvall, M. Herzberg, D. Murbach, T. Dawson, and G. Berger (2000), Paleoseismology of the Johnson Valley, Kickapoo, and Homestead Valley Faults: Clustering of Earthquakes in the Eastern California Shear Zone, *Bulletin of the Seismological Society of America*, *90*(5), 1200–1236, doi:10.1785/0119990023. 1.2, 1.3

Rollins, C., and J. P. Avouac (2019), A Geodesy- and Seismicity-Based Local Earthquake Likelihood Model for Central Los Angeles, *Geophysical Research Letters*, *46*(6), 3153–3162, doi:10.1029/2018GL080868. 5

Rosen, P. A., S. Hensley, G. Peltzer, and M. Simons (2004), Updated repeat orbit interferometry package released, doi:10.1029/2004EO050004. 3.2, 4.2

Ruch, J., J. K. Warren, F. Risacher, T. R. Walter, and R. Lanari (2012), Salt lake deformation detected from space, *Earth and Planetary Science Letters*, doi:10.1016/j.epsl.2012.03.009. 3.4.2

Savage, J. C., and R. O. Burford (1973), Geodetic determination of relative plate motion in central California, *Journal of Geophysical Research*, *78*(5), 832–845, doi:10.1029/jb078i005p00832. 1.2, 3.3.2, 3.4.3

Scholz, C. H., and R. Kranz (1974), Notes on dilatancy recovery, *Journal of Geophysical Research (1896-1977)*, *79*(14), 2132–2135, doi:https://doi.org/10.1029/JB079i014p02132. 1.2

Segall, P. (2002), Integrating Geologic and Geodetic Estimates of Slip Rate on the San Andreas Fault System, *International Geology Review*, *44*(1), 62–82, doi:10.2747/0020-6814.44.1.62. 1.2

Segall, P. (2004), Postseismic Deformation: Different mechanisms in different times and places., in *AGU Fall Meeting Abstracts*, vol. 2004, pp. G12A–01, AA(Geophysics, Stanford University, Stanford, CA 94305 United States). 1.2

Segall, P. (2005), *Earthquake and Volcano deformation*, 517 pp., doi:10.1002/0471743984.vse7429. 3.3.3, 3.4.3

Shabanian, E., O. Bellier, L. Siame, N. Arnaud, M. R. Abbassi, and J. J. Cochemé (2009), New tectonic configuration in NE Iran: Active strike-slip faulting between the Kopeh Dagh and Binalud mountains, *Tectonics*, *28*(5), 1–29, doi:10.1029/2008TC002444. (document), 4.4.3, 4.34, 4.5

Shen, L., A. Hooper, and J. Elliott (2019), A Spatially Varying Scaling Method for InSAR Tropospheric Corrections Using a High-Resolution Weather Model, *Journal of Geophysical Research: Solid Earth*, *124*(4), 4051–4068, doi:10.1029/2018JB016189. 3.4.1

Shen, Z.-K., R. W. King, D. C. Agnew, M. Wang, T. A. Herring, D. Dong, and P. Fang (2011), A unified analysis of crustal motion in Southern California, 1970–2004: The SCEC crustal motion map, *Journal of Geophysical Research: Solid Earth*, *116*(B11), doi:https://doi.org/10.1029/2011JB008549. 1.2

Siame, L. L., E. Shabanian, and O. Bellier (2009), Extrusion tectonics and subduction in the eastern South Caspian region since 10 Ma: COMMENT, *Geology*, *37*(12), e197–e198, doi:10.1130/G25701C.1. 2.4.2

Sibson, R. H. (1985), A note on fault reactivation, *Journal of Structural Geology*, *7*(6), 751–754, doi:https://doi.org/10.1016/0191-8141(85)90150-6. 1.1

Stein, R. S., A. A. Barka, and J. H. Dieterich (1997), Progressive failure on the North Anatolian fault since 1939 by earthquake stress triggering, *Geophysical Journal International*, *128*(3), 594–604, doi:10.1111/j.1365-246X.1997.tb05321.x. 2.5

Sudhaus, H., and S. Jónsson (2009), Improved source modelling through combined use of InSAR and GPS under consideration of correlated data errors: Application to the June 2000 Kleifarvatn earthquake, Iceland, *Geophysical Journal International*, *176*(2), 389–404, doi:10.1111/j.1365-246X.2008.03989.x. 3.3.1

Sykes, L. R. (1978), Intraplate seismicity, reactivation of preexisting zones of weakness, alkaline magmatism, and other tectonism postdating continental fragmentation, *Reviews of Geophysics*, *16*(4), 621–688, doi:https://doi.org/10.1029/RG016i004p00621. 1.1

Talebian, M., E. J. Fielding, G. J. Funning, M. Ghorashi, J. Jackson, H. Nazari, B. Parsons, K. Priestley, P. A. Rosen, R. Walker, and T. J. Wright (2004), The 2003 Bam (Iran) earthquake: Rupture of a blind strike-slip fault, *Geophysical Research Letters*, *31*(11), doi:https://doi.org/10.1029/2004GL020058. 2.1

Tchalenko, J. S., and A. W. Skempton (1975), Seismicity and structure of the Kopet Dagh, *Philosophical Transactions of the Royal Society of London. Series A, Mathematical and Physical Sciences*, *278*(1275), 1–28, doi:10.1098/rsta.1975.0019. 2.2.2, 3.1

Thatcher, W. (2009), How the Continents Deform: The Evidence From Tectonic Geodesy, *Annual Review of Earth and Planetary Sciences*, *37*(1), 237–262, doi:10.1146/annurev.earth.031208.100035. 1.1, 1.3

Trifonov, V. G. (1978), Late Quaternary tectonic movements of western and central Asia, *GSA Bulletin*, *89*(7), 1059–1072. 2.2.2, 2.4.2, 3.1, 4.4.5, 4.38

Trifonov, V. G., G. A. Vostrikov, K. Orazsakhatov, S. F. Skobelev, and V. I. Lykov (2009), Tectonic Aspects of the 1983 Kum-Dag Earthquake, West Turkmenia, *International Geology Review*, *28*(4), 377–389, doi:10.1080/00206818609466278. 2.2.2, 3.1

Tymofyeyeva, E., and Y. Fialko (2015), Mitigation of atmospheric phase delays in InSAR data, with application to the eastern California shear zone, *Journal of Geophysical Research: Solid Earth*, doi:10.1002/2015JB011886. 3.1, 3.2.1

Van Dijk, J., A. T. Ajayi, T. Eid, M. Eldali, H. Ellen, H. Guney, M. Hashem, R. Knispel, L. Rouis, and S. Santoni (2019), An integrated geological model for the greater Cheleken area central Caspian Basin, Turkmenistan; complex synsedimentary transcurrent faulting and compartmentalization in Plio-Pleistocene clastic reservoirs, *Society of Petroleum Engineers - Abu Dhabi International Petroleum Exhibition and Conference 2018, ADIPEC 2018*, (November), 0–9, doi:10.2118/192978-ms. 3.1

Vergne, J., R. Cattin, and J. P. Avouac (2001), On the use of dislocations to model interseismic strain and stress build-up at intracontinental thrust faults, *Geophysical Journal International*, *147*(1), 155–162, doi:https://doi.org/10.1046/j.1365-246X.2001.00524.x. 1.2, 3.2.2

Vernant, P., F. Nilforoushan, D. Hatzfeld, M. R. Abbassi, C. Vigny, F. Masson, H. Nankali, J. Martinod, A. Ashtiani, R. Bayer, F. Tavakoli, and J. Chéry (2004), Present-day crustal deformation and plate kinematics in the Middle East constrained by GPS measurements in Iran and northern Oman, *Geophysical Journal International*, *157*(1), 381–398, doi:https://doi.org/10.1111/j.1365-246X.2004.02222.x. 1.4, 2.2.1

Walker, R., and J. Jackson (2004), Active tectonics and late Cenozoic strain distribution in central and eastern Iran, *Tectonics*, doi:10.1029/2003TC001529. 1.4, 2.2.1

Walker, R., J. Jackson, and C. Baker (2003), Surface expression of thrust faulting in eastern Iran: source parameters and surface deformation of the 1978 Tabas and 1968 Ferdows earthquake sequences, *Geophysical Journal International*, *152*(3), 749–765, doi:10.1046/j.1365-246X.2003.01886.x. 2.1

Walker, R. T., Y. Bezmenov, G. Begenjev, S. Carolin, N. Dodds, C. Gruetzner, J. Jackson, R. Mirzin, and E. Rhodes (2021), Slip-rate on the Main Kopetdag (Kopeh Dagh) Strike-slip fault, Turkmenistan, and the active tectonics of the South Caspian, *Tectonics*. 1.3, 1.4, 1.4, 2.1, 2.1, 2.2.1, 2.2.2, 2.3, 2.4.1, 2.4.2, 2.2, 2.5, 2.6, 3.1, 3.1, 3.2, 3.5, 3.2.2, 3.3.1, 3.3.2, 3.4.3, 3.4.4, 3.4.4, 3.11, 3.5, 3.1, 4.1, 4.2, 4.1, 4.3, 4.14, 4.15, 4.20, 4.21, 4.23, 4.24, 4.4, 4.4.1, 4.32, 4.4.5, 4.5, 5, 5.1

Walpersdorf, A., D. Hatzfeld, H. Nankali, F. Tavakoli, F. Nilforoushan, M. Tatar, P. Vernant, J. Chéry, and F. Masson (2006), Difference in the GPS deformation pattern of North and Central Zagros (Iran), *Geophysical Journal International*, *167*(3), 1077–1088, doi:https://doi.org/10.1111/j.1365-246X.2006.03147.x. 1.4

Walpersdorf, A., I. Manighetti, Z. Mousavi, F. Tavakoli, M. Vergnolle, A. Jadidi, D. Hatzfeld, A. Aghamohammadi, A. Bigot, Y. Djamour, H. Nankali, and M. Sedighi (2014), Present-day kinematics and fault slip rates in eastern Iran, derived from 11 years of GPS data, *Journal of Geophysical Research: Solid Earth*, *119*(2), 1359–1383, doi:https://doi.org/10.1002/2013JB010620. 1.4, 1.4, 2.2.1

Walters, R. J., J. R. Elliott, Z. Li, and B. Parsons (2013), Rapid strain accumulation on the Ashkabad fault (Turkmenistan) from atmosphere-corrected InSAR, *Journal of Geophysical Research: Solid Earth*, *118*(7), 3674–3690, doi:10.1002/jgrb.50236. 1.4, 1.4, 2.1, 2.2.1, 2.5, 3.1, 3.2, 3.1, 3.2.1, 3.3.2, 3.4.3, 3.1, 4.1, 4.1, 4.2.2, 4.3.2, 4.4, 5

Wang, J. (2004), Historical earthquake investigation and research in China, *Annals of Geophysics; Vol 47, No 2-3 (2004)DO - 10.4401/ag-3337*. 1.3

Weatherall, P., K. M. Marks, M. Jakobsson, T. Schmitt, S. Tani, J. E. Arndt, M. Rovere, D. Chayes, V. Ferrini, and R. Wigley (2015), A new digital bathymetric model of the world's oceans, *Earth and Space Science*, *2*(8), 331–345, doi:https://doi.org/10.1002/2015EA000107. 3.1, 4.1

Weiss, J. R., R. J. Walters, Y. Morishita, T. J. Wright, M. Lazecky, H. Wang, E. Hussain, A. J. Hooper, J. R. Elliott, C. Rollins, C. Yu, P. J. González, K. Spaans, Z. Li, and B. Parsons (2020), High-Resolution Surface Velocities and Strain for Anatolia From Sentinel-1 InSAR and GNSS Data, *Geophysical Research Letters*, *47*(17), e2020GL087,376, doi:https://doi.org/10.1029/2020GL087376. (document), 1.2, 1.4, 4.1, 4.3.1, 4.3.4, 4.4.5, 4.37

Weldon, R., K. Scharer, T. Fumal, and G. Biasi (2004), Wrightwood and the earthquake cycle: What a long recurrence record tells us about how faults work, *GSA Today*, *14*(9), 4–10, doi:10.1130/1052-5173(2004)014¡4:WATECW¿2.0.CO;2. 1.3

Wells, D. L., and K. J. Coppersmith (1994), New empirical relationships among magnitude, rupture length, rupture width, rupture area, and surface displacement, *Bulletin of the Seismological Society of America*, *84*(4), 974–1002. 2.5

Wesnousky, S. G. (2006), Predicting the endpoints of earthquake ruptures, *Nature*, *444*(7117), 358–360, doi:10.1038/nature05275. 2.5, 5

Wessel, P., and W. H. F. Smith (1995), New version of the generic mapping tools, *Eos, Transactions American Geophysical Union*, *76*(33), 329, doi:https://doi.org/10.1029/95EO00198. 2.6

Wimpenny, S. (2020), Global Waveform Catalogue (gWFM) v1.0, *Global Waveform Catalogue*, doi:http://doi.org/10.5281/zenodo.3782608. 3.1, 4.1

Wright, T., B. Parsons, and E. Fielding (2001), Measurement of interseismic strain accumulation across the North Anatolian Fault by satellite radar interferometry, *Geophysical Research Letters*, *28*(10), 2117–2120, doi:https://doi.org/10.1029/2000GL012850. 1.2

Wright, T. J., Z. Lu, and C. Wicks (2003), Source model for the Mw 6.7, 23 October 2002, Nenana Mountain Earthquake (Alaska) from InSAR, *Geophysical Research Letters*, *30*(18), doi:https://doi.org/10.1029/2003GL018014. 2.5

Wright, T. J., J. R. Elliott, H. Wang, and I. Ryder (2013), Earthquake cycle deformation and the Moho: Implications for the rheology of continental lithosphere, *Tectonophysics*, *609*, 504–523, doi:10.1016/j.tecto.2013.07.029. 3.1

Yu, C., N. T. Penna, and Z. Li (2017), Generation of real-time mode high-resolution water vapor fields from GPS observations, *Journal of Geophysical Research*, *122*(3), 2008–2025, doi:10.1002/2016JD025753. 3.2.1, 4.2.1, 5.1

Yu, C., Z. Li, and N. T. Penna (2018a), Interferometric synthetic aperture radar atmospheric correction using a GPS-based iterative tropospheric decomposition model, *Remote Sensing of Environment*, *204*(October 2017), 109–121, doi:10.1016/j.rse.2017.10.038. 3.2.1, 4.2.1

Yu, C., Z. Li, N. T. Penna, and P. Crippa (2018b), Generic Atmospheric Correction Model for Interferometric Synthetic Aperture Radar Observations, *Journal of Geophysical Research: Solid Earth*, *123*(10), 9202–9222, doi:10.1029/2017JB015305. 3.2.1, 4.2.1, 5.1

Zhou, Y., J. R. Elliott, B. Parsons, and R. T. Walker (2015), The 2013 Balochistan earthquake: An extraordinary or completely ordinary event?, *Geophysical Research Letters*, *42*(15), 6236–6243, doi:10.1002/2015GL065096. 2.1

Zielke, O., J. R. Arrowsmith, L. G. Ludwig, and S. O. Akciz (2010), Slip in the 1857 and Earlier Large Earthquakes Along the Carrizo Plain, San Andreas Fault, *Science*, *327*(5969), 1119–1122, doi:10.1126/science.1182781. 1.3, 2.4.3

Zielke, O., Y. Klinger, and J. R. Arrowsmith (2015), Tectonophysics Fault slip and earthquake recurrence along strike-slip faults — Contributions of high-resolution geomorphic data, *Tectonophysics*, *638*, 43–62, doi:10.1016/j.tecto.2014.11.004. 1.4, 2.4.3

Zinke, R., J. F. Dolan, E. J. Rhodes, R. Van Dissen, and C. P. McGuire (2017), Highly Variable Latest Pleistocene-Holocene Incremental Slip Rates on the Awatere Fault at Saxton River, South Island, New Zealand, Revealed by Lidar Mapping and Luminescence Dating, *Geophysical Research Letters*, *44*(22), 11,301–311,310, doi:https://doi.org/10.1002/2017GL075048. 1.3

Appendix A

InSAR LOS definitions, decompositions and derivations

A.1 Definition of the InSAR line-of-sight in a Cartesian reference

The InSAR line-of-sight (LOS) velocity, V_{LOS}, can be defined by a vector in a Cartesian reference (north–south, east–west, vertical), using the LOS incidence angle, θ, measured from the vertical, and the LOS heading angle, ϕ, measured clockwise from north, with associated uncertainty σ_{LOS} (the geometry of the ascending and descending LOS is displayed in Figure A.1; β is the angle between the projection of the LOS in the horizontal plane and the north-south axis.),

$$\begin{aligned} V_{LOS} &= -V_E \cos\phi \sin\theta + V_N \sin\phi \sin\theta + V_U \cos\theta \,, \\ \sigma_{LOS} &= \sqrt{(-\sigma_E \cos\phi \sin\theta)^2 + (\sigma_N \sin\phi \sin\theta)^2 + (\sigma_U \cos\theta)^2} \,, \end{aligned} \tag{A.1}$$

where V_E, V_N, V_U, are the velocity, and σ_E, σ_N, σ_U, are their associated uncertainty, in the respective Cartesian axis directions.

The LOS geometry results in the different components affecting V_{LOS} and

σ_{LOS} differently. V_E is the predominant contribution to V_{LOS}, with a moderate contribution to σ_{LOS}. The LOS geometry is insensitive to V_N, therefore V_N and σ_N provide negligible contributions to both the LOS velocity and uncertainty. Whilst σ_U dominates the contribution to σ_{LOS} and is greater in magnitude than the contribution of V_U to V_{LOS}.

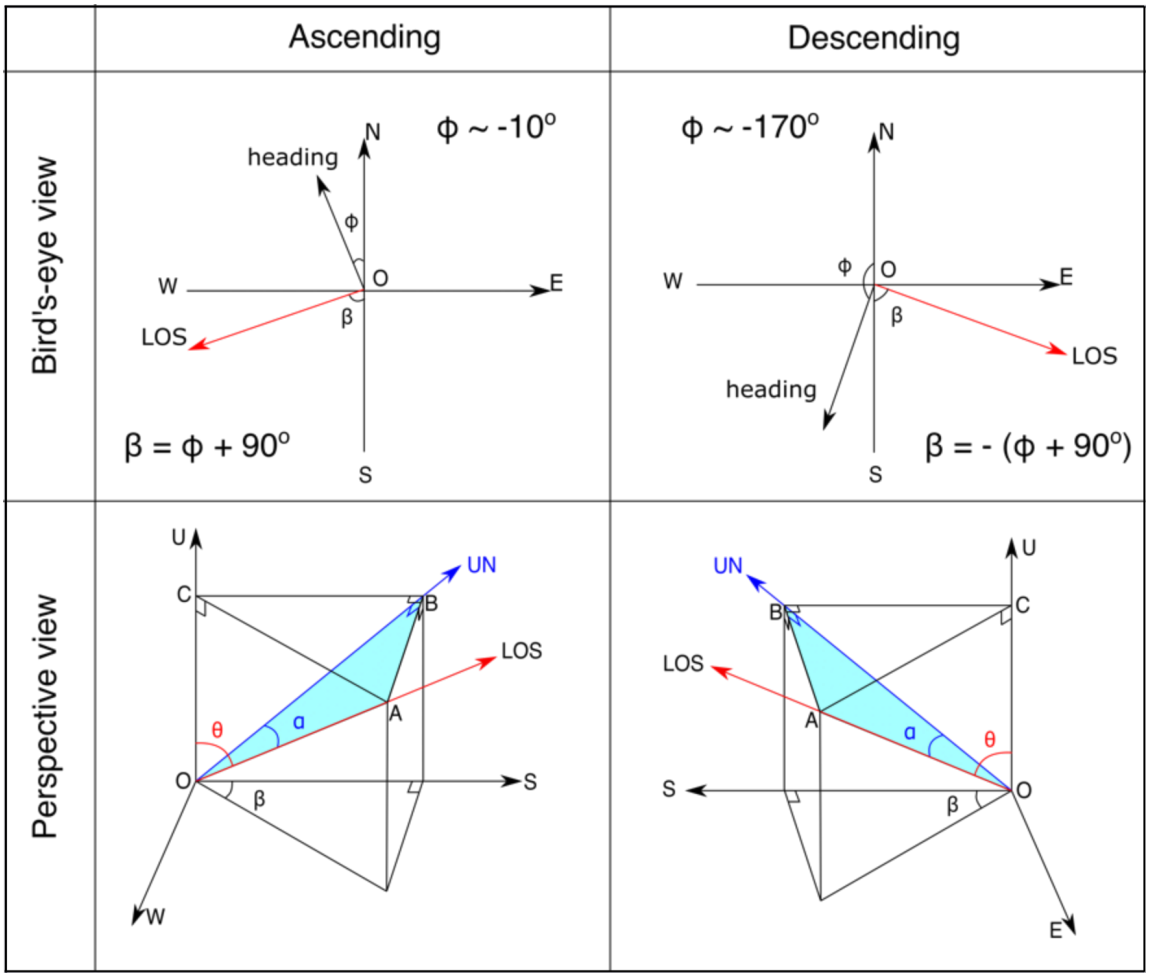


Figure A.1: Illustration of the definition of the LOS vector from a map view and perspective view (diagram from the thesis of Qi Ou, University of Oxford; 2020). The LOS incidence angle, θ, is measured from the vertical, and the LOS heading angle, ϕ, is measured clockwise from north. β is the angle between the projection of the LOS in the horizontal plane and the north-south axis, and α is the angle between the LOS vector and the V_{UN} plane. Note that there is an unrealistic perspective on the angle β in this sketch.

A.2 Decomposing InSAR LOS velocity fields to V_E and V_{UN}

The combination of the ascending and descending InSAR LOS velocity fields, allows for two velocity components to be resolved. Therefore following the approach of Lin Shen from the University of Leeds (personal communication), this geometry allows for the ascending and descending LOS to be decomposed into a V_E and V_{UN} (sub-vertical) component as follows,

$$V_{LOS} = -V_E \cos\phi \sin\theta + V_{UN} \cos\alpha \,, \tag{A.2}$$

where α is the angle between the LOS vector and the V_{UN} plane (Figure A.1; this assumes that the value of α is constant for all pixels). Through further inspection, the geometry of the LOS vector can be used to express $\cos\alpha$ in terms of θ and ϕ. Starting by recognising that $AB = OA \sin\alpha$, and $AB = AC \sin\beta = OA \sin\theta \sin\beta$, can be combined to give, $\sin\alpha = \sin\theta \sin\beta$. Following this, observing that $\sin^2\beta = \cos^2\phi$ (and the trigonometric identity $\cos^2\alpha = 1 - \sin^2\alpha$) is used to show that,

$$\cos\alpha = \sqrt{1 - \sin^2\theta \sin^2\beta} = \sqrt{1 - \sin^2\theta \cos^2\phi} \,. \tag{A.3}$$

The resulting expression decomposes V_{LOS} into V_E and V_{UN}, importantly expressed using only the known values for θ and ϕ,

$$V_{LOS} = -V_E \cos\phi \sin\theta + V_{UN} \sqrt{1 - \sin^2\theta \cos^2\phi} \,. \tag{A.4}$$

A.3 A method to merge InSAR LOS velocity fields across adjacent tracks

A potential method to merge the LOS velocity fields across adjacent tracks (V_{LOS_1}, V_{LOS_2}) (with the same look direction, and assuming the difference in heading, ϕ, is negligible).

The difference, x, in incidence angle, θ, between the LOS in the overlapping region of adjacent tracks can be used to describe the LOS velocity of a pixel in the overlapping region of adjacent tracks,

$$\begin{aligned} V_{LOS_1} &= -V_E \cos\phi \sin\theta + V_N \sin\phi \sin\theta + V_U \cos\theta \,, \\ V_{LOS_2} &= -V_E \cos\phi \sin(\theta + x) + V_N \sin\phi \sin(\theta + x) + V_U \cos(\theta + x) \,. \end{aligned}$$

Using the trigonometric addition formulae,

$$\begin{aligned} \sin(A + B) &= \sin A \cos B + \sin B \cos A \,, \\ \cos(A + B) &= \cos A \cos B + \sin B \sin A \,, \end{aligned}$$

it is possible to reformulate V_{LOS_2} as,

$$\begin{aligned} V_{LOS_2} = &-V_E \cos\phi[\sin\theta \cos x + \cos\theta \sin x] \\ &+ V_N \sin\phi[\sin\theta \cos x + \cos\theta \sin x] \\ &+ V_U[\cos\theta \cos x + \sin\theta \sin x] \,. \end{aligned}$$

Recognising that it is possible to express this as $V_{LOS_2} = a\cos x + b\sin x$, where,

$$a = -V_E\cos\phi\sin\theta + V_N\sin\phi\sin\theta + V_U\cos\theta = V_{LOS_1}\,,$$
$$b = -V_E\cos\phi\cos\theta + V_N\sin\phi\cos\theta + V_U\sin\theta = \frac{\mathrm{d}V_{LOS_1}}{\mathrm{d}\theta}\,.$$

We can simplify the equation further using the harmonic identity $a\cos x + b\sin x = R\cos(x-\alpha)$, to express V_{LOS_2} in terms of V_{LOS_1}, $\frac{\mathrm{d}V_{LOS_1}}{\mathrm{d}\theta}$ and x; where $R = \sqrt{a^2+b^2}$ and $\alpha = \tan^{-1}(\frac{b}{a})$.

It is important to recognise that the incidence angle only changes in the range direction, so it is only necessary to calculate the derivative of the scalar field $\frac{\mathrm{d}V_{LOS_1}}{\mathrm{d}\theta}$ in the range direction. However there are significant difficulties calculating derivatives of observational data as this is a noise amplifying process, so we envisage the need for low-pass filtering of the LOS velocity time-series rate-maps prior to referencing.

Appendix B

Supplementary Data

B.1 Chapter 2 Supplementary Material

Table B.1: Measured fault-displaced geomorphic features along the MKDF that contribute to COPD analysis. Locations are in EPSG:32640, WGS 84/UTM Zone 40N), with the location ID corresponding to supplementary KML file. Strike X/Y are the projection along strike of the MKDF from the location of the westernmost recorded offset (used for plotting distribution of measurements along strike). Offsets measurements follow the methods in *Kurtz et al.* (2018). Quality ratings are from 1=high to 3=low; measurements are preferred, minimum and maximum (in m).

Easting	**Northing**	**Loc. ID**	**Strike X (m)**	**Strike Y (m)**	**Quality**	**Pref. (m)**	**Min. (m)**	**Max. (m)**
428717.09	4309328.63	1	0	0	1	10.6	8.0	13.9
430265.67	4308240.65	2	1890	-102	3	10.8	7.8	18.4
430428.04	4308161.61	3	2069	-83	3	9.6	6.7	14.4
430690.29	4307968.61	4	2394	-108	2	18.9	13.6	24.4
431778.06	4307361.41	5	3638	-46	2	33.7	27.8	44.4
431958.91	4307245.50	6	3853	-49	3	9.9	6.8	14.2
431987.20	4307234.47	7	3883	-43	2	9.1	6.6	11.1
432120.77	4307179.33	8	4025	-19	3	39.4	32.4	50.0

432163.66	4307162.58	9	4071	-11	2	6.9	5.2	9.6
432504.94	4307006.54	10	4443	38	2	104.3	94.8	142.7
432564.58	4306966.51	11	4515	36	3	28.9	19.9	46.2
432725.11	4306850.51	12	4712	22	1	14.1	10.0	19.1
432803.13	4306813.74	13	4798	33	2	13.0	9.0	19.1
432980.82	4306750.02	14	4982	73	2	13.7	10.1	21.1
433257.36	4306574.79	15	5310	71	1	29.7	23.6	34.3
433445.25	4306472.67	16	5523	84	2	9.0	6.6	10.6
433513.47	4306458.78	17	5588	108	3	13.9	10.3	17.9
433590.26	4306386.48	18	5692	87	1	81.4	62.2	88.9
433655.01	4306333.58	19	5775	77	3	23.8	15.9	27.7
434080.23	4306064.80	20	6278	74	2	22.1	17.5	29.6
434096.98	4306059.08	21	6295	78	1	22.3	16.1	27.9
434165.19	4306023.14	22	6372	84	3	14.2	10.8	19.9
434309.39	4305936.95	23	6540	87	1	22.0	13.5	30.5
434845.72	4305649.79	24	7147	128	2	19.9	15.2	22.1
435170.86	4305489.67	25	7507	164	3	91.5	64.7	117.6
435313.01	4305421.04	26	7664	181	2	85.2	59.6	105.5
435790.11	4305143.28	27	8216	199	2	11.4	7.7	18.0
436194.91	4304895.74	28	8691	203	3	17.4	13.4	32.1
436807.83	4304513.61	29	9413	204	2	15.1	9.9	20.0
436854.40	4304452.75	30	9485	177	1	13.9	9.6	16.9
437116.64	4304280.37	31	9798	170	3	9.5	7.7	14.3
437212.63	4304224.82	32	9909	174	3	9.9	7.3	13.9
437320.88	4304161.92	33	10034	178	3	63.6	43.0	72.5
437387.46	4304120.25	34	10113	178	3	4.8	3.0	7.1
437745.28	4303917.24	35	10524	195	2	15.9	13.0	20.5

437773.47	4303889.46	36	10563	186	2	15.8	12.5	20.2
438136.60	4303681.96	37	10980	203	2	14.8	9.3	18.1
438301.63	4303591.68	38	11168	214	2	11.6	7.9	14.3
439045.26	4303135.41	39	12041	221	1	10.1	7.4	15.3
439348.76	4302933.22	40	12405	210	1	12.9	8.6	16.4
439377.35	4302907.08	41	12443	203	1	14.4	11.8	18.4
439476.61	4302836.21	42	12565	196	3	12.5	10.1	18.0
439559.33	4302877.46	43	12613	275	2	6.2	4.8	9.6
439994.15	4302568.45	44	13146	243	3	9.0	6.8	11.2
440083.61	4302491.04	45	13263	225	2	8.7	7.0	12.9
440139.98	4302451.01	46	13332	221	3	6.2	4.5	7.9
440436.53	4302253.31	47	13688	210	1	7.0	5.6	10.1
440595.43	4302150.58	48	13877	207	2	6.7	4.9	11.3
440721.85	4302042.54	49	14042	183	1	6.5	5.3	9.3
440839.49	4301959.00	50	14186	174	2	8.8	6.6	12.3
441197.73	4301748.02	51	14601	185	1	16.2	11.0	21.3
441497.55	4301544.20	52	14964	171	3	7.9	6.5	11.5
441685.45	4301405.11	53	15197	153	3	8.2	6.6	11.1
441765.10	4301351.60	54	15293	149	2	5.2	4.0	6.5
441900.82	4301260.81	55	15456	144	1	10.5	8.2	14.0
442485.24	4300926.58	56	16128	171	1	29.6	17.4	44.2
443082.03	4300512.18	57	16854	135	1	6.1	4.2	9.4
443213.97	4300444.17	58	17002	148	2	7.8	5.4	10.5
443629.39	4300195.00	59	17486	157	1	14.5	11.8	16.9
443744.98	4300100.64	60	17634	138	1	6.4	5.1	9.9
443819.74	4300047.54	61	17726	132	1	12.3	10.0	15.5
443876.72	4300011.18	62	17794	132	2	5.5	3.3	7.2

443997.22	4299941.54	63	17933	137	1	4.5	3.3	6.0
444019.28	4299925.61	64	17960	135	1	5.1	3.5	6.7
444142.64	4299840.64	65	18109	128	3	17.3	11.5	21.1
444174.29	4299816.54	66	18149	124	1	5.5	3.8	6.9
444266.00	4299734.85	67	18270	104	2	6.2	3.4	8.6
444406.10	4299632.53	68	18443	91	2	14.1	9.4	18.3
444506.59	4299571.25	69	18561	92	2	10.6	6.8	15.5
444608.71	4299503.86	70	18683	89	3	28.9	20.1	43.5
444669.98	4299472.40	71	18752	95	3	60.4	37.5	92.2
444760.66	4299380.50	72	18877	65	3	32.7	21.3	40.8
444877.89	4299217.51	73	19063	-11	3	10.1	6.9	12.9
445423.62	4298823.54	74	19735	-56	1	9.0	6.3	12.6
446516.29	4298081.34	75	21055	-106	2	9.2	5.5	14.7
449046.80	4296627.98	76	23971	2	1	8.1	5.0	12.3
449364.19	4296458.46	77	24330	27	3	8.7	5.9	12.9
449647.26	4296277.51	78	24666	23	2	7.5	5.4	12.9
450067.79	4296050.80	79	25143	54	3	34.6	25.2	45.9
450205.45	4295996.47	80	25288	81	2	7.7	6.2	10.7
450345.96	4295850.85	81	25484	32	1	7.9	5.8	10.6
450627.81	4295686.85	82	25810	42	2	17.7	14.6	21.3
450686.63	4295644.78	83	25883	38	1	7.8	5.6	11.2
450900.26	4295487.10	84	26147	17	1	10.2	7.6	13.5
451182.52	4295322.90	85	26474	27	2	12.4	10.3	14.9
451266.26	4295242.84	86	26587	4	3	13.6	11.1	18.9
451308.33	4295278.78	87	26604	57	3	15.7	11.0	21.1
451001.97	4295412.35	88	26273	8	1	11.4	8.8	13.9
451416.17	4295188.51	89	26743	37	2	11.8	8.1	16.7

451637.15	4295012.05	90	27024	5	3	20.2	16.2	27.3
451875.30	4294853.56	91	27310	-4	2	69.7	51.8	81.9
452251.09	4294657.49	92	27732	29	2	15.6	8.6	17.0
453619.32	4293767.44	93	29364	0	2	6.8	4.6	9.6
453214.28	4294018.22	94	28888	-2	2	19.7	13.7	24.8
453437.31	4293891.19	95	29145	8	2	11.2	7.5	15.0
453585.59	4293780.69	96	29329	-7	2	9.2	5.9	12.7
453672.39	4293770.69	97	29408	30	2	12.8	9.2	18.5
453815.35	4293627.31	98	29605	-15	2	15.7	9.0	16.7
453920.13	4293587.94	99	29715	7	2	10.8	6.7	12.9
454419.70	4293260.35	100	30312	-6	1	98.8	86.4	106.0
454502.62	4293187.94	101	30421	-24	2	86.6	66.5	102.7
454651.30	4293132.60	102	30576	8	1	24.7	20.8	27.0
454687.45	4293103.19	103	30622	2	2	27.5	17.6	34.8
454996.87	4292990.24	104	30945	70	1	11.4	8.6	13.3
455060.39	4292966.14	105	31011	84	2	10.7	8.1	15.3
455244.20	4292911.81	106	31196	135	2	28.5	20.6	39.7
455314.46	4292897.93	107	31263	160	1	26.4	17.2	34.8
455298.12	4292816.23	108	31292	82	1	34.0	25.7	44.6
455427.20	4292758.23	109	31432	102	2	73.3	57.4	84.9
455726.62	4292617.30	110	31761	141	1	17.9	12.7	28.4
455952.09	4292475.15	111	32028	140	1	21.6	16.7	32.4
456169.81	4292312.99	112	32298	118	1	27.4	21.3	35.2
456207.39	4292295.42	113	32339	123	1	22.0	16.2	27.0
456665.70	4291889.40	114	32943	21	1	19.5	13.0	24.4
456975.33	4291897.98	115	33201	193	2	15.6	10.8	18.7
457034.15	4291865.71	116	33268	196	1	6.0	4.3	7.1

457157.10	4291625.52	117	33500	58	1	18.6	14.2	25.7
457356.44	4291692.51	118	33633	220	1	22.2	16.9	25.7
458058.23	4291032.80	119	34578	33	1	42.5	34.4	48.4
457739.18	4291452.74	120	34085	220	2	44.2	31.2	51.3
457804.53	4291335.91	121	34202	155	1	14.0	8.3	19.3
457937.70	4291221.95	122	34376	129	2	40.2	28.7	58.2
457654.22	4291251.36	123	34120	4	3	12.9	7.8	15.6
457478.77	4291425.37	124	33879	59	2	20.1	15.8	32.1
458092.61	4290976.45	125	34637	3	2	9.0	6.1	13.4
458569.30	4290779.16	126	35146	88	3	9.6	6.8	14.5
458550.31	4290407.65	127	35327	-237	2	36.9	26.4	65.2
459085.01	4290347.20	128	35812	-5	1	42.5	31.8	64.6
458846.46	4290044.11	129	35770	-388	1	76.2	68.0	98.9
460663.77	4289184.47	130	37767	-154	2	8.0	5.8	11.9
460510.38	4289278.83	131	37587	-155	2	6.7	3.3	13.5
461018.53	4288962.67	132	38185	-154	1	18.5	13.0	22.7
461254.22	4288797.23	133	38473	-170	1	9.6	6.4	11.7
461440.08	4288602.80	134	38734	-236	1	8.0	6.0	12.5
461459.68	4288584.42	135	38760	-241	2	8.0	6.0	10.8
461670.05	4288739.23	136	38856	2	3	14.1	10.4	17.1
463597.24	4287502.98	137	41146	-26	2	9.5	6.7	11.6
463699.15	4287452.73	138	41259	-14	3	21.2	16.0	24.6
464035.94	4287138.82	139	41711	-102	1	47.0	36.9	54.9
464258.97	4286923.96	140	42014	-166	1	11.1	7.7	13.8
464619.45	4286532.44	141	42527	-307	3	11.0	8.4	14.4
464635.79	4286494.45	142	42561	-330	1	11.8	8.7	16.1
465701.30	4285510.63	143	43986	-600	2	41.8	34.1	60.4

465036.71	4286041.86	144	43141	-502	2	29.0	23.8	40.8
466241.10	4284827.86	145	44806	-893	2	17.0	12.5	21.3
466393.06	4284721.86	146	44991	-903	2	9.1	5.6	13.3
466706.76	4284529.47	147	45359	-899	1	11.6	9.2	16.2
466947.77	4284377.93	148	45643	-900	2	10.8	8.6	16.2
467040.49	4284320.74	149	45752	-900	2	14.1	11.2	18.0
467061.83	4284300.21	150	45781	-906	3	10.1	7.0	13.5
467184.99	4284214.03	151	45931	-914	2	65.6	48.8	77.9
468042.79	4283691.99	152	46935	-902	1	46.6	38.5	63.3
468309.12	4283512.26	153	47257	-913	2	60.1	43.7	79.6
468756.81	4283223.06	155	47789	-921	2	23.7	12.1	29.6
468861.38	4283163.02	156	47910	-916	1	13.3	7.9	16.6
469297.63	4282882.39	157	48429	-923	2	25.1	20.7	36.5
469866.64	4282500.06	158	49114	-946	1	12.4	9.8	18.0
470019.41	4282410.60	159	49291	-941	1	11.7	9.2	14.6
470050.04	4282386.50	160	49329	-945	2	9.9	7.4	14.9
470341.69	4282226.38	161	49662	-926	2	14.1	11.8	19.8
470384.38	4282197.58	162	49713	-928	1	17.2	11.9	20.6
470610.47	4282057.68	163	49979	-927	2	83.6	63.7	117.6
471515.86	4281556.89	164	51012	-872	3	13.9	10.2	18.2
471807.92	4281409.22	165	51338	-842	2	34.9	29.3	39.6
471966.41	4281320.99	166	51519	-833	1	38.6	31.8	51.4
472273.58	4281165.57	167	51862	-802	2	10.9	7.7	14.4
472378.15	4281113.90	168	51978	-791	3	7.4	5.4	9.2
472612.62	4281021.58	169	52226	-745	1	13.5	10.6	18.4
472787.85	4280954.18	170	52410	-709	3	20.7	16.0	24.0
472943.07	4280877.18	171	52583	-692	3	17.1	12.5	22.0

473097.68	4280814.28	172	52747	-663	3	21.7	15.4	28.2
473217.37	4280747.49	173	52884	-657	1	44.1	37.5	49.1
473243.92	4280751.99	174	52904	-639	2	44.4	36.4	48.0
473391.99	4280708.89	175	53053	-597	3	22.4	17.3	27.3
450490.35	4295806.23	176	25631	70	1	14.8	10.4	22.6
473587.65	4280627.20	177	53262	-562	3	13.7	10.6	16.1
473626.46	4280616.17	178	53301	-551	3	14.8	11.1	18.2
473865.01	4280516.29	179	53556	-509	2	9.6	6.7	12.3
474249.99	4280338.81	180	53976	-456	1	16.3	8.5	20.9
474474.35	4280311.55	181	54181	-360	3	9.4	6.5	12.2
474699.83	4280215.96	182	54423	-322	2	15.1	10.7	22.3
474882.42	4280157.55	183	54609	-275	2	26.6	20.2	36.1
475169.17	4280038.28	184	54915	-224	2	24.0	17.2	31.6
475263.12	4280006.41	185	55012	-201	1	6.3	4.1	9.7
475604.60	4279842.62	186	55388	-159	2	11.2	8.2	14.0
475825.59	4279716.40	187	55642	-149	3	17.0	12.3	24.9
476287.17	4279497.45	188	56150	-90	1	9.5	7.3	13.3
477798.53	4278732.79	189	57837	62	2	23.6	18.7	29.4
477817.73	4278708.07	190	57866	52	2	8.2	6.1	12.2
478839.74	4278061.66	191	59075	45	3	12.4	9.0	16.4
479136.09	4277823.31	192	59453	0	2	14.7	10.8	18.7
479355.44	4277660.33	193	59725	-22	3	9.3	4.5	11.2
479425.29	4277613.36	194	59810	-25	1	7.1	4.3	9.7
479743.60	4277358.59	195	60214	-72	1	29.4	21.7	35.3
479873.39	4277245.52	196	60384	-99	2	15.2	9.4	21.6
480031.67	4277137.89	197	60576	-107	3	28.6	18.1	38.3
480118.47	4277070.49	198	60685	-118	2	11.6	8.8	16.1

480393.78	4276854.82	199	61033	-155	1	18.2	13.9	23.4
481001.19	4276411.01	200	61783	-209	1	15.5	8.2	25.1
481345.13	4276152.85	201	62212	-246	2	25.2	18.5	36.4
481470.12	4276048.89	202	62373	-268	2	10.4	7.7	16.4
482304.84	4275540.95	203	63350	-256	2	65.9	53.3	79.4
483906.89	4274667.63	204	65171	-148	2	116.1	79.5	139.4
484274.92	4274432.75	205	65608	-152	1	8.0	4.7	14.6
484225.91	4274413.97	206	65576	-194	1	15.2	8.5	21.8
484170.35	4274529.77	207	65468	-125	3	25.6	19.6	43.4
484431.57	4274275.29	208	65824	-203	2	12.9	7.1	16.6
484576.17	4274153.36	209	66011	-230	2	15.5	11.3	21.8
484578.01	4274137.02	210	66021	-242	1	12.3	8.6	18.4
484727.31	4274023.05	211	66208	-260	1	8.2	5.5	10.3
484765.09	4274001.20	212	66252	-258	2	7.7	6.0	11.1
484777.55	4273992.01	213	66268	-260	1	8.5	4.8	13.8
484786.54	4273980.37	214	66281	-265	1	6.7	3.8	11.1
484883.14	4273903.37	215	66404	-279	2	7.3	3.0	10.3
484910.51	4273886.01	216	66436	-279	3	9.7	6.7	14.1
484983.83	4273816.16	217	66536	-299	3	18.7	13.7	25.8
485447.25	4273525.84	218	67082	-300	3	18.3	13.0	23.5
485511.28	4273497.96	219	67152	-290	2	7.2	5.0	11.0
485525.78	4273491.93	220	67167	-287	1	9.0	6.4	11.9
485553.45	4273487.23	221	67193	-277	2	8.3	5.9	13.2
485563.66	4273481.92	222	67204	-276	2	12.0	7.6	15.5
485668.64	4273411.67	223	67331	-280	2	19.1	12.3	24.6
485706.63	4273380.21	224	67380	-286	1	33.8	28.9	42.2
485728.89	4273382.87	225	67397	-272	1	11.8	8.7	21.0

485869.21	4273295.25	226	67563	-272	3	38.3	33.2	48.5
485940.28	4273252.77	227	67645	-270	3	33.7	27.6	39.3
486165.76	4273066.91	228	67935	-309	2	49.0	38.6	58.5
486186.59	4273057.11	229	67958	-306	1	28.5	19.4	35.9
486339.06	4272939.67	230	68149	-325	2	8.6	6.3	11.9
486359.79	4272936.10	231	68169	-317	1	11.1	7.8	13.8
486354.58	4272917.82	232	68174	-335	1	10.8	7.4	16.1
486386.54	4272909.04	233	68206	-325	1	7.6	5.4	10.9
486465.78	4272859.61	234	68299	-325	3	5.4	3.1	9.3
486692.08	4272752.59	235	68548	-296	3	8.1	4.5	10.9
486964.74	4272560.20	236	68881	-315	1	7.4	4.6	8.5
486971.89	4272541.00	237	68897	-327	2	12.4	8.4	16.5
487600.12	4272160.09	238	69632	-317	2	6.5	3.5	9.0
488933.32	4271329.53	239	71203	-315	3	15.9	11.9	20.7
488960.08	4271316.87	240	71232	-312	3	18.7	9.5	24.4
489074.75	4271234.05	241	71373	-321	3	18.7	6.7	25.6
489474.14	4270972.73	242	71850	-331	2	8.3	5.4	10.9
489755.68	4270777.79	243	72192	-347	1	15.6	11.6	19.0
450351.06	4295880.27	244	25473	59	1	6.9	5.5	9.3
450394.77	4295858.21	245	25522	64	1	7.3	4.5	9.6
450426.83	4295848.41	246	25554	73	2	9.3	6.6	13.6
451500.00	4295025.94	247	26900	-56	3	8.8	3.4	11.6